Validating a new *in vitro* model for dynamic fluid shear stress mechanobiology

Russell Peter Tucker

Department of Engineering Science

University of Oxford

A thesis submitted for the degree of

Doctor of Philosophy in Engineering Science

Trinity 2013

Abstract

Validating a new *in vitro* model for dynamic fluid shear stress mechanobiology

Russell Peter Tucker

Doctor of Philosophy in Engineering Science

Wadham College

Trinity 2013

In vitro mechanotransduction studies, uncovering the basic science of the response of cells to mechanical forces, are essential for progress in tissue engineering and its clinical application. Many varying investigations have described a multitude of cell responses, however as the precise nature and magnitude of the stresses applied are infrequently reported and rarely validated, the experiments are often not comparable, limiting research progress.

This thesis provides physical and biological validation of a widely available fluid stimulation device, a see-saw rocker, as an *in vitro* model for cyclic fluid shear stress mechanotransduction. This allows linkage between precisely characterised stimuli and cell monolayer response in a convenient six-well plate format.

Computational fluid dynamic models of one well were analysed extensively to generate convergent, stable and consistent predictions of the cyclic fluid velocity vectors at a rocking frequency of 0.5 Hz, accounting for the free surface.

Validation was provided by comparison with flow velocities measured experimentally using particle image velocimetry. Qualitative flow behaviour was matched and quantitative analysis showed good agreement at representative locations and time points. A maximum shear stress of 0.22 Pa was estimated near the well edge, and time-average shear stress ranged between 0.029 and 0.068 Pa, within the envelope of previous musculoskeletal *in vitro* fluid flow investigations.

The CFD model was extended to explore changes in culture medium viscosity, rocking frequency and the robustness to position on the rocking platform. Shear stress magnitude was shown to increase almost linearly with an increase in the viscosity of culture medium. Compared with 0.5 Hz, models at 0.083 and 1.167 Hz, the operational

limits of the see-saw rocker, indicated a change in shear stress patterns at the cell layer, and a reduction and increase in mean shear stress respectively. At the platform edge at 0.5 Hz, a 1.67-fold increase in time-average shear stress was identified.

Extensive biological validations using human tenocytes underlined the versatility of the simple *in vitro* device. The application of fluid-induced shear stress at 0.5 Hz under varying regimes up to 0.714 Pa caused a significant increase in secreted collagen ($p < 0.05$) compared to static controls. Tenocytes stimulated at a shear stress magnitude of 1.023 Pa secreted significantly less collagen compared to static controls. The potential for a local maximum in the relationship between collagen secretion rate and shear stress was identified, indicating a change from anabolic to catabolic behaviour. Collagen biochemical assay results were echoed with antibody stains for proteins, where a co-localisation of connexin-32 with collagen type-I was also identified. A custom algorithm showed that four hours of fluid-induced shear stress of 0.033 Pa intermittently applied to tenocytes encouraged alignment and elongation over an eight day period in comparison to static controls. Primary cilia were identified in human tenocyte cultures and bovine flexor tendon tissue; however primary cilium abrogation *in vitro* using chloral hydrate proved detrimental to cell viability. Collaborative investigations identified that ERK signalling and c-Fos transcription factor expression peaked after the application of 0.012 Pa at 0.083 Hz for 20 minutes and anabolic collagen gene expression relative quantities increased after 48 hours of rocking at 0.083 Hz.

In conclusion, validated shear stresses within a six-well plate, induced by cyclic flow from a see-saw rocker, provides an exceptional model for the *in vitro* study of dynamic fluid shear stress mechanobiology. Biological investigations have been linked to precise applied shear stress, creating a foundation for understanding the complex relationship between tenocytes and fluid-induced shear stress *in vitro*. Using this model, research is repeatable, comparable and accurately attributed to shear stress, accelerating the scientific advancement of musculoskeletal mechanobiology.

Acknowledgements

Thank you to...

- **Dr Mark Thompson** for guidance, illumination, edification, constant support, and belief in my abilities. I am forever indebted.
- **Dr Sarah Franklin** for schooling me in the art of cell culture, always having time, and being my biology guru.
- **Dr Philippa Hulley** for tenocytes, advice, and encouragement.
- **Prof Yiannis Ventikos** for all things CFD.
- **Dr Richard Bomphrey** for all things PIV.
- **Dr Per Henningsson** also for all things PIV.
- **Dr Andrew Jones** for joining me on the hunt for cilia.
- **Dr Nasim Zargar Baboldashti** for lunch at 12 without fail.
- **Tyler Grant** for solidarity in the face of adversity.
- **Dr Isaiah Adekanmbi** for showing me how it's done.
- **Sian Stokes** for moving to Oxford, and Jack's your one.
- **The Castle** for cups of tea and river swims.
- **Malie Ngoepe** for being my High Table date every Wednesday, and my CFD problem soundboard.
- **The Marlborough Gang** for 'have a tea', and a DIY hog-roast.
- **Wadham College** for letting me in, and giving me a scholarship.
- **EPSRC** for funding what has become an obsession.

Finally, thank you to...

- **Pryce & Kath** for supporting all of my endeavours.
- **Richard & Judy** for not thinking I was insane leaving a job to come and do this.
- **TMF** for being there every step of the way.

Publications

Journal Papers

- **Tucker, RP**; Franklin, SL; Chen; Ventikos, Y; Henningsson, P; Bomphrey, R; Thompson, MS 'See-saw rocking: a validated *in vitro* model for mechanotransduction research.' Royal Society Interface, 2013 (in press).
- **Tucker, RP**; Hulley, P; Thompson MS, 'An *in vitro* model predicts anabolic to catabolic transition in tendon cells with high cyclic fluid shear stress.' 2013 (in preparation).

Conference Proceedings

- Kalivodova, Z; Ingram, N; **Tucker, RP**; Thompson, MS; Hulley, P. 'Effect of nutrition and mechanical loading on human tenocyte metabolism.' BSMB, September 2013
- **Tucker, RP**; Jones, AK; Franklin, SL; Chen, D; Hulley, P; Ventikos, Y; Henningsson, P; Bomphrey, R; Thompson, MS. 'See-saw rocking: a validated fluid dynamics model for applying cyclic flow to cell monolayers.' ORS, January 2013
- Jones, AK; **Tucker, RP**; Pearson-Jones, T; Thompson, MS; Hulley P. 'Understanding mechanisms underlying mechanotransduction in tenocytes subjected to cyclic shear stress.' BSMB, September 2012
- **Tucker, RP**; Jones, AK; Bomphrey, R; Henningsson, P; Ventikos, Y; Hulley, P; Thompson, MS. 'Cyclic shear stress upregulates extracellular matrix secretion by human tenocytes: a model for understanding mechanotransduction in tendons.' BSMB, April 2012
- **Tucker, RP**; Franklin, SL; Chen, D; Ventikos, Y; Henningsson, P; Bomphrey, R; Thompson, MS. 'Validated cyclic shear stress significantly up-regulates ECM secretion by human tenocytes.' ESB, July 2012

- **Tucker, RP**; Franklin, SL; Chen, D; Bomphrey, R; Henningsson, P; Ventikos, Y; Thompson, MS. 'Computational fluid dynamics modelled cyclic shear stress significantly up-regulates collagen production in a validated in vitro stimulation device.' CMBBE, April 2012
- **Tucker, RP**; Franklin, SL; Chen, D; Bomphrey, R; Henningsson, P; Okech, W; Ventikos, Y; Thompson, MS. 'Validated In Vitro Cyclic Fluid Shear Stress Alters Human Tenocyte ECM Synthesis.' Histology and Histopathology: TERMIS, June 2011

Scholarships & Awards

- EPSRC Doctoral Grant Studentship
- Senior Scholar, Wadham College, University of Oxford
- European Society of Biomechanics Travel Award

Contents

List of Abbreviations

Ca^{2+}	Calcium ion
K^{+}	Potassium ion
LTB_4	Leukotriene B_4
Na^{+}	Sodium ion
PGE_2	Prostaglandin E_2
AMG	Algebraic Multi-Grid
AP1	Activator Protein 1
APC/C	Anaphase Promoting Complex
B-cat	Branched chain amino-acid transaminase 1
BMP	Bone Morphogenetic Protein
Bo	Bond number
CFD	Computational Fluid Dynamics
CFL	Courant-Friedrichs-Lewy
CGS	Conjugate Squared Solver
CMC	Carboxymethylcellulose
CMOS	Complementary Metal Oxide Semiconductor
COX-2	Cyclooxygenase-II
DAPI	4',6-diamidino-2-phenylindole
ddH_2O	double distilled water
DMB	Dimethylmethylene Blue
DMEM	Dulbecco's Modified Eagle Medium
dsDNA	double stranded Deoxyribonucleic Acid
DSH	Dishevelled gene
E2	Dinoprostone
ECM	Extra-Cellular Matrix
ERK1/2	Extracellular signal-Regulated Kinases
FCS	Foetal Calf Serum
FFT	Fast Fourier Transform
FUD	First-order Upwind Differencing
GAG	Glycosaminoglycans
Gly	Glycine
GPU	Graphical Processing Unit
HBSS	Hank's Balanced Salt Solution
HEPES	Hydroxy Ethyl Piperazine Ethane Sulfonic acid
hTSCs	human Tendon Stem Cells
IgG	Immunoglobin G
IL-1β	Interleukin-1β
MDCK	Madin-Darby Canine Kidney
MEK 1/2	Mitogen-activated protein Kinases
MMP-1	Matrix Metalloproteinase-1
MMP-3	Matrix Metalloproteinase-3
mRNA	messenger Ribonucleic Acid
mTOR	mammalian Target Of Rapamycin
Nd:YLF	Neodymium-doped yttrium lithium fluoride
P100	Transcription factor of the nuclear factor-kappaB
p21	Cyclin-dependent kinase inhibitor 1
PBS	Phosphate Buffered Saline
PBST	Phosphate Buffered Saline with Tween1000
PCM	Peri-Cellular Matrix

PCR Polymerase Chain Reaction

PDGF Platelet Dervived Growth Factors

PDGFαs Platelet Derived Growth Factor Alpha Receptors

PIV Particle Image Velocimetry

PLIC Piecewise Linear Interface Construction

POD Proper Orthogonal Decomposition

PS Penicillin and Streptomycin

qPCR quantitative Polymerase Chain Reaction

RAM Random Access Memory

Re Reynolds number

Rheb Ras homolog enriched in brain, GTP-binding protein

RMS Root Mean Square

Runx2 Core-binding factor subunit alpha-1

SIMPLEC Semi-Implicit Method for Pressure-Linked Equations Consistent

SLIC Single Line Interface Construction

STAT1 Signal Transducer and Activator of Transcription 1

STAT6 Signal Transducer and Activator of Transcription 6

SUD Second-order Upwind Differencing

TE Tris Ethylenediaminetetraacetic acid

TERMIS Tissue Engineering & Regenerative Medicine International Society

TGF Transforming Growth Factor

TI Transfinite Interpolation

TNF Tumor Necrosis Factor

TSC2 Tuberous sclerosis protein 2

UCMD Ullrich Congenital Muscular Dystrophy

UTS Ultimate Tensile Strength

VEGF Vascular Endothelial Growth Factor

VoF Volume of Fluid

We Weber number

Chapter 1

Introduction

1.1 Motivation & aims

The musculoskeletal system encompasses all tissues that allow the body to move and perform tasks (1). The functions of these tissues at the macroscopic scale are well known: bones provide structure that allow muscles to exert force; tendon connects muscle to bone, transmitting muscle force; cartilage protects bone-to-bone interfaces; and ligaments connect and provide stability to those interfaces. Forces such as tension, compression, gravity, friction and impact are constantly acting on these tissues, yet little is known about their effect on tissue behaviour.

Mechanical forces are detected by cells embedded in tissues (2). Astronauts returning from zero gravity conditions have shown a reduction in bone density (3) and tennis players consistently have thicker wrist bones on their racket arm (4). Thus, the presence, or lack thereof, of force can have a positive and/or negative impact on tissue mechanical function.

Musculoskeletal disease, such as osteoporosis which causes a reduction in bone density, can lead to a loss of tissue mechanical function (5). The role of mechanobiological investigations is to understand why disease manifests in previously healthy tissue, and whether the consequences can be reversed through the development of mechanostimulation strategies.

Tendon injury and disease is extremely painful and debilitating (6), causing difficulty for individuals to complete everyday tasks or athletes from performing training routines (7). Furthermore, immobilisation impacts on exercise that is prescribed as

essential for a healthy lifestyle (8). Tendon disease may be due to mechanical damage, resultant from overuse or a single traumatic event (9), or it may be due to matrix degradation, due to compromised normal cell function (10). Tendons have the ability to heal in response to injury; however after a long recovery time, newly formed tissue does not match the mechanical function of tissue prior to damage (11). Additionally, repaired tissue has an increased risk of further injury (12). The absence of mechanical stimulation has been shown to be damaging to the healing process (13), yet the reason for this is not fully understood. Healing is controlled by elongated fibroblast-type cells, known as tenocytes, that regulate the synthesis and secretion of tendon matrix (14). Thus, developing new therapies for tendon healing requires an intricate understanding of how tenocytes respond to mechanical forces.

It is widely accepted that growing tendon tissue *in vitro* has some specific challenges, including generating appropriate fibril distributions (15). Commercially, musculoskeletal tissue engineering has been focussed on biodegradable patches and scaffolds using synthetic materials for tendon repair (16, 17, 18). Patches are seeded with host cells, growth factors, and sutured at the tear site, and are hypothesised to improve healing time and encourage alignment of new tissue at a repair site. In 2004 using a novel *in vitro* culture system tenocytes in a monolayer between silk suture pins grew tendon-like constructs with aligned collagen fibrils after twelve days and mechanical testing showed an overall similar ultimate tensile strength (19). Tendon tissue engineering is constantly evolving; however one aspect remains consistent: researchers are interested in reducing the time taken for tissue to grow, heal, and/or mature; however, limited progress has been made due to a lack of crucial mechanobiological understanding.

In vivo, cells are exposed to complex mechanical forces. In musuloskeletal tissue, cyclic loading causes fluid flow as well as a primary tension or compression (20, 21, 22, 23). To understand how cells respond to these forces, systematic approaches using *in vitro* techniques have been developed, where cultured cells are exposed to a defined stimulus (24, 25, 26, 27, 28, 29, 30, 31, 32, 33). The precision and homogeneity of the stimulus varies across devices (34) and research institutions as principles of a device are maintained, but geometry and conditions altered (35).

In recent years, effort has been made to characterise stresses within cell-stimulation devices and in rare cases, validate calculations (36). Characterisation has indicated that in a popular *in vitro* device, cells are exposed to two types of stress, as a primary

applied stretch also induces significant fluid-induced shear stress (37, 38). This creates difficulty for mechanobiologists, as understanding which force caused a cell response may not be possible.

Characterising the effect of these fluid forces on cell behaviour is essential, as they may have a significant role in matrix maintenance or tissue healing *in vivo* (14). As a result, a fluid-cell stimulation device is required that is relevant for musculoskeletal investigations, as understanding how mechanical forces are detected, and how the cell responds, could provide a foundation for new pharmacological targets, developing new clinical therapies and refining tissue engineering techniques.

This thesis has two overall aims:

1. To identify, design, characterise and validate an *in vitro* model for the application of cyclic, flow-induced shear stress to cell monolayers.

2. To biologically validate the *in vitro* model for use with human tenocytes and to capture their response using a computational model.

Within this chapter, the composition, structure and mechanical properties of tendon are introduced. Evidence of key mechanotransducers in tendon is detailed and the background of tendon collagen and proteoglycan matrix secretion provided. Current cell-stimulation devices and their merits for mechanotransduction research are presented. Tenocytes, including previous *in vitro* tenocyte-fluid flow studies, are introduced and additionally, existing models that estimate tendon interstitial flow are examined. Subsequently, an *in vitro* fluid shear stress cell stimulation device is presented as suitable for musculoskeletal mechanotransduction research and the objectives of the thesis established. Finally, the outline of the thesis is detailed.

1.2 Tendon physiological background

Tendon is a fibrous connective tissue that transmits forces created by muscle directly to bone, thus allowing motion to occur. This transmission requires tendons to be able to undergo regular and large cyclic loading.

Tendon interfaces with muscle and bone at the myotendinous and osteotendinous junctions respectively (39). To allow for optimal integration the structure of tendon at these different locations is highly specialised and this variance in tendon properties can

continue along the length of the tissue as identified in the Supraspinatus (also known as rotator cuff) tendon (40). Furthermore, one tendon is not the same as another, so the structure and properties of a flexor and patellar tendon may differ due to functional adaptation. This is highlighted when considering *in vivo* forces: peak forces in the Achilles' can reach 9 kN during sprinting (41), where as peak forces in hand flexor tendons are reported to be relatively small at 35 N (42).

In order to understand the mechanical properties of tendon *in situ*, it is essential to understand its composition. Within this section, the composition, structure and mechanical properties of tendon will be considered. Additionally the pericellular matrix and tendon pathology and healing are also discussed.

1.2.1 Composition

Tendon is mainly composed of collagen fibres orientated in the direction of the axial force transmission (14). Interspersed within the collagen fibres are tendon cells which are either a type of elongated fibroblast known as tenocytes, or immature tendon cells known as tenoblasts (11). Tendon cells are discussed in detail in Section 1.6. Tendon properties and composition vary dependent on tendon type and location; however the typical composition of healthy tissue is as follows. Collagen is the most abundant protein within tendon and accounts for over 60 % of the dry mass (43). The majority is collagen type I, approximately 5 % is collagen types III and V (44) and there are also some trace amounts of types II, VI, IX, X and XI (45). Elastin is found within tendon tissue at a concentration of 2 % (46).

Proteoglycans are proteins with a covalently bonded glycosaminoglycan (GAG) side-chain (47). Proteoglycan content of about $1 - 5$ % (46) is small in comparison to collagen and can vary considerably dependent on tendon function and location (14). The most abundant within tendon are aggrecan and decorin. It is hypothesised that aggrecan holds water and resists compression (48), while decorin is thought to facilitate fibrillar slippage during deformation (49). Riley, Harrall *et al.* (50) found the mean sulphated GAG content of Supraspinatus tendon and Bicep tendon to be $12.3\,\mu g\,mg^{-1}$ and $1.2\,\mu g\,mg^{-1}$ respectively. The most abundant GAG in their investigation varied between chondroitin sulphate at 56 % and dermatan sulphate at 67 % for Supraspinatus and Bicep tendon respectively. Hyaluronic acid (a non-sulphated GAG) was found to be relatively consistent at $9.8 - 10.3\,\mu g\,mg^{-1}$. Tenocytes, (Section 1.6), synthesise all

of the extracellular matrix components, including collagen and proteoglycans, and are active in generating energy (51, 52).

1.2.2 Structure

Tendon form varies with anatomical locations from, for example, the wide and flat form of the Supraspinatus tendon to the long thick form of the Achilles' (53); however the tissue consistently is highly organised with a widely accepted defined hierarchy. This hierarchy breaks down into five sub-levels from macro to micro: tertiary bundles, the tendon itself; secondary bundles known as fasicles; primary bundles known as fibres; fibrils; and the collagen molecule, tropocollagen which are triple helix polypeptide chains (Figure 1.1) (11). The collagen fibres mainly run in the direction of tension; however they can also form plaits and spirals by running horizontally and transversely through the tissue (54).

A crimp pattern is visible in tendon at rest, but during loading these fibres become straightened, indicating that the crimp waveform is partially responsible for the well-documented force-response behaviour (Figure 1.2) (55, 56).

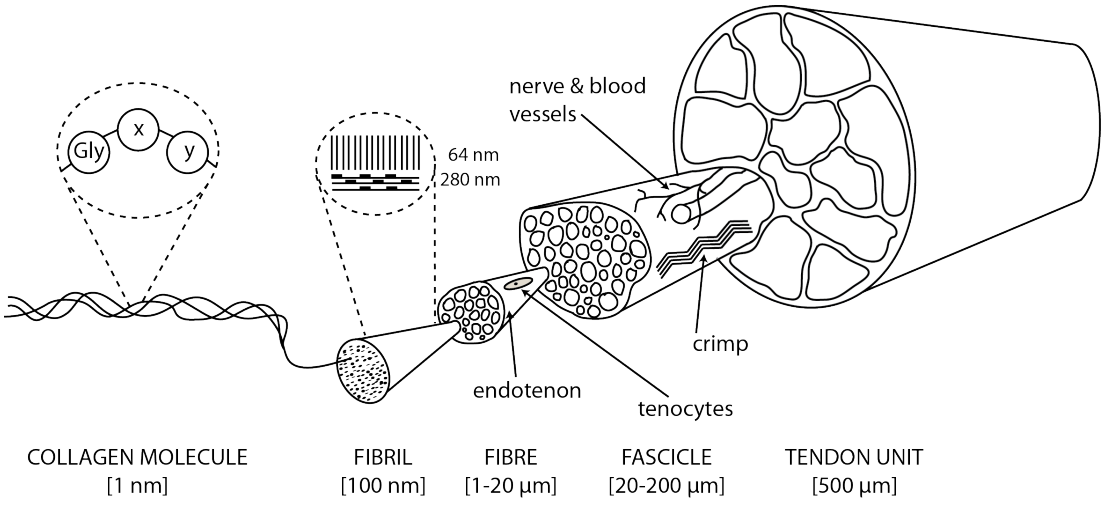

Figure 1.1: Tendon composition: hierarchical structure of tendon, showing the characteristic 64 nm spacing and features of fibrils and fascicles respectively. Inspired by Silver *et al.* (57).

1.2.3 Mechanical properties

The structure of tendon is vital in allowing the tissue to perform its function. High, cyclic loading demands tendon tissue to be able to withstand large forces and work has shown tendon to change composition and structure in response to its external environment (58).

Tendon mechanical properties are characterised by a widely-accpeted stress-strain relationship (Figure 1.2).

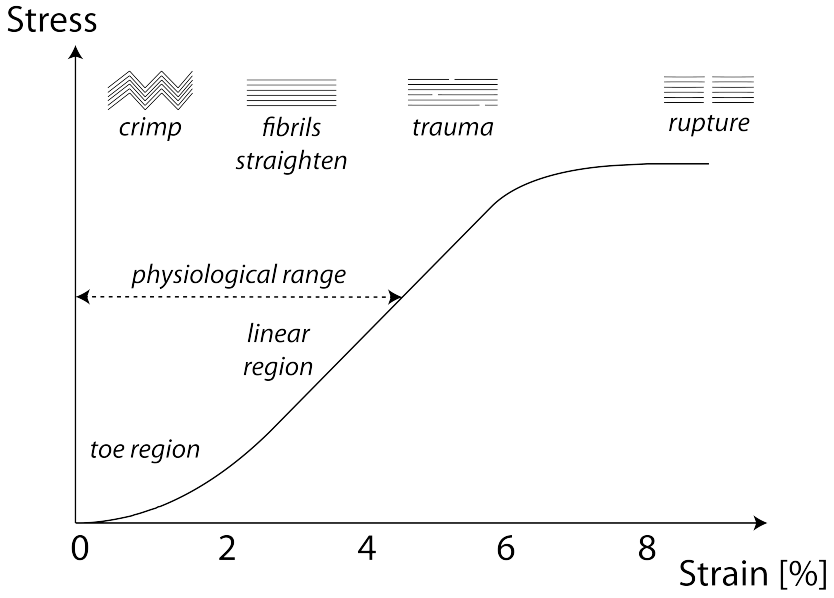

Figure 1.2: Tendon stress-strain relationship: a typical stress-strain curve for tendon tissue force response. Crimp patterns occurring in unloaded tendon straighten as strain increases, leading to microtrauma and then finally rupture.

The 'toe region', where crimped fibrils become straight, occurs up to 2 % strain. Consequently, mechanical properties are believed to be influenced by crimp pattern angle and wavelength, where tendon with a relatively small crimp angle fails before that with a larger crimp angle (59, 60, 61), although this is not a clear structure-property relationship. After the toe region, the fibres are straight and linearly respond to the force applied up to 4 % strain. The gradient of this linear region is known as the Young's Modulus E and indicates the tendon mechanical properties (Equation 1.1)

(14).

$$E = \frac{\text{stress}}{\text{strain}} = \frac{\sigma}{\epsilon} = \frac{FL}{A\Delta L} \tag{1.1}$$

where E is the Young's Modulus, σ is the stress ($\frac{F}{A}$), ϵ is the strain ($\frac{\Delta L}{L}$), F is the force, A is the cross-sectional area, L is the original length, and ΔL is the change in sample length.

The Young's Modulus is a measure of the tendon's resistance to elastic deformation. Tendon stiffness is determined from the cross-sectional area, length and Young's Modulus of a sample (Equation 1.2).

$$k = \frac{AE}{L} \tag{1.2}$$

where k is the stiffness, A is the cross-sectional area, E is the Young's Modulus, and L is the sample length.

Reported values for the Young's Modulus and stiffness of tendon are as high as $0.9 - 1.8\,\text{GPa}$ and $161\,\text{N}\,\text{mm}^{-1}$ respectively (62).

Up to 4 % strain is considered to be the maximum physiological limit of tendon response, after which damage starts to occur (14). Initially this damage is in the form of microtrauma, but beyond 8 %, catastrophic rupture becomes prevalent (63).

Tendon ultimate tensile strength (UTS) and failure strain are dependent on collagen fibre orientation, diameter and thickness (64). UTS is the stress that tendon can undergo before failure or rupture, and a study across several mammals indicated values in tendon of up to 100 MPa (65). In mature rabbit tendons, failure strain has been reported to be 15 ± 5 % strain (66).

Loading during healing is reported to have a significant impact on resultant tissue mechanical properties (14). As a result, the influence of mechanical force on tendon healing and structure is significant, moreover, mechanical force could be a significant causative factor in the development of pathological conditions (9).

1.2.4 Pericellular matrix

The pericellular matrix (PCM) consists of structures found in the immediate vicinity of the cell (67) and in bone tissue it is thought to amplify strain through its deformation induced by fluid flow (Section 1.7). The exact components of the tendon PCM are

not entirely clear and previous work has associated all proteins found within tendon as the ECM (68); however it is possible to isolate potential PCM proteins as they are reported to have cell interactions. Collagens type VI and IX are hypothesised to be cell-associated and/or mediate cell-matrix interactions (68). Additionally, recent work has shown that elastic fibres are closely associated with tenocyte location, suggesting that glycoproteins, elastin and fibrillin, may form part of the PCM (69). Furthermore, proteoglycans may have a PCM function, as it is noted that decorin and aggrecan are found in the vicinity of cells (70), and may assist in fibrillar sliding (71).

Little work has been performed on the PCM of tenocytes; however investigation into other cells has shown a prevalent PCM and alludes to its presence in tendon as scanning electron microscopy has shown structures surrounding tenocytes in rat tail tendon (72). Chondrocytes that retained their *in vivo* PCM, known as chondrons, were shown to produce significantly more ECM over an eight week period than chondrocytes without a PCM (73). Additionally, support for the existence of a PCM in musculoskeletal tissues was obtained from a particle exclusion assay performed on human smooth muscle cells, where a PCM zone was found surrounding each cell (74).

Genetic mutations in proteins that form part of the PCM can have devastating effects. Ullrich Congenital Muscular Dystrophy (UCMD), where patients suffer from joint laxity and a predisposition to hip dislocation, is caused by the mutation of collagen type VI (75). Additionally, down-regulation of collagen type VI, resulting in tissue laxity and wasting, may cause Bethlem myopathy or joint hyper-laxity (76), and up-regulation, resulting in increased fibrosis and stiffness, may cause Bullets Keratopathy, or Scleroderma (77). Furthermore, mutation of fibrillin-1 and fibrillin-2 causes Marfan & Beal's syndrome, where patients suffer from hyper-flexibility and joint contractures (78).

1.2.5 Pathology and healing

Repetitive tendon tissue microtrauma, started due to periods of exertion is the driving force behind overuse injuries (79). Microtrauma occurs at low-magnitude forces and its accumulation results in injury on the microscopic scale (46). Injury has been defined as the inability of the tendon to successfully transmit further tensile forces after overuse at a repeated strain of $4-8\,\%$ (79, 80, 81, 82); however injury is more easily identifiable as the presence of pain or the inability of an individual to complete daily tasks (83).

Spontaneous rupture occurs in tendon usually due to: previous significant wear or growing abnormal tissue; tendon degeneration or disease; or a single traumatic event, which is considered to be extremely rare (84).

Recovery from the injured state has three phases: inflammation; proliferation; and maturation and remodelling (46). The inflammatory phase lasts a few days, although there is rapid cell migration and site cleaning in the first 24 hours (14). The secondary phase, proliferation, is the repairing phase and lasts approximately six weeks. During this stage of healing, tenocytes produce large amounts of collagen and proteoglycans which re-establish continuity at the damage site (14). Remodelling, the final phase, has a decrease in cellular activity as ECM synthesis is down-regulated and newly produced tissue may become aligned (14). The driving force behind alignment is unknown.

1.3 Mechanotransduction

The ability of a cell to sense mechanical forces from its external environment, convert them into a biochemical signal, and potentially a biological response, is the process of mechanotransduction (85). The biological response to a mechanical stimulus is vital for cells to grow and perform their individual roles (85) and mechanical stress in the form of blood pressure has been shown to influence the formation of tissue patterns during the remodelling of blood vessels (86).

Tendon mechanotransduction encompasses the interaction between mechanical forces, the PCM/ECM, and humoral factors such as cytokines (14). Mechanical loading pathways are numerous and complex (Figure 1.3); however this section will focus on the various ways in which tendon cells are known to sense their mechanical environment and the cell-cell communication pathways used as part of this process. Thus, gap junctions, ion channels, the cytoskeleton, the primary cilium and the glycocalyx, will be discussed individually (Figure 1.4).

1.3.1 Gap junctions

In essence, a gap junction is a form of ion channel, permitting electro and chemical communication between cells that causes a change in intracellular concentrations (88) potentially leading to a signalling cascade allowing cells to coordinate their activities. Gap junctions are located on the surface membrane of a cell and join the cytoplasm

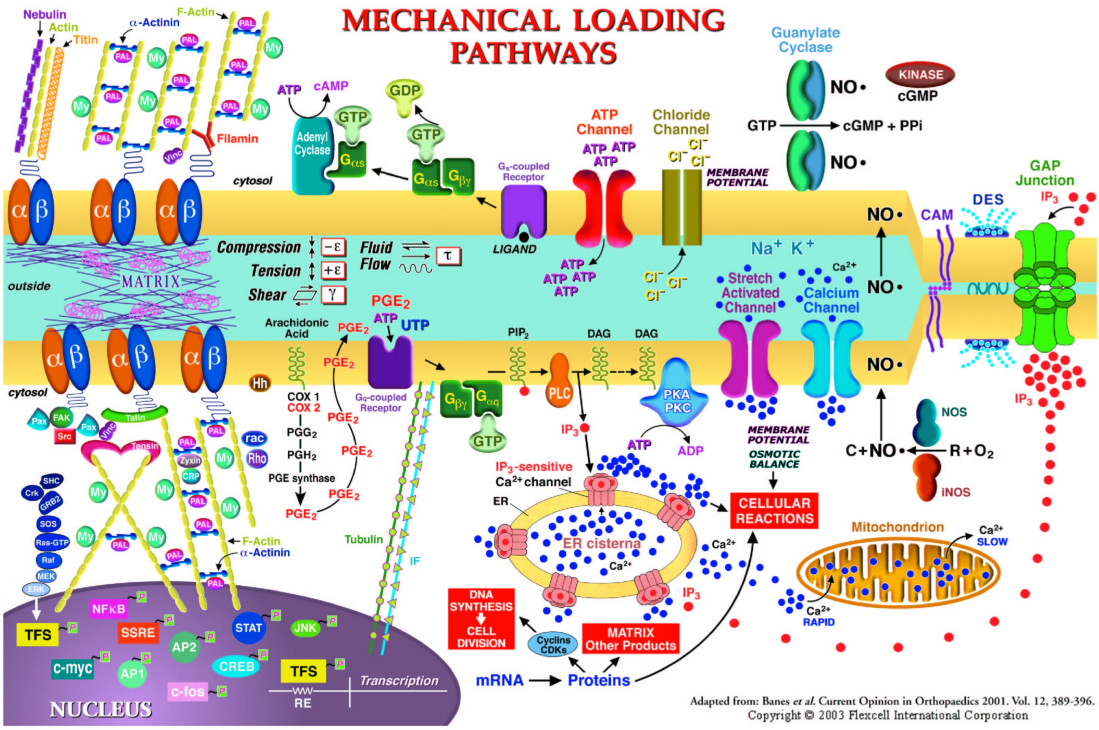

Figure 1.3: Mechanical loading pathways: the various mechanisms by which cells sense mechanical forces are numerous and complex. Figure used with permission (87).

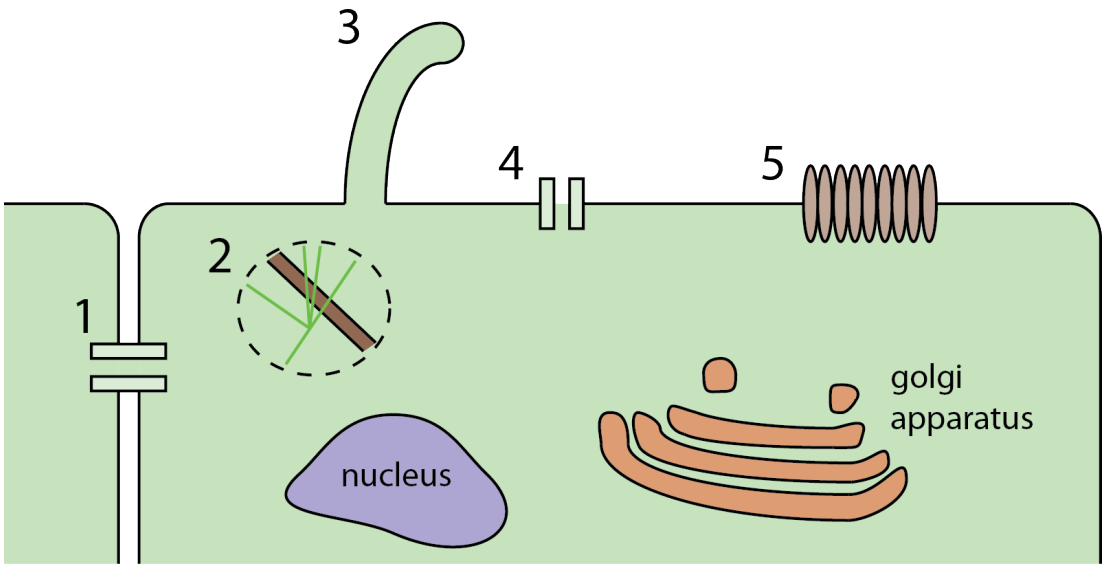

Figure 1.4: Mechanotransducers: schematic showing a cell's various detectors of mechanical force and communication pathways. The five key structures involved in musculoskeletal cell mechanotransduction have been identified as: 1. gap junctions; 2. the cytoskeleton; 3. the primary cilium; 4. ion channels; 5. the glycocalyx.

of two adjacent cells together through the use of hemi-channels (88). Hemi-channels, or connexons, are formed from six connexins which are the principal proteins found in their formation (88, 89). Gap junction plaques are formed at the membrane as gap junctions cluster in hundreds to thousands (88). Substantial evidence has been obtained that tenocyte to tenocyte communication through gap junctions is important for tissue response to mechanical stimuli (90).

1.3.2 The cytoskeleton

The cytoskeleton is an internal dynamic meshwork of filaments within a cell that provide structure, and link extracellular matrix with internal organelles (91). Cytoskeleton filaments are polymers of actin, tubulin and vimentin and are thought to be preloaded in tension or compression under a 'tensegrity' model (92). External coupling to the extracellular matrix or other cells is achieved with integrins or cadherins, selectins and cell adhesion molecules (93). These connections allow the cell to sense its external environment, by transmitting load to the cytoskeleton (94, 95). α and β cross-membrane

integrins have been shown to transmit mechanical forces to actin filaments which initiate gene transcription events (96). Actin is thought to assist in preserving gap junction connections during tissue deformation (97), and tension generated by optical tweezers applied to actin has shown a link with ion channels due to a Ca^{2+} ion influx (98). Figure 1.5 shows the structure of the cytoskeleton within a cell and the numerous and complex signalling pathways identified as a result of cell mechanical deformation.

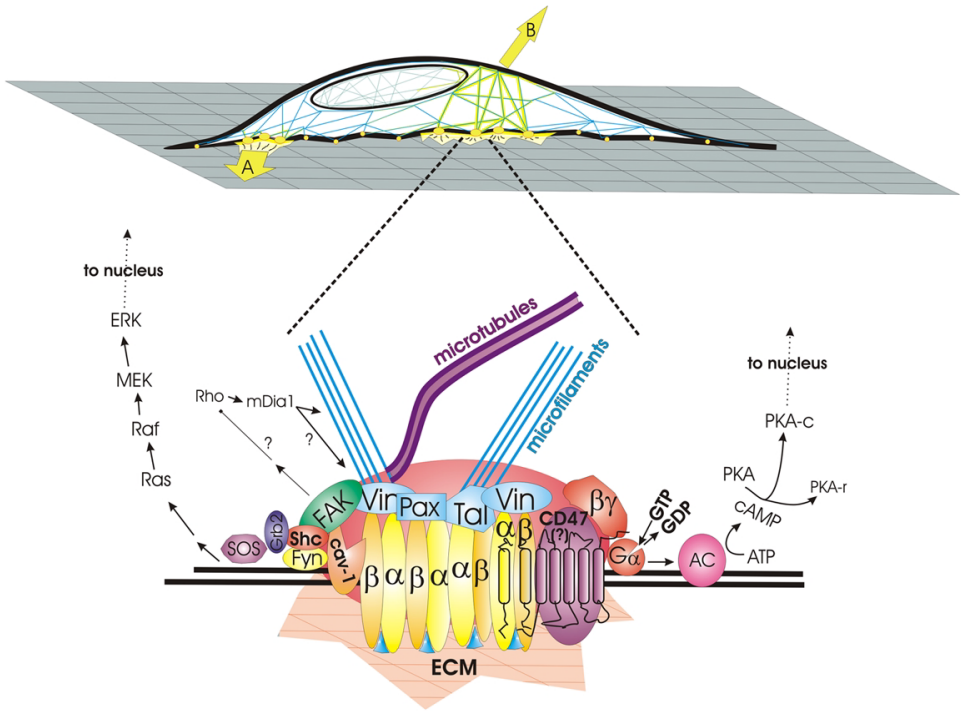

Figure 1.5: Cytoskeleton communication pathways: forces acting on the cytoskeleton may originate from the extracellular matrix, other cells, or in culture, from substrate deformations. These forces can induce signalling pathways. Figure used with permission (99).

Models of cell behaviour, accounting for cytoskeleton mechanics, include a tensegrity model, a soft glass rheology model and mixture theory. Tensegrity accounts for cell migration and contractile cytoskeleton stress seen in durotaxis (100). The soft glass rheology model accounts for local and global cell power law viscoelasticity (101). Mixture theory uses the balance of mass and momentum to represent multiple material phases when determining cell and tissue behaviour (102).

Cell motility is achieved with the cytoskeleton, providing traction with their environment and generating the motion itself (103). In addition, the cytoskeleton also causes local collagen fibril deformation (104) and the contraction of the extracellular matrix on a larger scale (105).

1.3.3 Primary cilia

Primary cilia are hair-like organelles that extend from the cell membrane into the extracellular space (106). As suggested by their name, most cells have only one cilium and this is aptly called the primary cilium (107). It is constructed from nine doublet microtubles, known as axonemes, in a peripherial structure (107).

The primary cilium was first identified in the 19th Century (108) in the rabbit kidney, yet obtained little attention as its role was not clear. In 1961, Barnes suggested that the primary cilium may have a sensory function (109) and in 1995 a review by Wheatley addressed the role of primary cilia in normal and pathological tissues, confirming that cilia are organelles consistently found in cells and that they have a role in sensing environmental cues (110). In addition, the importance of primary cilia in kidney has been identified due to the existence of polycystic kidney disease, the mutation of the polycystin receptor-like protein localised to the primary cilium (111).

In tendon, primary cilia were first identified in 1967 when Ross and Klebanoff obtained an image of fibrocytes with a ciliary process (Figure 1.6 (a)) (112). Subsequently, an investigation by Brooker *et al.* identified ciliated fibroblasts in the ear chambers of rabbits *ex vivo* (113) which eliminated speculation that primary cilium growth is induced by *in vitro* culturing (Figure 1.6 (b)). Work by Beertsen *et al.* showed that at least 70 % of their fibroblast culture population exhibited a cilium structure (114). They also identified the structure of the cilium at various positions along the shaft; Figure 1.6 (c) shows the previously described nine axonemes structure of the cilium. In rat extensor tendon, primary cilia have been shown to orientate in the direction of collagen alignment and the long axis (115).

Various cilium signalling mechanisms have been documented (107); however two of particular interest are that of Wnt signalling, and the chemosensation-/receptor-based signalling model where platelet derived growth factor (PDGF) receptors are activated by PDGF in flow, causing downstream signalling (116). Both of these signalling mechanisms require a fluid flow; although the former of the two requires a bending effect

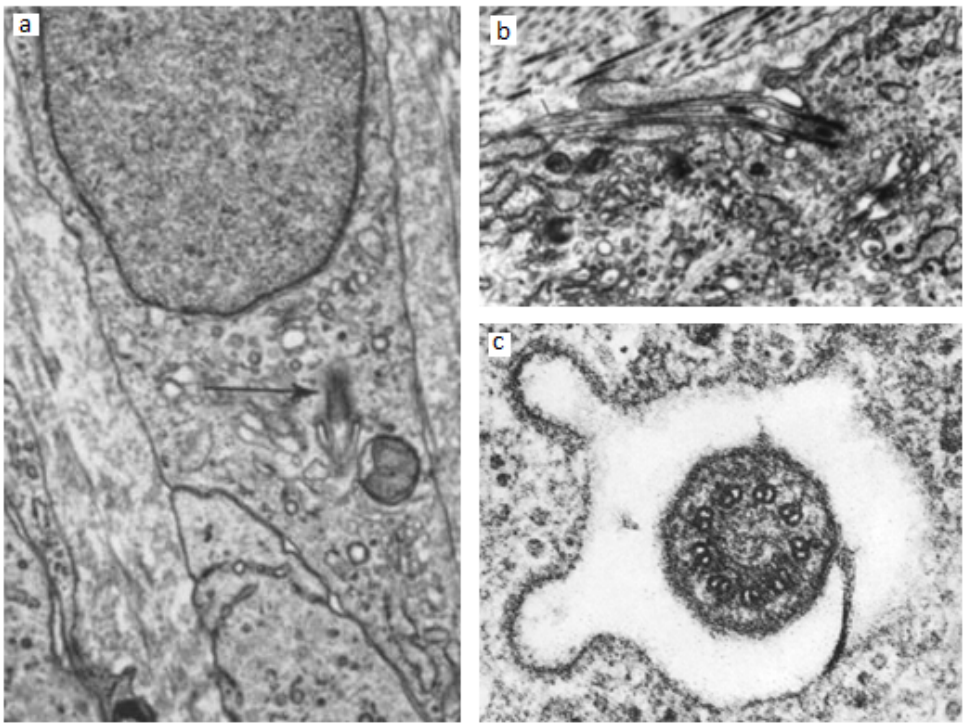

Figure 1.6: Primary cilia: a) electron micrograph image of a fibrocyte showing a primary cilium as identified by the arrow (image used with permission (112)); b) *ex vivo* imaging of fibroblast cilia in rabbit ear chambers (image used with permission (113)); c) cilium nine axoneme structure (image used with permission (114)).

on the shaft of the cilium to activate a calcium channel and the latter requires fluid flow as the form of PDGF transport. The cilium has various specific mechanosensors potentially acting as signal antennae, as passive cilia bending is required for fluid flow mechanosensation of urine by cells (107).

In 1985, Poole *et al.* suggested that the cilium could act as a probe within connective tissue, sensing stimuli from the surrounding environment and transducing signals to the nucleus to result in a gene transcription event (117). They tested mature rabbit flexor digitorum profundus tendon, six-day posthatch chick long digital flexor tendon and three-month-old rat tail tendon (amongst other connective tissues) using electron microscopy. Poole *et al.* found that a consistent relationship between the primary cilium location and the Golgi apparatus exists, with their close proximity amongst all tissues tested. This is of particular relevance considering the key role of the Golgi in the secretion of proteins. Further evidence obtained by Poole *et al.* showed that microtubules throughout the Golgi converged on the basal section of the cilium. This, in tandem with Moran *et al.* who suggested that cilium deflection may cause microtubules to slide and the cilium to bend near its base (118), gives reason to hypothesise that cilium bending may have a direct impact on the response of the Golgi apparatus. Identified primary cilium pathways are summarised in Figure 1.7.

Primary cilia have been investigated in bone cells. Chris Jacobs's lab in Stanford found that fluid flow cellular response was independent of stretch-activated ion channels and a calcium ion flux (120, 121). They showed that cilia extend from bone cells and deflect during steady flow, experiencing shear stress of 0.03 Pa. To reach the conclusion that the cilium is the primary transducer of fluid flow, Malone *et al.* used chloral hydrate to remove 90 % of cilia from the cell population (confirmed through α-tubulin staining) and showed that untreated cells exhibited significant changes in gene expression in comparison to treated cells after application of 1 Hz oscillatory laminar flow with an estimated cell surface shear stress of 1 Pa (120).

Stress deprivation resulted in a significant increase in primary cilium length in rat tendon cells and this increase was instantaneous (122). Furthermore, the application of cyclic loading saw a reversal of this extension to cilia length matching that of fresh controls. Renal collecting duct chief cells showed a reduction in cilia length with the application of fluid shear stress *in vitro* (123).

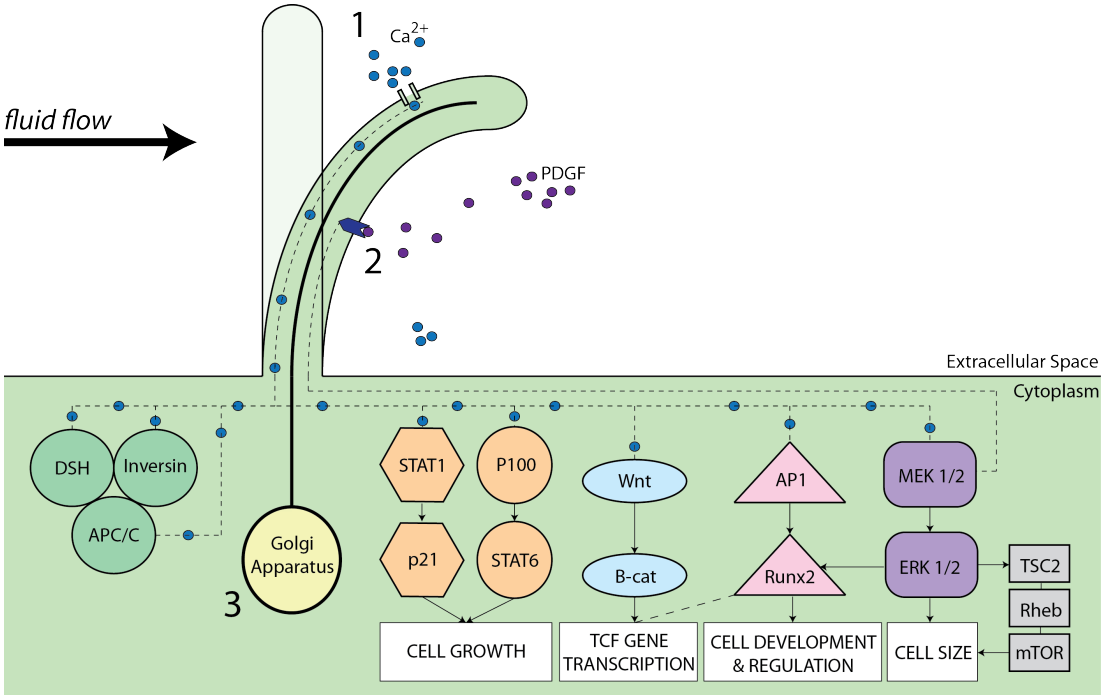

Figure 1.7: Primary cilium fluid flow responses: mechanotransduction pathways of fluid flow signals detected by the primary cilium and its receptors. Three mechanosensation channels have been identified: 1) polycystin-1 gated Ca^{2+}channel; 2) PDGF activated receptor; and 3) microtubule deformation linked to the Golgi complex. Polycystin-1 is a transmembrane protein, belonging to a family of seven other polycystins known for the activation of G-proteins that ultimately initiate Ca^{2+}channels (119). Schematic inspired by Fliegauf *et al.* (107) and Dalagiorgou *et al.* (119).

A lag exists between the start of cilium bending and the moment calcium signalling is induced, likely due to the viscoelasticity of the cell membrane (124). After the application of fluid flow, inducing shear stress ranging from $19-55\,\mathrm{mPa}$, cilium bending occurs in the first $0.5\,\mathrm{s}$, whereas the maximum calcium response occurs at $30\,\mathrm{s}$ (124). Thus, although studies appear to show that a change in cilia length is immediate after the application of flow, a cell response, such as protein synthesis, may be delayed.

Chen *et al.* modelled ciliary motion in the embryo node using computational fluid dynamics in order to investigate a hypothesis for the production of marked left-right asymmetry of internal organs (125). They created a model including an active and passive cilium with a length of $6\,\mu\mathrm{m}$ and circumference of $0.2\,\mu\mathrm{m}$. For the active cilium, Chen *et al.* increased the passive cilium stiffness reported by Schwartz *et al.* (126) by two orders of magnitude to $10^{-23}\,\mathrm{N\,m^{-2}}$. The active cilium was set to rotate at a frequency of $10\,\mathrm{Hz}$ to generate fluid flow within the defined field. This generation of fluid flow had an impact on the movement of the passive cilium, inducing deformation and rotation in the opposing direction of the oscillating active cilium. Chen *et al.* analysed the pressure and shear stress distributions in the active and passive cilium, identifying that maximum shear stress, ranging from $0.949\,\mathrm{Pa}$ (active) to $0.0147\,\mathrm{Pa}$ (passive), induced by fluid flow, occurs close to the tip.

Taking rat kangaroo kidney epithelial cells, Schwartz *et al.* used a parallel plate flow chamber to investigate the effect of fluid induced shear stress on cilia length *in vitro* (126). Steady flow of Hank's Balanced Salt Solution (HBSS) was applied at $0.17-4.20\,\mathrm{ml\,s^{-1}}$ for approximately three minutes while continuous imaging was completed using video recording software. Figure 1.8 shows the bending effect on a cilium induced by fluid flow.

Modelling the cilium as a uniform cantilevered beam, Schwartz *et al.* applied a unidirectional load, in the form of fluid drag, perpendicular to the long axis and created a heavy elastica model that accurately calculated the deflection of the cilium tip, and as such was used to calculate a flexural rigidity of $1.4-1.6\times10^{-23}\,\mathrm{N\,m^{-2}}$.

Schwartz *et al.* identified that in a given flow field, cilia that were longer had higher shear forces acting on them which caused an increase in bending in comparison to shorter cilia (126).

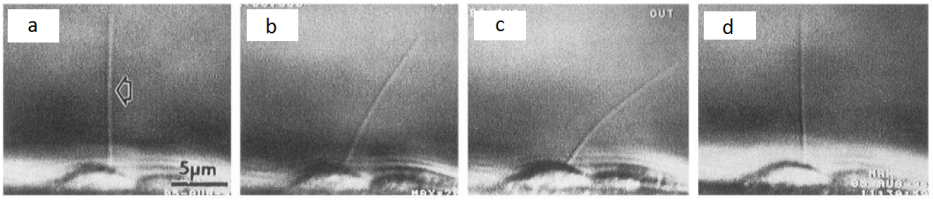

Figure 1.8: Primary cilium bending induced by fluid flow: a) No flow, b) passive bending in the direction of flow, c) increased flow considerably increases cilium bending, d) at the cessation of flow, the cilum returns to its original condition. Figure adapted from (126) with permission.

1.3.4 Ion channels

Ion channels sense mechanical forces in the external environment and transduce them into internal electrical or chemical signalling pathways (127). An ion channel response involves the movement of cations (Ca^{2+}, Na^{+}, K^{+}), from the intracellular to the extracellular space or *vice versa* (128). This change in ion concentrations causes signalling pathways within a cell to be activated and gene transcription events to occur (129). Their existence was first considered in studies of mechanosensory neurons (130) and their response is caused by forces on the plane of the cell membrane (131, 132, 133).

At present there are two models hypothesised to explain ion channel mechanical gating: the bilayer model; and the tethered model. The bilayer model assumes that the tension in the lipid bilayer of a cell membrane is enough to gate channels directly (127). In the tethered model, the ion channel requires direct connections with the extracellular matrix or the cytoskeleton (134). The tethered model is considered to be the overriding model in literature. Ion channels are also known to be crucial in signalling pathways sparked by other mechanoreceptors, as seen with the primary cilium (Section 1.3.3).

1.3.5 Glycocalyx

Positioned on the surface of the cell, the role of the glycocalyx is varied and its structure complex (135). Chondroitin sulphate and hyaluronan, both of which are glycosaminoglycans, play a role in the assembly of the glycocalyx structure and are attached to anchoring foci linked to the cell cytoskeleton (136). The glycocalyx has been hypothesised in endothelial cells to be a transducer of fluid shear stresses, passing cues to

the actin cytoskeleton within the cell (137). Tarbell and Pahakis (138) support the glycocalyx as a mechanotransducer of fluid flow in endothelial cells; however they note that stress is transmitted to other regions of the cell, mainly intercellular junctions and that investigations of the glycocalyx, which involve its degradation, cause fluid stress to occur closer to the cell membrane, potentially activating other signalling mechanisms that the glycocalyx would normally override.

1.3.6 Summary

This review of mechanosensors suggests that there may be more than one sensor of a particular type of stress and as such, investigations into fluid flow by targeting specific mechanotransducers, *e.g.* the abrogation of the glycocalyx or primary cilium, may not give 'clean cut' results. While fluid flow may trigger a signalling cascade, influences may be the result of growth factors that may not be monitored or controlled. Furthermore, mechanotransducers are not necessarily acting independently of each other and interactions such as: the primary cilium axoneme with cytoskeleton microtubules; gated ion channels activated by protein interaction with the cytoskeleton and/or the extracellular matrix; and the glycocalyx interaction with the cytoskeleton, clearly shows that biological mechanosensitivity can be extremely complex.

1.4 Matrix secretion

Matrix secretion, performed by tendon cells, is essential for the remodelling, healing and maintenance of healthy and damaged tendon tissue (139). Within this section, as key components of tendon, the structure, synthesis and secretion of collagen and proteoglycans are discussed in turn.

1.4.1 Collagen structure and synthesis

Collagen is a triple helix consisting of three amino acid chains, two of which are identical (140). Common amino acid sequences are glycine-proline-X and glycine-X-hydroxyproline (140), where X represents any amino acid.

Collagen synthesis requires modification of amino acids in the polypeptide chain, including the hydroxylation (the introduction of a hydroxyl group to an organic compound) of proline and lysine, followed by the glycosylation (attachment of a carbohy-

drate to a hydroxyl molecule) of the hydroxylysine hydroxyl group (141). Ascorbic acid is required for propyl and lysyl hydroxylase (141).

1.4.1.1 Collagen secretion & fibrillogenesis

After synthesis, initiated by the transcription of mRNA, collagen is stored as tropocollagen within the Golgi apparatus or pre-packed secretory vesicles (Figure 1.9) (142). The assembly of collagen fibrils is complex and the exact process remains unclear. Formation starts with short fibrils that act as precursors for the long fibrils found in mature tendon (Figure 1.9) (143). This process occurs both inside and outside of the cell. Canty and Kadler have shown that fibril formation can start deep within a cell cytoplasm in 'fibripositors' (Figure 1.9) (144). Fibril segment length in embryonic tendon has been shown to increase from 22 µm at twelve days, to 37 µm at 16 days, followed by a rapid increase to 106 µm at 17 days (143, 145), suggesting that the short fibrils bind to form large fibrils at the 17 day time-point.

1.4.1.2 Ascorbic acid & proline

The generation of new collagenous structures requires ascorbic acid (vitamin C) and proline (146, 147), yet the presence of ascorbic acid in cell and tissue culture medium has been varied *in vitro*.

In vitro tissue cultures modelling damage, media is often supplemented with ascorbic acid as it is recognised that tenocytes require ascorbic acid and proline for repair purposes (148, 149, 150, 151), where the concentration of supplemented ascorbic acid ranges from $50\,\mu g\,ml^{-1}$ to $150\,\mu g\,ml^{-1}$. In *in vitro* tissue models without damage, ascorbic acid has not been supplemented (152, 153, 154, 155, 156, 157, 158).

Recent *in vitro* tenocyte culture has recognised the importance of culture medium supplemented with ascorbic acid to ensure conditions do not inhibit cell processes (19, 159, 160, 161, 162, 163).

Additionally, previous studies have found ascorbic acid to be extremely unstable at 37 °C in culture medium, showing a significant reduction in ascorbic acid levels after 24 hours (147); however a stable version in the form of L-ascorbic acid 2-phosphate has been shown to be effective in collagen synthesis (164).

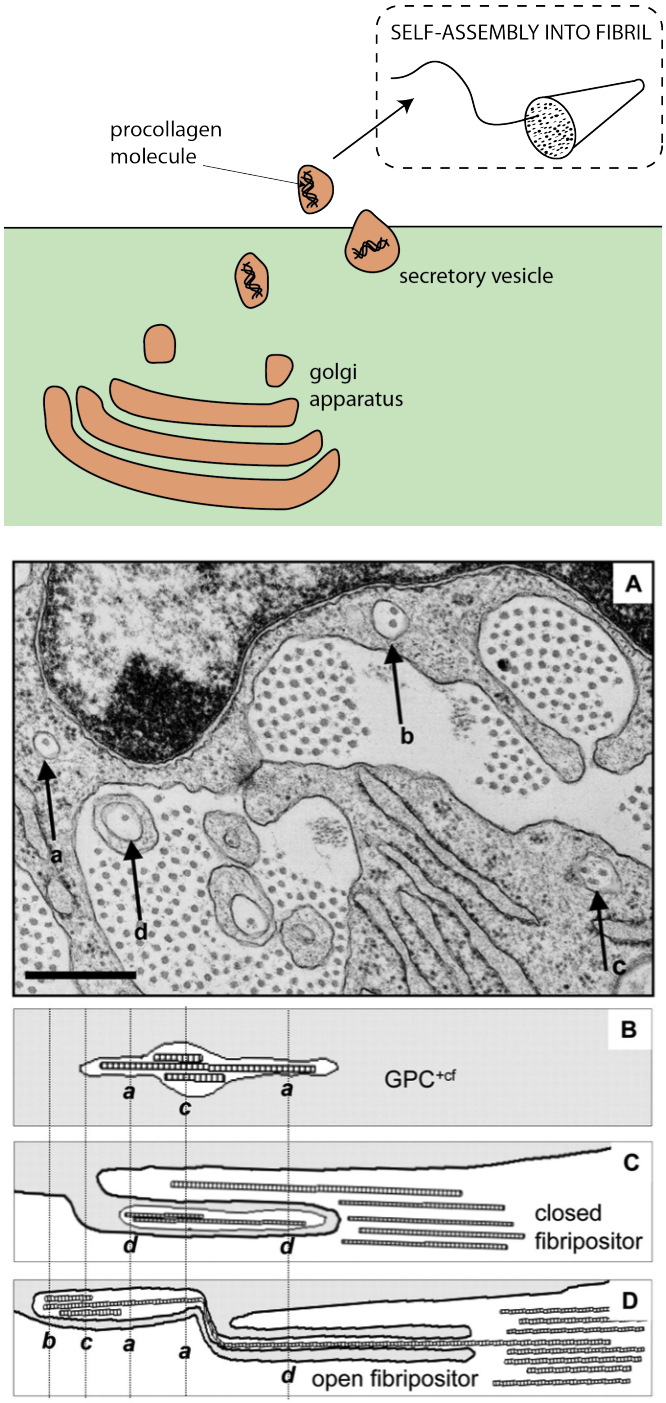

Figure 1.9: Collagen secretion: top - collagen in the form of procollagen is manufactured within the cell and subsequently secreted into the extracellular space. Fibril formation occurs outside of the cell; however whether the cell plays a further role in the fibril formation is not clear. Bottom - fibril formation occurs deep within the cell in cytoplasm structures known as fibripositors, before being secreted into the extracellular space. Figure used with permission (144).

1.4.2 Proteoglycan structure and secretion

Proteoglycans consist of a protein core with at least one glycosaminoglycan (GAG) side chain. GAGs are covalently attached long chain polysaccharides (165) and proteoglycans with fewer than four GAG side chains appear to play a role in collagen fibril assembly and alignment in tendon (166).

Proteoglycan secretion begins similarly to collagen with protein synthesised by ribosomes, but then glycosylation occurs in the Golgi apparatus. Fully-formed proteoglycans, with their glycosaminoglycan side-chains, are secreted from the cell in secretory vesicles (167).

1.5 Studying cell mechanobiology *in vitro*

Mechanobiologists use *in vitro* testing techniques to establish the response of cells to applied forces. *In vitro* cell devices have been established for two over-arching purposes: cell testing; and cell stimulation. Cell testing devices are dominated by single cell techniques, where as cell stimulation is achieved with monolayer and three-dimensional construct devices. Within this section, these two categories are presented in turn and the merits of devices discussed.

1.5.1 Cell testing: targeting a single cell

Targeting individual cells allows researchers to obtain key information, such as the mechanical properties of a cell. Four key techniques are used (Figure 1.10): atomic force microscopy; magnetic twisting cytometry; optical tweezers; and micro-pipetting.

Atomic force microscopy

Atomic force microscopy is a technique whereby an oscillating cantilever tip interrogates a structure at a force resolution of 10^{-12} N and a displacement resolution of 1 nm (Figure 1.10) (168, 169). Imaging live cells in fluid is difficult, but has provided information on micro and nano scale cell structure dynamics (170, 171, 172, 173).

Magnetic twisting cytometry and optical tweezers

Magnetic twisting cytometry and optical tweezers are similar devices in principle, both requiring the displacement of a micro-bead next to a cell (Figure 1.10)

(174). By analysing deformation of a portion of a cell, elastic and viscoelastic properties are obtained (175). Although these techniques may be applied to large cell populations, deformation mechanics are calculated to obtain mechanical properties of individual cell components, or an individual cell as a whole (176).

Micro-pipetting

Micro-pipetting is a relatively old technique (177), yet provided the basis for the formation of early models aimed at understanding cell mechanics. A shear stress is applied using suction at the cell surface causing localised deformation (Figure 1.10) (178), from which mechanical properties such as the Young's modulus are obtained (179).

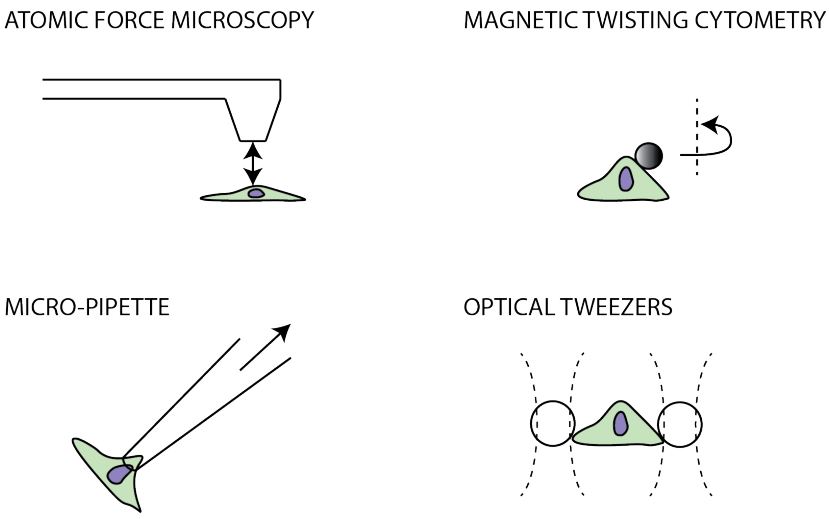

Figure 1.10: Single cell devices: obtaining the mechanical properties of a cell is dominated by single cell testing regimes that include atomic force microscopy; magnetic twisting cytometry; micro-pipette aspiration; and optical tweezers.

1.5.2 Cell stimulation: targeting cell populations

Cell stimulation for the purposes of studying mechanotransduction is dominated by *in vitro* systems that apply a force to a group of cells. These stimulation devices are divided into two categories: monolayer stimulation strategies; and three-dimensional stimulation scaffolds, and are discussed in turn.

1.5.2.1 Monolayer stimulation strategies

The first group of monolayer stimulation tools focus on applying a primary tensile or compressive force to cell populations. They consist of: substrate bending; membrane deformation; and uni/bi-axial stretching.

Substrate bending

Applying bending to a cell monolayer causes longitudinal strain along a substrate (34). Holographic interferometry has shown four-point bending to create a homogeneous stretch across the substrate at low strain values ($< 0.3\,\%$ strain) (180); however the vast majority of bone-cell substrate bending tools are in the range of $1 - 10\,\%$ strain (34) as this level of strain is required to elicit a biological response. A commercial substrate bending device is not prevalent in investigations and previous research has used various methods and geometries (181, 182, 183). Substrate bending occurs within a medium bath that provide cells with nutrients. As a result, a fluid shear stress may be present and this has not been characterised.

Membrane deformation

Membrane deformation involves the stretch of a cell monolayer using a flexible substrate. Flexercell, a commercially available device (24) has dominated membrane deformation investigations; although other commercial devices are available (184, 185). Brown *et al.* identified that unintended fluid shear stress was applied and used a finite element model to estimate normal and shear stresses within a membrane deformation system (37). Maximum normal stress was calculated to be 70 Pa and maximum shear stress to be 0.05 Pa at 1 Hz and a pressure wave of 1 kPa. Validation was achieved using particle image velocimetry for flow visualisation; although capturing flow behaviour at the cell layer proved difficult (186). More recently, using computational fluid dynamics, fluid shear stress in the Flexercell system has been shown to be in the range of $0.09 - 3.5$ Pa for varying conditions ($1 - 2.5$ Hz, $20 - 40$ kPa) and flow verification completed by tracking the movement of fluorescent microspheres (38).

Uni/bi-axial stretch

Stretching of cell-seeded substrates using uni-axial or bi-axial models allows re-

searchers to measure cell deformations through the use of live stain imaging and comparison to substrate markers (181, 187). The choice of substrate and grip conditions may lead to heterogeneity in local strains across a stretching device (34); however this may be limited to earlier iterations of stretching devices (188). They have been used for a variety of experiments including culturing strips of bone (189) and delivering cyclic tension to flexor tendon explants from chicken (190). Devices are created for experiment-specific conditions and as a result, a standard platform does not exist; however strain rates reported are typically $< 10\,\%$ (191, 192).

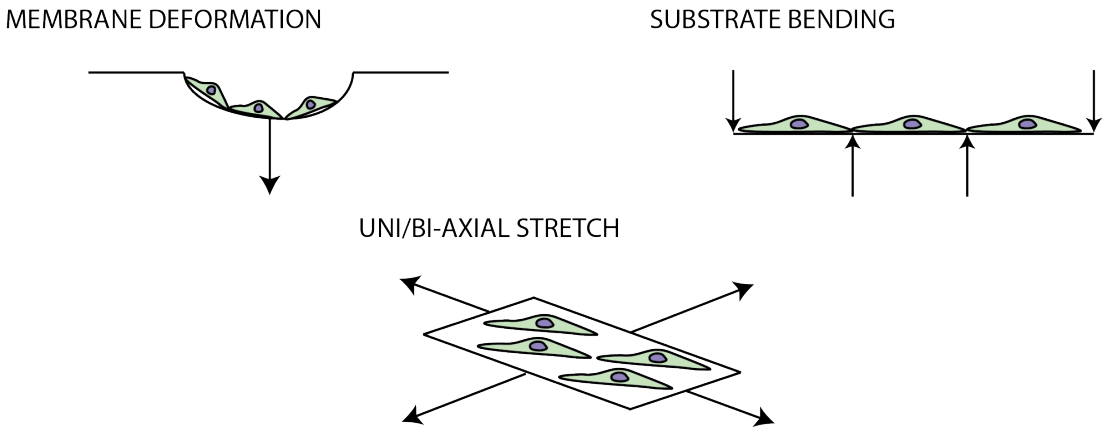

Figure 1.11: Stretching and bending a cell monolayer: cells in the musculoskeletal system respond to tensile and compressive forces. This has been studied *in vitro* using substrate bending, membrane deformation and stretching devices.

The second group of monolayer testing strategies are concerned with applying a fluid-induced shear stress to cell populations. They consist of an: orbital shaker; see-saw rocker; cone-flow chamber; and parallel flow chamber.

Orbital shaker

Orbital shakers apply a fluid shear stress across a cell monolayer and are popular tools for endothelial cell investigations at a high frequency of rotation (193, 194, 195, 196) (Figure 1.12). Shear stresses across the radius of a six-well plate were characterised using computational fluid dynamics, and validated using particle image velocimetry and free surface visualisation (36). Wells were subjected to

two speeds (100 rpm, 200 rpm), and two fluid depths (2 ml, 4 ml) and shear stress at the well base was reported to be in the range of $0.02 - 3.80$ Pa. Due to the extensive validation of this device, confidence in the reported shear stresses is high.

See-saw rocker

Cyclic flow across a cell monolayer can be induced with a commercially available see-saw rocker (Figure 1.12). Musculoskeletal investigations have shown bone cells to increase mineralised matrix deposition and collagen secretion in response to cyclic rocking at 45 cycles per minute (cpm) (197) and that fluid force is detected by the primary cilium (198). A mathematical model of a rocking culture system presented an estimate of shear forces for partially filled culture wells, and has the advantage of adaptability for research-specific scenarios (199); however assumptions limit the accuracy of reported values and no validation has been performed.

Cone flow chamber

Plate and cone arrangements generate flow through the rotation of a cone in fluid causing shear stress to act on a cell monolayer (34) (Figure 1.12). Turbulent flow can be induced and at $100 - 130$ rpm a shear stress of 1 Pa is reported (200). Reported shear stress was based upon mathematical modelling where a range for varying geometries of $0.01 - 100$ Pa was presented (201). No validation of plate and cone arrangement reported shear stresses has been performed; however the cone flow chamber has proved popular for a range of cell types, including endothelial cells and chondrocytes (202, 203, 204).

Parallel flow chamber

Parallel plate flow chambers are popular cell stimulation devices with various geometries used to create uniform laminar flow (25, 26, 27, 28, 29, 30, 31, 32, 33). A pressure gradient across a rectangular chamber causes flow and generates shear stress at a cell monolayer (Figure 1.12). Shear stress within parallel plate flow chambers has been characterised using mathematical modelling for varying flow conditions and geometries (35); however, again, no validation was performed and thus confidence in reported values is low. For a width/height ratio of 80, maximal shear stress is reported to be 0.5 Pa for a flow velocity of $0.11\,\mathrm{m\,s^{-1}}$ (35).

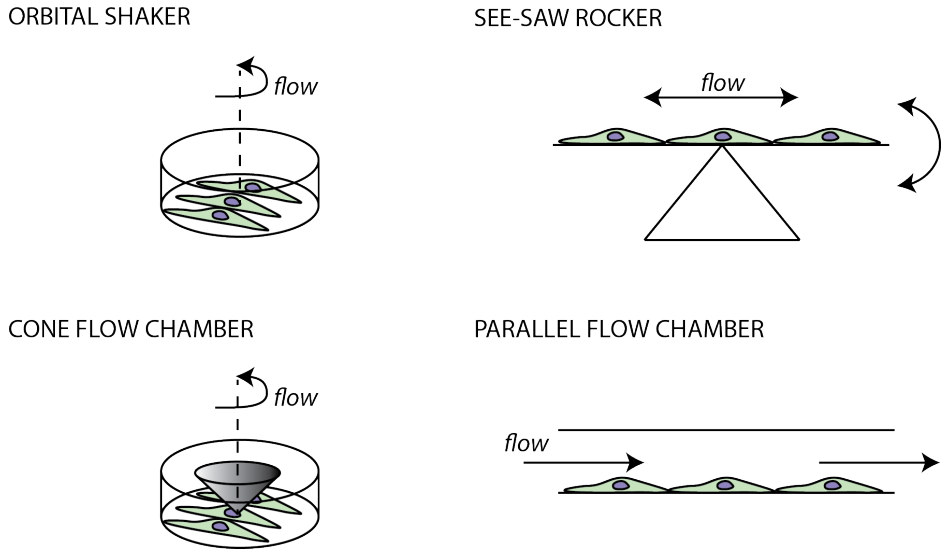

Figure 1.12: Inducing shear stress across a cell monolayer: fluid flow devices are divided into four key groups: orbital shakers; see-saw rockers; cone flow chambers; and generic parallel flow chambers that are the most popular fluid stimulation technique.

1.5.2.2 Three-dimensional stimulation in cell scaffolds

Three-dimensional systems are also used, including: compression and tensile stimulation; and perfusion bioreactors, in an attempt to mimic the *in vivo* environment as best as possible.

Compression & tensile stimulation

Compressive and tensile loading has been used to encourage a biological response in cell-seeded scaffolds (205), a founding principle of musculoskeletal tissue engineering. The structure, density and material composition of scaffolds can influence cell behaviour (206), potentially leading to a change in scaffold mechanical properties (207). The secretion of collagen and formation of fibres has been identified after exposure of an avian tenocyte-seeded scaffold to tensile loading (208). Additionally tensile stimulation of a collagen gel with fibroblasts has shown to create a bioartificial tendon (209). Scaffolds and testing regimes vary due to experiment specific conditions. Compressive and tensile systems have not been used to estimate the forces required to initiate cell response. As a result, compressive and tensile stimulation is not an ideal tool for mechanotransduction research.

Perfusion bioreactor

Perfusion bioreactors involve the seeding of a scaffold with cells and the circulation of culture medium that provide key nutrients to encourage both proliferation and matrix formation (210). They were first utilised to encourage cell matrix production in the late 1980s (211). Designing cell specific scaffolds that encourage cell adhesion, growth and matrix formation is popular (212, 213, 214). With the advancement of manufacturing techniques, the ability to produce scaffolds with pore size and pattern uniformity is improving (215). This combined with a computational fluid dynamics coupled mathematical biology model, allows optimal geometries to be established (216). Perfusion flow rates vary dependent on the cell type; a typical bone cell study used a range of $0.01 - 1\,\mathrm{ml\,min^{-1}}$ (217). Mathematical models of perfusion flow rates have been validated against experimental laser-Doppler techniques for a specific bioreactor (218) reporting a maximum shear stress of $4.4 \times 10^{-3}\,\mathrm{Pa}$; however with a large range of cell specific scaffold-reactor arrangements, shear stresses are more than likely to vary from experiment to experiment.

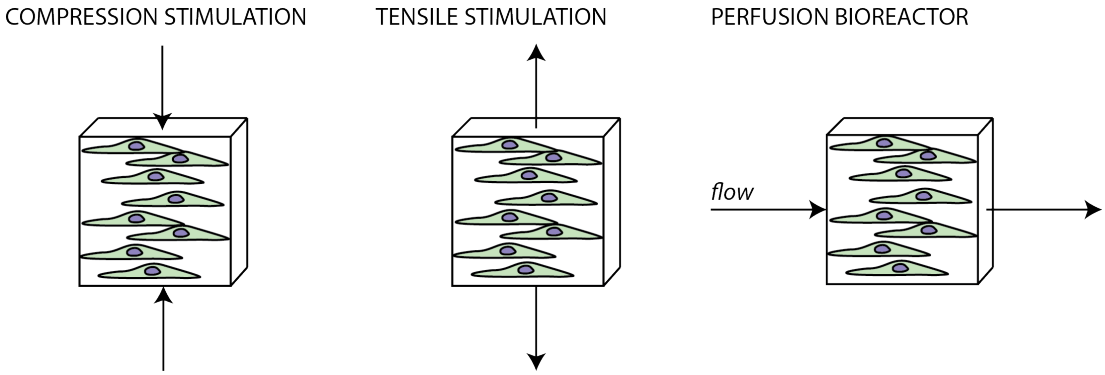

Figure 1.13: Three-dimensional cell stimulation devices: cells seeded in scaffolds are stimulated using compressive and tensile stimulation regimes. Fluid flow stimulation is achieved using perfusion bioreactors, which are popular tools for developing tissue engineering techniques and studying tissue growth.

1.6 Tendon cells

1.6.1 Structure, location & function

Tenocytes dominate the cellular components of tendon, with the remaining $5 - 10\,\%$ consisting of chondrocytes at insertion sites (139), endothelial cells in vascular networks, synovial cells in the tendon sheath (39), and human tendon stem cells (hTSCs) (219, 220). Tenocytes are characterised by the expression of tenomodulin and scleraxis (221) and a spider-like structure in culture (Figure 1.14), where as hTSCs are characterised by a cobble-stone shape in culture (Figure 1.14) (222), and require a specific matrix coordinated by the presence of biglycan and fibromodulin *in vivo* (219).

Tenocytes are fibroblast-like cells that are sparsely populated in the dense tendon fibre network (155), arranged in parallel chains (223) and stretched in the direction of collagen alignment (14) (Figure 1.14). In tissue they become can very elongated ($80 - 300\,\mu m$) due to the low cell number to matrix ratio and to ensure cell-cell communication is maintained (39). Tenocytes are hypothesised to apply a force to the matrix that they adhere to (104), potentially causing the formation of a crimp pattern observed in unloaded tissue (224).

Tenocytes are stimulated by chemical and mechanical influences. Chemical factors include cytokines and growth factors that bind to specific receptors on the cell surface and cause biochemical signalling leading to a biological response, such as proliferation, migration and matrix synthesis (225). Examples include transforming growth factor β (TGF-β), which increases matrix synthesis (225, 226), and tumour necrosis factor α (TNF-α), a pro-inflammatory cytokine, that has a role in tendon healing and matrix degradation (227).

Experiments which expose tenocytes to mechanical stimulation have been varied. Due to cyclic loading *in vivo*, cyclic stretching *in vitro* has proved popular, indicating a change in gene expression, cell proliferation and matrix secretion (228, 229, 230, 231, 232, 233). In contrast to tensile testing, compressive testing has shown tendon cells to become more spherical allowing them to withstand deformation, and their surroundings to be more fibrocartilaginous (234).

Mechanical overstimulation of tenocytes has been shown to up-regulate inflammatory mediators prostaglandin E_2 (PGE_2) and leukotriene B_4 (LTB_4) that can lead to

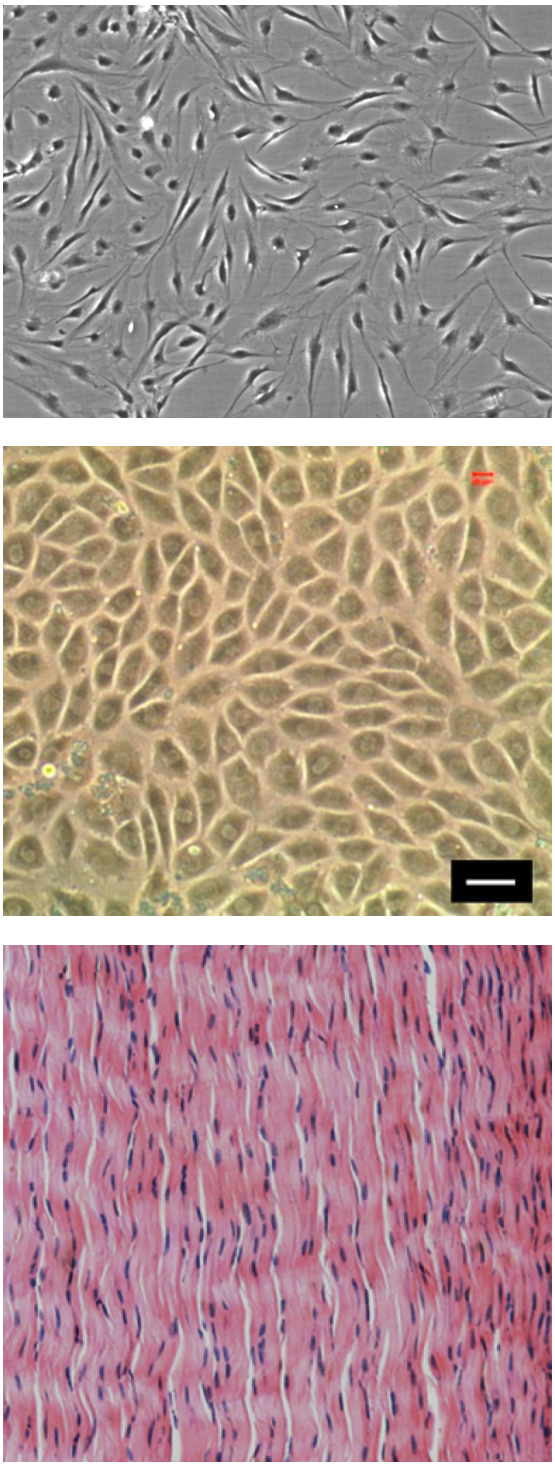

Figure 1.14: Tendon cells in culture & in tissue: top - human tendon cells have a spider-like structure in culture; middle - hTSCs exhibit a cobble stone shape in culture. Figure used with permission (222); bottom - hematoxylin and eosin stain indicating the distribution of tenocytes (purple) in collagen fibres (pink). Figure used with permission (208).

tendinopathy (229, 235). Conversely stress deprivation has also been shown to affect tenocyte behaviour; Lavagnino *et al.* showed that a lack of stimulation causes a matrix degrading enzyme, matrix metalloproteinase-1 (MMP-1), to be up-regulated (228). Furthermore, the Young's modulus of rat tail tendon fascicles has been shown to decrease with static loading in comparison to fresh controls and high frequency, low magnitude stimulation (236). In addition, Arnoczky *et al.* showed that inhibiting the expression of MMPs reduced the rate of matrix degradation (237).

Finally, tenocytes have been exposed to fluid-induced shear stress using varying loading regimes and is discussed further in Section 1.6.2.

1.6.2 Tenocyte fluid flow investigations

Previous tenocyte fluid flow investigations have been dominated by the use of unvalidated parallel flow chambers with differing geometries (Figure 1.12) for analysing changes in gene expression and protein secretion.

After five minutes of flow in a parallel flow chamber, human tenocytes responded to an estimated shear stress of $0.5 - 1.0\,\text{Pa}$ with an increase in calcium signalling, a pre-cursor to gene expression (238). Conversely using the same device, chicken flexor tenocytes were exposed to two minutes of shear stress at the same flow rates and showed no change in calcium signalling (239). Although the duration of applied flow and source of tenocytes are different, the use of the same device and flow rates make the findings comparable, alluding to differences between human and animal tendon cell response.

A different flow chamber device was used to investigate rabbit tenocytes. Application of a range of estimated shear stress (0.1, 1 and 2.5 Pa) for three hours resulted in an increase in collagenase-I (MMP-1), stromelysin-I (MMP-3), cyclooxygenase-II (COX-2) and interleukin-1β (IL-1β) (240). No calcium signal was identified.

A cone viscometer (Figure 1.12) rotating at 50 rpm generated an estimated shear stress of 0.41 Pa on rat flexor tendon cells for six and twelve hours (241, 242). The investigation concluded that the mechanical shear had an overall anti-fibrotic response with decreased transcription of collagen type-I and collagen type-III. Sheared rat tenocytes showed an increase in MMPs, consistent with extracellular matrix degradation. Additionally genes within the bone morphogenetic protein (BMP) and vascular endothelial growth factor (VEGF) cytokine families that are considered to have a key role in tendon healing (243) were up-regulated with the application of mechanical shear stress.

Although not tenocytes, fibroblasts have shown increased proliferation and alignment when exposed to interstitial fluid flow in a three-dimensional flow chamber at a flow rate of $0.012\,\mathrm{ml\,min^{-1}}$ (weighted average velocity of $6.3 \times 10^{-6}\,\mathrm{m\,s^{-1}}$) generating an estimated shear stress between 15 and 33 mPa (244).

Investigations into the effect of fluid shear stress on matrix secretion is limited to one investigation that used porcine tenocytes in a perfusion bioreactor (245). No estimate of fluid shear stress was made. Cells were subjected to $0.1\,\mathrm{ml\,min^{-1}}$ for seven days and showed an increase in matrix formation and tenocyte proliferation.

1.7 Fluid flow in tendon tissue

The water content of tendon amounts to $60 - 70\,\%$ of its weight (225), and this fluid is free to move during loading (21). Interstitial fluid flow has been identified in tendon as a result of experimental studies (246, 247, 248); however shear stress has not been quantified *in vivo*. A poroelastic model has shown that the mechanical response of tendon is caused by both matrix and fluid factors (249), and suggestion has been made that glycosaminoglycans (GAG), a side-chain of a proteoglycan protein found in tendon, may transfer force through the matrix by interaction with fluid (250). Additionally Haut & Haut have shown that tendons respond differently to strain rate dependent on their hydration (251) and hydrostatic stress has been indicated as an important factor in regulating tendon composition (252).

An interstitial finite element model applied Darcy's law to experimental results and established a range of $7.62 \times 10^{-2} - 2.23 \times 10^{4}\,\mathrm{Pa\,s^{-1}}$ for the shear rate across the radial direction of a tendon and a maximal fluid velocity of $0.6\,\mathrm{mm\,s^{-1}}$ within the model (21).

More recently, a finite element model estimated the level of fluid-induced shear stress acting on cells in tendon and reported a maximum shear stress of $4.59 \times 10^{-4}\,\mathrm{Pa}$ at $3\,\%$ strain and a strain rate of $6\,\%\,\mathrm{strain\,min^{-1}}$ (253). Additionally, a maximum velocity magnitude of $1.2 \times 10^{-4}\,\mathrm{mm\,s^{-1}}$ was reported and experimentally stimulated tendons were shown to reduce collagenase expression compared to static controls.

Tissue-level strains within bone, measured by strain gauges attached to a human tibial shaft, are reported to be $< 0.2\,\%$ (254); however, *in vitro* experiments have identified that for a cellular response, a dynamic substrate strain must be at least ten-fold larger (255, 256). You *et al.* have suggested that oscillatory fluid-induced shear

stress of 2 Pa at 1 Hz has more influence over metabolic response of bone cells than substrate strain ranging from 0.1 to 10 % at 1 Hz (256). Building on these findings, a model presented the idea that GAG side-chains act as tethering elements across the bone pericellular matrix, amplifying the fluid flow signal induced by strain to allow for detection by cells (Figure 1.15) (257). Based on the findings of Robinson *et al.* (250), this model may be relevant for tendon mechanics *in vivo*.

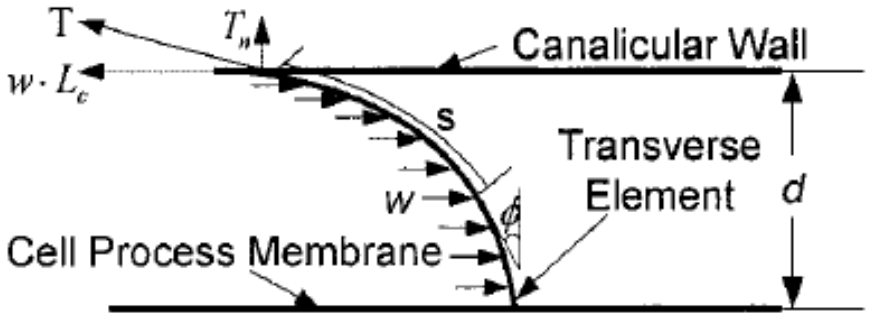

Figure 1.15: Idealised Han *et al.* model of the osteocyte process: tethering elements, which ensure the osteocyte process remains central to the pericellular matrix, experience deflection due to fluid flow, w. Figure adapted with permission (257).

1.8 Design of an *in vitro* fluid flow cell stimulation tool

1.8.1 *In vitro* model prerequisites

Tendon is exposed to cyclic forces *in vivo* and mechanical response is determined by both a matrix and fluid flow element (Section 1.7). Understanding the effects of fluid flow on tenocyte mechanosensation is essential (Section 1.1) and to achieve this, a stimulation device is required that applies characterised fluid shear stress.

In vitro investigations using tenocytes have shown a biological response for estimated shear stresses ranging from $0.1 - 2.5$ Pa and as a result shear stresses should be easily changeable (Section 1.6.2). In addition, unvalidated tendon tissue models have indicated that *in vivo* tenocytes experience fluid-induced shear stress at a much lower maximum of 4.59×10^{-4} Pa (228). Furthermore, fibroblasts have shown a positive (anabolic) response to estimated shear stresses in the region of $15 - 33$ mPa (244).

The device should generate cyclic flow conditions to mimic the loading found in musculoskeletal tissues. To act as a useful model for multiple research institutions, the device should be commercially available and give the researcher the freedom to alter the frequency of flow oscillation and magnitude of shear stress with ease.

1.8.2 Model design

In this thesis a see-saw rocker is proposed as a suitable method of applying fluid shear stress to cell cultures for mechanobiological investigations.

A Stuart SSL4 (Bibby Scientific, United Kingdom) see-saw rocker with a tilt angle of $7\,^{\circ}$ was used to generate flow at a range of $5-70$ cycles per minute (cpm) using a digital selection method, allowing accurate speed selection and reproducibility (Figure 1.16). The device allows the application of consistent cyclic flow across a cell monolayer.

The simple see-saw rocker stimulation device allows for high output through the use of a six-well plate experiment design. Six-well plates are popular tools as they require low levels of fluid consumables in comparison to bioreactors, and are regularly used for methods such as the growth of biofilms (258, 259, 260). Six-well plate wells have a diameter of 35 mm, generating a cell layer growth area of $950\,\mathrm{mm}^2$.

Video-capturing of platform motion allowed inspection at 0.2 s intervals to establish vertical displacement over time. Analysis of platform displacement indicated a sinusoidal profile, with peak angular velocity when the platform is horizontal (Figure 1.16). As a result, future modelling of a well requires a sinusoidal velocity boundary condition for rotating surfaces.

Visual analysis of the free surface of fluid within a six-well plate indicated that at 30 cpm a volume of 2 ml ensured that a cell monlayer remained entirely covered by culture medium during a full cycle (Figure 1.17). Thus, biological results using this arrangement would show changes caused by fluid-induced shear stress as opposed to nutrient starvation that might be present in a model where cells are exposed to air.

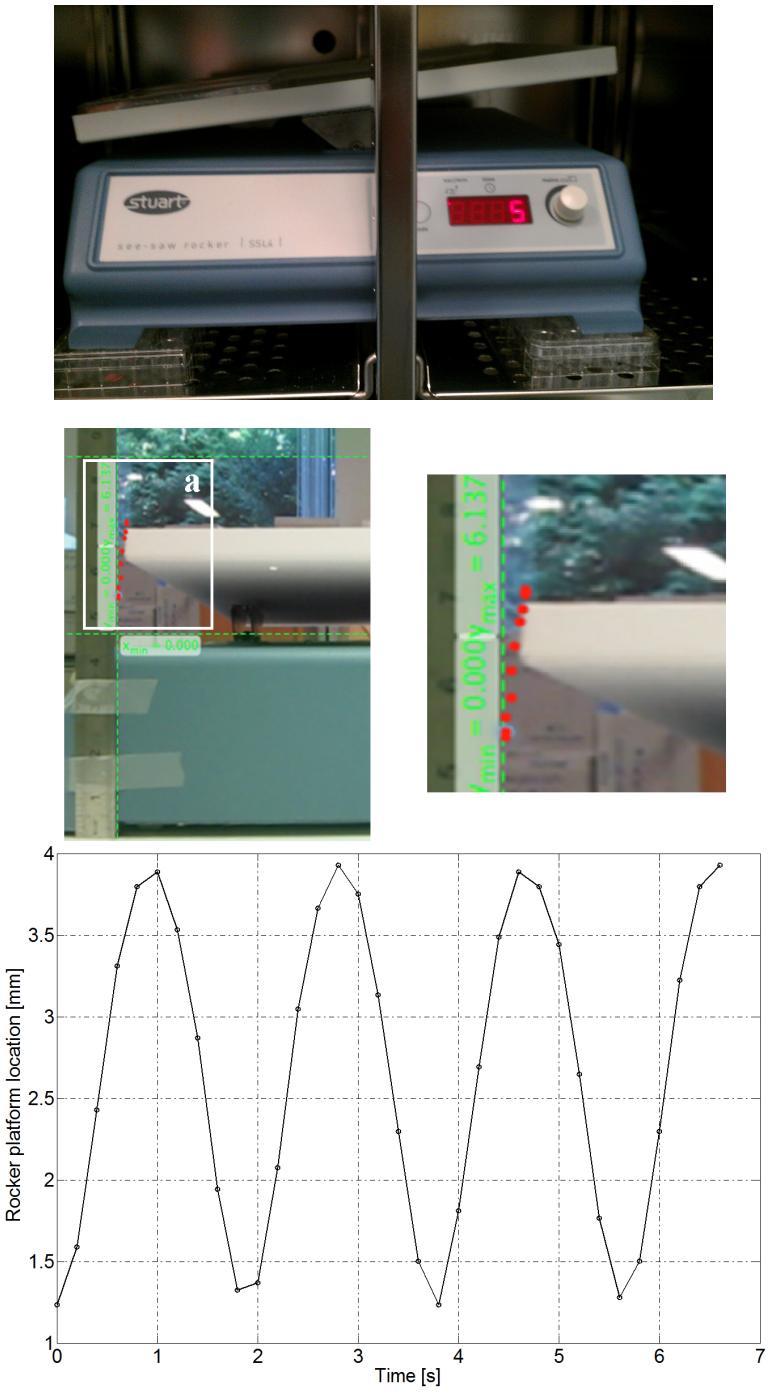

Figure 1.16: Stimulation device: top - Stuart SSL4 see-saw rocker within incubator showing digital input and maximal tilt angle of 7 °. Middle - video capturing of rocker motion allowed the inspection of platform movement (red dots). Bottom - sinusoidal displacement of the rocking platform at 30 s. x-axis - time in seconds. y-axis - vertical position (z-direction) of the corner of the rocking platform from an arbitrary origin applied to side-on video capture (middle figure). Analysis shows sinusoidal behaviour, the z-displacement reduces for each time step as the rocker reaches its maximum and minimum positions.

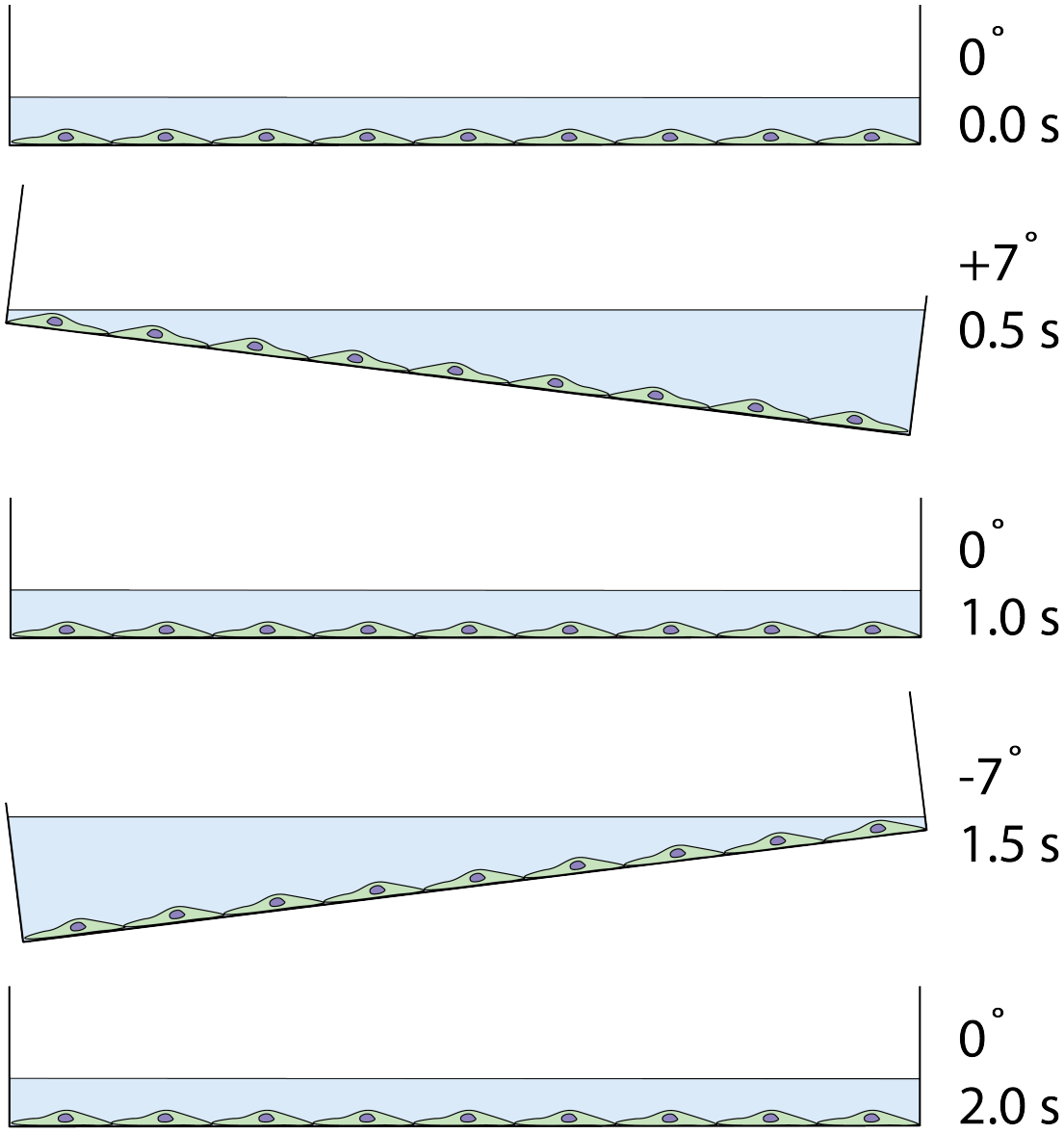

Figure 1.17: Fluid flow profiles: it is essential that during stimulation, cells remain covered with fluid so that any biological response is a result of induced shear stress, rather than factors such as nutrient, or oxidative stress. Visual inspection confirmed that at maximal angle of tilt of 7 °, with 2 ml of fluid, a cell monolayer remains covered for the entire cycle (t = 0 − 2 s) at a frequency of 30 cpm. Schematic not to scale.

1.9 Thesis objectives

The thesis aims detailed in Section 1.1 will be achieved with the following core objectives:

1. Establish an *in vitro* tool for applying physically-relevant, fluid-shear stress to cell culture monolayers as the sole method of stimulation.
2. Within the established tool, determine the range of shear stress using computational fluid dynamics.
3. From the fluid dynamics model, the pattern of flow velocities influencing cell characteristics will be determined and compared to an experimental flow measurement technique. Agreement will result in the validation of reported shear stresses at the cell layer.
4. A change in relevant model parameters will be considered by adapting the validated tool and performing further computational fluid dynamics for a change in frequency of rocking and the viscosity of the added culture medium.
5. To ensure that the tool is useful for *in vitro* cell investigations, a series of preliminary tenocyte biological validations will be completed, focussing on tenocyte alignment and matrix secretion. This will be achieved using microscopy techniques and biochemical assays.
6. The adapted computational models and preliminary biological validations will act as a foundation for the formulation of a mathematical model to predict tenocyte response to fluid-induced shear stress, and further biological investigations will be completed to establish whether relationships can be validated experimentally.
7. Finally, an investigation into the mechanosensor responsible for tenocyte flow detection will be performed.

1.10 Thesis outline

In order to address the overall aims of this thesis, significant scientific knowledge of tendon structure, cell mechanosensation, and matrix secretion is required as presented within Chapter 1.

The arrangement, evaluation and results of a computational fluid dynamics model created to characterise the velocity and fluid-induced shear stress within the well of a six-well plate is presented in Chapter 2. In Chapter 3, an experimental flow capturing technique called particle image velocimetry, is used to verify the velocity flow fields of the computational model.

Within Chapter 4, expansion of the computational fluid dynamics model in Chapter 2 is presented. The impact of different flow viscosities and frequencies on the resultant shear stress magnitude across the well base is considered as well as the effect of placing a well at the edge of the rocking platform.

Chapter 5 details the materials and methods for all biological investigations that are reported in Chapter 6.

Chapter 6 presents biological validation of the rocking platform for use with human tenocytes. A mathematical model is used to predict the behaviour of tenocytes to changes in shear stress magnitudes computed in Chapter 4. Additionally, within Chapter 6, consideration of the primary cilium as the key sensor of fluid flow in human tenocytes *in vitro* is presented.

Finally, in Chapter 7 the thesis is concluded with some final remarks and discussion, highlighting the limitations of this study and recommended future direction of further work.

Chapter 2

CFD estimation of shear stress within the *in vitro* model

The characterisation of *in vitro* cell stimulation tools is essential in order to link applied stress with observed biological response. Computational fluid dynamics (CFD) has been used to characterise previous *in vitro* tools (Section 1.5.2), but a novel model is required for the investigation of cyclic shear stress applied to musculoskeletal cells. Cyclic flow induced by the see-saw rocker generates shear stresses that are experienced by cells at the well base. Characterising these shear stresses is essential so that a biological response can be mapped to a mechanical stimulus.

CFD is an iterative process whereby the behaviour of a fluid is solved using a series of governing equations. The work presented in this chapter used a finite difference technique known as the 'finite volume' method to complete the iterative process. This is the most validated and well-established method and has a series of commercial CFD codes, of which CFD-ACE (ESI CFD, France) was utilised.

Within this chapter, CFD was used to determine the range of shear stress within the *in vitro* model in order to achieve the second thesis objective. The modelling arrangement is presented, including the governing equations and varying techniques used to predict fluid behaviour. Subsequently, model accuracy and stability is evaluated, and the shear stress and velocity results from the modelling presented. In addition, the limitations and intended use of the model are discussed with an evaluation of the impact of key assumptions on model results.

2.1 Modelling arrangement & methods

Before introducing the methods used for modelling, this section provides an assessment using simple well-known tools for flow determination to define the scope and range of the problem. Model dimensions and design are described earlier in Section 1.8. Computational modelling was performed for a single well at an arbitrary oscillation of 30 cpm (0.5 Hz). This frequency was chosen as it was near the middle of the Stuart SSL4 operating range of $5 - 70$ cpm.

2.1.1 Dimensionless numbers

Dimensionless numbers act as a tool to understand flow characteristics and behaviour. Evaluation of the Reynolds, Weber and Bond numbers assisted in identifying assumptions that could be made to simplify the model arrangement.

2.1.1.1 Reynolds number

The Reynolds number Re is a measure of the relative importance of inertial forces and viscous forces in a flow field (261). Pioneering experiments for varying geometries defined the Reynolds number and established ranges to determine whether flow is laminar or turbulent (262). In turbulent conditions, inertial forces are much larger than viscous forces, where as in laminar conditions, inertial forces may still dominate viscous forces up to a transition value.

The geometry of the flow was assumed to be similar to that of an open, rectangular channel (Equation 2.1), where transition to turbulent flow occurs at a Reynolds number of 600 (263).

$$Re = \frac{\rho \, V \, D_H}{\mu} \tag{2.1}$$

where ρ is the fluid density, V is the fluid velocity, D_H is the hydraulic radius, and μ is the dynamic viscosity.

The hydraulic radius D_H of 1.86 mm was determined from the flow wetted perimeter (39.16 mm) and cross sectional area (72.8 mm^2) (Figure 2.4).

Viscosity μ of $7.8 \times 10^{-4}\,\text{kg}\,\text{m}^{-1}\,\text{s}^{-1}$, and density ρ of $1000\,\text{kg}\,\text{m}^{-3}$ were used to represent cell culture medium (35).

An upper bound for velocity V was estimated by calculating the velocity required for a fluid particle to move from one edge of the well to the other during a quarter of a complete cycle. At 30 cpm this suggested a speed of $0.07\,\mathrm{m\,s^{-1}}$, as a particle would be required to move 35 mm in half a second. Reynolds number was determined to be 167 and flow concluded to be laminar.

Turbulent flow was estimated to occur at a flow velocity of $0.25\,\mathrm{m\,s^{-1}}$, and applying the previous assumptions, this would occur at 107 cpm. As the see-saw rocker is limited to a maximum of 70 cpm, it was concluded that flow within the well is laminar at all applicable rocking frequencies.

The use of the calculation for an open, rectangular channel as a model for the flow field within a culture well placed on a see-saw rocker provides a good estimation of the Reynolds number; however, at different locations within the well the dimensions of the hydraulic radius change. As the horizontal distance across the base of the well converges as it reaches the wall, the hydraulic radius is reduced to 0.5 mm, reducing the Reynolds number almost four-fold (1.86/0.5). Therefore, the use of the open, rectangular channel calculation may over-estimate the average Reynolds number within the well.

2.1.1.2 Bond number

To further ascertain the forces that dominate flow behaviour the Bond number Bo was considered. The Bond number is a measure of how important surface tension forces are in relation to body forces (Equation 2.2). A value of less than one signifies that surface tension is key.

$$Bo = \frac{\rho\ g\ L^2}{\sigma} \tag{2.2}$$

where ρ is the fluid density, g is the external force, L is the characteristic length, and σ is the surface tension of the fluid.

Fluid density ρ of $1000\,\mathrm{kg\,m^{-3}}$ was used to represent cell culture medium. Gravity drives inertial flow with the rotating surfaces of the well. For the external force g gravitational acceleration of $9.8\,\mathrm{m\,s^{-2}}$ was used. The characteristic length L of 0.035 m was determined from the width of the dish. The surface tension σ was estimated to be $0.072\,\mathrm{N\,m^{-1}}$ based on the reported surface tension of water.

The Bond number was calculated to be 167 and signified that inertial forces override any surface tension effects.

2.1.1.3 Weber number

The Weber number We is especially useful when considering fluid problems where an interface is present. It represents the importance of hydrodynamic forces to surface tension and as with the Bond number, a value of less than one would signify that surface tension is the dominating force (Equation 2.3).

$$We = \frac{\rho\, V^2\, L}{\sigma} \tag{2.3}$$

where ρ is the fluid density, V is the fluid velocity, L is the characteristic length, and σ is the surface tension of the fluid.

As in the Reynolds number calculation, fluid density ρ of $1000\,\mathrm{kg\,m^{-3}}$ and velocity V of $0.07\,\mathrm{m\,s^{-1}}$ were used. The characteristic length L of $0.035\,\mathrm{m}$ and surface tension σ of $0.072\,\mathrm{N\,m^{-1}}$ used were the same as for the Bond number calculation.

The Weber number was calculated to be 2.4 and thus it was concluded that hydrodynamic forces override surface tension effects.

2.1.1.4 Concluding model assumptions

In conclusion, dimensionless number analysis has shown that: the Reynolds number indicates laminar flow; and that inertial and hydrodynamic forces override surface tension effects.

2.1.2 Conservation laws & resultant governing equations

2.1.2.1 Navier-Stokes equations

Flow is described through a series of mathematical formulae, known as 'governing equations', that define the conservation of mass, momentum and energy.

Using the finite volume method, across a control volume, fluxes and forces are evaluated to ensure conservation of mass and momentum are derived.

The conservation of mass is governed by a partial differential equation known as the continuity equation. This dictates a balance of masses that enter and exit a control volume during a period of time ∂t, with the rate of change in the fluid density ρ. In

three-dimensions, for a flow velocity vector $U(u_1, u_2, u_3)$ the continuity equation can be expressed in vector form (Equation 2.4).

$$\frac{\partial \rho}{\partial t} + \nabla.(\rho U) = 0 \tag{2.4}$$

The rate of change in momentum for a Newtonian fluid is also governed by a partial differential equation, known as Navier-Stokes (Equation 2.5), that encompasses the sum of all forces acting on a control volume surface, such as surface friction, pressure and body forces (*e.g.* gravity).

$$\rho \frac{\partial \underline{U}}{\partial t} + \rho \underline{U} \cdot \nabla \underline{U} + \underline{\nabla} P = \mu \nabla^2 \underline{U} + f \tag{2.5}$$

where P is pressure acting on the fluid, μ is the dynamic viscosity, and f encompasses other body forces.

2.1.3 Discretisation using the finite volume method

The finite volume method required that a domain was divided into a grid of computational cells known as control volumes, an example of which is shown in Figure 2.1. This process is known as discretisation. Using the generated grid, an implicit finite volume method was employed by fluid dynamics software (CFD-ACE, ESI CFD, France) to approximate a flow solution.

The fluid dynamics software assigns a node to each centre of a control volume. The values of variables at neighbouring nodes are used together with differencing methods to estimate a variable in a given control volume.

2.1.3.1 Generalised transport equation

The governing equations can be represented as a generalised transport equation that is more convenient for mathematical evaluation (Equation 2.6) and can be integrated over each control volume, V (Equation 2.7).

$$\frac{\partial}{\partial t}(\rho\varphi) + \nabla \cdot (\rho U \varphi) = \nabla \cdot (\Gamma \nabla \varphi) + S_\varphi \tag{2.6}$$

$$\int_V \frac{\partial}{\partial t}(\rho\varphi) dV + \int_V \nabla \cdot (\rho U \varphi) dV = \int_V \nabla \cdot (\Gamma \nabla \varphi) dV + \int_V S_\varphi dV \tag{2.7}$$

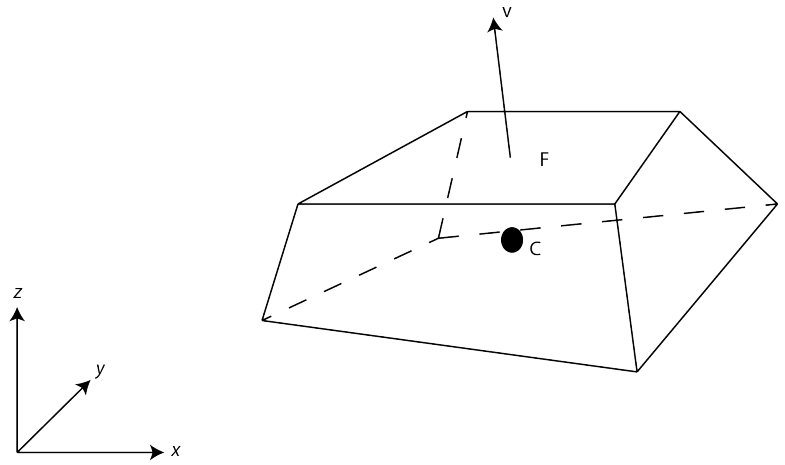

Figure 2.1: Representative three-dimensional control volume: a domain is divided into computational cells that act as control volumes for evaluation of governing equations. Control volume centre, C, face, F and normal vector, v.

where φ is the conserved quantity being solved for, Γ is the diffusion coefficient, and S is the source term. The continuity equation may be recovered by setting $\varphi = 1$, $\Gamma = 0$ and $S_\varphi = 0$. Similarly, the Navier-Stokes equation may be recovered by setting $\varphi = U$, $\Gamma = \mu$ and $S_\varphi = f - \nabla P$.

The general transport equation (Equation 2.6) is divided into its separate terms. On the left-hand side, the first term represents the transient properties of the flow and the second term represents convection properties. On the right-hand side, the first term represents diffusion and the last term represents source properties.

2.1.3.2 Temporal discretisation

The flow within the culture well placed on the rocker changes over time, requiring a transient model solution that evaluates the fluid motion at pre-defined time intervals for a set number of cycles. As the model is transient, temporal discretisation is required and involves integrating every term in the differential equations over a given time step size δt. Temporal discretisation is achievable through explicit or implicit methods, or a combination of the two. The implicit method evaluates the function of a variable φ at a future time step and is solved iteratively at each time step before moving on to the next. The explicit method evaluates the function of a variable φ at the current time

step and φ can be expressed explicitly using existing solution values.

Within CFD-ACE an implicit first-order Euler method is available as well as a second-order Crank-Nicholson method where explicit and implicit calculations are combined. Temporal discretisation within this model was achieved with the default implicit first-order, backward step Euler method (Equation 2.8).

$$\frac{\varphi_i^{n+1} - \varphi_i^n}{\Delta t} + O(\delta t) = k\frac{\varphi_{i+1}^n - 2\varphi_i^n + \varphi_{i-1}^n}{\Delta x^2} + O(\Delta x^2) \tag{2.8}$$

where n is the time step number, i is the current control volume, φ is the variable of interest, k is the diffusion coefficient, δt is the size of the time step, and Δx is the distance between the centre nodes of two control volumes.

The implicit method is numerically stable and convergent and is preferred where the model has large time-step values. For smaller values Crank-Nicholson is preferred, but comes at an increased computational cost and strict constraint on the Courant-Friedrichs-Lewy (CFL) condition (Section 2.1.4).

Discussed further in Section 2.1.8, the high computational cost of this study led to the decision to use a constant time-step value that resulted in a fluctuating CFL number, thus the implicit Euler scheme was selected to encourage model stability.

2.1.3.3 Spatial discretisation

Within CFD-ACE, the value of a variable at a control volume central node is the mean value for that variable within the control volume. To define the algebraic expression for each centre node, spatial differencing schemes are used.

Within the see-saw rocker model, this was established with a combination of a second-order upwind differencing scheme (SUD) (Figure 2.2) (Equation 2.9) and a first-order upwind scheme (FUD) (Equation 2.10), linked together by a blending factor of 0.1 (Equation 2.11). This resulted in a differencing scheme that was 10 % first-order and 90 % second-order.

$$\varphi_e^{\mathrm{SUD}} = \begin{cases} f(\varphi_W, \varphi_C) & \text{if } V_F^n \text{ is } >0 \\ g(\varphi_C, \varphi_{EE}) & \text{if } V_F^n \text{ is } <0 \end{cases} \tag{2.9}$$

$$\varphi_e^{\mathrm{FUD}} = \begin{cases} \varphi_C & \text{if } V_F^n \text{ is } >0 \\ \varphi_E & \text{if } V_F^n \text{ is } <0 \end{cases} \tag{2.10}$$

where V_F^n is a velocity component in the direction that is normal to the control volume face, F (Figures 2.1 & 2.2) and WW, W, C, E and EE subscripts refer to west-west, west, centre, east and east-east control volumes, respectively. e represents the face of the east control volume, E (Figure 2.2).

$$\varphi_F = \alpha\varphi_F^{\mathrm{FUD}} + (1-\alpha)\varphi_F^{\mathrm{SUD}} \tag{2.11}$$

where α is the blending factor: $\alpha = 0$ yields a fully second order scheme and $\alpha = 1$ yields a fully upwind scheme. φ_{EE} is the variable from a neighbouring downwind control volume to control volume E (Figure 2.2).

First order spatial differencing is known to provide stable solutions, but can result in diffusive results due to non-physical oscillations in the model solution. As such, the use of blending generates a second-order solution whilst encouraging model stability from the first-order scheme.

2.1.3.4 Pressure-velocity coupling and solver

Within CFD-ACE equations are solved separately; however the continuity equation does not include a pressure term and therefore, a pressure-velocity coupling method is used to derive a pressure correction equation known as the semi-implicit method for pressure-linked equations (SIMPLE).

A first guess of pressure was made and estimated velocities calculated from discretised momentum equations. A pressure correction value was then calculated and used to correct guessed pressure and resultant estimated velocities. Finally, all other discretised transport equations were solved. If convergence was achieved then the solution was stopped, otherwise the algorithm returned to the start with the new guess for pressure being the previously iterated value. For this model, a slightly altered algorithm was used that manipulated momentum equations to remove less significant terms in velocity corrections. This is known as the SIMPLEC (SIMPLE-Consistent) algorithm (264).

An algebraic multi grid (AMG) solver (265) was utilised to find the pressure distribution, permitting 50 sweeps and a convergence criterion of 0.1. The AMG solver created a fine-coarse hierarchy of grids, starting with the problem-defined grid geometry. For the first few iterations the fine grid was used to obtain residuals. These

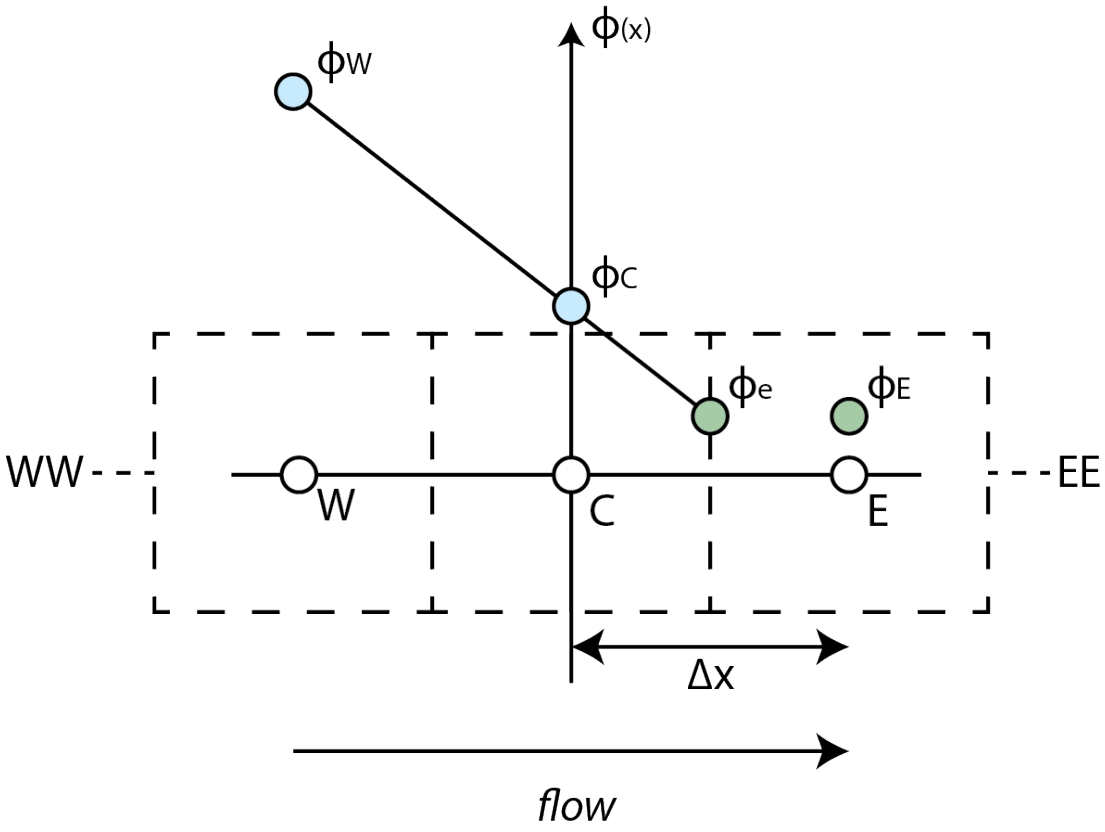

Figure 2.2: Second-order differencing scheme: W, C & E represent the centre nodes of west, centre & east control volumes respectively. To determine the velocity in a given control volume a second order scheme is employed. Δx is the distance between two centre nodes.

residuals were then transferred as source terms on to a coarser grid for subsequent iterations. The corrections from these iterations were then interpolated back on to the finer grid to update the solution. This process reduced the time to completion and memory requirements of the calculations.

2.1.3.5 Numerical method boundary conditions

Computational volume boundary conditions were dealt with by CFD-ACE by setting boundary coefficients to zero. A control computational volume adjacent to the west boundary of a given control volume (Figure 2.3) can be represented by a finite-volume equation for the central node, P (Equation 2.12).

$$a_P\varphi_P = a_E\varphi_E + a_W\varphi_W + a_N\varphi_N + a_S\varphi_S + S \tag{2.12}$$

where a_W is set to zero after the connections to the boundary node, B, are incorporated into the source term, S in its linearised form.

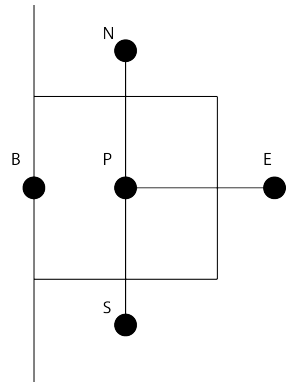

Figure 2.3: Computational boundary control volume

2.1.3.6 Velocity solver

A conjugate-gradient-squared (CGS) solver was selected for determining flow velocity as industry recognised best practice for structured grides. The linear, iterative solver established the solution at each control volume of the discretised well. The solver was permitted to perform 50 sweeps with an individual convergence criterion of 0.0001.

2.1.4 Courant-Friedrichs-Lewy condition

The Courant-Friedrichs-Lewy (CFL) condition is a dimensionless number that determines the percentage of fluid that has changed in a control volume during a given time step (Equation 2.13).

$$CFL = \frac{u\delta t}{\Delta x} \tag{2.13}$$

where u is fluid velocity, δt is time step size, and Δx is the length of a given control volume (Figure 2.2).

As discussed in Section 2.1.3.3, the calculations of flow velocities in a control volume required knowledge of the conditions in the upwind control volume(s) and the conditions during the previous time step. If the fluid was moving too fast and the fluid in a control volume fluid entirely changed as the solution stepped from one time step to the next, or in extreme cases, the control volume fluid moved through several control volumes in one time step, then the solution would become unstable and ultimately diverge.

To encourage the model to remain stable, a CFL value of 0.25 was desired. Grid geometry and time step size were dependent on satisfying this condition. A value of 0.25 indicates that no more than 25 % of the fluid in any given control volume may change during a single time step.

2.1.5 Geometry & grid generation

Varying grid sizes and shapes were investigated for a single domain in order to establish a solution that produced grid independent results, that is, increasing control volume grid density had no further impact on the solution.

Using geometry and grid generation software (CFD-GEOM, ESI CFD, France) a domain was established to represent a single cell culture well with a height of 6.21 mm and a diameter of 35 mm (Figure 2.4). In accordance with cylindrical geometry best-practice, a butterfly pattern was used for meshing the base of the well using five structured faces where the spatial resolution of points around the circumference of the well varied between 36 and 396 points (Figure 2.4). By extruding the grid pattern at the base of the well, the grid for the entire cylindrical structure was obtained resulting in ten grids varying between 5,265 and 1,470,150 control volumes. A representation of the

grid of the discretised domain is displayed in Figure 2.4b. This grid resulted in hexahedral control volumes that are optimal for free surface calculations as they provide a structured coordinate system for the computation of the orientation of the interface.

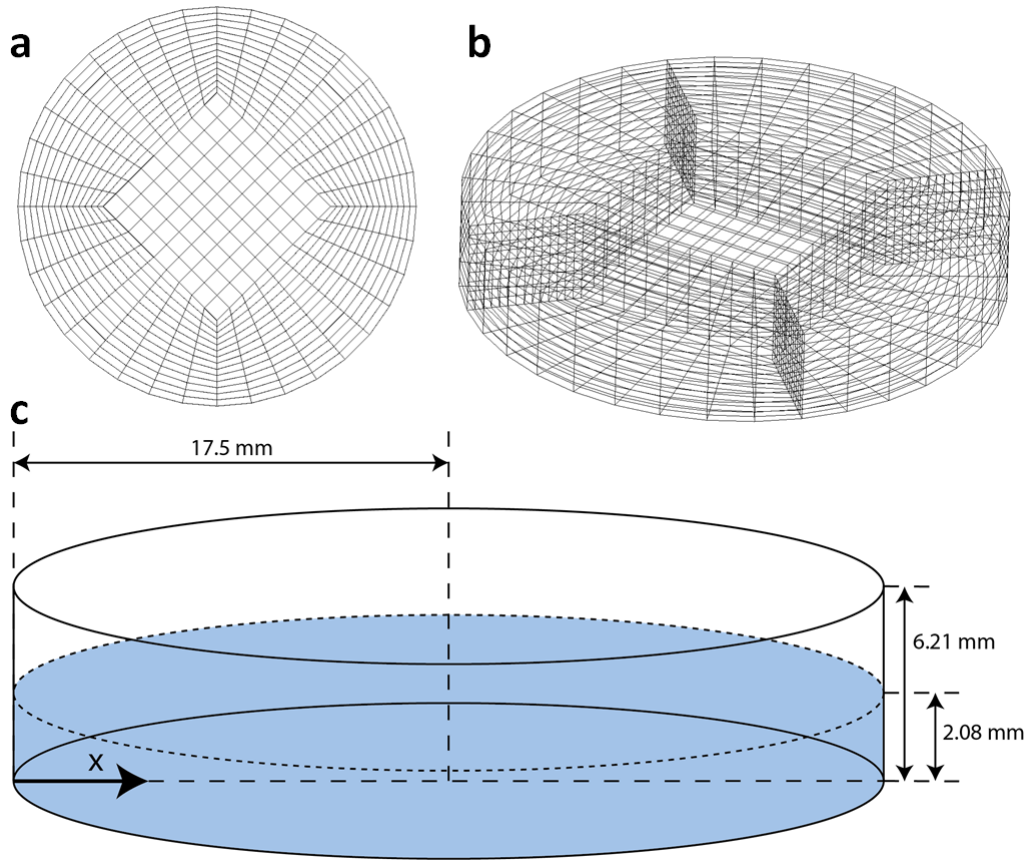

Figure 2.4: Model characteristics: a) butterfly grid pattern, b) representation of extruded three-dimensional grid structure, c) model geometry, where blue represents the culture medium depth (not to scale). The origin and direction of the x-axis at the base of the well is shown.

2.1.6 Boundary and initial conditions

The cell culture well is commonly used with 2 ml of fluid in biological experiments. The well was filled with liquid up to a depth of 2.08 mm (based upon 2 ml of fluid), with a viscosity of $7.8 \times 10^{-4}\,\mathrm{kg\,m^{-1}\,s^{-1}}$, and density of $1000\,\mathrm{kg\,m^{-3}}$ to represent cell culture medium (35). The base and vertical boundaries of the model were assigned

no-slip conditions, while the top of the well as an outlet with zero pressure to represent interaction with air. No-slip conditions dictate that at a wall, the fluid velocity is zero relative to the wall. The outlet condition allowed a flux of air across control volume surfaces that were assigned this condition. Video capturing showed the motion of the rocker to be sinusoidal (Figure 1.16) and the motion of the well was modelled by sinusoidal rotation about the y-axis at a frequency of 0.5 Hz, with a maximum rocking amplitude of $\pm 7\,^{\circ}$, and the origin of the coordinate system and centre of rotation located 35 mm below the bottom centre of the model. The model was required to move $28\,^{\circ}$ during one complete cycle, with angular velocity determined from a sinusoidal computation for each time step (Equation 2.14) (Figure 2.5).

$$|v| = \sqrt{\left(\frac{14}{0.637}\cos(2\pi f T)\right)^2} \tag{2.14}$$

The velocity expression assumed the well started level at $0\,^{\circ}$. The frequency, f, was 0.5 Hz. CFD-ACE required that all velocities were absolute as constraining angle conditions dictated a change in direction rather than the sign of the velocity component. A high number of significant figures was required for the amplitude to achieve a high level of angular displacement accuracy.

Under angle limits of $\pm 7\,^{\circ}$ an amplitude of $\frac{14}{0.637}$ produced a frequency of 0.5 Hz; however due to rounding limitations, an error was compounded within the results and an accumulated displacement of $0.24\,^{\circ}$ was achieved over six cycles. During six cycles, $168\,^{\circ}$ of displacement was expected and thus the error in the parametric expression was less than 0.15 %. This was assumed to have a negligible effect on generated results.

2.1.7 Grid deformation

Due to the existence of rotating surfaces, the grid was re-meshed at each time-step (0.001 s) using a grid deformation scheme.

Grid re-meshing was achieved through a standard transfinite interpolation (TI) scheme, which determined the interior node distribution based on the motion of the boundary. As a result, the grid geometry remained consistent, but at a different angle from the origin for a given time step in accordance with the moving boundary.

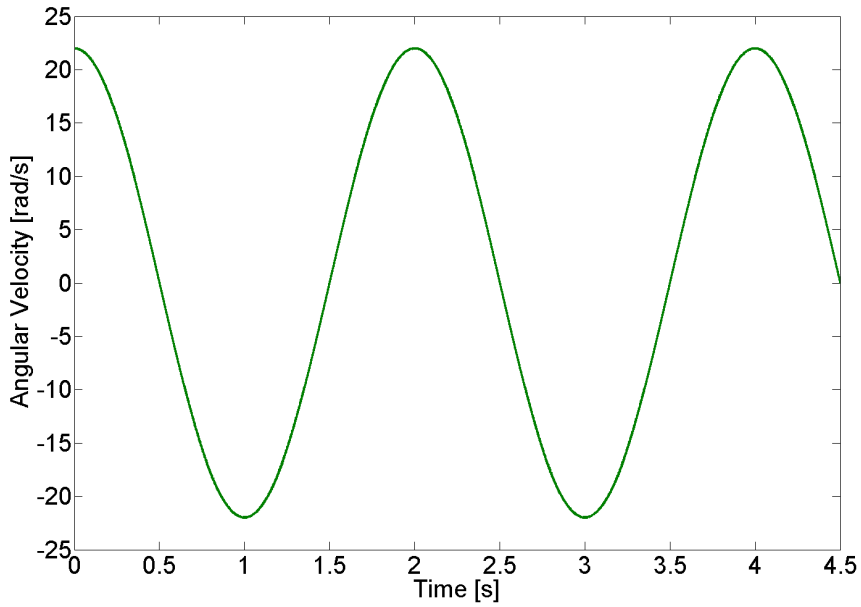

(a) Angular velocity

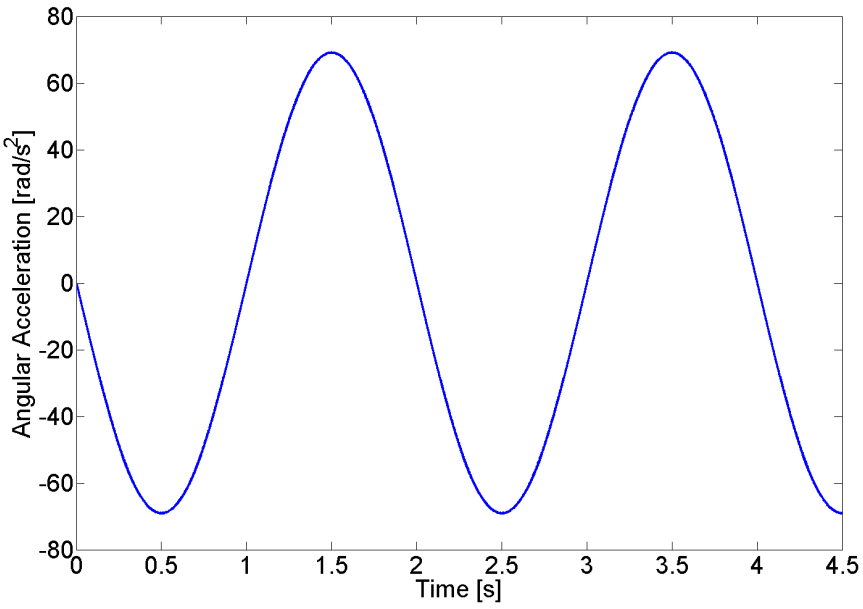

(b) Angular acceleration

Figure 2.5: Well angular velocity and acceleration: the resulting velocity and acceleration profiles at 0.5 Hz achieved with the sinusoidal velocity expression (Equation 2.14).

2.1.8 Free surface reconstruction

As the model included two fluids, culture medium and air, it was necessary to employ a reconstruction scheme to establish the shape and structure of the interface where the two fluids met.

The Volume of Fluid (VoF) technique (266) was employed in order to track and locate the free surface of the liquid within the domain. Within the model, Bond and Weber numbers were calculated to be greater than 1 (Section 2.1.1), signifying that gravitational and inertial forces override capillary effects. Thus, computational modelling of surface tension was neglected in the model of the free surface and a single line interface construction (SLIC) scheme employed to track the free surface (267). A static contact angle was assigned as the free surface-wall interaction boundary condition. Contact angle measurements confirmed the material of the well to be slightly hydrophilic, (water: $84.95 \pm 1.39°$, media: $79.74 \pm 1.47°$ n = 6) (Figure 2.6), therefore, a static contact angle of $90\,°$ was deemed an appropriate assumption as although it was technically possible to represent contact angles other than $90\,°$, the computational cost of this justified the simplifying assumption.

The process by which the SLIC scheme determined the fluid flux at the media and air interface was through a process of inspecting upwind and downwind control volume properties from a previous time step (Figure 2.7).

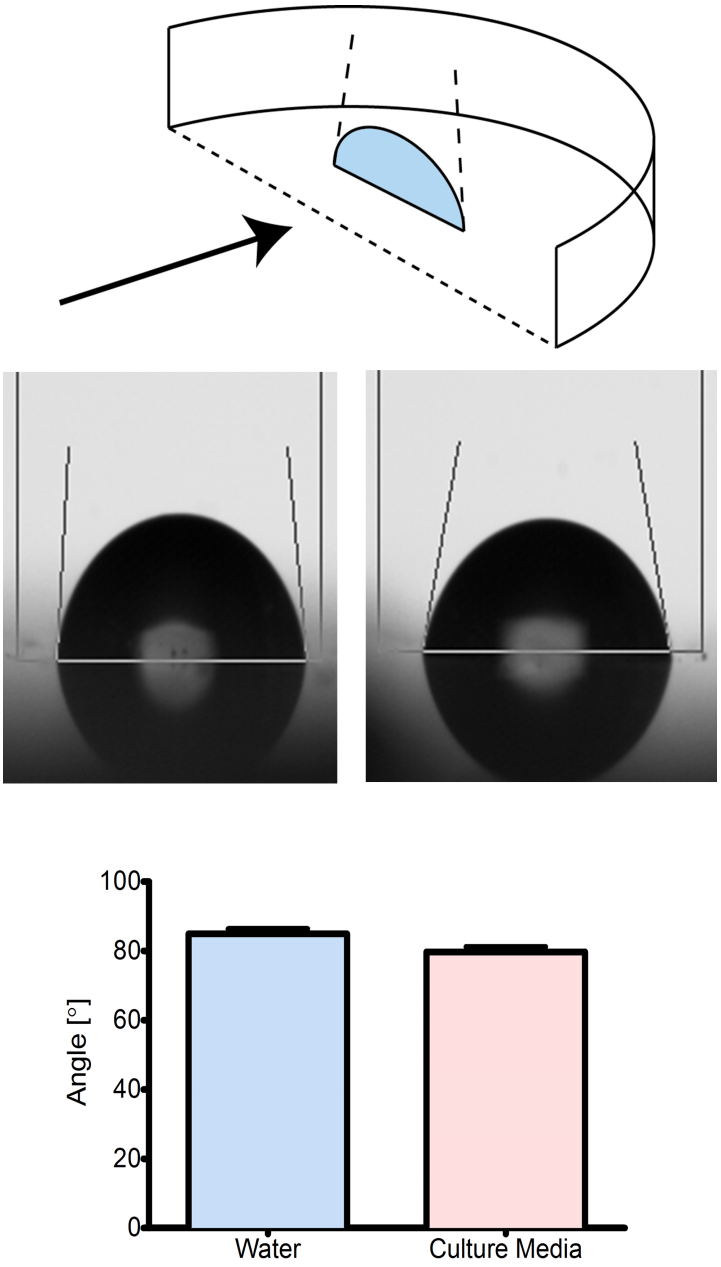

Figure 2.6: Contact angle measurements: top - a six-well plate was cut in half to allow for contact angles to be measured; middle - side profile of a water droplet (left) and DMEM droplet (right); bottom - measurements indicate water has a contact angle of 84.95 ± 1.39 °, and medium has a contact angle of 79.74 ± 1.47 ° (n = 6).

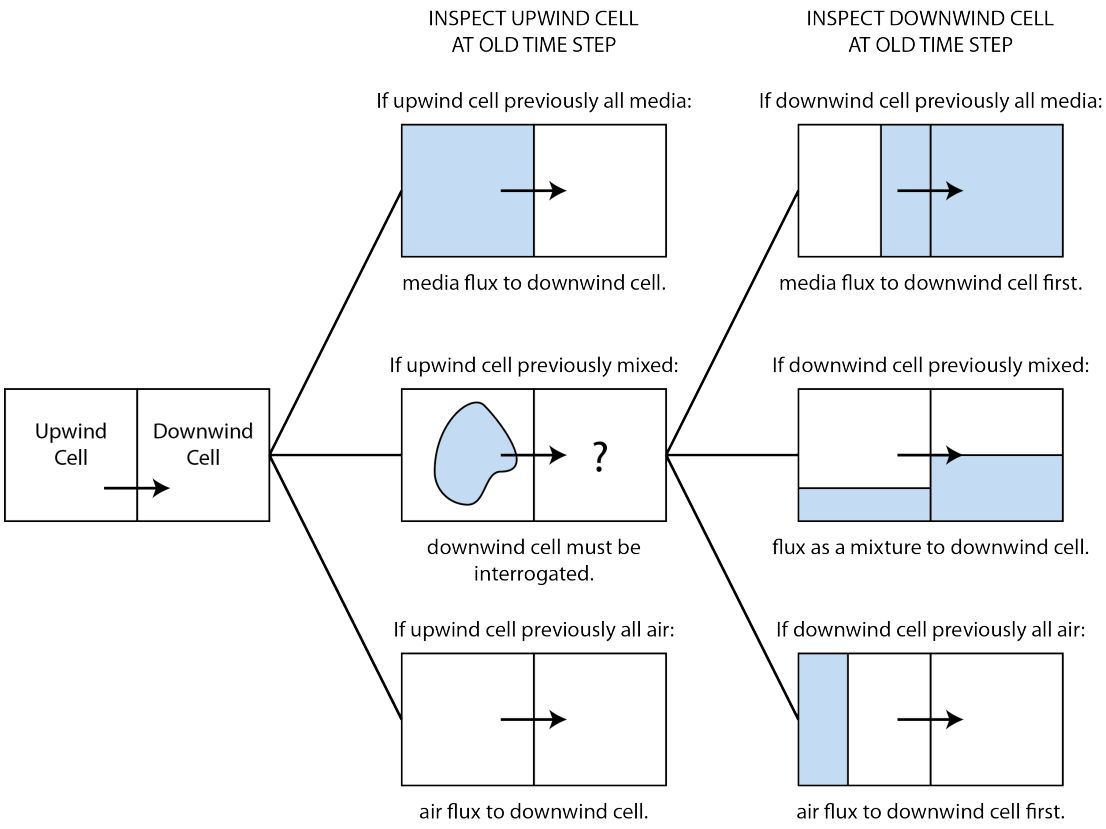

Figure 2.7: SLIC scheme for free surface modelling: schematic representing the method of determining the flow of air and culture medium in a control volume where the interface is present from an upwind control volume to a downwind control volume.

2.1.9 CFD solver criteria

2.1.9.1 Convergence criteria & minimum residual

A residual is the difference between two adjacent iterations. The convergence criteria and minimum residual are conditions where, if satisfied, the iterative procedure stops, and the model progresses on to the next time step.

The convergence criterion is the minimum reduction in residuals for each variable in the solution. The default value in CFD-ACE is 1×10^{-4}. In this model it was set to 1×10^{-18}. The minimum residual is the minimum value of the residual below which the convergence criteria is not applied. Within this model it was set to 1×10^{-18}.

By setting the convergence criteria and minimum residual to such low, virtually

unachievable and matching values, it was ensured that the solution iterated the full 45 iterations per time step. By completing all 45 iterations, model stability and the consistency in the solution across multiple cycles was encouraged. Attempts at relaxing the convergence criterion to 1×10^{-8} resulted in divergence.

2.1.9.2 Under relaxation

Under relaxation was a constraint on a variable to prevent a significant change from one iteration to the next, encouraging model stability, but reducing the convergence rate (Equation 2.15).

$$a_C(1+I)\varphi_P = \sum a_{nb}\varphi_{nb} + S_U + a_C I\varphi_P^* \tag{2.15}$$

where φ_P^* is the new value of φ_P, a is a link coefficient, $_C$ indicates a value in the control volume centre, $_{nb}$ indicates a value at a neighbouring control volume, S_U are source terms.

When convergence is achieved, φ_P^* has no impact on φ_P, but prior to this point under relaxation links the two together and assists in removing any oscillations in the numerical solution. Relaxation factors (I) for pressure and velocities were reduced from 1 to 0.8 and 0.2 respectively. Values of I in the range of 0.2 – 0.8 are common practice (268).

2.1.9.3 Flotsam & jetsam

Due to the use of a SLIC free surface reconstruction scheme, there was the likelihood of tiny isolated droplets of media appearing in the air and *vice versa*. This is known as flotsam and jetsam. A filter was applied to the solver ensuring that droplets were removed at the point of their initial formation so that they did not grow and impact on future flow calculations. Flotsam and jetsam is mainly generated in conditions with poor convergence, a large CFL number, or poor grid quality and therefore its impact on the solution was expected to be minimal due to careful model refinement.

2.1.9.4 Parallel computing

A cluster arrangement of computer cores was used to reduce the time to completion for each model by dividing the domain grid into similar sized groups of control volumes

where grid density was in excess of 150,000 control volumes (Figure 2.8). Each group of control volumes was assigned a separate computer core for the parallel computation of governing equations.

The discretisation of the domain into groups of control volumes was achieved using a python script to create a sun grid engine (.sge) file for submission to the cluster arrangement. Each core had a random-access memory (RAM) of 8 gigabytes. The number of cores used was dependent on the grid density and is discussed further as part of the results in Section 2.2.1.2.

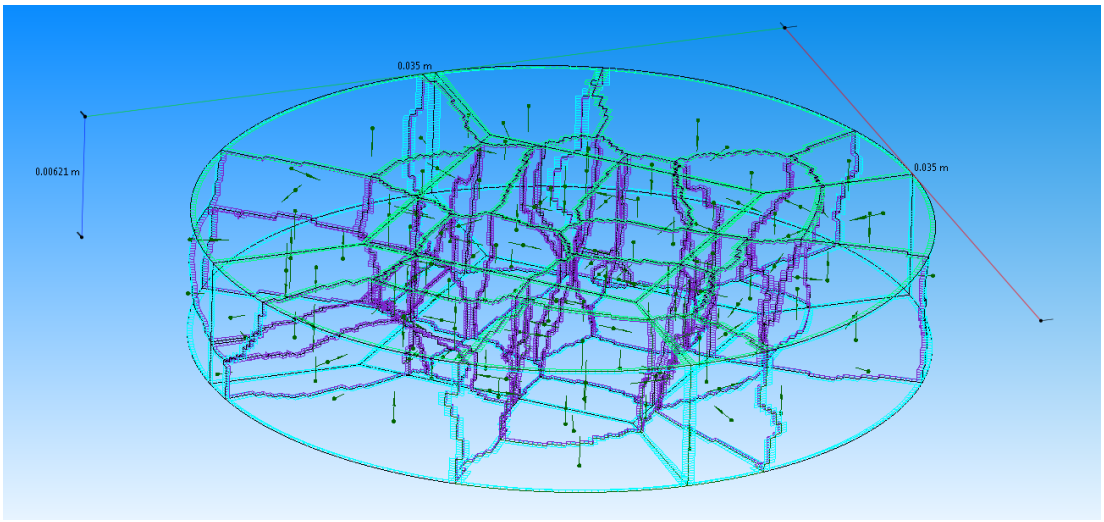

Figure 2.8: Domain decomposition: the cylindrical domain is decomposed into separate volumes to enable parallel computing. Walls (blue), outlet (green) and boundaries of newly formed volumes (purple) are shown.

2.1.10 Data extraction

Data files were acquired every tenth time step to minimise the effect of memory transfer on the speed of model progress; however, monitor points at the well base along the centre line recorded: x, y, z locations; u, v, w velocities; and strain rate, for each calculated time step.

Model evaluation and analysis was completed using visualisation software (CFD-VIEW, ESI CFD, France & Matlab, Mathworks, United Kingdom). Shear stresses,

calculated from model parameters and CFD velocity results, were obtained at the base of the well at the no-slip surface (Figure 2.9).

Additionally, further shear stress analysis and velocity analysis was completed by making a vertical slice through the domain for a planar view, and a further horizontal cut to obtain data at varying depths (Figure 2.9). For a complete two-second cycle, data was extracted every 0.05 s, resulting in 40 time-points documenting transient behaviour.

2.2 Fluid dynamics evaluation

2.2.1 Grid evaluation & independence analysis

2.2.1.1 Grid integrity

Within the flow domain, increasing levels of grid density were applied, and a total of ten models tested. This was achieved by altering the discretisation of three characteristic dimensions (Figure 2.10): two of which generated the butterfly grid (a & b); and the third defined the discretisation of the three-dimensional extrusion (c).

Grid refinement reduced the minimum control volume size. This impacted on several model outputs, including: grid quality; time to completion; and the CFL number. Time to completion and the CFL number are discussed in Section 2.2.1.2 and Section 2.2.1.3, respectively.

The grid quality was evaluated by analysing the volume and centroid angle of the smallest control volume within the grid (Table 2.1). These were computed automatically by the CFD-GEOM software. The centroid angle is an angle formed between two corner nodes of a volume and the centroid. An angle of less than 5 ° is considered to be detrimental to the model successfully completing. Table 2.1 indicates that for all models the centroid angle was above 5 °. This was encouraged by using a butterfly grid, which ensured hexahedral control volumes.

Figure 2.9: Data extraction: two key methods of data extraction were employed: 1. a vertical slice was made parallel with the direction of flow in the x-z plane (a). From this slice, flow contour plots were created for key variables such as volume of fluids, velocity magnitude and shear stress. Additionally, single line graphs were plotted for key variables at varying heights from the well base (b). 2. a horizontal slice was made parallel with the direction of flow in the x-y plane. From this slice, planar contour plots of shear stress were made at varying heights from the well base. For all data analysis, the coordinate system shown has been applied.

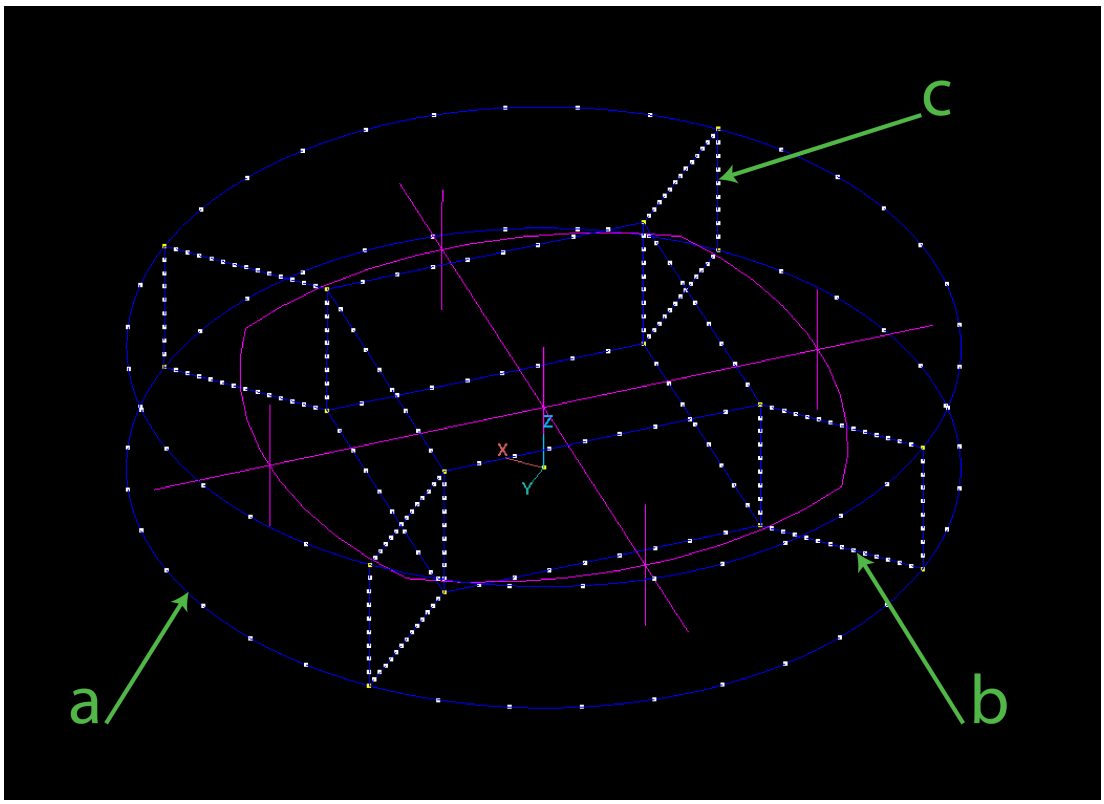

Figure 2.10: Discretised dimensions: the dimensions of the well domain are discretised to generate a structured grid. Increasing dimension discretisation increased the density of the grid (Table 2.1). 'a' represents a quarter of the circumference; 'b' is the distance from the well edge to the central cuboid domain; and 'c' is the height of the well.

Model	Number of control volumes	a	b	c	Smallest control volume [mm^3]	Smallest centroid angle [°]
1	5265	10	15	10	5.12×10^{-4}	56.86
2	12825	20	15	10	2.25×10^{-4}	53.61
3	46835	30	15	20	6.79×10^{-5}	52.02
4	107640	40	20	25	2.86×10^{-5}	50.28
5	177625	50	20	30	1.78×10^{-5}	49.64
6	310930	60	25	35	1.03×10^{-5}	48.80
7	497835	70	30	40	6.30×10^{-6}	48.22
8	747340	80	35	45	4.13×10^{-6}	47.79
9	1068445	90	40	50	2.86×10^{-6}	47.47
10	1470150	100	45	55	2.06×10^{-7}	47.21

Table 2.1: CFD models: ten models were created ranging from coarse (5265 control volumes) to fine (1470150 control volumes) be altering the discretisation of key dimensions a, b and c. CFD-GEOM software was used to identify the smallest control volume and centroid angle.

2.2.1.2 Time to completion

With an increasing grid density there were more control volumes for the generalised transport equation to be integrated over, increasing the computational cost. For example, an increase in the resolution by a factor of two in a three-dimensional model theoretically increases the solution time by a factor of 16. This is because as well as each dimension doubling, the time-step size may be required to be halved for a CFL constraint to hold true.

Time to completion was reported for each model and weighted to 24-cores for direct comparison (Table 2.2). To reduce the time to completion, models were split over multiple cores through a parallel computing arrangement (Section 2.1.9.4). The parallel computing arrangement significantly reduced the predicted time taken for models to complete (Figure 2.11); however the predicted parallel computing completion time based upon Model 1 was not matched. It is hypothesised that the difference was due to the intensive free surface calculations, as increased grid refinement increased the number of control volumes at the medium-air interface.

Model	No of cores	Approximate No of control volumes per core	Time to completion [h] (weighted to 24 cores)
1	1	5265	0.9375
2	1	12825	2.75
3	1	46835	10.25
4	1	107640	23.125
5	8	22203	140
6	8	38866	77.5
7	8	62229	122.5
8	16	46709	346
9	16	66778	454
10	24	61256	1362

Table 2.2: CFD time to completion: model 10 was completed using 24 cores, thus all other completion times were weighted to 24 cores for direct comparison.

2.2.1.3 CFL evaluation

Based upon the smallest control volume and vertical discretisation (dimension c) (Table 2.1), the smallest dimension in the x-direction was estimated (Table 2.3). Equation 2.13 was then used to estimate a CFL value for the defined time step of 0.001 s and an average velocity of $35\,\mathrm{mm\,s^{-1}}$ (Table 2.3).

Analysis shows that all CFL values are under the recommended maximum of 0.25. Additionally, the maximum time step size is also calculated, indicating that a time step of 0.001 s was suitable.

It is noted that when the platform is at 0 °, maximal velocities of *circa* $80\,\mathrm{mm\,s^{-1}}$ are identified near the medium-air interface and if this velocity occurs in a control volume smaller than $0.0328\,\mathrm{mm^3}$ the CFL condition would not have been satisfied. This limitation was not considered to have a large impact on the reported results for the following reasons:

1. The peak velocity of the culture medium occurred for a short period of time (0.02 s) extending over only 20 time steps.

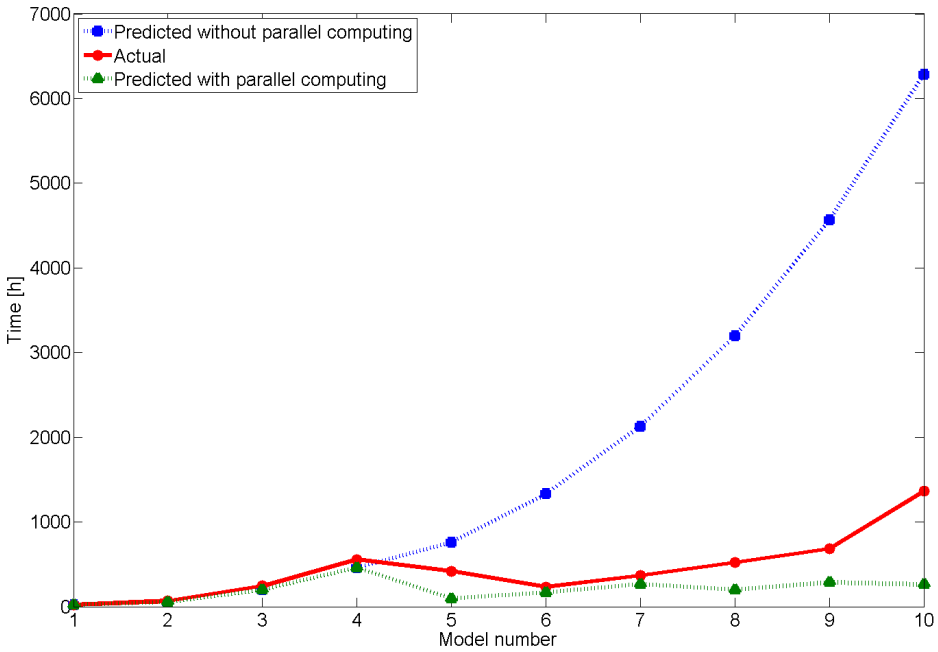

Figure 2.11: Time to completion: actual time to completion *vs.* predicted values for models without and with parallel computing arrangements. Predicted values are based on the time taken for Model 1 to run with 5,265 control volumes on a single core arrangement.

2. Divergence was not reported during the simulations, indicating that the velocity occurred in a control volume large enough to ensure a satisfactory CFL number.

In the worst-case scenario, a velocity of $80\,\mathrm{mm\,s^{-1}}$ in Model 10 would suggest a CFL number of 0.43, *i.e.* 43 % of fluid within the volume has changed. This was still acceptable for the stability and convergence of the model, but may have created some diffusivity at the medium-air interface. As the shape of the interface was not paramount, this maximum was not considered to have a significant impact on the model results.

In conclusion, it was surmised that the CFL condition was satisfied to a suitable level in each model, thus providing reliable results for analysis.

Model	Smallest estimated dimension [mm]	Predicted CFL number	Maximum time-step size for CFL = 0.25
1	1.28	0.027	0.009
2	0.82	0.043	0.006
3	0.62	0.056	0.004
4	0.46	0.076	0.003
5	0.40	0.088	0.002
6	0.32	0.108	0.002
7	0.27	0.127	0.001
8	0.24	0.147	0.001
9	0.21	0.167	0.001
10	0.19	0.186	0.001

Table 2.3: Predicted CFL numbers: the smallest estimated dimension was used to estimate the CFL number and maximum time step size for each model. Analysis indicates that for a mean velocity of $35\,\mathrm{mm\,s^{-1}}$ the desired CFL condition of 0.25 was satisfied for each model and that the selected time step size of 0.001 s was suitable.

2.2.1.4 Grid independence

Ten models were run to completion with an increasing grid control volume density in order to identify a model that completed flow calculations in the shortest time, and produced grid independent results. Of the ten models run, the ninth most-dense model was determined to provide grid independent results (Figure 2.12).

This was ascertained through both qualitative and quantitative analysis. A comparison of x-directional velocities across the diameter of the well was completed at the final time step of the simulation (12,000) for models nine and ten.

Qualitative analysis was achieved through comparison of plots in Matlab (Mathworks, United Kingdom) and showed good correlation.

Quantitative analysis was achieved by calculating the area under each plot with a baseline of $0\,\mathrm{mm\,s^{-1}}$; the percentage error between the two areas, and thus the two models, was calculated to be just 0.79 %.

A summary of all differences between the areas under the curve for the preceding nine models to the tenth is shown in Figure 2.12. It was noted that qualitative analysis indicated that flow fields were not similar until a grid resolution of 310,930 control volumes, and this is represented in the quantitative analysis by a large jump from the first five models to the sixth.

The difference in x-directional velocities between the eighth and ninth models was 1.17 % and hence the eighth model was not used as this was above 1 %, the level of error that was deemed to be acceptable between two models for grid independence to have been achieved.

2.2.2 Iterative convergence

Preliminary models were run with 100 permitted iterations for each time step. From this data it was quickly identified that the maximum number of iterations permitted could be reduced to 45, as convergence was reached within 30-45 iterations during each time step (Figure 2.13). This assisted in reducing the time to completion.

2.2.3 Initial transient effects

As the fluid started from a static position, it was necessary for the computational model to complete a series of rocks to ensure that the initial transient effects caused by the starting motion were not transferred into the results analysis. As a result, the model was run for six complete cycles. Other computational, cyclic models indicate that results are repeated by the third cycle (38), thus six cycles were deemed to be an appropriate number to ensure the flow field was repeating.

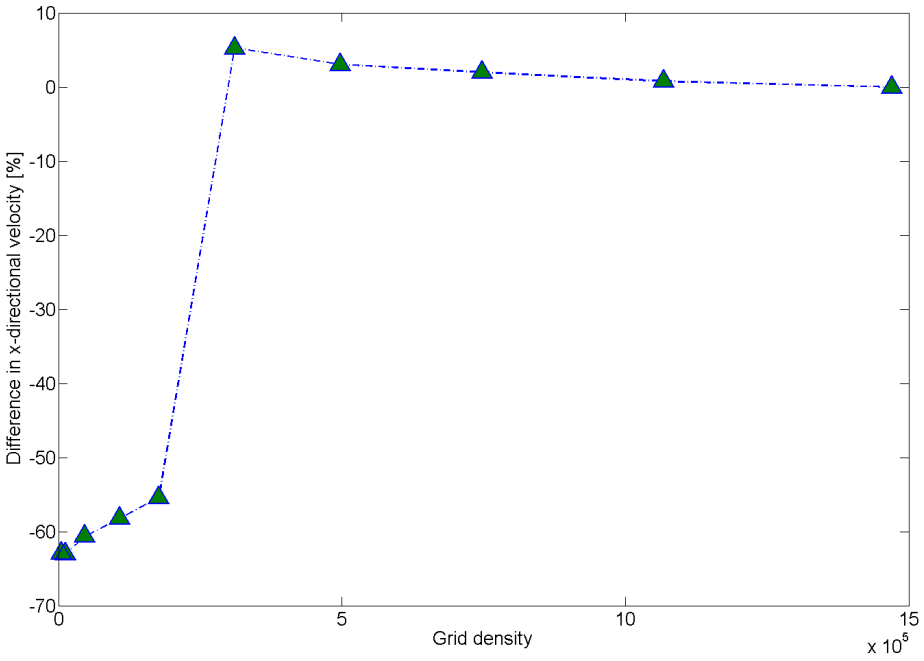

Figure 2.12: Grid independence: X-axis is the grid density with ten datums, ranging from 5,265 to 1,470,150 control volumes, Y-axis is the percentage difference from the most dense model, determined from plots of x-component velocities for each model and the difference between the area underneath to a baseline of $0\,\mathrm{mm\,s^{-1}}$.

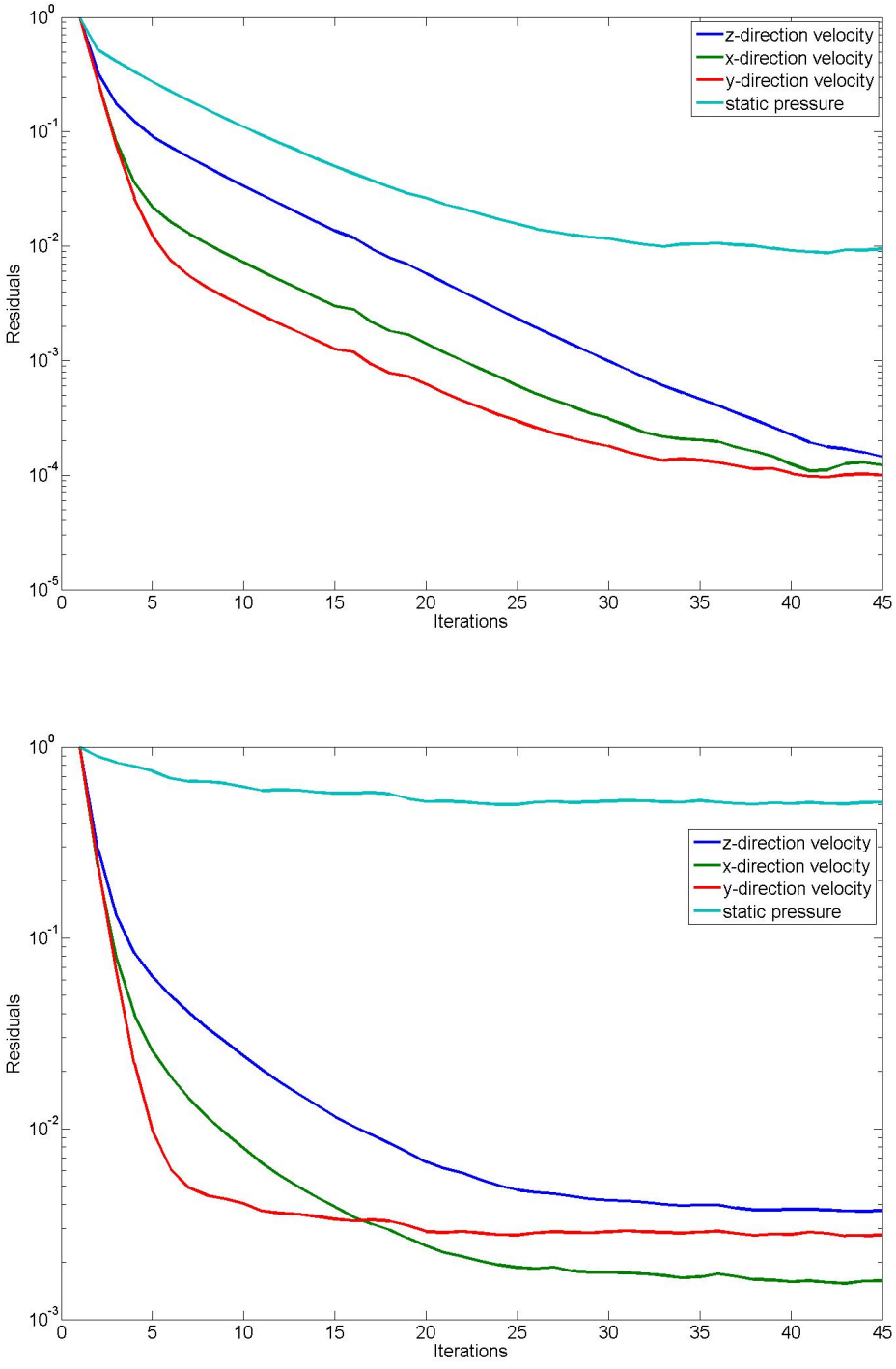

Figure 2.13: Residuals convergence: top - 10,000th time step / 0 °; bottom - 10,500th time step / 7 °. X-axis in the number of iterations, up to a prescribed maximum of 45. Y-axis is the residuals for x-, y- and z- component velocities and static pressure.

The sixth cycle was used for analysis and inspection showed that reported flow velocities of the sixth cycle matched that of the fifth to within 99 %, confirming that a repeating flow field had been achieved (Figure 2.14).

The flow field was similar after the first cycle is completed, suggesting that initial transient effects are quickly resolved. Large oscillations are shown at the start of the first cycle, but these quickly reduced to form a repeating flow pattern after the fourth cycle.

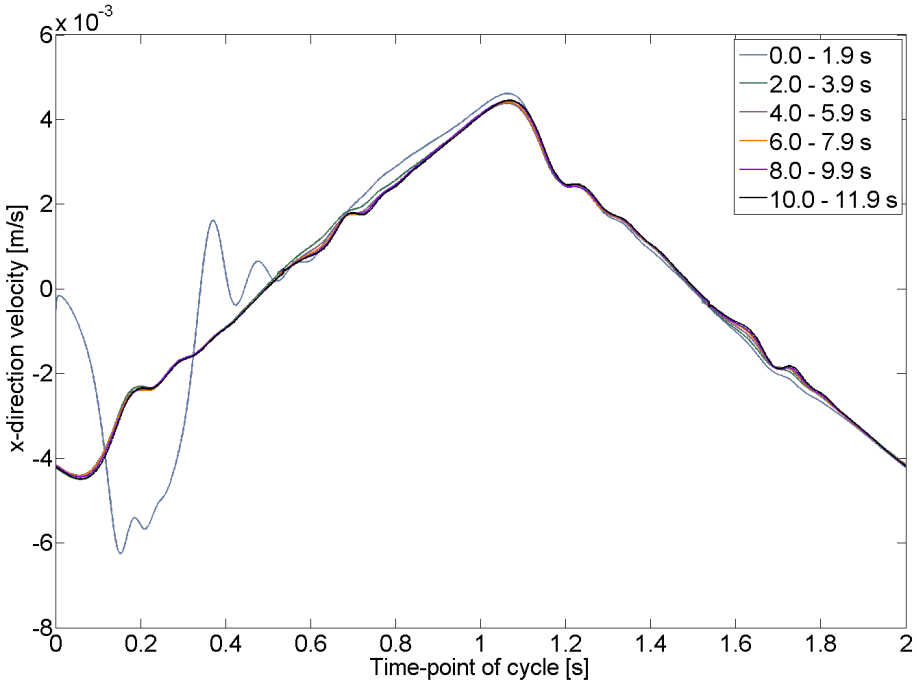

Figure 2.14: Initial transient effects: X-axis represents the time taken for one complete cycle at 0.5 Hz. Y-axis is the x-component velocity at the centre of the well. Six complete cycles are represented from t=0 s to t=12 s.

2.3 Fluid dynamics results

2.3.1 Velocity profiles

Analysis of CFD velocity magnitude every 0.25 s of a 2 s cycle (Figure 2.15) confirmed that the rocking system generated phase-symmetric fluid behaviour about the axis of

rotation, and that the free surface remained close to horizontal throughout a cycle. In addition flow was symmetrical about the x-direction (Figure 2.16)

Peaks of $\pm 80\,\mathrm{mm\,s^{-1}}$ are identifiable at the medium-air interface at the start, middle and end of a cycle, suggesting that the free surface reached the highest velocity at the sinusoidal peak angular velocity, *i.e.* when the platform was at $0\,^\circ$. Correspondingly, velocities reached zero at $\pm 7\,^\circ$ when $\mathrm{t} = 0.5\,\mathrm{s}$ and $1.5\,\mathrm{s}$ (Figure 2.15); this corresponded with a prescribed angular velocity of zero as the rocker changed direction (Figure 2.5).

A two-dimensional numerical model of the velocity magnitude of the well base correlated with CFD flow magnitude velocities extracted 0.4 mm above the well base (Figure 2.17). The numerical model is based upon the angular displacement of the well base during a complete cycle at six different locations along the x-axis ($\mathrm{x} = 0, 3.5, 7, 10.5, 14, 17.5\,\mathrm{mm}$) . Differences between peak and trough velocity time-points were present due to fluid inertia (Figure 2.17).

Comparison of velocity magnitude (Figure 2.18) with directional velocities (Figure 2.19), 0.4 mm above the well base and thus outside of the prescribed no slip condition zone, indicated that flow was primarily in the x-direction during a cycle; z-direction velocities were small, in the region of $\pm 5\,\mathrm{mm\,s^{-1}}$, apart from when the angular velocity was at its peak ($\mathrm{t} = 0\,\mathrm{s}$, $1\,\mathrm{s}$, $2\,\mathrm{s}$) and a maximum of $20\,\mathrm{mm\,s^{-1}}$ was reached.

What appeared to be vortical flow was present after culture medium had moved over to a constraining wall (Figure 2.15 b & f); however closer inspection indicated that this was the fluid being forced to slow down and no dominating back flow was created (Figure 2.20).

Above the well base at z=0.4 mm, peak velocity magnitude of $61\,\mathrm{mm\,s^{-1}}$ occured at $\mathrm{t} = 0.82\,\mathrm{s}$, when the rocker was moving at an angular velocity of $18.9\,\mathrm{rad\,s^{-1}}$ and had moved a total of $10.4\,^\circ$. At this point, the rocker was returning to the $0\,^\circ$ position having previously displaced to the $-7\,^\circ$ position (Figure 1.17). It was thus $3.6\,^\circ$ away from the horizontal point and peak angular velocity, *i.e.* between positions d) and e) in Figure 2.15.

2.3.2 Shear stress

As with the velocity profiles, analysis of shear stress every $0.25\,\mathrm{s}$ of a $2\,\mathrm{s}$ cycle (at the base of the well) indicated that shear stress was both phase-symmetric about the axis of rotation and symmetric about the x-axis (Figure 2.21). Further inspection showed

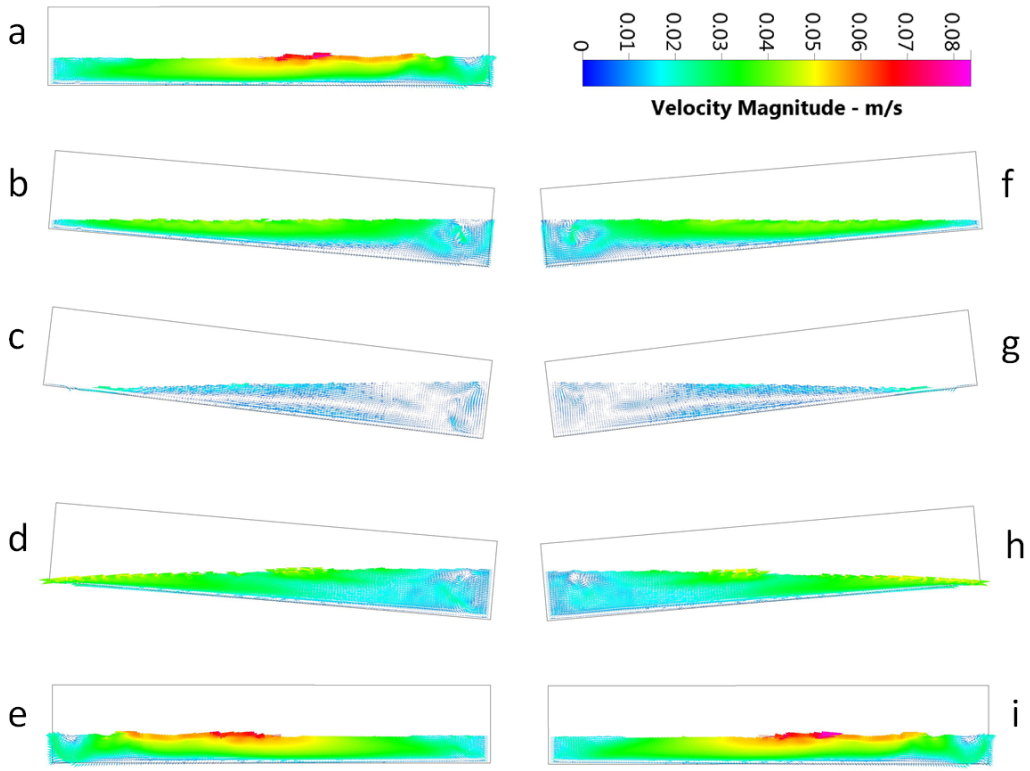

Figure 2.15: CFD velocity magnitude x-z plane ($\mathrm{m\,s^{-1}}$): velocity magnitude vectors shown at 0.25 s intervals (y = 0). In image 'a' the domain is at the start of its sixth cycle. The model progresses in 0.25 s intervals [a = 0, b = 0.25 ...], reaching maximal angles of tilt at positions 'c' & 'g'. At position 'i' the model is at the start of the seventh cycle and the flow field matches that of position 'a'.

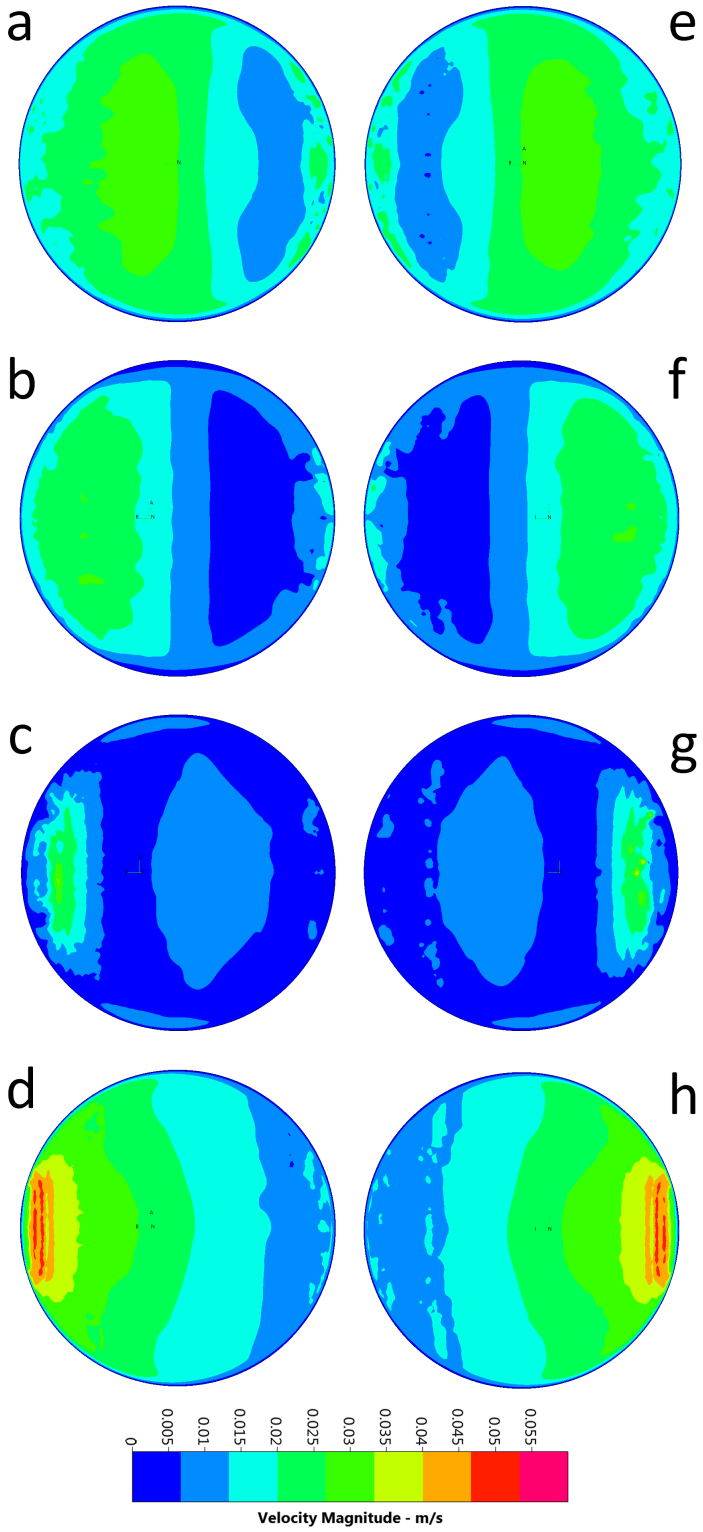

Figure 2.16: CFD velocity magnitude x-y plane ($\mathrm{m\,s^{-1}}$): velocity magnitude contour maps shown at 0.25 s intervals, 0.4 mm above the base.

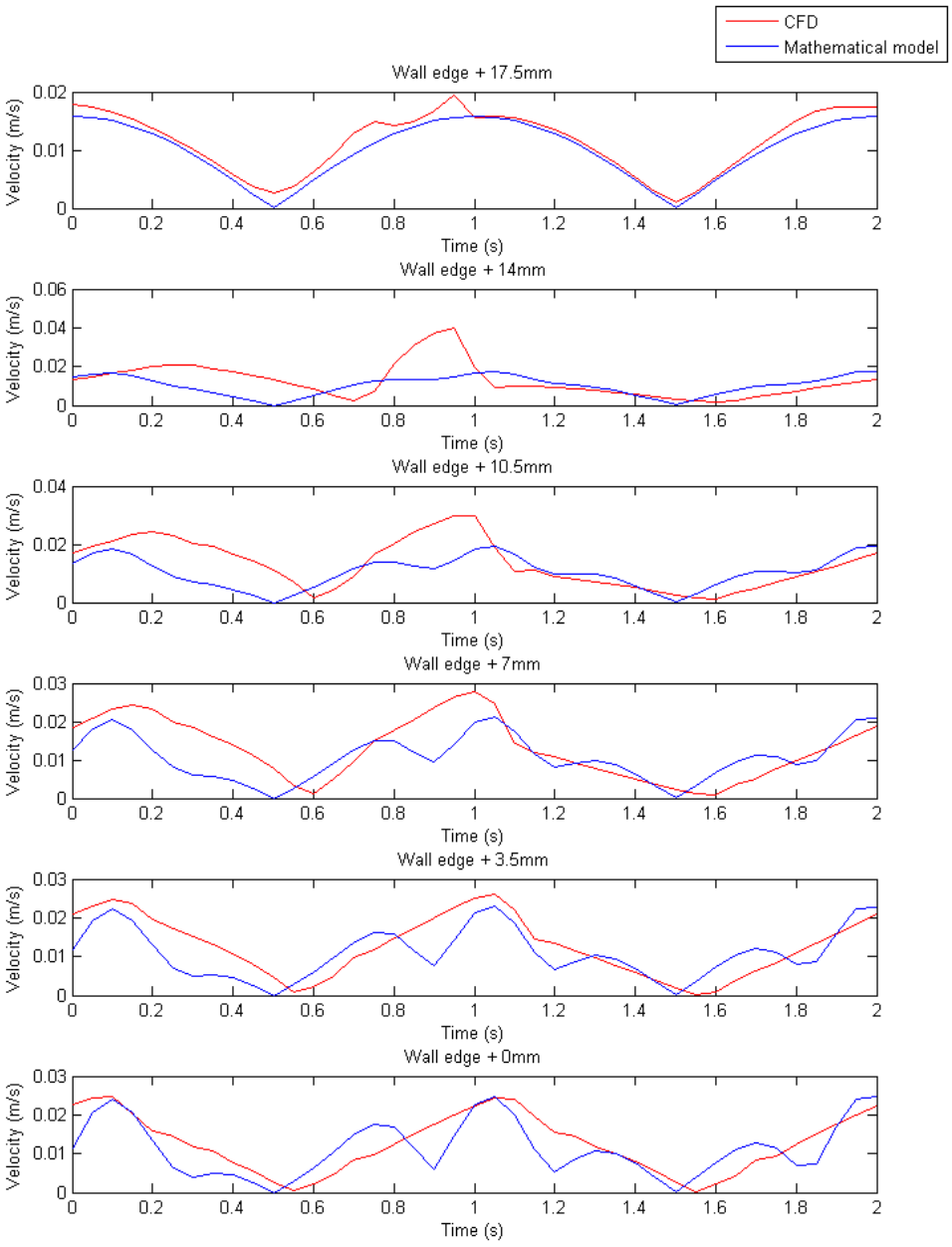

Figure 2.17: Comparison of CFD flow velocity magnitude with a mathematical model of well base velocity magnitude ($\mathrm{m\,s^{-1}}$): CFD velocity magnitude was extracted for the centre line of the well (y = 0) in the x-direction at z=0.4 mm and compared with a mathematical model of well base velocity at six centre line positions, $0, 3.5, 7, 10.5, 14, 17.5$ mm x-axis - one complete cycle of 2 s at 30 cpm. y-axis - velocity magnitude calculated from velocity vectors in the x- and z-directions.

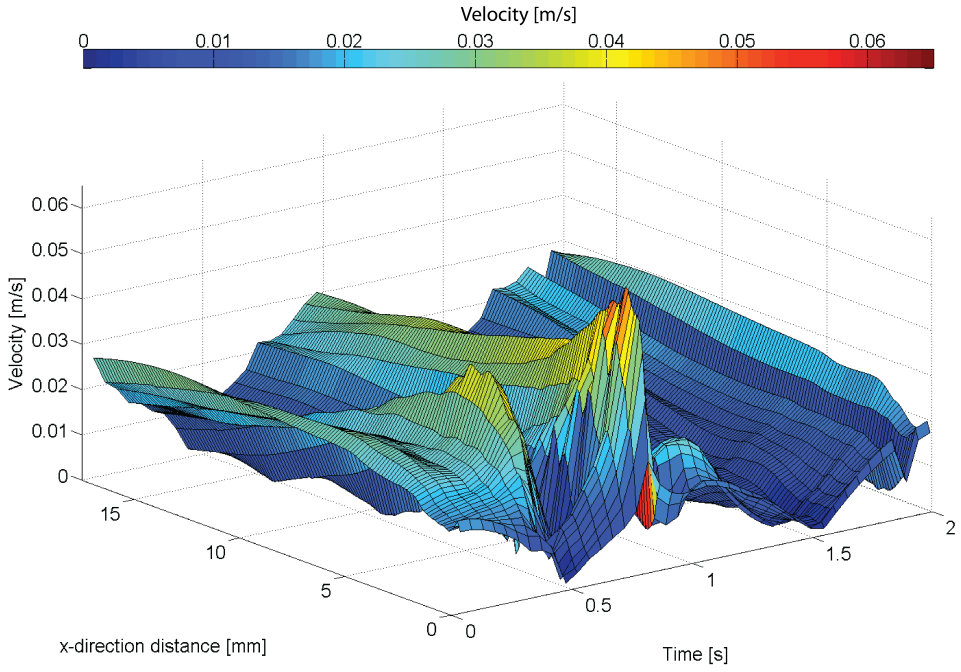

Figure 2.18: Velocity magnitude ($\mathbf{m\,s^{-1}}$): velocity magnitude is extracted for the centre line of the well in the x-direction (y = 0) at z=0.4 mm. As a phase symmetric flow field has been identified (Figure 2.15), only one half of the dish is shown (well wall = 0 mm, well centre = 17.5 mm).

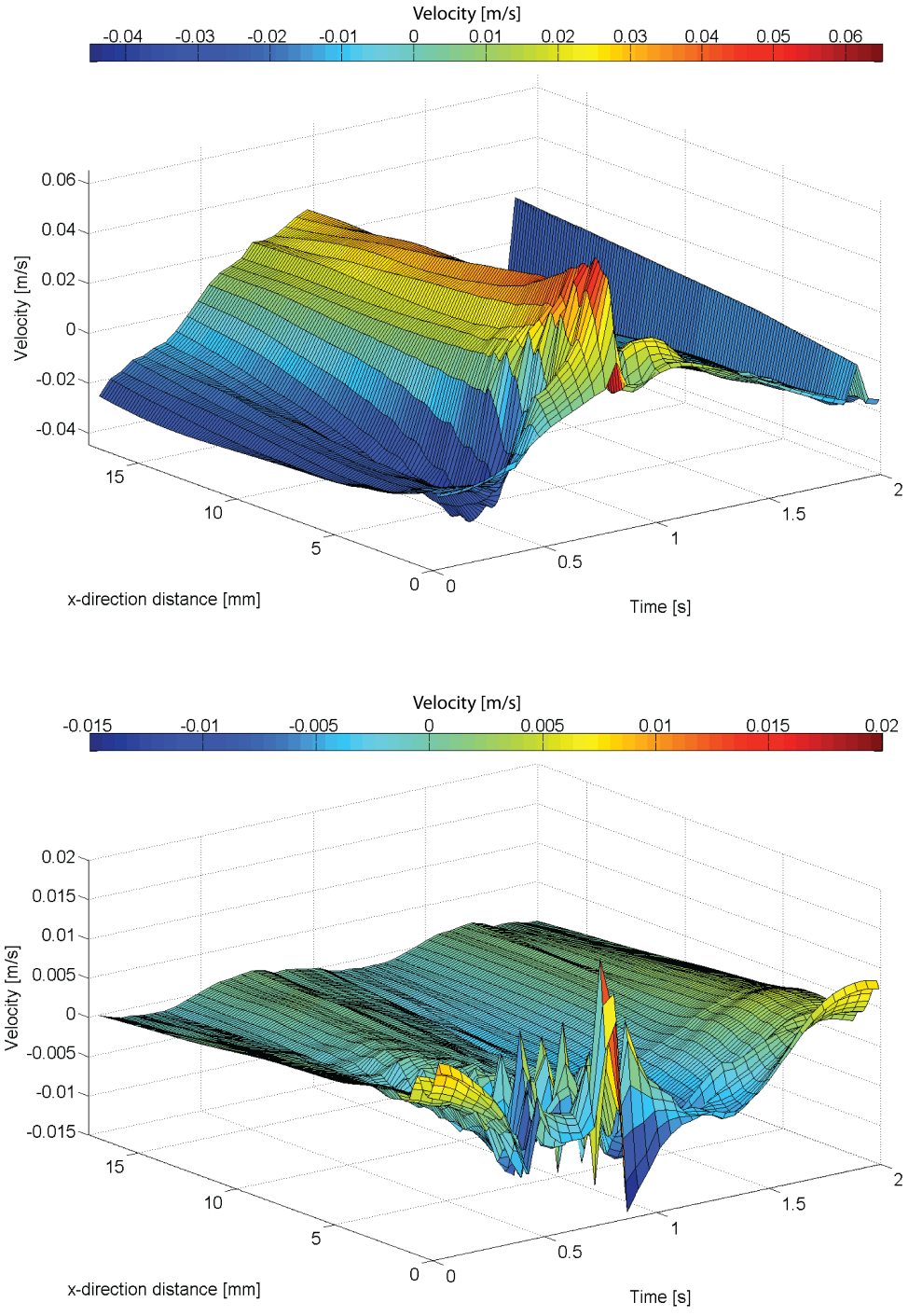

Figure 2.19: Component velocities ($\mathrm{m\,s^{-1}}$): top - x-component velocity at z=0.4 mm; bottom - z-component velocity at z=0.4 mm, (x-direction: well wall = 0 mm, well centre = 17.5 mm) (y = 0).

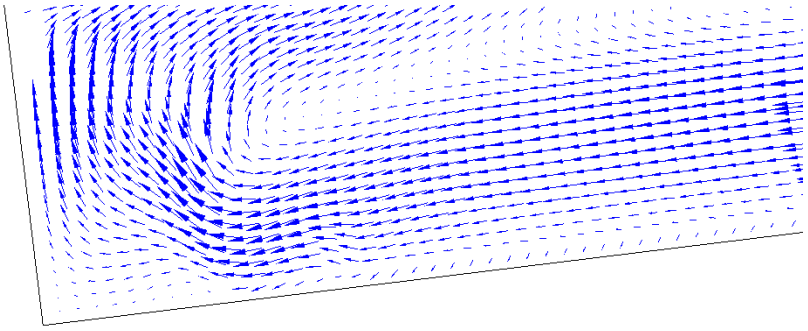

Figure 2.20: Flow deceleration: velocity magnitude vectors at t=1.25 s at the edge of the well extracted at y = 0, correlating to Figure 2.15(f).

that the vast majority of the well was subjected to similar shear stresses, reaching a peak of 0.22 Pa near the well edge as the rocker approached the zero degree position (0.9 s) (Figure 2.22). As might be expected, this peak correlated with a peak in velocity magnitude identified at the same location (Figure 2.18). The peak in shear stress fell across the diameter of the well during the time step reaching a low of 0.04 Pa at the opposite edge. This is identifiable in Figure 2.22 at 1.9 s due to the phase-symmetric properties of the flow.

Shear stress was at its lowest when the rocker was at its largest angle of tilt of $\pm 7^\circ$ (t = 0.5 s & 1.5 s) as flow velocity at these time-points is virtually zero, causing the strain rate to be very low. This behaviour is characterised by dark blue areas in Figure 2.22.

The peak area of shear stress occurs for a very short period of time of just 0.1 s ultimately having little effect on the time-averaged shear stress across the well. Across the centre line of the well mean shear stress is 0.033 ± 0.017 Pa during a complete cycle (Figure 2.23), with a shear stress range of $0 - 0.22$ Pa.

2.4 Discussion

An accurate, grid-independent, stable CFD model was created that characterised the shear stresses at the base of a six-well plate and showed mean shear stress of 0.033 ± 0.017 Pa across the well centre line. Velocities were shown to peak at $\pm 80\,\mathrm{mm\,s^{-1}}$ at the medium-air interface, and velocity magnitude was mainly driven by x-component

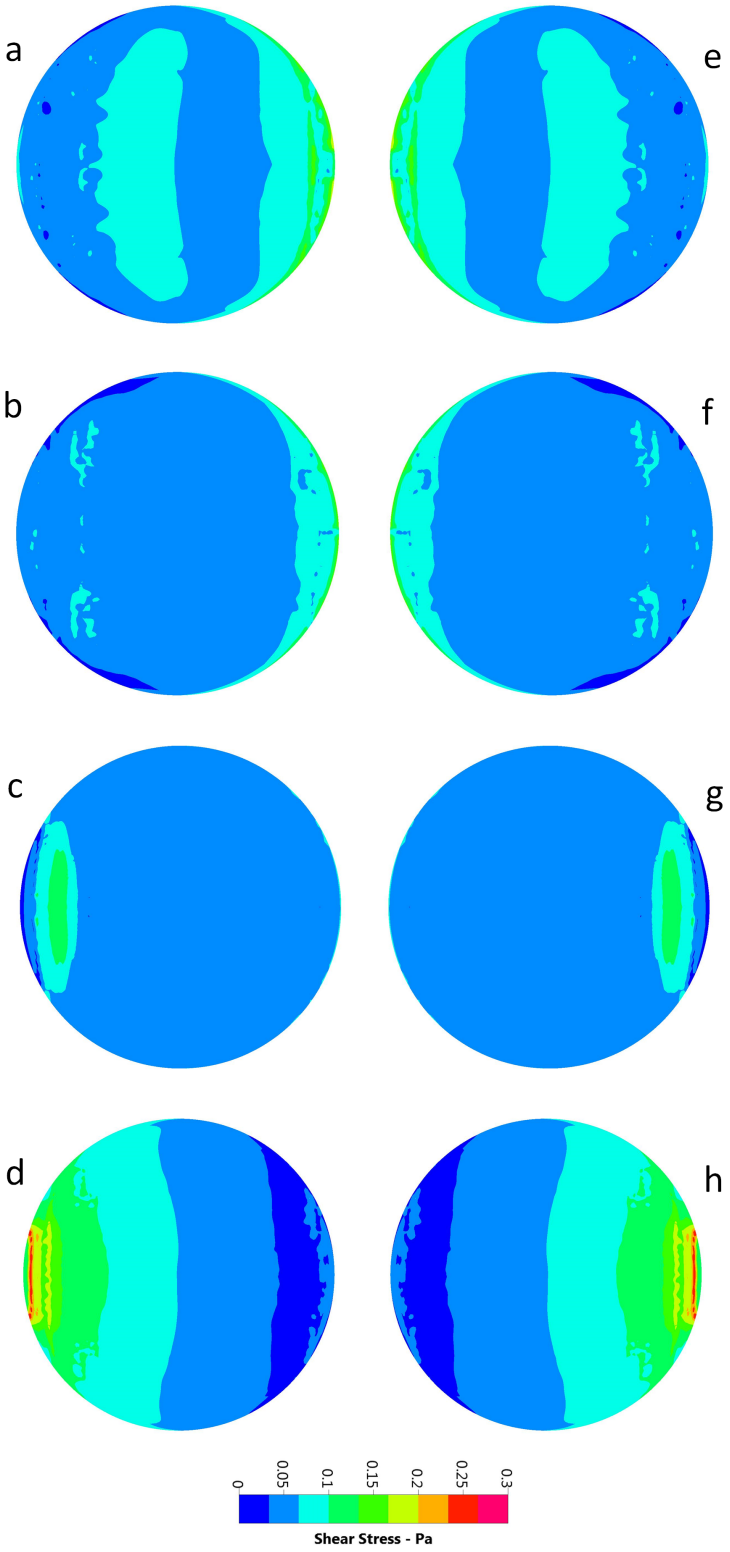

Figure 2.21: CFD shear stress profiles x-y plane: shear stress generated at the well base shown at 0.25 s intervals and directly comparable with velocity vectors and magnitudes shown in Figure 2.15 & Figure 2.16.

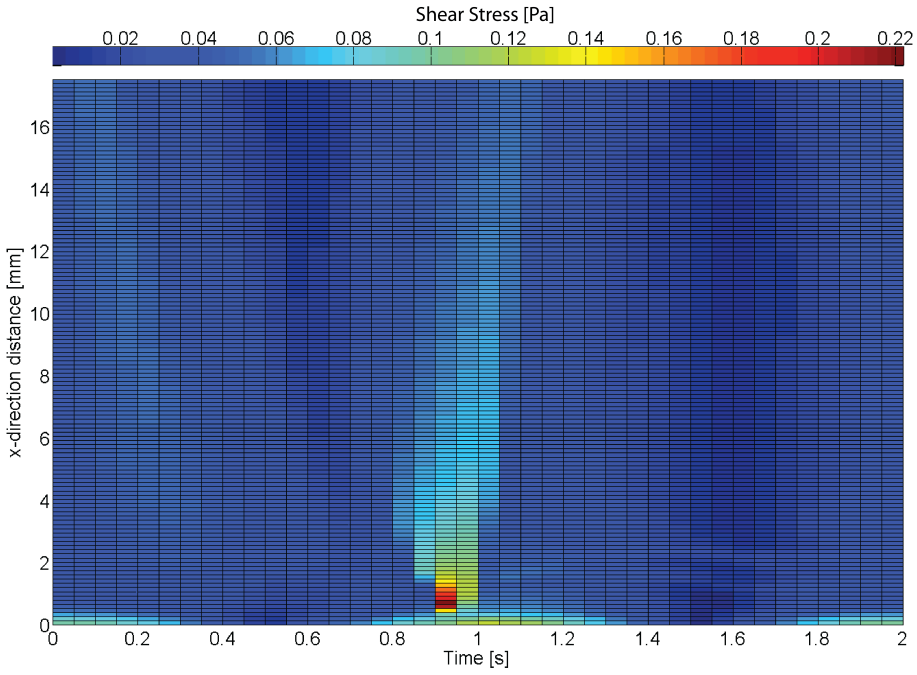

Figure 2.22: Shear stress distribution (Pa): shear stress values extracted z=0.1 mm above the base of the well (well wall = 0 mm, well centre = 17.5 mm) for a complete cycle at 0.5 Hz, (y = 0).

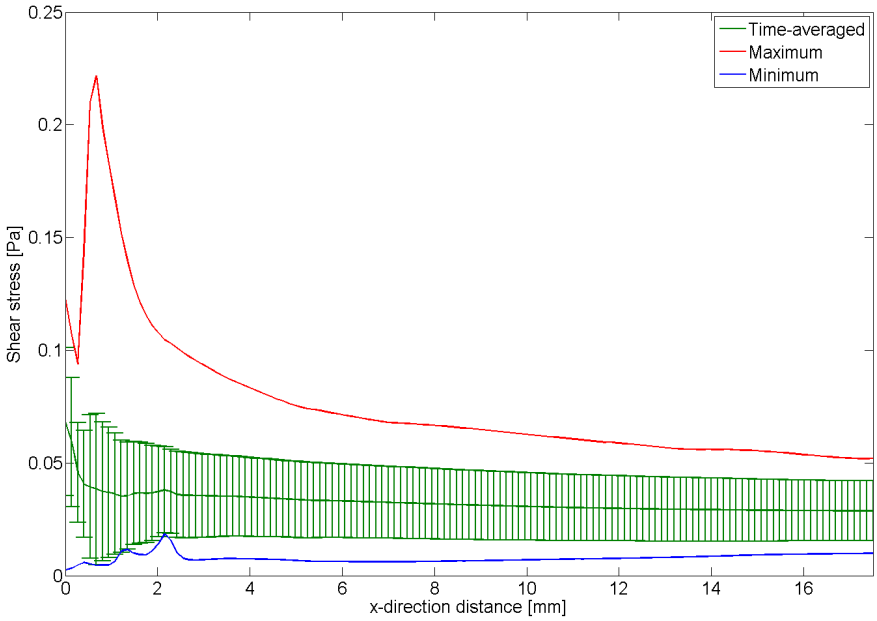

(a) Time-averaged shear stress at 0.1 mm above the well base

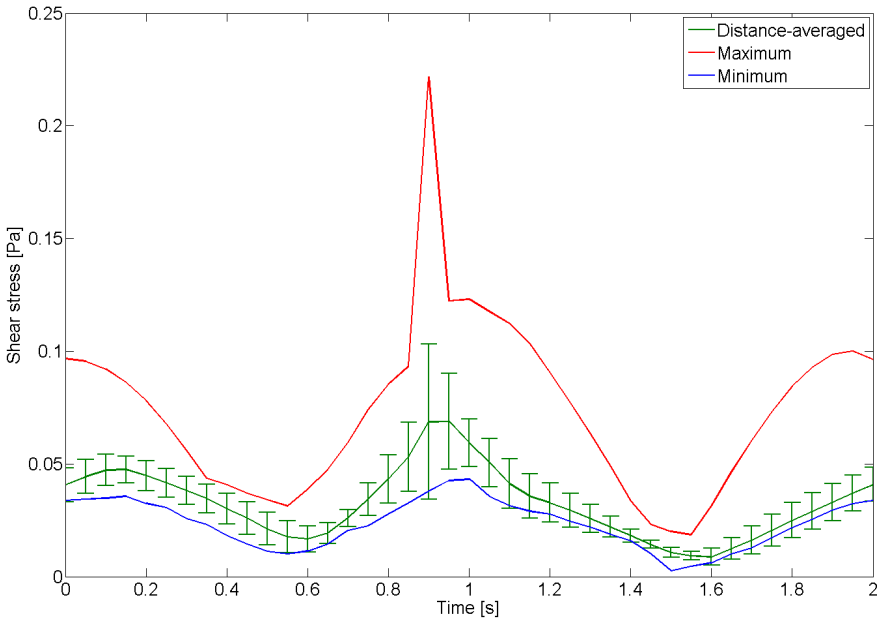

(b) Distance-averaged shear stress at 0.1 mm above the well base

Figure 2.23: Maximum, minimum & average shear stresses (Pa): rocking frequency of 0.5 Hz (well wall = 0 mm, well centre = 17.5 mm), (y = 0).

velocities. A mathematical model, quantifying shear stress within a square rather than circular rocking well, reported a maximum shear stress of 4.8 Pa at the well base at a maximum tilt angle of 7 ° (199). Differences are likely due to the geometry of the well and the origin of rotation located directly below the well base in the mathematical model compared to 35 mm below in the CFD simulation.

Re-evaluation of the Reynolds number using a CFD-generated peak velocity of $80\,\mathrm{mm\,s^{-1}}$ confirmed that flow was laminar (Re = 191) and well below the turbulent transition value of 600 (263).

Time to completion was successfully reduced with parallel computing strategies and a constant time step, yet remained extremely high due to extensive free-surface calculations that increased with increasing grid densities. Rejecting the auto-time step function in favour of a fixed time step size of 0.001 s resulted in a CFL number over 0.25 during peak flow velocity; however, some diffusivity at the media-air interface was considered to have negligible impact on the model results, and this method allowed for time to completion to be significantly reduced. Convergence at each time step and a repeating flow field supported that the selection of a fixed-time step size of 0.001 s was appropriate.

By enacting a fixed time step value 0.001 s, rather than using an auto-time step function, the rate of convergence fluctuated at different stages of the cycle. At time-points of high velocity the full 45 iterations were necessary to achieve convergence. At times of reduced flow velocity, convergence occurred slightly earlier at 30 iterations; although the full 45 iterations were performed. Relaxing the convergence criteria slightly could have modestly improved the time taken to complete the full transient solution; however early models with a relaxed convergence criterion led to instability in the solution and ultimately divergence.

The most significant limitation of the rocker was the modelling of the free surface that did not account for surface tension and was reconstructed using a first order scheme. The free surface reconstruction scheme was limited to a first order approach as a second order scheme caused the time taken for each iteration to increase and consistently resulted in divergence. This limited the accuracy of the media-air interface profile and caused some diffusivity. In addition, this assumption may have presented errors in flow calculations where fluid depth was small as surface tension may have an increased role in flow behaviour. Within the see-saw rocker model, this may have

occurred at the edges of the well along the midline at $\pm 7^\circ$ when the media has collected at the opposite side of the well. Therefore shear stress results reported at the well-edge may be inaccurate at t=0.5 and 1.5 s; however the impact on the global results is minimal, as it would only effect the edge of the well for a short period of a cycle.

As a first order scheme was enacted, the contact angle was limited to 90°; however media and air measurements indicated that the contact angle of 90° was an appropriate assumption as values were largely similar, thus the impact on model results was considered small and would be localised to the well edges where the fluid meets the well walls.

For free surface calculations it is recommend that the number of control volumes computed is never above 10,000 due to the time taken to complete fluid-interface calculations (268); however for the shear stress in a six-well plate to be computed and for the results to be relevant for future biological studies, a three dimensional model was required, and at a high resolution. Angular frequency and well geometry conditions dictated that a grid size in excess of 10,000 was required. This caused the model to be computationally intensive. A structured, hexahedral mesh was used as best practice for free-surface calculations. Preliminary models using an unstructured, triangular mesh resulted in divergence.

The burden of free surface calculations was compounded further by a sinusoidal angular velocity impacting on an imposed Courant-Friedrichs-Lewy (CFL) condition of 0.25. Estimations of CFL number based upon angular velocity were utilised for programming the model arrangement, and a fixed time step size of 0.001 s was chosen to encourage a CFL value of less than 0.25. As such, an auto-time step function was not enacted with a SLIC scheme. Determining the method of transient progression, that is whether to use the auto-step function or not, was a trade-off between the sharpness of the fluid-air interface and the speed of acquiring the solution, therefore the auto-time step was not enacted. An auto-time step may have increased the sharpness of the free surface, but would have had a limited impact on the velocities calculated within the flow field and the resulting shear stress reported at the cell layer.

As vortical flow was not identified during the velocity analysis, it is concluded that biological cells seeded in a monolayer at the base of the well would experience a frequency of flow stimulus that matches twice the rocking frequency of 0.5 Hz; a mechanotransducer such as the primary cilium may experience a bending induced by

flow moving in one direction and then as the see-saw rocker changes the direction of rotation, the flow may cause the cilium to bend again, but in the opposite direction. Within the operational limits of the rocker, this gives a frequency of bending for the primary cilium a range of $0.166 - 2.334\,\text{Hz}$, *i.e.* double $0.083 - 1.167\,\text{Hz}$. The average walking frequency of men and women is $2\,\text{Hz}$ (269), therefore this model could act as a platform for investigating the effect of different loading frequencies on musculoskeletal cell behaviour that are relevant to the *in vivo* environment.

One minor limitation of this model is that it did not consider the cell monolayer in the geometry; however, the tenocyte height would have a minimal impact on the overriding strain rate within the solution. Furthermore, as shown in Chapter 6, when stimulated, tenocytes secrete proteins that alter the surface structure at the well base, and as a result the shear stress. This model could therefore be adapted to include the shape and structure of tenocytes at the cell layer and additionally update the structure based upon a rate of matrix secretion. However, it is noted that the impact on time to completion could be huge as extensive additional calculations would be required in between each time step, including recalculating and updating all geometry. Additionally, by not including the geometry of tenocytes, a model has been created that can be used across research institutions for a variety of cell types, and importantly, will allow for results to be repeatable and comparable.

While CFD is a mature and reliable method, proper verification is still necessary, the accepted standard of which is to make experimental flow field measurements using a high fidelity technique, such as particle image velocimetry (PIV) (Chapter 3).

Chapter 3

Particle image velocimetry flow validation

Particle image velocimetry is a technique whereby velocity vectors are derived from the motion of microspheres seeded in a flow field. Verifying CFD simulations with PIV data justifies the simplifications and assumptions of the CFD model and thus increases confidence in computationally derived values such as shear stress. Detailed and accurate knowledge of shear stress is essential for understanding cell behaviour in tissue engineering methods. PIV has previously been used to validate CFD modelling (36, 270, 271, 272, 273) and also for the capture of flow around the beating wings of insects (274), thus its ability to produce results in a small flow field, and its precedent for comparison with CFD models, make it an ideal approach for validation of the see-saw rocker fluid dynamic estimations.

Experimental capturing of flow velocities was completed in collaboration with Dr. Richard Bomphrey and Dr. Per Henningsson of the Department of Zoology, University of Oxford, using their existing experimental set-up, software and expertise.

Within this chapter the use of PIV to experimentally validate the CFD modelling of the see-saw rocker is presented in order to achieve the third thesis objective (Section 1.9). Firstly, the principles of PIV and the experiment arrangement are presented. This is followed by an outline of methods for processing, extraction and noise reduction of acquired data. Finally, PIV experimental results and CFD estimations are compared qualitatively and quantitatively and discussed.

3.1 Principles of laser sheet PIV

PIV is a method for tracking the displacement of a light-reflective particle over a time step δt by taking images in quick succession (Figure 3.1). A laser is focused through a custom lens to create a thin sheet of light to illuminate particles in one plane only. As a particle moves along the plane highlighted by the laser sheet, a high-speed camera captures its displacement. Data processing of particle displacements results in an approximation of the particle velocity over a period of time (Equations 3.1 & 3.2).

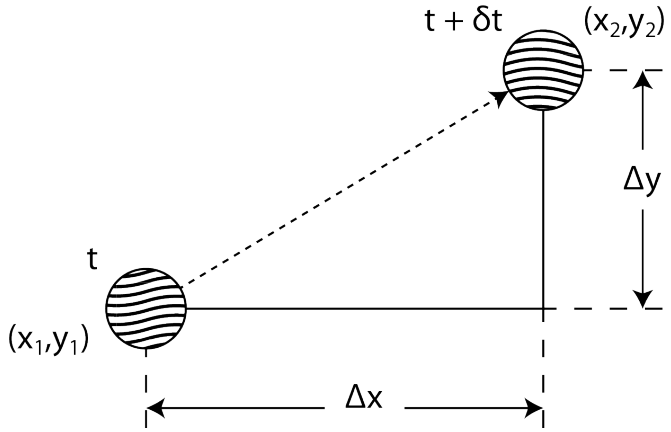

Figure 3.1: Principle of PIV: a particle, at time t and position (x_1,y_1), moves by Δx and Δy to position (x_2,y_2) after time δt has elapsed.

$$U = \lim_{t_2 \to t_1} \left(\frac{x_2 - x_1}{\delta t} \right) \tag{3.1}$$

$$V = \lim_{t_2 \to t_1} \left(\frac{y_2 - y_1}{\delta t} \right) \tag{3.2}$$

The processing assumes that the direction of travel of the particle is straight and that the speed of travel in between successive images is constant. The selection of an appropriate frame capture rate that ensures the full behaviour of the flow is captured is essential. Capture rate is dependent on the pulse frequency of the laser and camera frame speed.

Captured data is evaluated by dividing images into interrogation windows of a defined pixel size and establishing the movement of particles in between time steps

(Figure 3.2). Acquisition of displacement and resulting velocity vectors is discussed in detail in Section 3.2.4.

3.2 Arrangement & methods of flow validation experiments

3.2.1 Platform arrangement

A single well cut from a standard six-well plate (Greiner Bio-One, Germany) was placed on the rocker and positioned within a laser sheet PIV set-up designed for small volume flow capture (Department of Zoology, University of Oxford) (Figure 3.3). As the well rocks, high rotating walls inhibit the ability of a static camera to capture fluid motion. As a result, the walls of the well were cut down to a height of *circa* 6 mm to enable a clearer path for image capture. To reduce interference with image capturing, the exterior of the well was coated in a black matt paint and a black card was placed on the rocker platform surface to reduce laser glare.

The rocking platform was placed with its centre directly underneath the laser sheet. The well was placed in the centre of the platform, achieved through the use of prepared marks on the platform surface.

3.2.2 Fluid seeding & laser specification

The fluid was seeded with a circa 1 % suspension of 48 μm fluorescent beads (Duke Scientific, United Kingdom). The suspension was illuminated by a 10 mJ laser (Nd:YLF, 527 nm, Litron LDY-300PIV; Litron Lasers Ltd, United Kingdom) producing pulse pairs with a repetition rate of 125 Hz and a pulse separation interval of $\delta t = 4$ ms (Figure 3.4). The sheet optics chassis was equipped with a -10 mm cylindrical lens spreading the beam into a 2 mm thick sheet across the diameter of the well perpendicular to the tilt axis, (Figure 3.3).

3.2.3 Image capturing

A flow field area of approximately 60 × 60 mm was recorded using a high-speed (2000 frames per second) CMOS-sensor camera (Photron SA3: 1024 × 1024 px; Photron Ltd,

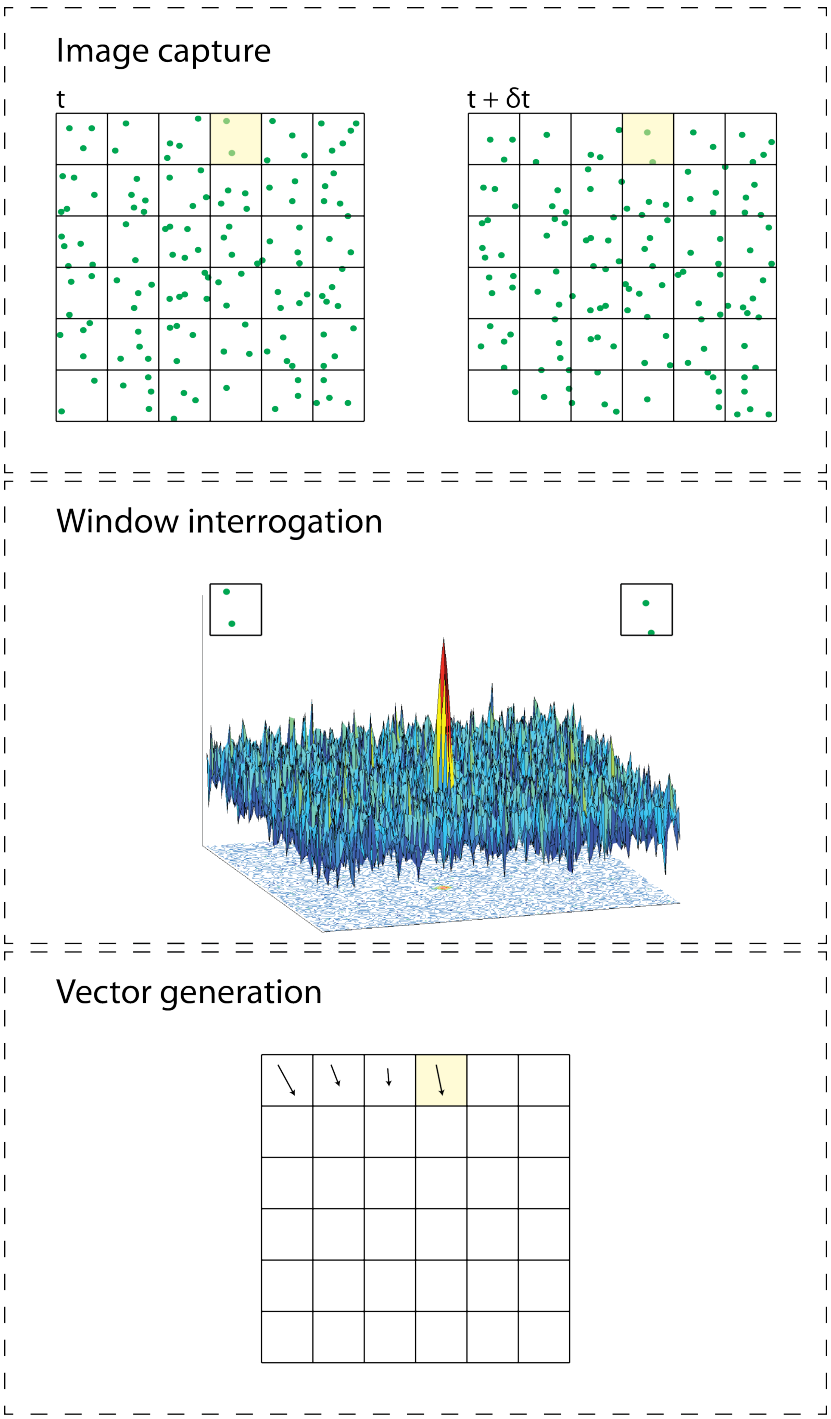

Figure 3.2: PIV data capture, window interrogation & vector generation: images of particles were captured and discretised into a grid format (top). Particle motion was evaluated between time steps through a cross-correlation technique (middle). The cross-correlation technique was used to define the magnitude and direction of a velocity vector (bottom).

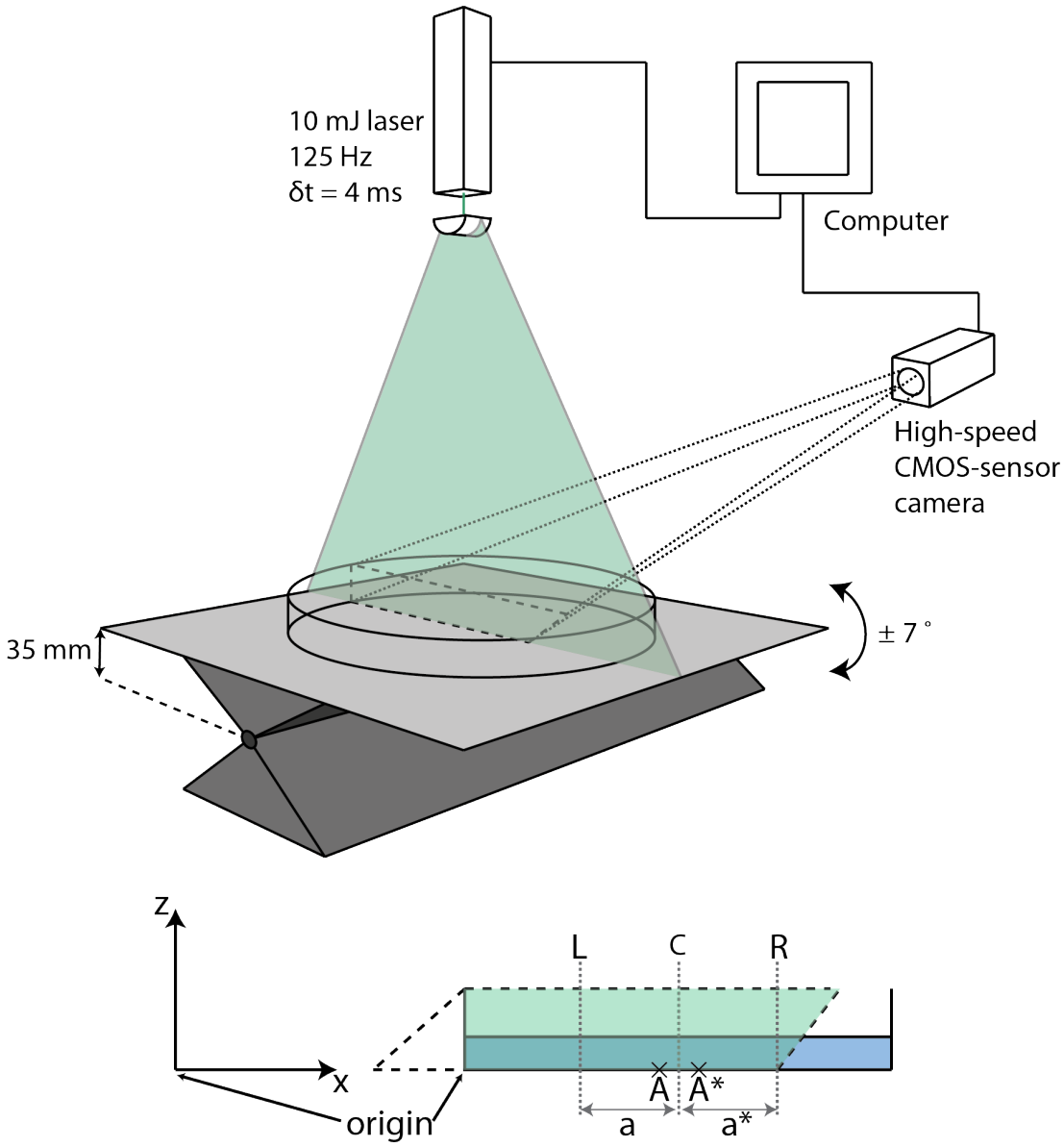

Figure 3.3: PIV experimental set-up: A 2 mm thick laser sheet highlights a central plane within the well geometry. A high-speed camera captures the motion of fluorescent microspheres in this plane. Well side-profile: the overlap of camera capture and laser sheet covers 70 % of the well base. 'a' and 'a*' represent zones at the base of the well on the central axis either side of the mid-point.

United Kingdom) (Figure 3.4). The camera was equipped with a 105 mm lens (Sigma 105 mm f2.8 EX DG), set to aperture 2.8 and mounted on a Scheimpflug adapter.

The laser and camera were controlled by DaVis 7.2.2 software package (LaVision, Germany) and were triggered by a common high speed controller signal. The camera was calibrated with the built in calibration routine in DaVis 7.2.2 using a 105 × 105 mm dual plane calibration plate (type 11; LaVision, Germany). The calibration plate allowed the transformation of the coordinate system to a view perpendicular to the laser sheet.

3.2.4 Data processing

The recorded PIV data (125 frames per second) were processed using the graphical processing unit (GPU) module of DaVis 8.0.8., providing a more advanced data processing system than the data acquisition software (version 7.2.2.). Raw images were filtered by subtracting a sliding minimum over three frames to reduce noise.

Vector fields were computed from the filtered images using multi-pass cross-correlation. For two successively acquired windows, the following method was applied:

1. The two-dimensional fast-fourier transform (FFT) of each window was calculated.
2. The cross product of the first window FFT and the second window FFT-conjugate was computed.
3. The inverse FFT of the cross product was calculated.
4. The location of the maximum was found in the correlation plane (displacement determination).
5. The second interrogation window was shifted based on the displacement vector and the process applied again to obtain a smaller displacement vector.
6. This process was repeated from a 64 × 64 pixels window reducing stepwise to 8 × 8 pixels for the final pass.
7. The final displacement was the sum of all displacements from each pass.

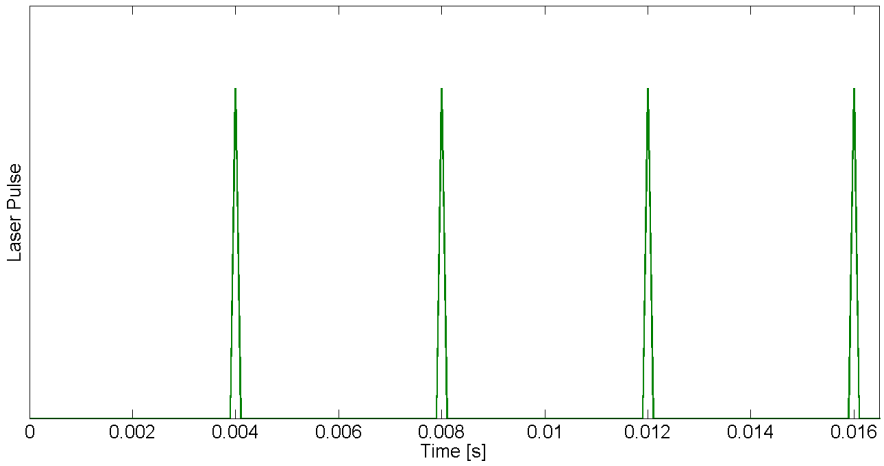

(a) Laser pulse frequeny

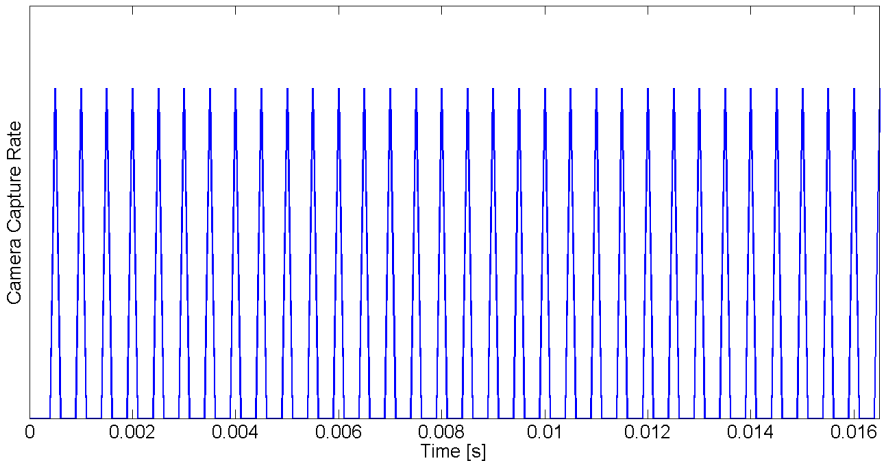

(b) Camera capture rate

Figure 3.4: Laser pulse and camera capture rate: a laser pulse pair repetition rate of 125 Hz and a pulse separation interval of $\delta t = 4$ ms synchronises with a camera capture rate of 2000 Hz, resulting in an effective data acquisition frequency of 250 Hz.

Reducing the window size during the iterative process of multi-pass cross-correlation allowed the acquisition of a higher spatial resolution and wider velocity dynamic range.

Vectors were considered erroneous and deleted if the magnitude was equal to or more than twice the neighbourhood root mean square (RMS) or less than three times the neighbourhood RMS (closest neighbour vectors). Empty spaces were filled by interpolation (an average of all non-zero neighbour vectors) and the final vector fields were subject to a 3×3 smoothing.

3.2.5 Noise reduction

3.2.5.1 Proper orthogonal decomposition

Proper orthogonal decomposition (POD) is a technique that identifies the periodic vectors from a signal, reducing non-periodic noise from the final signal used for analysis. Within PIV, it was first developed for the analysis of turbulence in data post-processing by Lumley *et al.* (275). The linear POD procedure decomposed the set of signals in modal base. Vector fields were reconstructed using the first 20 modes identified from POD analysis performed in DaVis 8.0.8 on acquired vector fields. As the flow was laminar, the computation was completed over six cycles as sufficient for a good representation of the flow.

3.2.5.2 Low-pass filter

A fast fourier transform indicated that some low amplitude signal was present in excess of 2 Hz (Figure 3.5). This was concluded to be noise as 2 Hz is equivalent to a rocker oscillation of 120 cpm and dimensionless number calculations suggested that the fluid profile was laminar (Section 2.1.1). The signal less than 2 Hz included the velocity signal, and this was indicated by a large peak in amplitude at 0.5 Hz, the frequency of the rocker at 30 cpm. A low-pass filter by-passed the signal at lower frequencies and attenuated the signal above a pass band threshold. A pass band of $2 - 3$ Hz (signal attenuation of 45 dB) was used as the rocker was rotating at 0.5 Hz and flow frequencies were expected to be low since no higher frequency instabilities emerged (Figure 3.6). Although some noise was likely still present within the signal at under 2 Hz, the process assisted in removing some of the erroneous data.

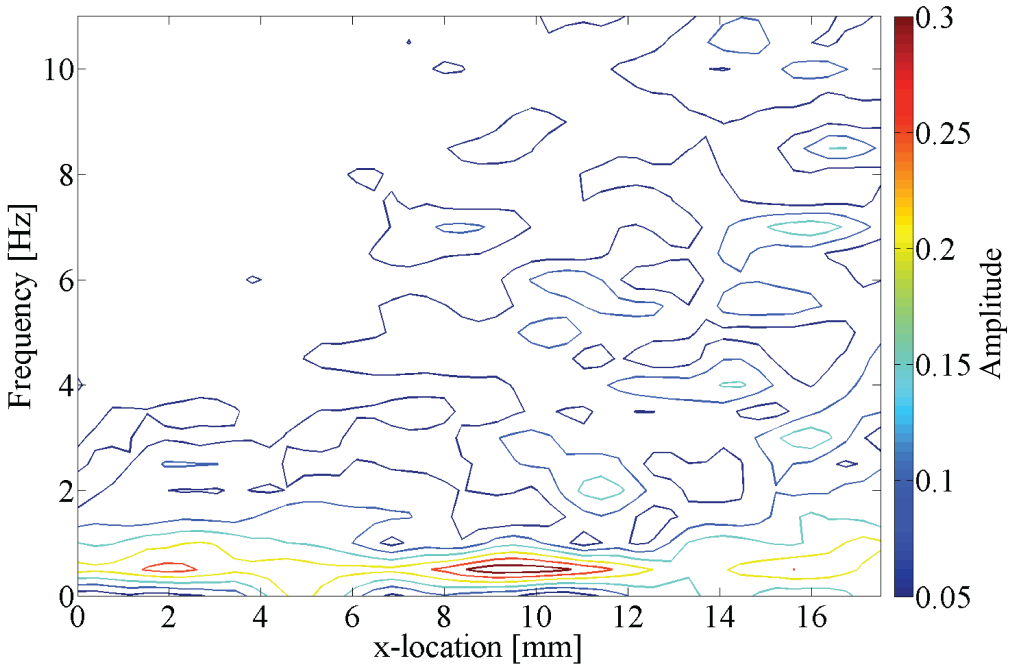

Figure 3.5: Fast fourier transform: sampling frequency of 22.5 Hz used. The fast fourier transform shows that frequency amplitude peaks at 0.5 Hz and suggests that some low amplitude noise is present above 2 Hz.

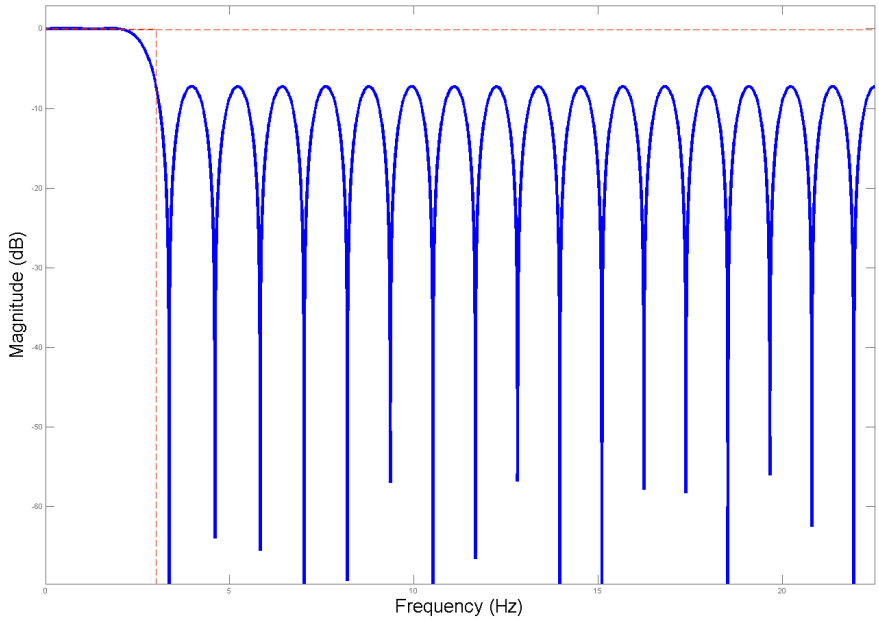

(a) Overall filter design with a signal attenuation of 45 dB

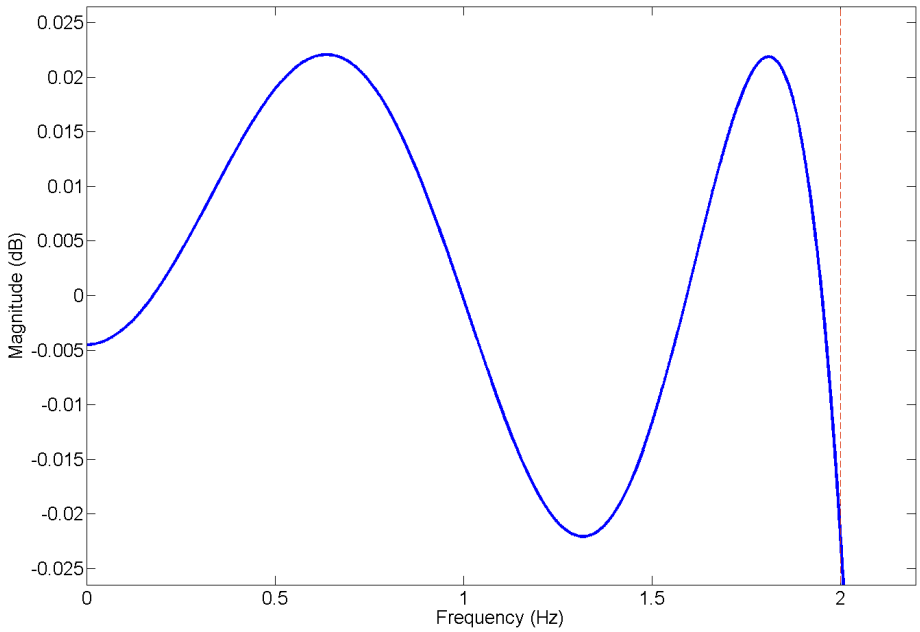

(b) Magnified filter at a low frequency, indicating a cut-off of 2 Hz

Figure 3.6: Low-pass filter design

3.3 Evaluation of PIV velocities

Visual inspection of vector distributions at different time steps allowed for the identification of the start of a see-saw rocker cycle, based upon when the lowest row of non-zero vectors were completely horizontal. From this starting point, PIV velocities were obtained every 0.045 s at the base of the well. Although, this equates to only *circa* 10 % of the acquired data, it was deemed to provide an appropriate representation of flow behaviour. Acquisition of flow data at a higher resolution was necessary for the implementation of accurate multi-pass cross correlation and POD analysis.

Vector identification at the well base was achieved by defining a spatial mask that selected velocity vectors nearest to the well-base at each stage of rotation ($\delta t = 4\,\mathrm{ms}$), while ensuring they were not subject to boundary effects from the interrogation windows. This was to avoid selecting velocities within the boundary layer at $0\,\mathrm{mm\,s^{-1}}$. The base layer vector mask was applied over a POD velocity magnitude contour map and corresponding values extracted in Tecplot (Tecplot Inc., United States of America) (Figure 3.7). Where the mask presented two vectors in the z-direction, the vector with the smallest z-coordinate (*i.e.* that closest to the well base) was used.

The spatial resolution of velocity vectors was set at 0.44 mm and the minimum number of vectors obtained for each extraction was 40 to ensure that coverage of at least half of the well was obtained.

Due to the angle of the camera, for part of the cycle around 70 % of the length of the well base was imaged. Assuming symmetry the see-saw rocker should show velocity-time profiles that are phase-shifted symmetric around the central point (Figure 3.3). Thus roughly 20 % of captured data was reflected about the mid-point and phase shifted to provide an internal consistency check for each cycle (Section 3.4.1).

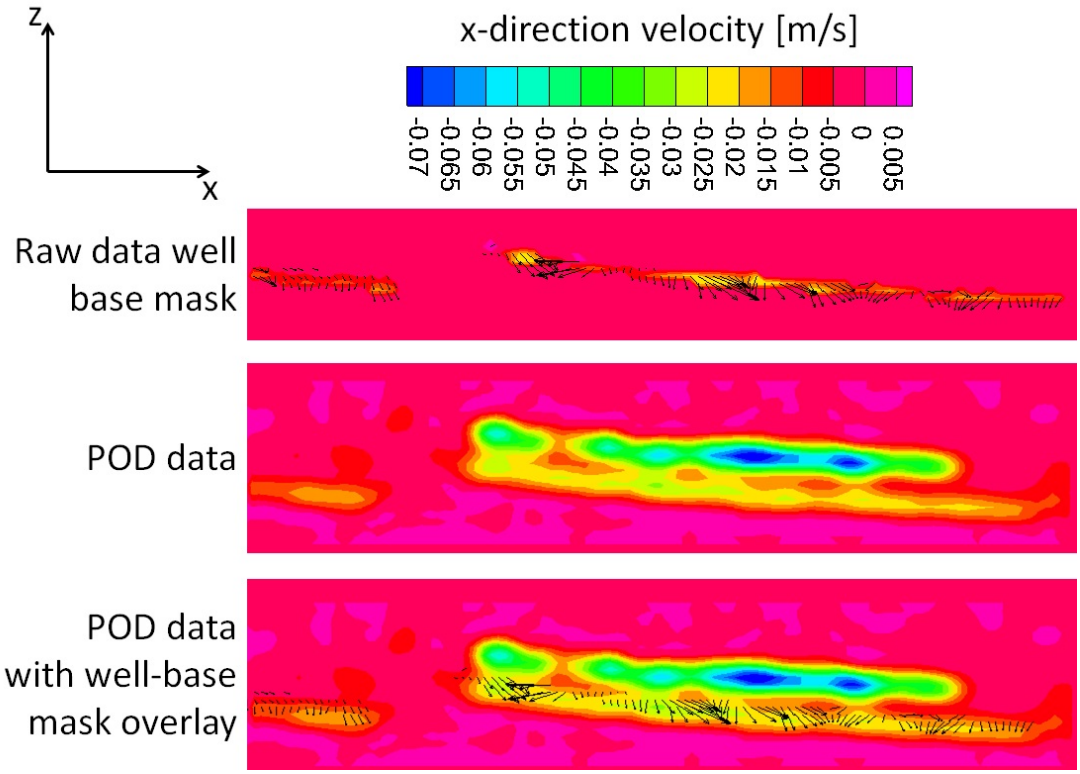

Figure 3.7: PIV data extraction: a vector mask identifies vectors deemed to be closest to the base of the well. The mask is used to extract PIV POD processed velocities (contour map) to obtain the PIV data for analysis.

3.4 PIV results

3.4.1 Velocity vector consistency check

To provide an internal consistency check for acquired velocity vectors after the application of POD, x-component PIV velocities were compared at the spatial resolution of 0.044 mm within zones a and a*, defined in Figure 3.3. PIV velocities within a* were phase-shifted symmetric about the central point of the well for direct comparison with velocities in zone a. An mean positive correlation across data points of 0.678 was achieved, a representation of which is shown in Figure 3.8 for comparable velocity profiles at x=15 mm and x=20 mm, equivalent to A and A* in Figure 3.3 where a positive correlation of 0.697 was identified. This analysis confirms that separate PIV data

positively correlated, but additionally that some noise was present due to the difference between respective signals.

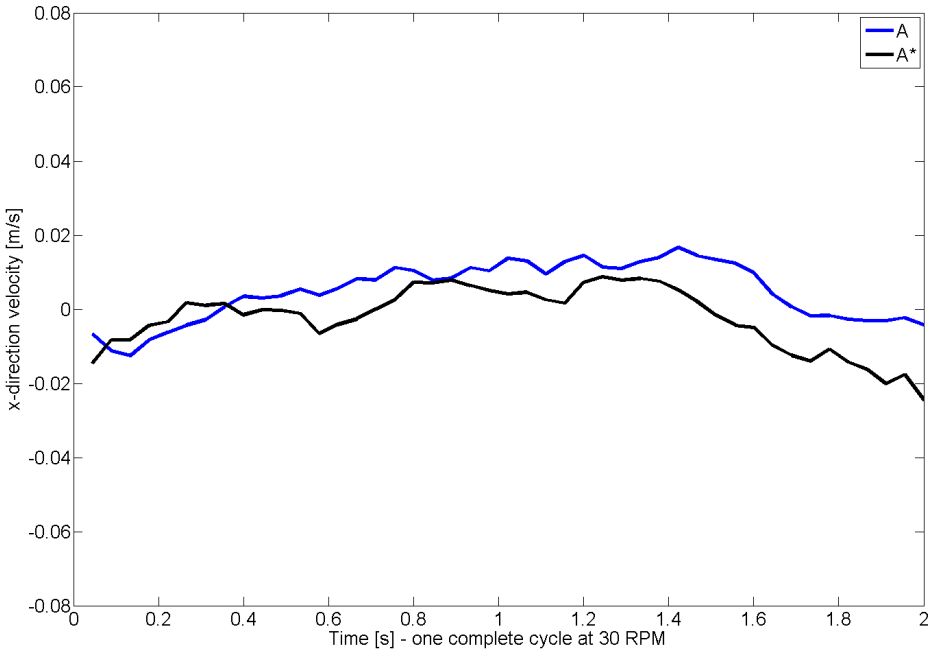

Figure 3.8: PIV comparison: comparison of PIV velocities either side of the centre at positions A and A* (Figure 3.3) (x=15 mm and x=20 mm respectively, y = 0) for one complete cycle shows a positive correlation of 0.697. Velocities at A* have been phase shifted symmetric about the centre point to allow for direct comparison.

3.4.2 Raw PIV velocities

Raw velocity vectors were obtained in the x- and z-direction (Figure 3.9) and used to generate velocity magnitude (Figure 3.10). Velocities were not measured in the y-direction due to the use of a single camera arrangement.

Initial inspection showed a clear cluster of positive velocities in both the x-direction and z-direction at 0.8 s. z-component velocities appeared relatively smooth across the well radius, except for a notable sharp peak of 0.029 $\mathrm{m\,s^{-1}}$; however x-direction velocities appeared to have some notable isolated peaks that potentially were the cause of noise identified in the comparison of additional captured velocity vectors (Figure 3.8).

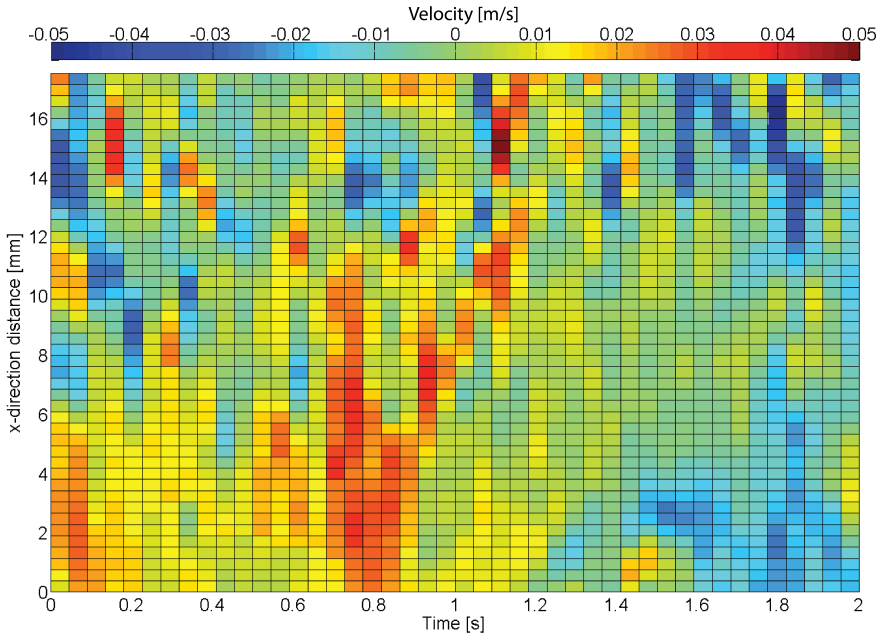

(a) x-component

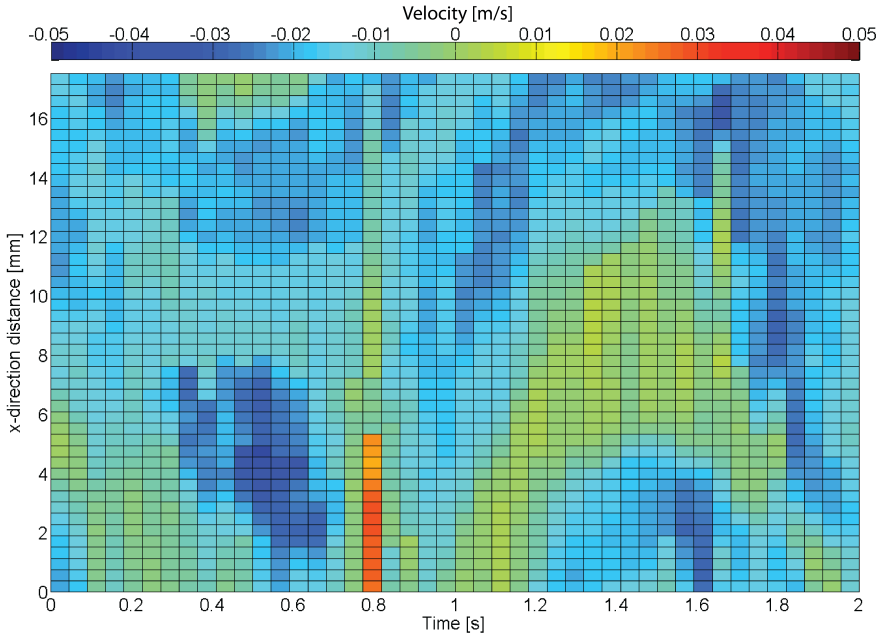

(b) z-component

Figure 3.9: Raw x- and z-components of PIV velocities ($\mathrm{m\,s^{-1}}$): velocities extracted at the base of the well obtained for an entire cycle from $0 - 2\,\mathrm{s}$ and one half of the well along the x-direction centre line (y = 0).

Qualitative analysis of the velocity magnitude across the well radius showed a clear area of peaks from 0.5 to 0.8 s followed by an area of low velocity (dark blue) from 1.2 to 1.7 s. Additionally some notable peaks were identified close to the centre of the well between 14 and 16 mm at 0.05, 0.15, 1.1, 1.65 and 1.75 s (Figure 3.10).

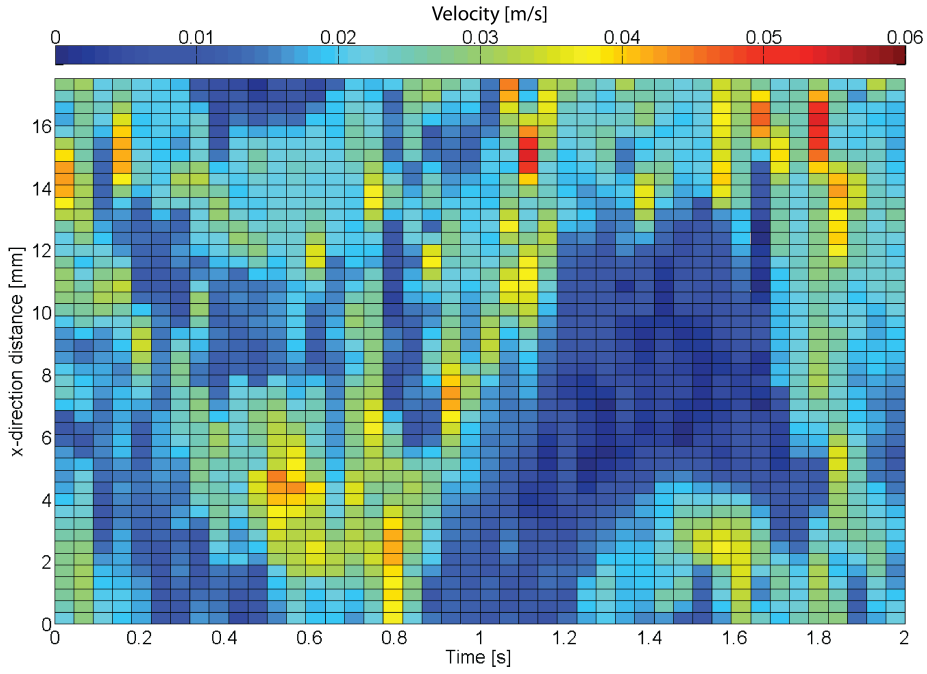

Figure 3.10: Raw PIV velocity magnitude ($\mathrm{m\,s^{-1}}$): velocity magnitudes extracted at the base of the well obtained for an entire cycle from $0-2$ s and one half of the well along the x-direction centre line (y = 0).

3.4.3 Filtered PIV velocities

Prior to the application of a low-pass filter, raw PIV velocity magnitude had a range of $0-55\,\mathrm{mm\,s^{-1}}$ (Figure 3.10). Post-filtering this reduced to $0-36\,\mathrm{mm\,s^{-1}}$ indicating that some noise above 2 Hz was present in the raw signal (Figure 3.11). From the filtered PIV velocity magnitude (Figure 3.11), five key trends were identified:

1. From $0.7-1.1$ s velocities rise to peak velocities at 0.8 s before reducing. A clear maximum at the well edge decreases along the centre line. This decrease is flanked

by other regions of peak velocity starting near the centre of the well and reducing towards the edge.

2. An identifiable region of dark blue is present from 1.15 to 1.6 s, dominating the second half of the cycle. At this stage of the cycle, the fluid depth was high as culture medium is collected on one side of the well due to a maximum angle of tilt, hence a region of low velocity is present.

3. After the region of dark blue, velocities start to increase once more and are generally consistent across the radius of the well, with some identifiable peaks at 1.6 s and 1.8 s. The peak at 1.8 s is exactly one second after the 0.8 s, indicating that the velocity magnitude continues to fall across the well centre line after 17.5 mm at 0.8 s.

4. At the start of the cycle, from 0 to 0.6 s, a diagonal dip in velocity magnitudes is identifiable, starting at 0.1 s / 16 mm and continuing towards the well edge and finishing at 0.6 s.

5. The dark blue region after the peak in velocity at 0.8 s starts with a pocket of low velocity immediately near the well edge and then continues diagonally up to the 10 mm and the start of the dark blue region at 1.15 s.

In addition, it was noted that low-pass filtering eliminated notable peaks identified earlier within the raw data between 14 and 16 mm at 0.05, 0.15, 1.1, 1.65 and 1.75 s, suggesting that these peaks were specifically high frequency (> 2 Hz) elements of noise.

Post filtering, x-component velocities continued to dominate z-component velocities (Figure 3.12).

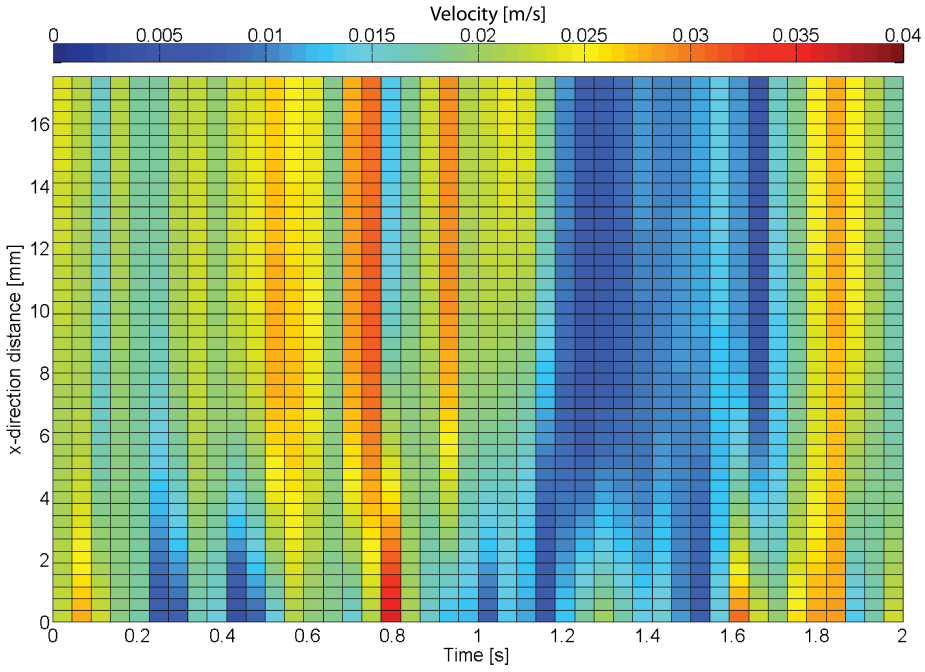

Figure 3.11: Filtered PIV velocity magnitude ($\mathbf{m\,s^{-1}}$): velocity magnitudes extracted at the base of the well obtained for an entire cycle from $0 - 2\,\mathrm{s}$ and one half of the well along the x-direction centre line (y = 0) and subjected to a low-pass filter.

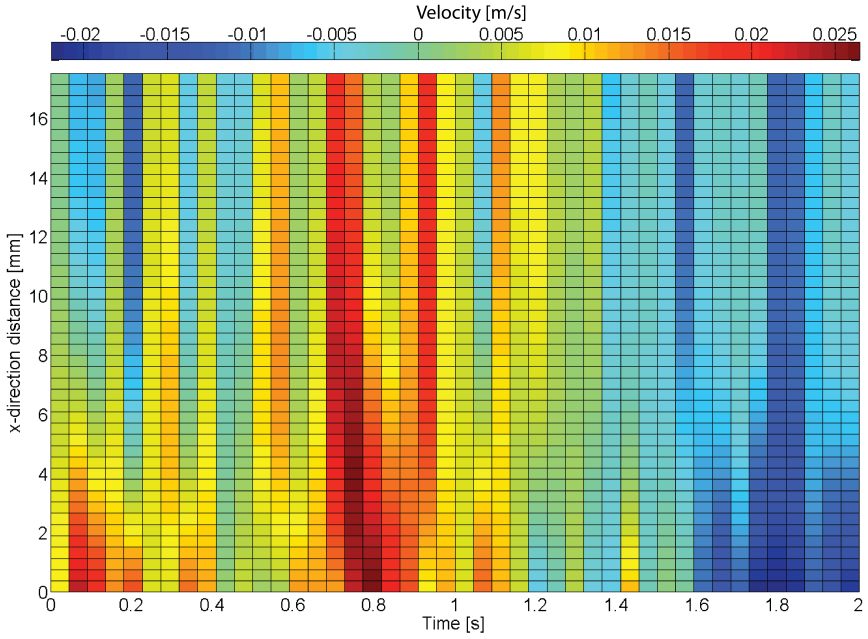

(a) x-component

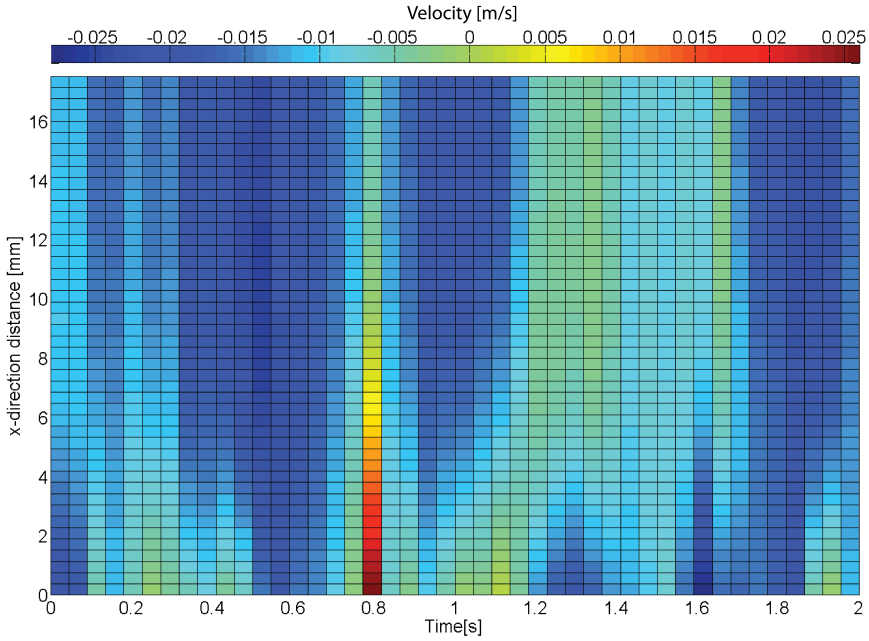

(b) z-component

Figure 3.12: Filtered x- and z-components of PIV velocities ($\mathrm{m\,s^{-1}}$): velocities extracted at the base of the well obtained for an entire cycle from $0 - 2\,\mathrm{s}$ and one half of the well along the x-direction centre line ($\mathrm{y} = 0$) and subjected to a low-pass filter.

3.5 Validation of CFD using PIV

3.5.1 Qualitative comparison of filtered-PIV and CFD velocities

Fluid flow was expected to oscillate with the angular frequency of the see-saw rocker. Fluid inertia was expected to cause minimal out-of-phase effects due to the low rocking frequency. Peaks of velocity were expected to occur at 0 ° as the bulk of the fluid was being displaced from one side of the well to the other. At maximal angles of tilt, it was expected that the fluid would reach its lowest velocity, as the angular velocity passes through zero to change direction. Due to boundary layer effects, flow velocities were expected to be low at the well base, in contrast to higher fluid velocities at the air-media interface.

A qualitative comparison of low-pass filtered PIV and CFD velocity magnitude patterns indicates that flow followed this pattern as expected, with a clear peak in velocity magnitude occurring in both analyses at 0.8 seconds (Figure 3.13). At 0.8 s, velocity was maximum near the well edge and reduced across the radius of the well to the centre. Prior to 0.8 s, the well was accelerating towards the 0 ° position causing the flow to be directed across the well from one side to the other (Figure 3.14).

An area of matching low velocity magnitude, indicated by dark blue, is visible in both the PIV and CFD surface plots (Figure 3.13). During this period, the well was reaching its maximal angle of tilt of 7 ° with zero angular velocity and maximum angular acceleration (Figure 3.14). For the half of the well analysed, during this time-period, the fluid depth was at its maximum as the bulk of the culture medium has displaced to this side of the well.

Fluid velocities then begin to increase once more, only as the rocker moves back towards the horizontal start-point ($1.5 - 2.0$ s).

3.5.2 Quantitative analysis of filtered-PIV and CFD velocities

Filtered PIV velocities result in the removal of signals above 2 Hz and the smoothing of remaining data points (Figure 3.12). Velocity magnitudes were smoothed along the x-direction centre line, potentially attenuating, or masking some peaks in flow velocity that are also present in the CFD. It was therefore necessary to consider raw data and filtered data along side CFD for quantitative analysis purposes (Figures 3.15 & 3.16).

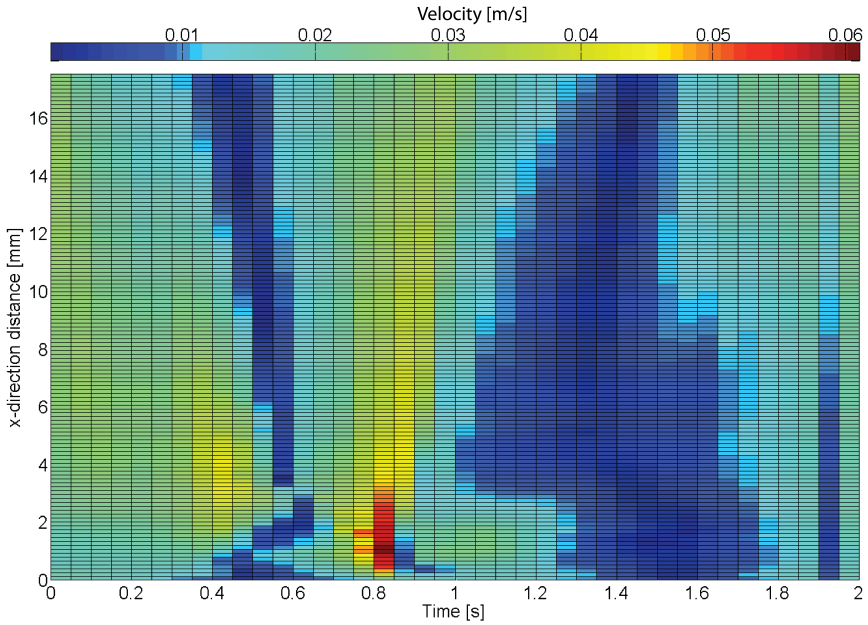

(a) CFD velocity magnitude

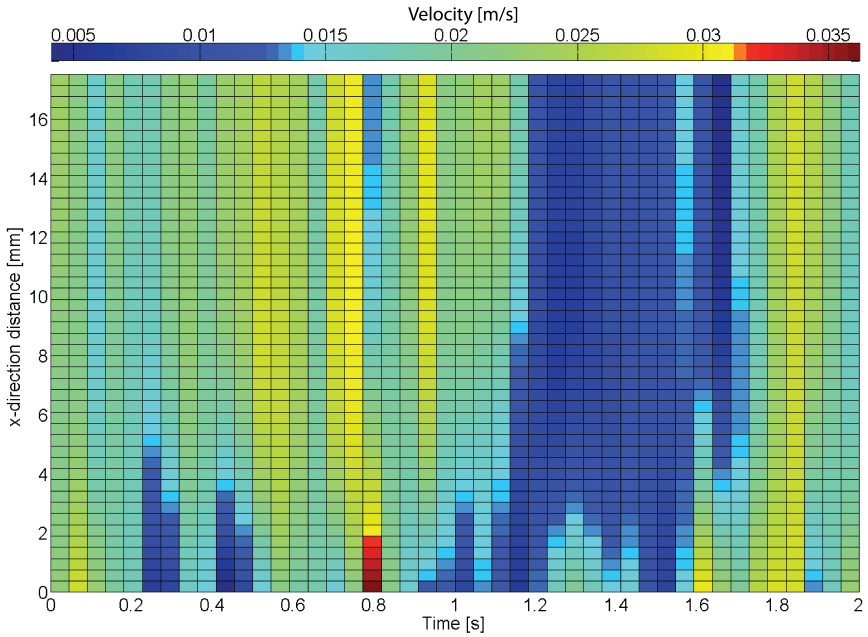

(b) PIV velocity magnitude

Figure 3.13: Qualitative comparison of PIV with CFD velocity magnitudes subject to a low-pass filter ($\mathbf{m\,s^{-1}}$): velocity magnitudes are presented along the centre line of the well (y = 0) for one half of the diameter due to phase-symmetric flow behaviour. One complete cycle is shown.

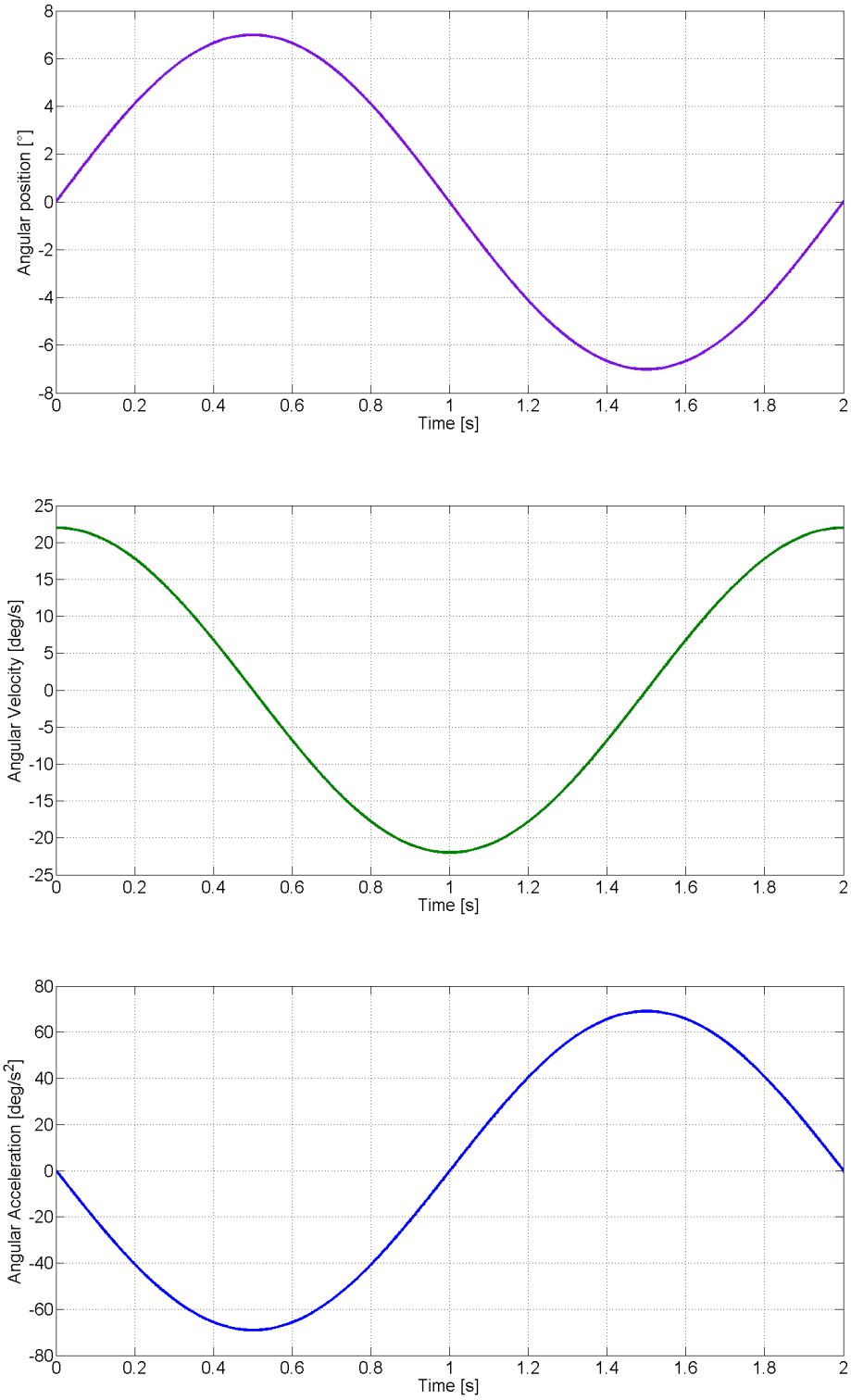

Figure 3.14: See-saw rocker cycle characteristics: angular displacement, velocity and acceleration at 0.5 Hz.

As the resolution of the PIV was limited to 0.44 mm, CFD velocity magnitude was extracted 0.1 mm above the well base (and thus securely away from the no-slip condition) and additionally at 0.4 mm. This provided a range for the CFD across the well centre line and was used as a tool for quantitative analysis.

Quantitative analysis comparing PIV and CFD velocity magnitude was performed at 0.8 s, as the instant that the velocity peak occurred at the base of the well.

Analysis showed that the filtered-PIV signal fell within the CFD velocity magnitude envelope at 0.1 mm and 0.4 mm along the z-axis (Figure 3.15).

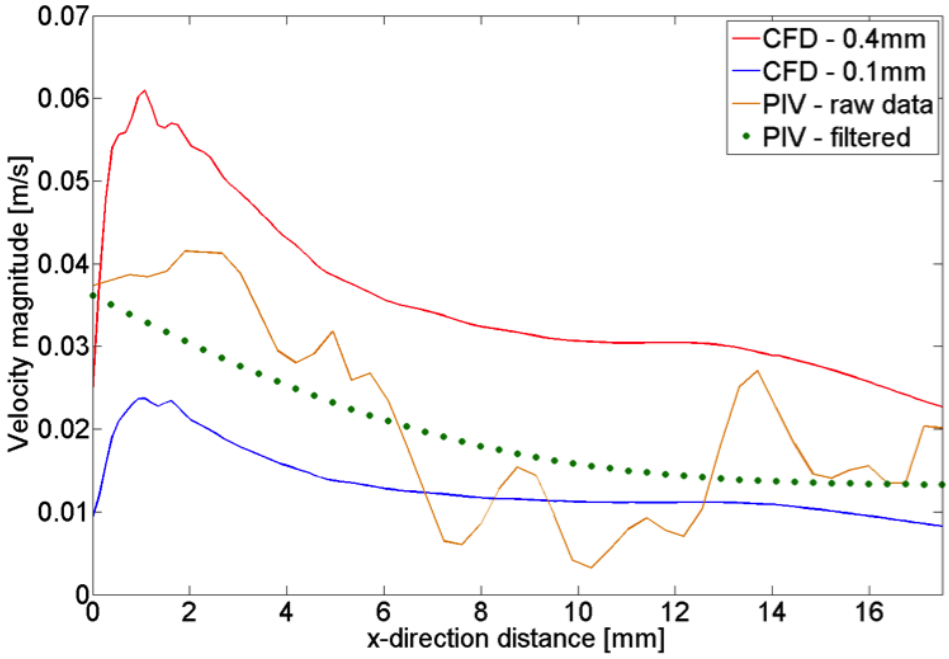

Figure 3.15: Quantitative comparison of PIV with CFD velocity magnitudes: PIV raw and filtered velocity magnitudes with CFD velocity magnitudes at 0.1 and 0.4 mm above the base of the well are compared at 0.8 s, (y = 0).

Further analysis of x-component velocities indicated good agreement at 1.25 s and 1.75 s (Figure 3.16). A comparison of x-component velocities was made as qualitative analysis indicated that they were the dominating component of velocity magnitude (Figure 3.12). At 1.25 s, over 77 % of the filtered PIV velocities fall within the envelope of CFD velocities at 0.4 mm and 0.1 mm above the well base. This is echoed in the

analysis at 1.75 s which shows that over 65 % of the filtered PIV velocities fall within or near to the CFD envelope. Differences appear to be localised to the well edge where fluctuations in CFD velocities are also identified. At 1.75 s from $0 - 4$ mm along the x-axis, the pattern of raw and filtered PIV is similar to that of the CFD, albeit at a larger magnitude, suggesting that potentially PIV at this time-point and location has been extracted at a height above the 0.4 mm CFD data extraction upper boundary.

3.6 Discussion

Physical validation of a simple *in vitro* system for cell culture mechanical stimulation has been achieved using particle image velocimetry and computational fluid dynamics. The CFD result has been compared with detailed, internally consistent PIV characterisation of the actual fluid flow and shows good agreement.

Qualitative comparison of PIV and CFD velocity magnitudes indicated good agreement between the experimental PIV flow capturing and computational flow modelling techniques (Figure 3.15). This agreement holds over the entirety of a cycle along the mid-line of the base of the well.

Quantitative comparison indicated that filtered PIV velocity magnitudes match that of CFD extracted at the same spatial resolution (Figure 3.15). Further analysis of x-component velocities provided good agreement for the majority of the well radius with some differences noted near the well edge, which potentially were due to the identification of the correct PIV vectors at the base of the well (Figure 3.16)

Potential sources of error may exist in the acquisition of experimental PIV velocities. They include:

1. Flow visualisation through the free surface during PIV experiments, causing distorted velocity readings. Visual inspection of the rocker during experiments indicated that the free surface appears relatively horizontal throughout an entire cycle, and therefore the distortion of velocity readings through a 'wave' is considered unlikely. If this did occur, it would move along the free surface with the motion of the rocker, generating a cyclic error in the capture of the results for a small fraction of the captured distance at each time point. As a result, if the error does exist, it is considered to be negligible.

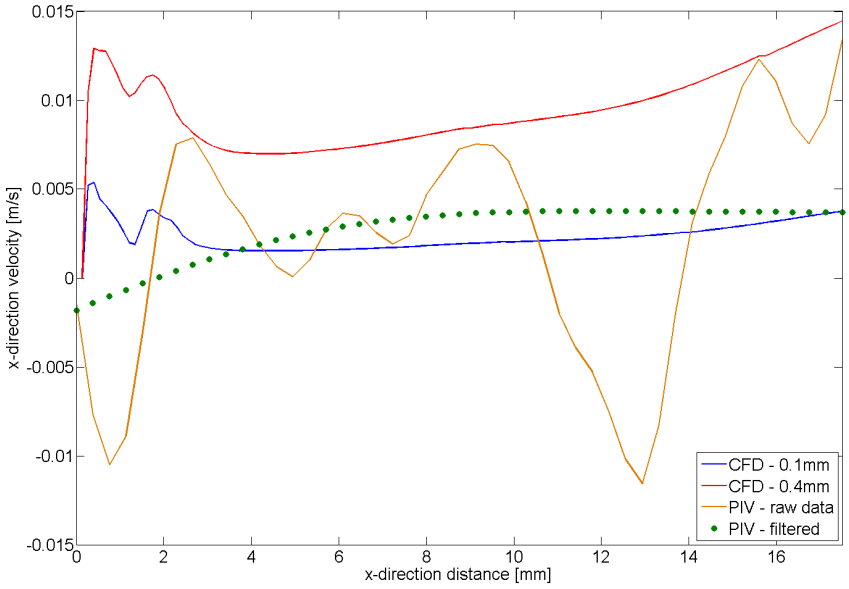

(a) x-component at 1.25 s

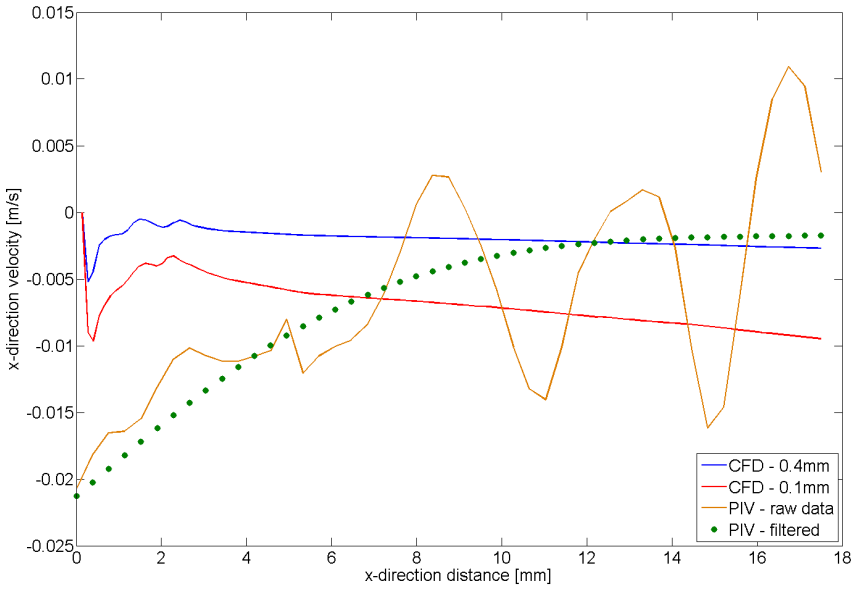

(b) x-component at 1.75 s

Figure 3.16: Quantitative comparison of PIV and CFD x-component velocities at 1.25 & 1.75 s: PIV raw and filtered velocity x-components with CFD velocity x-components at 0.1 and 0.4 mm above the base of the well (y = 0) are compared at different time points. x-axis - x-direction distance from the well edge (0 mm) to the well centre (17.5 mm). y-axis - x-direction velocities captured in the centre of the well.

2. Background, cyclic noise not eliminated through POD (for example, periodic glare from the well) may remain present in the readings. Although glare was reduced through the use of black surfaces for data capture, it is possible that it was not eliminated, potentially contributing noise to the final signal. As this noise would be periodic, it would be present throughout the entire signal, inflating components of x- and z-velocities. Due to use of black surfaces in the experimental approach, the presence of this noise is considered to be negligible.

A fixed grid was used to calculate velocity vectors for the rotating platform, thus comparable velocity vectors were translated during each time step. PIV vectors were identified through the use of a mask; however, it is noted that within the CFD solution a spatial difference of 0.3 mm between data points can produce differences of $0.04\,\mathrm{m\,s^{-1}}$ for extracted velocities (Figure 3.15).

Noise removal techniques, although successful, have inherent limitations that will impact on the final solution. The use of a low-pass filter may have removed some of the signal that provided accurate contributions to the overall solution. For example, an area of peak velocity at 0.5 s / 4 mm (Figure 3.10) is comparable with a peak in CFD velocity magnitude at 0.4 s / 3.5 mm (Figure 3.13), but is eliminated and smoothed after the application of a low pass filter (Figure 3.11). Additionally, comparison of the raw-PIV data with the CFD boundary at 0.4 mm shows a very similar general trend, albeit at a lower magnitude. A peak in the raw PIV data is present in the 0.4 mm CFD signal at 2 mm. In addition, at 14 mm, a large peak in the PIV, where some noise may be present, is also reflected by a small increase in the 0.4 mm CFD signal that was otherwise following a gradual descent.

Analysis has shown that it is clear that the PIV and CFD velocity magnitudes indicate that flow behaviour matches. A clear peak in both the CFD and PIV data is present and practically coincident, and in addition, flow velocities follow predictions as they increase and decrease when reaching the 0 ° and 7 ° positions respectively. Quantitative analysis has indicated that PIV velocity magnitudes obtained at a resolution of 0.44 mm fall within the range of CFD velocities obtained at the same resolution (Figure 3.15). Additionally, good agreement between x-component velocities has been achieved at varying time-points (Figure 3.16). The matching of PIV with CFD confirms that the selection of a vector spatial resolution of 0.44 mm was appropriate and

that data recorded at 250 Hz provided an accurate level of temporal resolution for data processing techniques.

In conclusion, agreement between CFD and PIV is achieved to a high level of confidence, resulting in the validation of underlying CFD modelling assumptions. The CFD model can now be used to provide accurate estimations of shear stress profiles for cells seeded at the base of the well of a six-well plate and biological response can confidently be attributed to specific shear stresses.

With successful validation, the CFD model provided a foundation for further expansion. For Newtonian flow, it was hypothesised that increasing the dynamic viscosity of the medium would yield a similar shear stress pattern, but at an increased magnitude. Thus, two models using alternative medium viscosities were considered in Section 4.1. Furthermore, rocking frequencies at the limit of the Stuart SSL4 operating range were also considered (Section 4.2). Additionally, the model provided shear stresses for wells placed only above the axis of rotation and a model displaced from the central axis was considered in Section 4.3.

Chapter 4

Extending the CFD model - shear stress magnitude, frequency, & robustness to position

A validated model for characterising the shear stress and generated velocities in a six-well plate placed on a Stuart SSL4 rocker has been presented at a rocking frequency of 0.5 Hz (30 cpm) (Chapter 2). However, for the see-saw rocker to act as a versatile platform for fluid flow investigations it is beneficial to understand the effect of a change in key model parameters. This will give researchers the freedom to change experimental conditions while continuing to have a fully characterised testing environment.

Musculoskeletal cells are likely sensitive to shear stress magnitude and frequency (Section 1.6.2), thus the ability to independently vary these parameters for *in vitro* cell monolayer investigations would benefit experiment design and mechanobiology discoveries.

Furthermore, to increase experiment throughput it would be beneficial to understand the model robustness by checking the effects of platform position on shear stress magnitude.

Within this chapter the following model conditions are presented and evaluated in relation to the 0.5 Hz base-scenario in order to achieve objective four of this thesis (Section 1.9):

1. A change in the viscosity of the fluid to investigate whether shear stress magnitude is altered at a maintained oscillation of 30 cpm.

2. A change in the rocking frequency to 5 and 70 cpm, so that the the operational limits of the platform are characterised.

3. The effect of placing a well at the edge of the platform, thus increasing its vertical displacement during a cycle.

4.1 Varying fluid viscosity

Shear stress is determined from viscosity and strain rate (Equation 4.1), as such a method of increasing shear stress magnitude is to increase the viscosity of the fluid.

$$\tau = \mu \frac{du}{dh} \tag{4.1}$$

where μ is the dynamic viscosity, u is the fluid velocity, and h is the height of the fluid.

Within cell culture experiments, carboxymethyl cellulose (CMC) salts are added as a biologically inert compound to increase fluid viscosity (38). They are particularly advantageous as high viscosities can be achieved at low concentrations. A large concentration of CMC salts causes fluids to exhibit non-Newtonian psuedoplastic behaviour, known as shear-thinning. To ensure Newtonian flow behaviour, CMC concentration must not exceed 0.5 % (276). Within this section of the thesis, the effect of CMC concentrations of 0.1 % and 0.2 %, generating viscosities of 20 mPa s and 31 mPa s respectively (276), on fluid flow behaviour within the rocking system are considered using CFD modelling.

4.1.1 Dimensionless numbers

A change in the viscosity of the fluid required re-evaluation of the system dimensionless numbers to ascertain whether the modelling assumptions would continue to hold for the new conditions. To calculate new dimensionless numbers, viscosity values were altered and the change assumed to have a negligible affect on surface tension.

A change in viscosity did not affect the Weber number or Bond number; however it did affect the Reynolds number and a marked fall was seen to 6.5 and 4.2 for viscosities of 20 mPa s & 31 mPa s respectively (Table 4.1). Even though there was a large difference in comparison to the base-scenario Reynolds number of 167, no change in the modelling assumptions was required as the value indicated that flow was still laminar and that Stokes' flow was not present as inertial forces continued to dominate viscous effects.

Dimensionless number	Base-scenario	20 mPa s	31 mPa s
Reynolds	167	6.5	4.2
Bond	167	167	167
Weber	2.4	2.4	2.4

Table 4.1: Dimensionless numbers for a medium viscosity of 20 mPa s & 31 mPa s

4.1.2 Model methods & arrangement

A domain was established as per the validated CFD model arrangement presented in Chapter 2. Fluid viscosity was increased to 20 mPa s & 31 mPa s by altering secondary fluid properties within the VoF condition. All other aspects remained consistent.

4.1.3 Model evaluation

Although the base-scenario indicated that the vast majority of initial transient effects were removed after the first cycle, both viscous models were run for six complete cycles and the sixth cycle used for analysis.

To complete six cycles on a 24-core arrangement, 1008 hours of computation time was required for each model, 554 h (122 %) more than the base-scenario (Table 2.2).

Evaluation of the CFL number using the smallest dimension of 0.21 mm indicated that both of the models were within the CFL prescribed condition of 0.25 (Table 4.2). Consistent with the base-scenario, the maximum velocity of 80 mm s^{-1} and 60 mm s^{-1} for the 20 mPa s & 31 mPa s models respectively, peaked at the fluid-air interface, and would support a CFL number larger than 0.25; however model iterative convergence

indicated an appropriate selection of the time-step size. Additionally, maximum velocities within the viscous models were either similar or slightly lower than the base-scenario, encouraging a reduced CFL number across the model system compared to the base-scenario as the same grid density and time step size were used (Equation 2.13) (Table 2.3).

Condition	Average velocity ($mm\,s^{-1}$)	CFL
20 mPa s	25	0.12
31 mPa s	15	0.07

Table 4.2: CFL number evaluation for models with an increased fluid viscosity

4.1.4 Results from models with an increased fluid viscosity

Under viscosity conditions of 20 mPa s, mean shear stress along the x-direction radius is 0.714 ± 0.509 Pa, a 21.6-fold increase on the base-scenario reported shear stress, compared to a 25.64-fold increase in viscosity. Shear stress across the entire dish radius ranges from 0 to 9 Pa (Figure 4.1).

Similarly, under viscosity conditions of 31 mPa s, mean shear stress along the x-direction radius is 1.023 ± 0.702 Pa, a 31-fold increase on the base-scenario reported shear stress, compared to a 39.74-fold increase in viscosity. Shear stress across the entire dish radius ranges from 0 to 12 Pa (Figure 4.2).

The shear stress profiles for both cases are similar to that of the base-scenario (Figure 4.3). Peak shear stress occurs near the well edge at *circa* 1 s when the well is at 0 °, lasting for a twentieth of the complete cycle time. For the remainder of the well, the shear stress is much lower for the entire cycle, as fluid velocity becomes increasingly homogenous across its depth.

Distance-averaged shear stress indicates a similar profile for both viscosity conditions as peaks occur near the 0 ° position (Figures 4.1 & 4.2).

As Newtonian fluid behaviour is maintained at CMC concentrations of 0.1 and 0.2 %, the strain rate remains largely similar to the base-scenario and the change in shear stress is driven by the increase in viscosity; however it is noted that the peak shear stress is shifted temporally to later in the cycle by 0.2 s and 0.25 s, and spatially further

from the well edge by 0.5 mm and 1 mm, respectively for the 20 mPa s and 31 mPa s cases. This could be explained by the reduced inertial dominance of the flow properties signified by a fall in the Reynolds number.

A prediction of the change of shear stress at the same strain rate provides very similar results (Figure 4.4). For the 20 mPa s scenario, a 21.64-fold increase identified in computational results is very similar to the 25.64-fold increase prediction based on the increase in fluid viscosity (20/0.78). Additionally, for the 31 mPa s condition, a computational-predicted 31.00-fold increase is similar to a predicted 39.74-fold increase (31/0.78). Differences identified may be due to the reduced velocity, resulting in a change in fluid depths during parts of the cycle, creating slightly different strain rate profiles.

4.1.5 Conclusion of increased viscosity modelling

The shear stress distributions for the base-scenario and increased viscosity conditions are similar and the magnitudes appear to show an approximately linear variation with viscosities. As viscosity change is assumed to be the overriding factor determining the increase in shear stress profiles, the change in viscosity was used to estimate the profile of maximum shear stress using the base-scenario condition.

It is concluded that for Newtonian flow an increase in viscosity is a good indicator of the change in the shear stress magnitude at the base of a six-well plate.

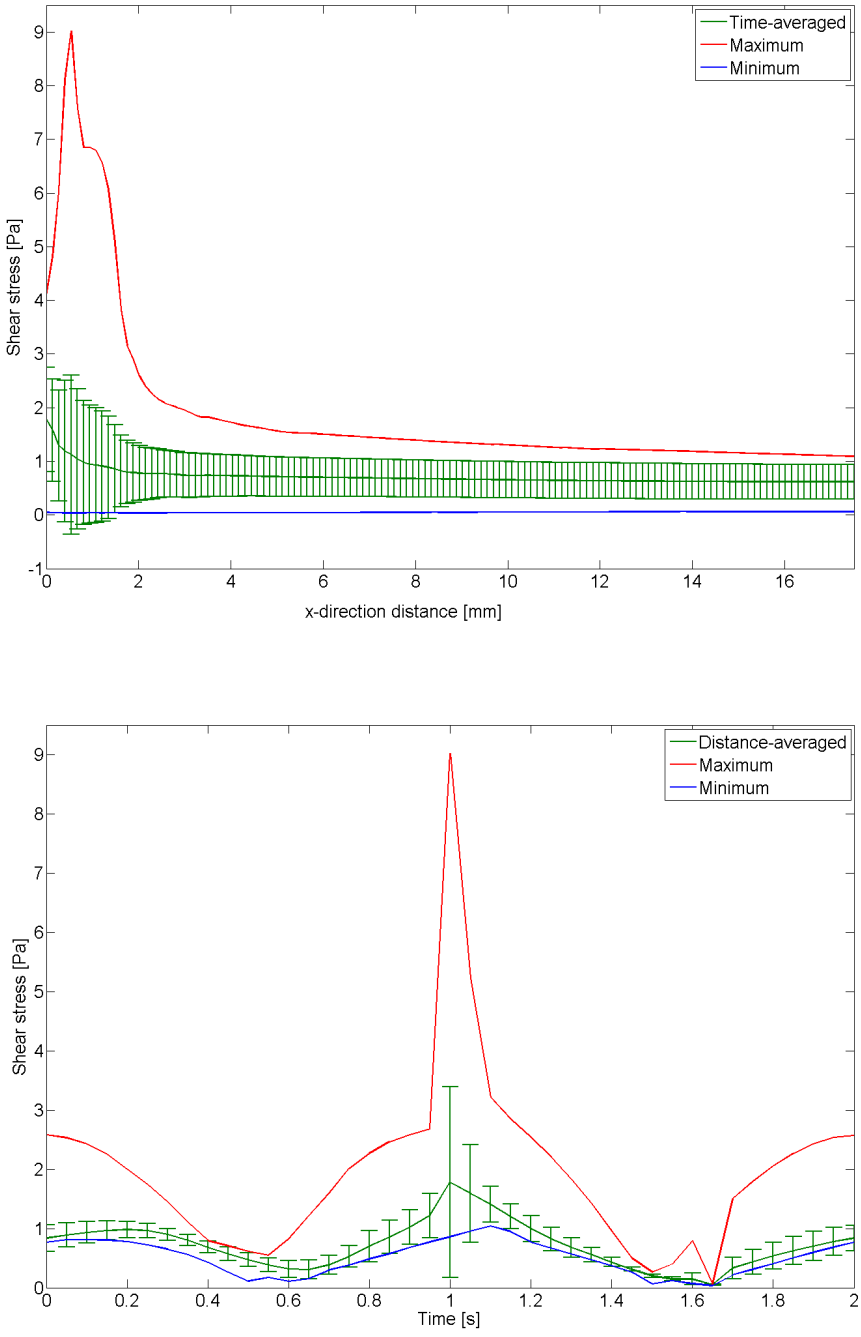

Figure 4.1: Maximum, minimum & average shear stress from a medium viscosity of 20 mPa s: time-averaged and distance-averaged shear stress profiles (y = 0) are very similar to the base-scenario. Time-averaged shear stress is homogenous across the well radius, with a small peak of 2 Pa near the well edge.

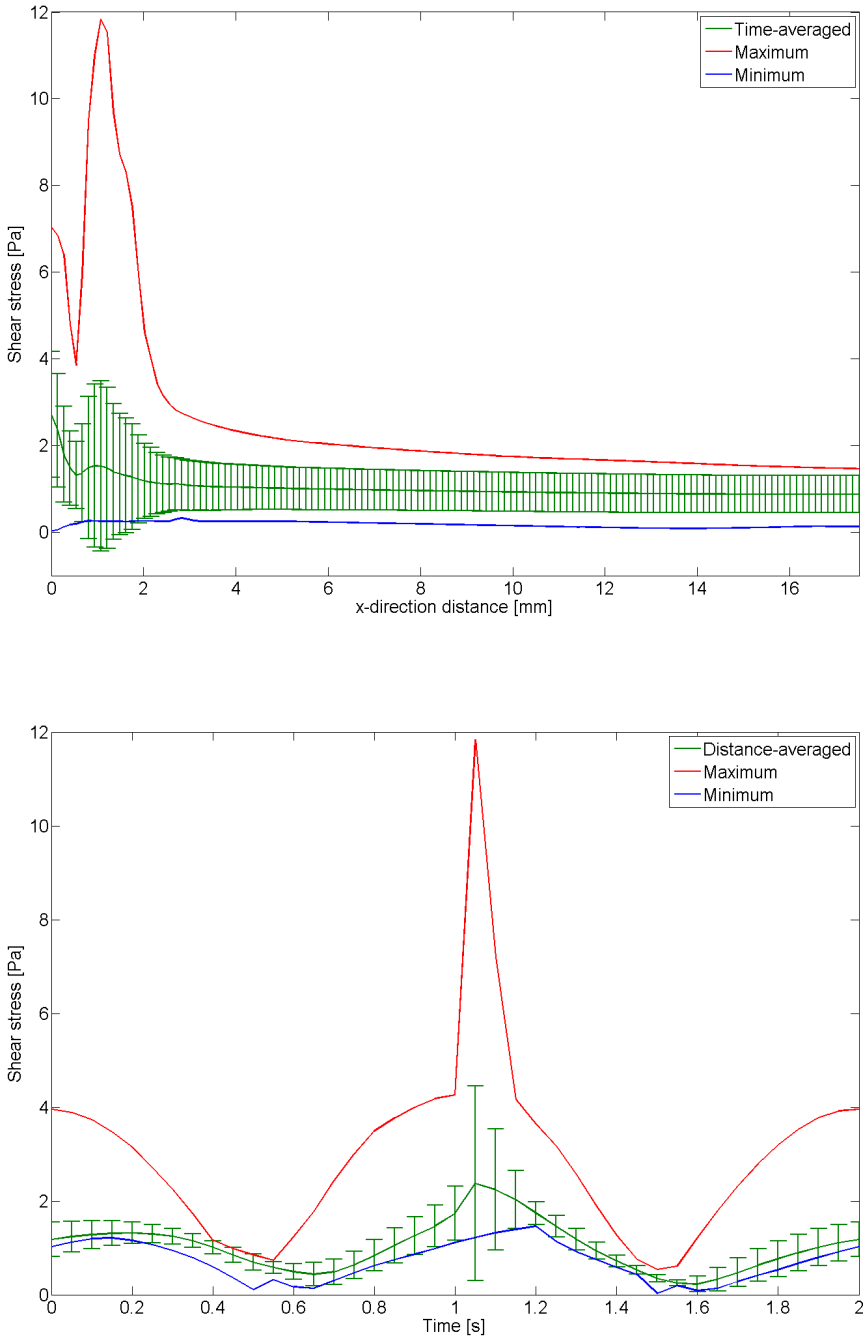

Figure 4.2: Maximum, minimum & average shear stress from a medium viscosity of 31 mPa s: time-averaged and distance-averaged shear stress profiles (y = 0) are very similar to the base-scenario. Time-averaged shear stress is homogenous across the well radius, except for a small peak of just under 3 Pa near the well edge.

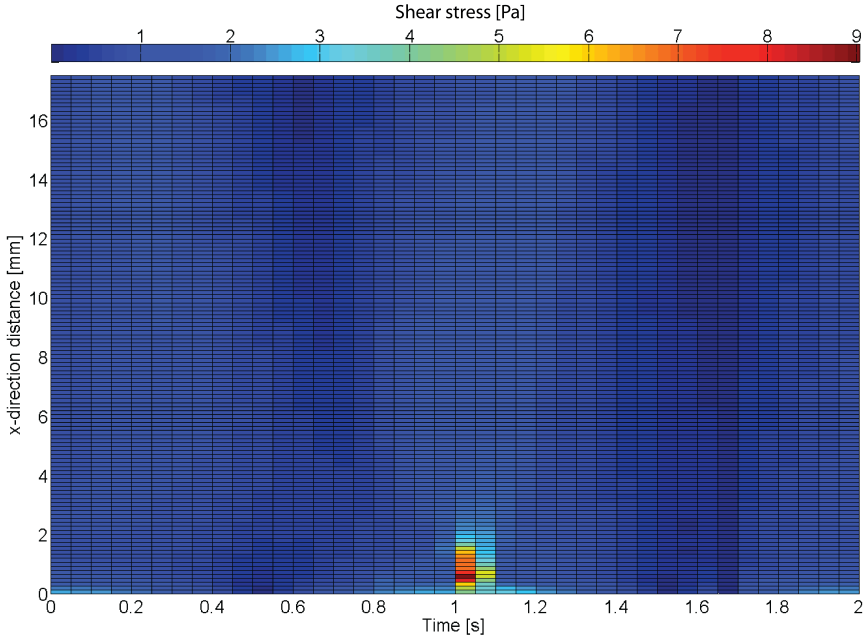

(a) 20 mPa s, shear stress peaks at 1 s at 0.5 mm from the well edge(y = 0).

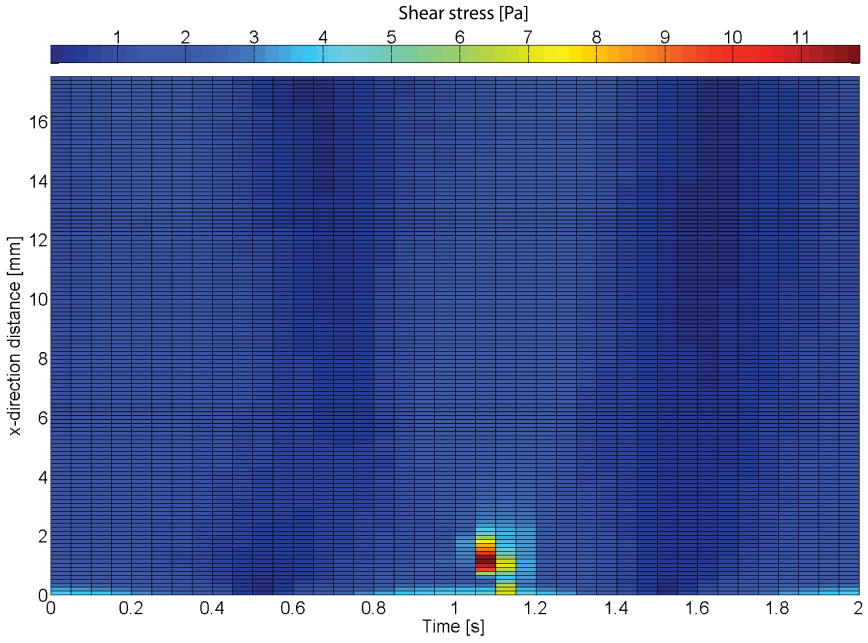

(b) 31 mPa s, shear stress peaks at 1.05 s at 1 mm from the well edge (y = 0).

Figure 4.3: Shear stress distributions from a medium viscosity of 20 and 31 mPa s (Pa)

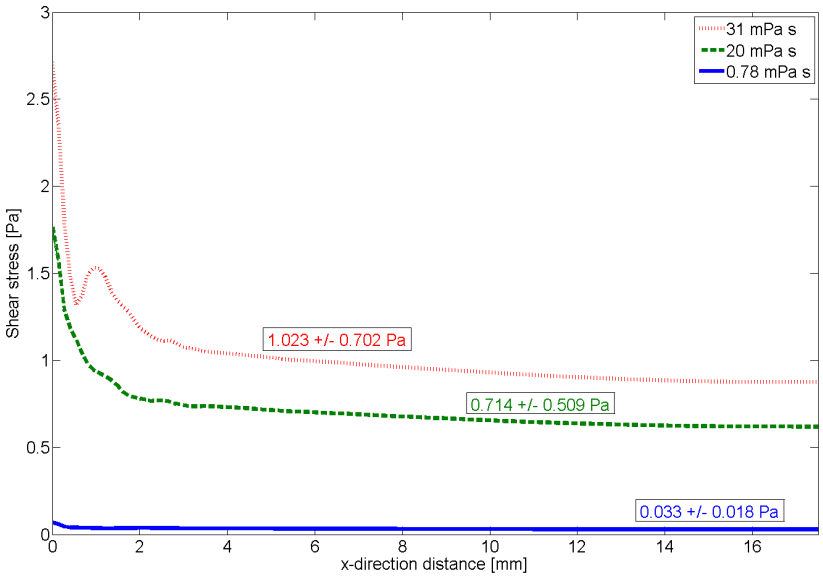

(a) Time-averaged shear stress profiles for each viscosity condition

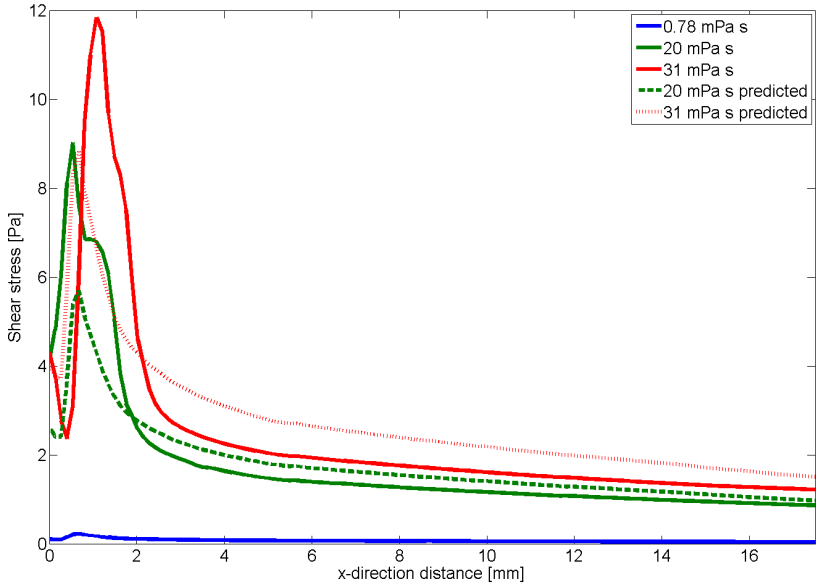

(b) Comparison of predicted maximum shear stress patterns based on an increased viscosity within the base-scenario condition (dashed lines) and maximum profiles determined by fluid dynamics modelling (solid lines)

Figure 4.4: Shear stress comparison for different fluid viscosities

4.2 Varying rocking frequency

The Stuart SSL4 see-saw rocker has an operating range of $5-70$ cpm ($0.083-1.167$ Hz). These two limits were modelled in order to understand the effect a change in oscillation frequency had on the shear stress profile at the base of a well.

4.2.1 Dimensionless numbers

To determine the dimensionless numbers of the model at 0.083 and 1.167 Hz it was necessary to re-evaluate the estimated maximal velocity in the domain. At 0.083 Hz the rocker completed one cycle every twelve seconds giving a maximal velocity over 35 mm in three seconds of $0.012\,\mathrm{m\,s^{-1}}$. Applying the same principles to the 1.167 Hz condition, a maximal velocity of $0.163\,\mathrm{m\,s^{-1}}$ was estimated and used for dimensionless number calculations.

Under the 0.083 Hz condition, the Reynolds number is reduced to 29, confirming that flow is dominated by inertial rather than viscous effects. Interestingly, the Weber number is reduced to 0.07, suggesting that the presence of flotsam and jetsam in the solution is likely reduced as hydrodynamic forces dominate inertial effects.

At 1.167 Hz, the Reynolds number increases, but remains in the laminar range. The Weber number also increases, suggesting that flotsam and jetsam may be more prevalent in the model solution and that the solution may consist of 'sloshing' effects, rather than steady flow.

Dimensionless number	Base-scenario	0.083 Hz	1.167 Hz
Reynolds	167	29	388
Bond	167	167	167
Weber	2.4	0.07	12.9

Table 4.3: Dimensionless numbers for a rocking frequency of 0.083 Hz & 1.167 Hz

4.2.2 Model methods & arrangement

A domain was established as described in Section 2.1.5 and a grid size of 1,068,445 cells used as a basis to obtain grid independent results (Section 2.2.1.4). All aspects of the

arrangement were consistent with the validated base-scenario presented in Chapter 2 except for altering the time step size and sinusoidal displacement profile for the rotating surfaces (Table 4.4).

Condition	Time-step size (s)	Parametric expression amplitude
0.083 Hz	0.003	$\frac{2.33}{0.637}$
1.167 Hz	0.0002	$\frac{32.676}{0.637}$

Table 4.4: Sinusoidal angular velocity amplitudes for a rocking frequency of 0.083 Hz & 1.167 Hz

As with the base-scenario, error inherent in the use of a parametric function due to rounding limitations was present in both conditions. Both scenarios were run for two complete cycles (discussed in Section 4.2.3) presenting a displacement error of 0.017 % and 0.026 % for the 0.083 Hz and 1.167 Hz conditions respectively.

4.2.3 Model evaluation

For both frequency conditions, the second cycle was used for analysis. This was due to a significant increase in the time to completion for each model. Although use of the second cycle will result in some error in the analysis, initial transient effects were negligible in the base-scenario after the first cycle (Section 2.2.3).

The 0.083 Hz model was run on a 24-core arrangement, taking 1488 hours to complete two cycles. A full six cycles would have taken 4464 hours to complete. The 1.167 Hz model was run on a 40-core arrangement, taking 864 hours to complete two cycles. Reduced to a 24-core arrangement and run for a full six cycles, it is hypothesised the solution would take 4320 hours to complete. These times are an increase of 983 % and 952 % for the 0.083 Hz and 1.167 Hz conditions respectively, on the base-scenario time to completion of 454 h. Use of the second cycle was considered an appropriate approximation given the large increase in time to completion.

A reduced rocking frequency presented a computational challenge as a longer cycle would mean that maintaining the base-scenario time step size would have increased the number of time steps required to complete the desired number of cycles. Thus, identifying a maximum time step size permitted ensuring convergence presented a challenge,

but was overcome with a time step size of 0.003 s. Although the rocking frequency decreased six-fold, the time step size could only be increased three-fold.

Evaluation of CFL numbers indicated that the selection of time step sizes was appropriate (Table 4.5). In both cases, the CFL number based on average velocity was less than 0.25, supporting model stability and result accuracy.

Condition	Average velocity ($mm\,s^{-1}$)	CFL
0.083 Hz	8	0.095
1.167 Hz	100	0.114

Table 4.5: CFL summary for a rocking frequency of 0.083 Hz & 1.167 Hz

4.2.4 Model results

4.2.4.1 Rocking frequency of 0.083 Hz

The shear stress distribution at 0.083 Hz is quite different in comparison to the distribution at 0.5 Hz (Figures 4.5 & 2.22). A peak of 0.03 Pa occurs at 3.5 s 4 mm from the well edge, just after the first quarter of a cycle when the well has started to return to the 0 ° position. At this time-point and location, the fluid depth is very low as most of the culture media has moved over to the other side of the well where the opposite edge is at −7 °. Nearer the well edge, at *circa* 1 mm, from $4-9$ s, a peak in shear stress appears to be fairly constant from $3.75-8.5$ s.

Across the well centre line in the x-direction, a mean shear stress of 0.012 ± 0.004 Pa occurs, with a shear stress range of $0.005-0.029$ Pa (Figure 4.5). Near the well centre the time-averaged shear stress has its smallest standard deviation as the maximum and minimum values come close to converging. Near the well edge, peaks in shear stress are identified and the time-averaged shear stress standard deviation is at its largest. A region of maximum shear stress occurs at $0.5-4.5$ mm between 0.025 and 0.029 Pa.

FFT of shear stresses along the x-direction centre line at the well base, at a sampling frequency of 3.42 Hz, indicated that shear stresses occur at low frequencies close to the angular rocking frequency of 0.083 Hz (Figure 4.6). Above 0.1 Hz (equivalent to a rocking oscillation of 6 cpm) amplitudes are zero, indicating that no shear stresses are present at this frequency. Therefore, it was concluded that shear stresses within the

well were driven by laminar, steady flow, cyclic velocity conditions, closely following the frequency dictated by the see-saw rocker.

4.2.4.2 Rocking frequency of 1.167 Hz

Analysis of shear stress along the x-direction centre line indicates that the shear stress distribution can be clearly divided into two separate intervals (Figure 4.7). From 0 to 0.42 s, shear stress peaks occur and regions of shear stress in excess of 0.4 Pa are prevalent. After 0.42 s for the rest of the cycle, shear stress levels dramatically fall to less than 0.2 Pa. Shear stress ranges from 0.008 to 1.314 Pa, peaking 0.08 s through a cycle at the well wall. At this time-point the well had moved 3.87 ° from the horizontal starting position.

Mean shear stress of 0.248 ± 0.169 Pa is constant across the well radius, although rises slightly towards the centre point (Figure 4.7), a different profile to the time-averaged shear stress identified in the base-scenario.

Fast fourier transform of shear stresses along the x-direction centre line at the well base, at a sampling frequency of 51 Hz, indicated that shear stresses occur at a frequency range of $0 - 2.5$ Hz, with peaks close to the rocking platform frequency of 1.167 Hz (Figure 4.8). Above 2.5 Hz, the remainder of the amplitudes are zero, except for a couple of small peaks, one near the centre of the dish at 5 Hz and the other at the quarter-point along the dish diameter (*circa* 8 mm) where a frequency of $5 - 8$ Hz was identified. These peaks could signify that conditions may be in the transition phase from a laminar state; however amplitudes are low, and for turbulent conditions, numerous isolated frequency peaks would be expected, therefore the flow is not turbulent. The Reynolds transition number of 600 for an open-channel is an estimate applied to this scenario and although the Reynolds number at 1.167 Hz was determined to be 388, it may be that the transition number is smaller for a well on a rocking platform.

4.2.5 Conclusion of modelling at 0.083 & 1.167 Hz

Average shear stress showed a non-linear relationship with rocking frequency (Figure 4.9). Predicting maximum shear stress based on the increase/decrease in rocking frequency indicates that the base-scenario may be used to accurately estimate the response at 5 cpm; however at 70 cpm, the maximum shear stress is 1.314 Pa, 260 % higher

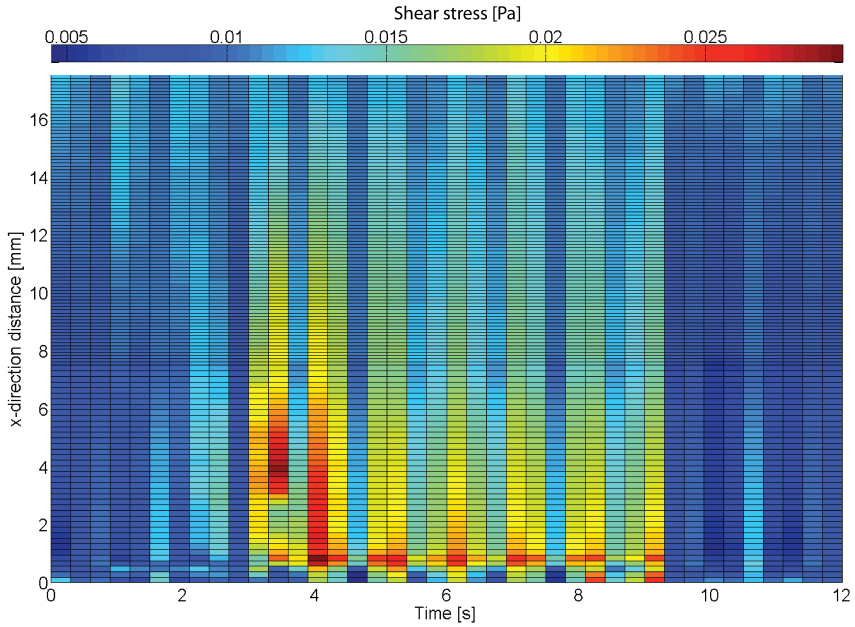

(a) Shear stress distribution along the x-direction centre line (Pa)

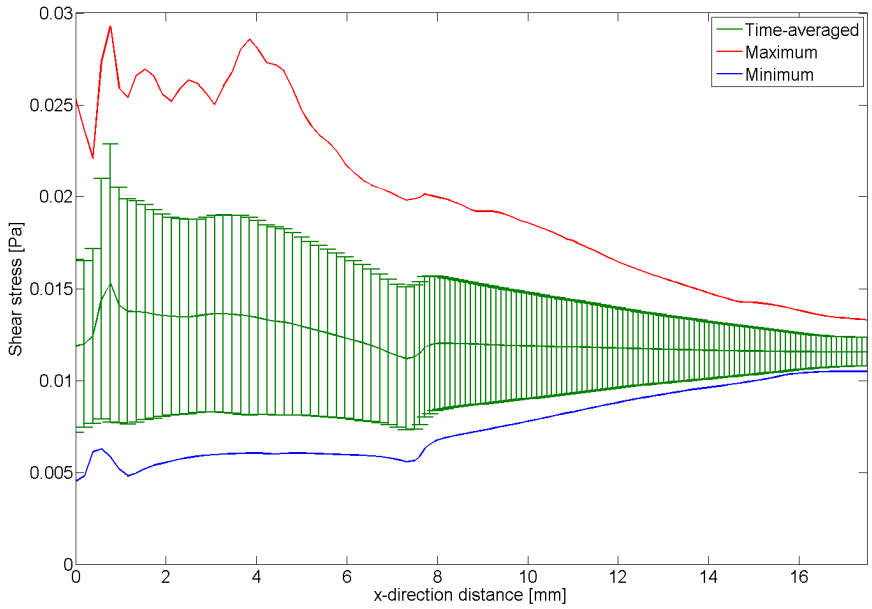

(b) Maximum, minimum & time-averaged shear stress with standard deviation (Pa)

Figure 4.5: Shear stress behaviour for a well at a rocking frequency of 0.083 Hz: shear stress values extracted 0.1 mm above the base of the well (y = 0). Comparative base-scenario shear stress distributions are shown in Figures 2.22 & 2.23.

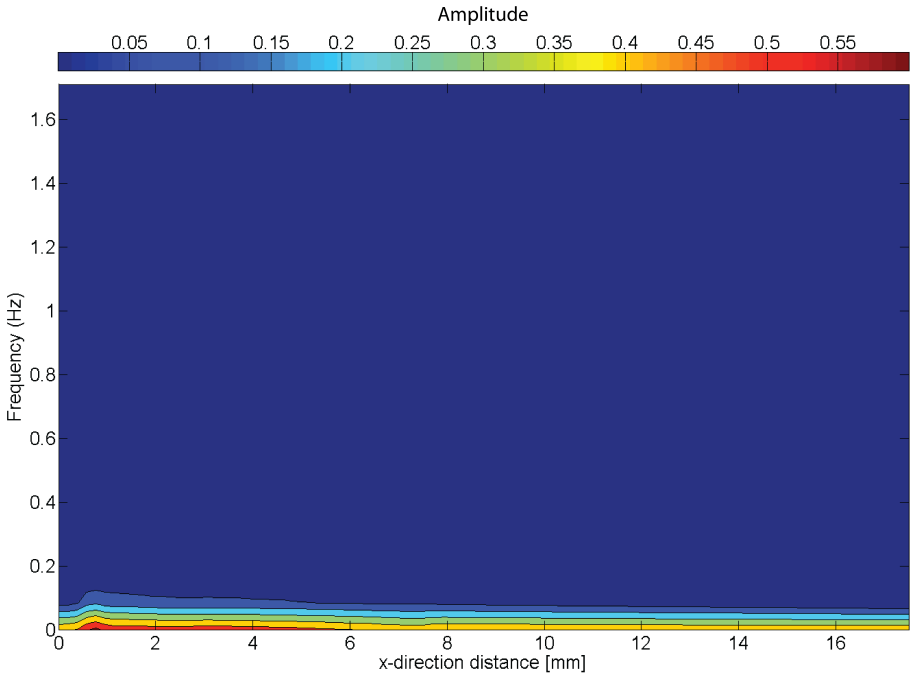

Figure 4.6: Fast fourier transform of shear stress at a frequency of 0.083 Hz: sampling frequency of 3.42 Hz used. The fast fourier transform shows that frequency amplitude peaks at 0.083 Hz and supports a conclusion of laminar conditions as flow of other amplitude peaks are low and localised around the rocking frequency.

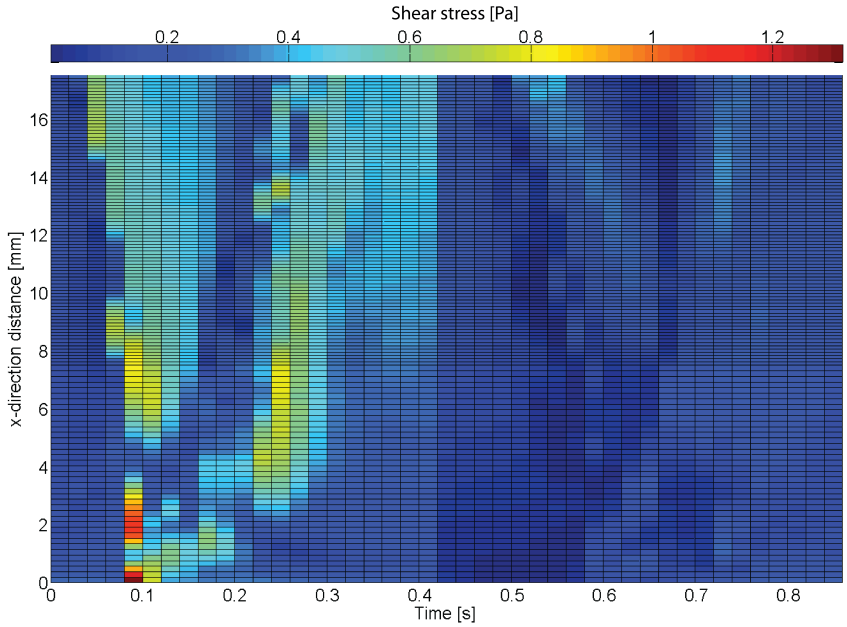

(a) Shear stress distribution along the x-direction centre line (Pa)

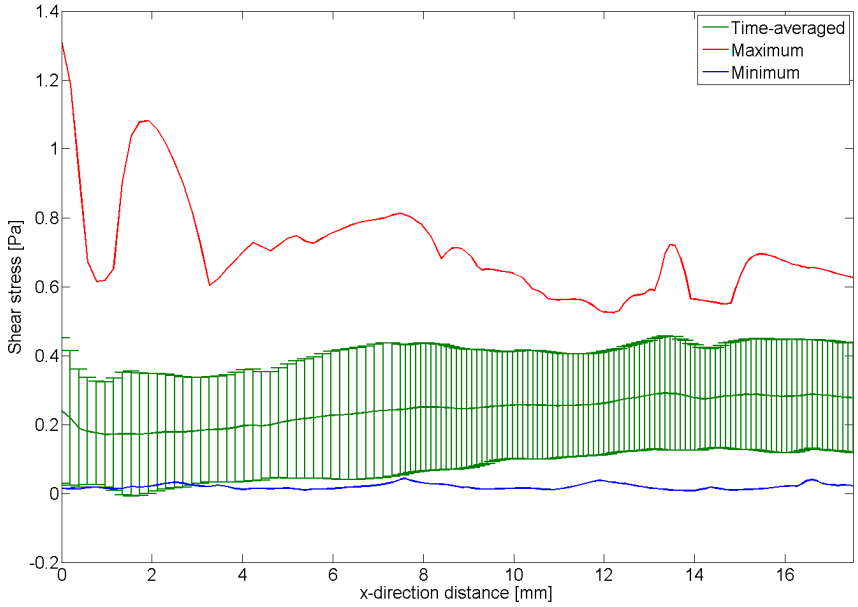

(b) Maximum, minimum & time-averaged shear stress with standard deviation (Pa)

Figure 4.7: Shear stress behaviour for a well at a rocking frequency of 1.167 Hz: shear stress values extracted 0.1 mm above the base of the well (y = 0). Comparative base-scenario shear stress distributions are shown in Figures 2.22 & 2.23.

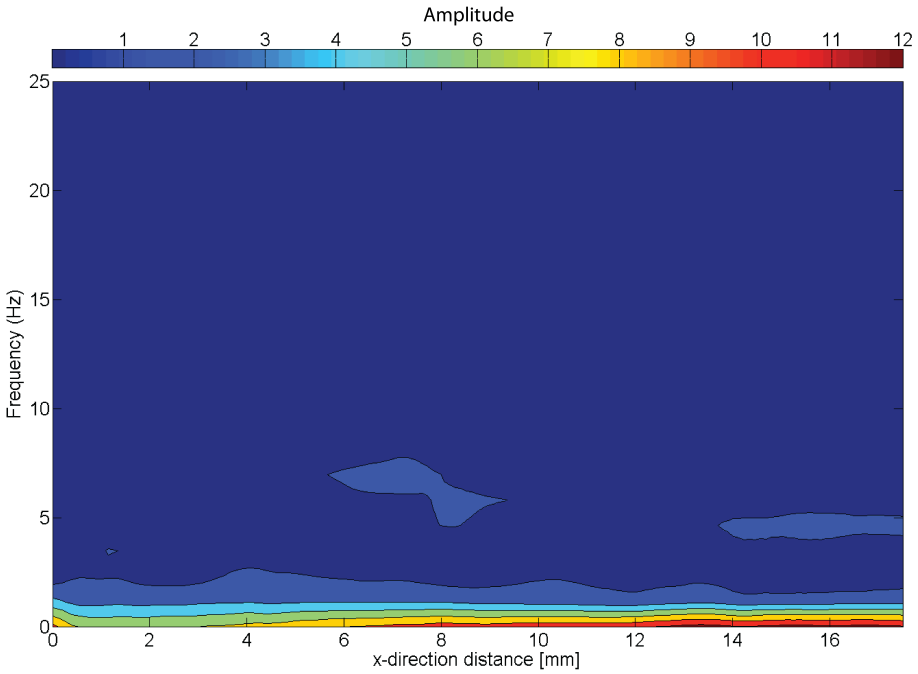

Figure 4.8: Fast fourier transform of shear stress at a frequency of 1.167 Hz: sampling frequency of 51 Hz used. The fast fourier transform shows that frequency amplitude peaks near 1.167 Hz. There are some rises in amplitude between 5 and 8 Hz.

than the predicted maximum of 0.5 Pa. In addition, the profile of the maximum shear stress at 70 cpm is very different to that at 5 cpm.

The stability inherent in these models suggests that they are good indicators of flow behaviour; however improvements of model assumptions could include: a PLIC scheme for the 70 cpm condition, where the shape of the free surface may take more of a wave form; a dynamic contact angle estimate for the 70 cpm condition, as the fluid is moving much more quickly over the well surfaces; and a surface tension scheme for the 5 cpm condition, where inertial effects are reduced.

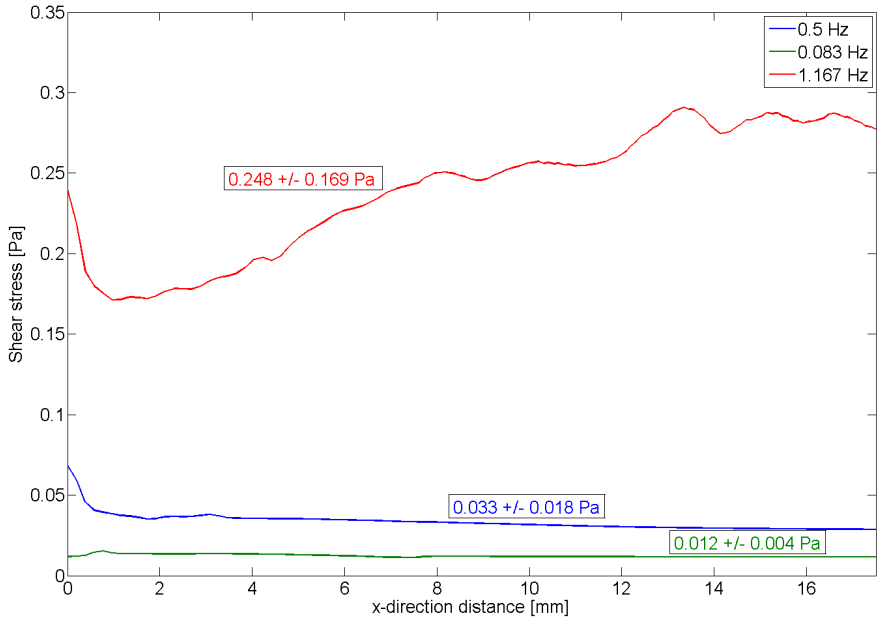

(a) Time-averaged shear stress profiles for each viscosity condition

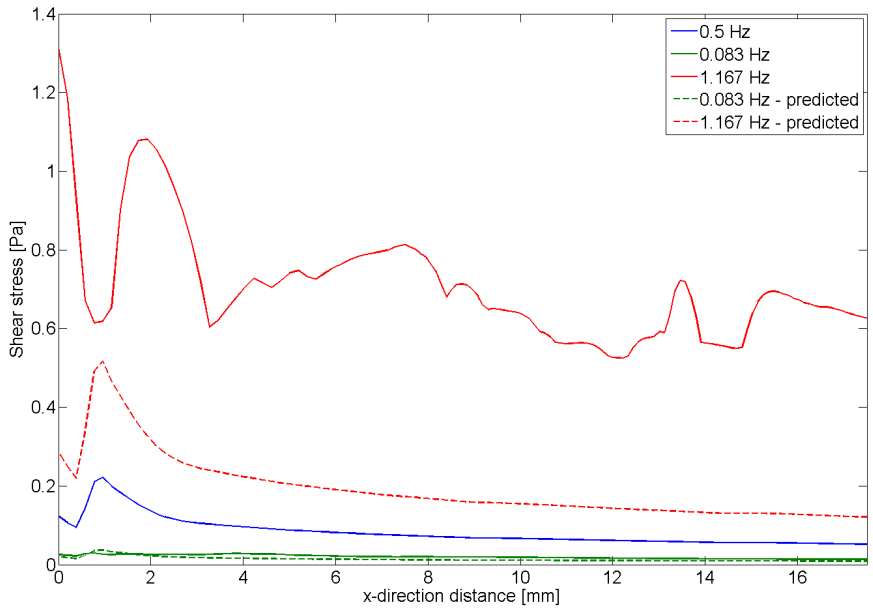

(b) Comparison of predicted maximum shear stress patterns based on an increased viscosity within the base-scenario condition (dashed lines) and maximum profiles determined by fluid dynamics modelling (solid lines)

Figure 4.9: Shear stress comparison for different rocking frequencies (Pa)

4.3 Characterising flow at the platform edge

It is hypothesised that the see-saw rocker platform will not produce the same velocities within wells placed in the centre of the platform as those placed at the edge. The platform is 355 × 355 mm and the largest distance of the centre of a well from the axis of rotation is 160 mm. As angular velocity across all areas of the platform is consistent, fluid velocity is partly driven by displacement from the origin of rotation. Figure 4.10 shows the velocity vectors of a particle (green) at a given displacement d from the origin of rotation. Angular velocity is determined from the velocity vector acting perpendicular to the displacement and is defined by Equation 4.2.

$$V = \omega d \tag{4.2}$$

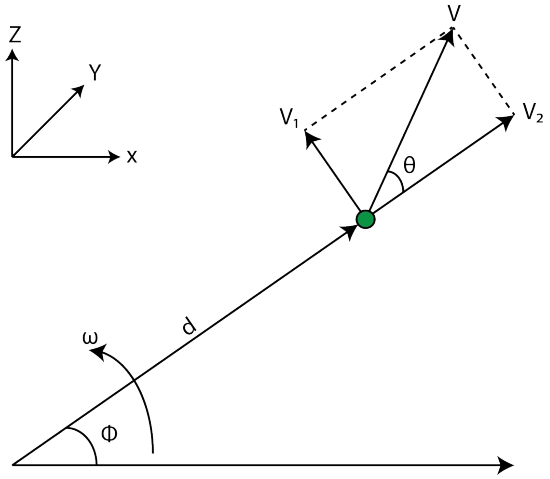

Figure 4.10: Angular velocity: a particle at a given angle Φ and distance d from the centre of rotation is subjected to a velocity magnitude consisting of x- and z-direction velocity components.

Within the rocking system at 0 °, V_1 is equivalent to the Z-component velocity of a fluid particle, and is determined from displacement from the centre of rotation and the angular velocity.

Considering two locations on the rocking platform, 10 mm and 160 m from the centre, it is possible to consider the effect of well position on flow velocities. Based on an oscillation of 30 cpm, the z-component velocity for 10 mm and 160 mm at 0 °,

are 2.4 mm s^{-1} and 41 mm s^{-1} respectively. Assuming that the maximal x-component velocity (V_2) is constant at 80 mm s^{-1}, this would result in a velocity magnitude of 80 mm s^{-1} for the particle 10 mm from the origin, and 90 mm s^{-1} for the particle 160 mm from the origin. In summary, a *circa* 17-fold increase in displacement results in a 12.5 % increase in velocity magnitude.

The assumed increase in velocity magnitude is based on a two-dimensional simplification of the three-dimensional rocker model. This was considered appropriate as velocity in the y-direction is negligible based on findings presented in Chapter 2.

4.3.1 Dimensionless numbers

For the Reynolds, Bond and Weber numbers, all variables remain the same (Chapter 2) except for an estimated 12.5 % increase in velocity magnitude based on conclusions from Section 4.3. As such, based on a maximum of 80 mm s^{-1} obtained from computational and experimental investigations for a well placed on the axis of rotation, for the calculation of the dimensionless numbers, the velocity magnitude was hypothesised to be 90 mm s^{-1} within a well at the edge of the platform.

Dimensionless numbers are reported in Table 4.6. The Bond number is not altered as a velocity term is not present in its calculation, but is shown for clarity.

Dimensionless number	Base-scenario	Platform edge
Reynolds	167	215
Bond	167	167
Weber	4.0	2.4

Table 4.6: Dimensionless numbers for a well at the rocking platform edge

As expected, with an increase in velocity the Reynolds number increases; however at a value of 215 it remains in the laminar region of flow. Additionally, the increase in inertial force driven by the increase in velocity, causes the Weber number to increase from 2.4 to 4.0 as inertial forces continue to dominate surface tension effects.

4.3.2 Model methods & arrangement

A domain was established as described in Section 2.1.5 and a grid size of 1,068,445 cells used as a basis to obtain grid independent results as model characteristics have not changed significantly (Section 2.2.1.4). The centre of the domain was displaced from the centre of rotation by 0.16 m in the x-direction. All other aspects of the arrangement were consistent with the validated base-model presented in Chapter 2.

4.3.3 Model evaluation

The third cycle was used for analysis. This decision was based on the analysis of the base-scenario in Chapter 2 that concluded initial transient effects were negligible after the second complete cycle.

The model was not run for an entire six cycles due to an increased time to completion. To complete three cycles on a 32-core arrangement, 504 hours of computation were required. For comparison, if this was reduced to a 24-core arrangement and increased to six cycles, it was hypothesised that total completion time would have been in excess of 1300 hours, almost a three-fold increase over the base-scenario (Table 2.2).

The large increase in processing time was identified during preliminary models and and the core arrangement increased to 32 from the 16 that were used for the grid independent model. The cause of increased computational cost is difficult to identify; however it could have been due to a larger displacement during each time step, causing an increased number of sweeps for the velocity and pressure solvers for each iteration. In addition, although using a 32-core arrangement over a 16-core arrangement will reduce the time to completion, this will not be linear, as there will be an added factor of memory transfer and communication as each core processed results for its respective segment of the domain.

As per the validated model, convergence criteria and the minimum residual were set at 10^{-18} to ensure that the full 45 iterations were completed for each time step. Inspection confirmed that iterative convergence was achieved within 45 iterations for each time step, encouraging model stability and accuracy.

Average velocity within the displaced model was $40\,\mathrm{mm\,s^{-1}}$ indicating a CFL of 0.19, satisfying a desired condition of 0.25. As with the base scenario, peaks in flow appear

near the media-air interface; however the model remained stable during iteration, and as such, results are considered to be reliable.

4.3.4 Platform edge results

Placing the well at the edge of the rocking platform increased the vertical displacement of the well by c.25 mm and increased the impact of the z-component velocity on the overall velocity magnitude. Inspection shows that velocity magnitude (Figure 4.11) consisted mainly of z-component velocities as x-component velocities are significantly reduced in comparison to the base-scenario (Figures 4.12 & 2.19). The magnitude profile is significantly different. Velocities peak at the well edge (x=0 mm) when t = $0, 1, 2$ s. In addition velocities are not phase symmetric about the centre of the well as the origin of rotation is not directly beneath the well, instead one half of the well is exposed to a larger shear stress than the other, although this difference is small (Figures 4.13 & 4.14).

The change in the profile and magnitude of velocities produced different shear stress patterns to the base scenario (Figure 4.14 & 2.16).

An investigation of time-averaged shear stress indicated that although the shear stress is larger, it follows a similar pattern to the base-scenario, showing little variation across the well diameter, as between 5 and 30 mm, equating to 71 % of the well diameter, time-averaged shear stress remains constant (Figure 4.14). The mean shear stress for the x-direction centre-line is 0.055 ± 0.025 Pa, a 1.61-fold increase on the base-scenario condition. Fluctuations in the time-averaged shear stress are localised around the well edges.

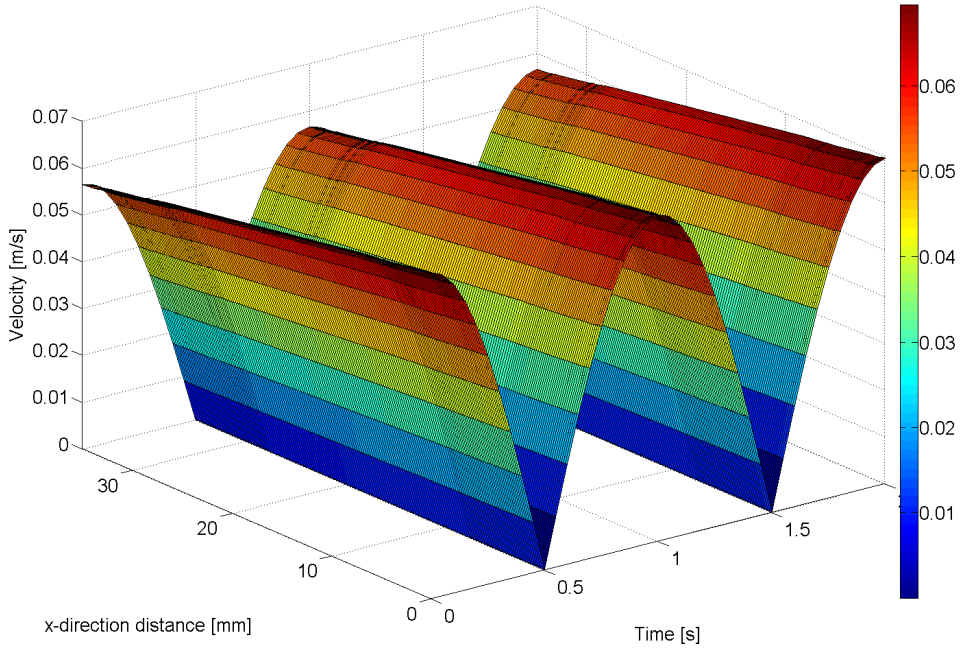

Figure 4.11: Platform edge model velocity magnitude: magnitude of x-component and z-component velocities along the x-direction centre line (y = 0) for the entire diameter of the well. Velocities have been extracted 0.4 mm above the base of the well outside of the no-slip condition. Comparative base-scenario velocity magnitude shown in Figure 2.18.

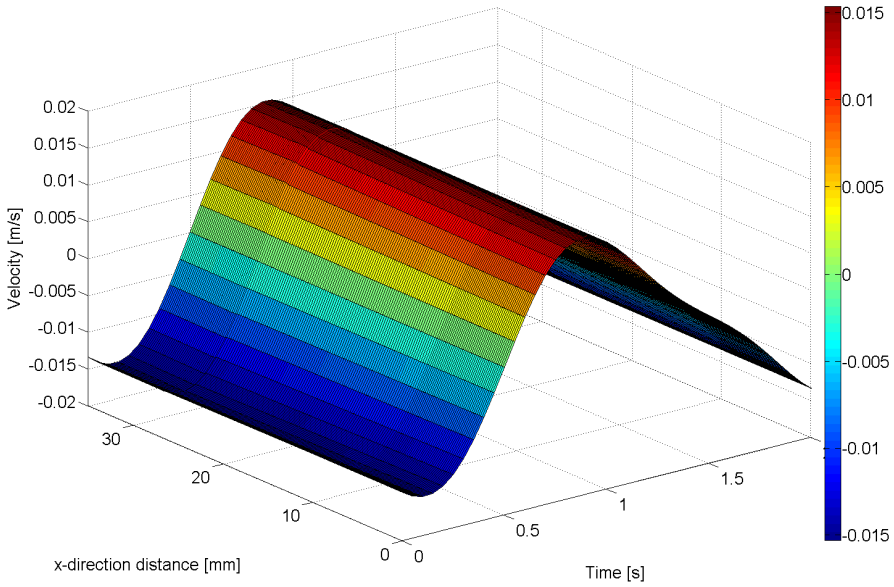

(a) x-component velocities

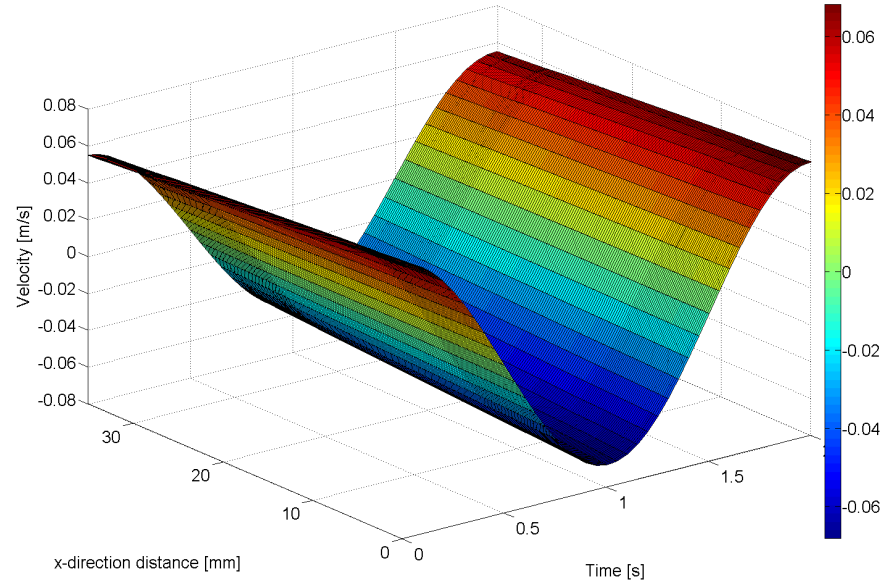

(b) z-component velocities

Figure 4.12: Edge model x- and z-component velocity profiles: velocities have been extracted 0.4 mm above the base of the well outside of the no-slip condition along the x-direction centre line (y = 0) for the entire diameter of the well. z-component velocities are larger than x-component velocities. Comparative x- and z-component velocities for the base scenario are reported in Figure 2.19.

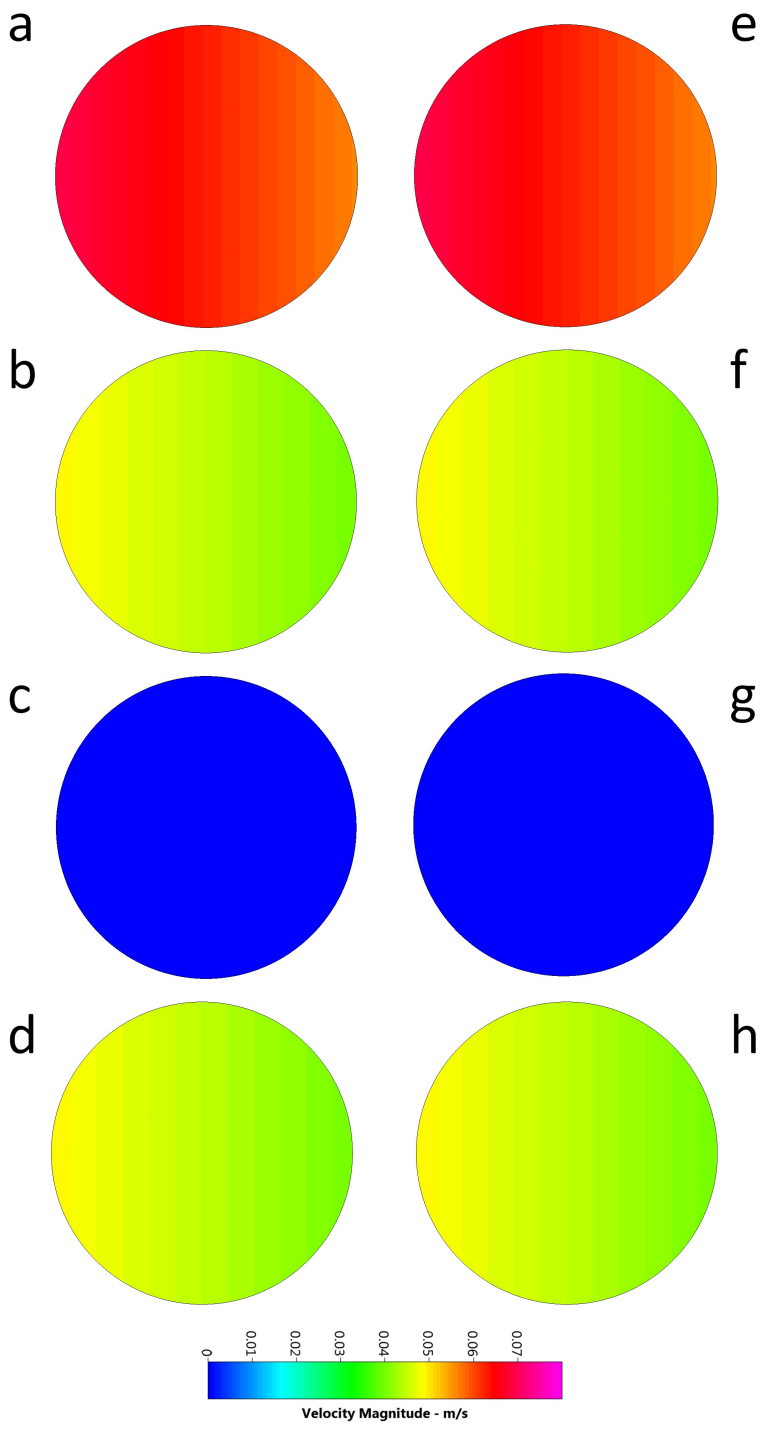

Figure 4.13: Edge model velocity magnitude profiles x-y plane ($\mathrm{m\,s^{-1}}$): velocity magnitude vectors shown at 0.25 s intervals, 0.4 mm above the base. Flow is symmetric about the x-axis. In image 'a' the domain is at the start of its third cycle. The model progresses in 0.25 s intervals [a = 0, b = 0.25 ...], reaching maximal angles of tilt at positions 'c' & 'g'.

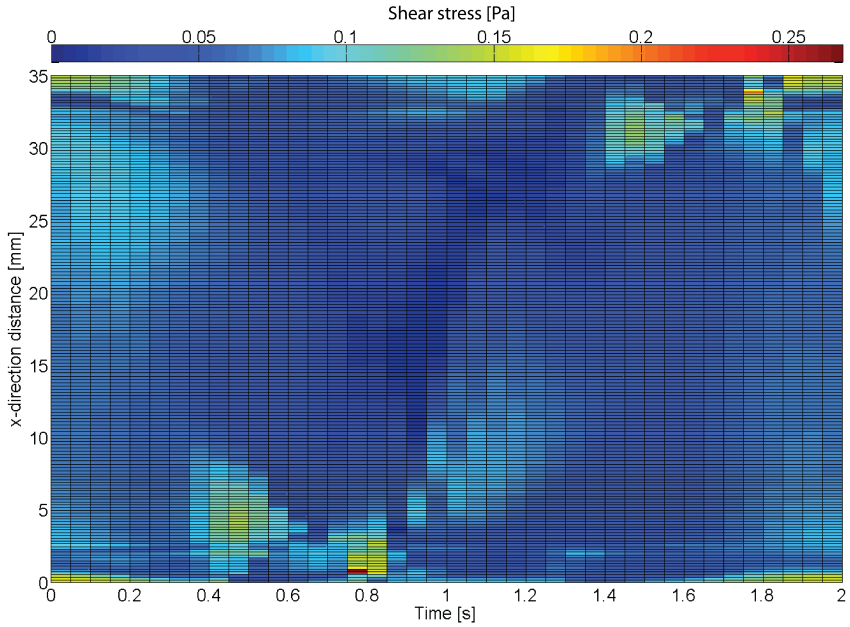

(a) Shear stress distribution along the x-direction centre line (Pa)

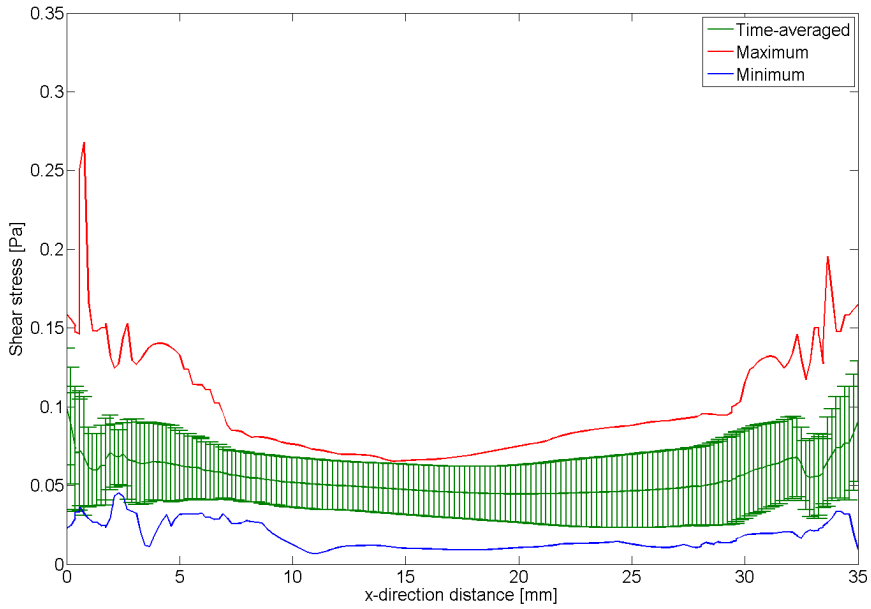

(b) Maximum, minimum & time-averaged shear stress with standard deviation (Pa)

Figure 4.14: Shear stress behaviour for a well placed at the platform edge at a rocking frequency of 0.5 Hz: shear stress values extracted 0.1 mm above the base of the well (y = 0). Comparative base-scenario shear stress distributions are shown in Figures 2.22 & 2.23.

4.4 Discussion

Modelling different parameters has indicated versatility of the see-saw rocker for applying a change in shear stress magnitude at different frequencies. The shear stresses generated under different model parameters are summarised in Table 4.7.

Condition	Mean shear stress (Pa)	Increase
Base-scenario (0.5 Hz, 7.8×10^{-4} mPa s)	0.033 ± 0.018	-
20 mPa s (0.5 Hz)	0.714 ± 0.509	21.64-fold
31 mPa s (0.5 Hz)	1.023 ± 0.702	31.00-fold
0.083 Hz (7.8×10^{-4} mPa s)	0.012 ± 0.004	$\frac{1}{2.72}$-fold
1.167 Hz (7.8×10^{-4} mPa s)	0.248 ± 0.169	13.78-fold
Edge of platform (0.5 Hz, 7.8×10^{-4} mPa s)	0.055 ± 0.025	1.61-fold

Table 4.7: Shear stress summary for varying model conditions

Increasing the viscosity of culture medium using a biologically inert compound, such as CMC, maintained the time-averaged shear stress profile within a culture well while increasing its magnitude. The increase in viscosity was approximately linear with the increase in computed shear stress. The multiple-increase in viscosity on the base-scenario provided a close estimate to computed shear stress. For 20 mPa s and 31 mPa s, estimated mean shear stress is 0.714 Pa and 1.023 Pa respectively.

A well placed at the edge of the platform had a 1.61-fold increase in mean shear stress to 0.055 Pa in comparison to that placed at the centre. Flow was no longer phase-symmetric about the centre point of the well, as the axis of rotation is not located directly underneath. Velocity profiles appeared smoother and shear stress along the x-direction centre line was representative of shear stress across the well in the y-direction. z-component velocities drove overall velocity magnitude, where as at the centre of the platform x-component velocities were largest.

Shear stress is proportional to rocker frequency; although the relationship is not linear. At 0.083 Hz, mean shear stress of 0.012 Pa was just over a third of mean shear stress reported in the base-scenario. At 1.167 Hz mean shear stress increased to 0.248 Pa.

Going forward, improvements in computational capacity and solver code may allow for the refinement of high frequency models where peak velocities require small time

step sizes. This would allow for more cycles of a given condition to be completed, thus assisting in ensuring that initial transient effects are removed as at a higher flow velocity, initial transients may be more prevalent. At high fluid velocities where the free surface is more likely to take a waveform rather than remain horizontal during a cycle, enacting a second order free surface reconstruction scheme may provide more accurate results. However, given the high mesh density, a first order, single line reconstruction scheme is concluded to be a fair approximation.

The range of mean shear stress for all modelled conditions is $0.012 - 1.023\,\text{Pa}$, supporting the see-saw rocker as a versatile tool for experimental research of cell biology. A further model scenario could include modelling a non-Newtonian fluid to determine shear stress distributions for CMC concentrations in excess of $0.5\,\%$. In addition, modelling the effect of Newtonian flow at a range of viscosities at $0.083\,\text{Hz}$ and $1.167\,\text{Hz}$ could assist in determining whether the relationship between shear stress magnitude and viscosity identified at $0.5\,\text{Hz}$ is also present at alternate frequencies.

Chapter 5

Biological materials & methods

The materials and methods detailed within this chapter are applicable to biological investigations presented in Chapter 6.

5.1 Cell culture for mechanical stimulation

5.1.1 Cell extraction

Tenocyte populations were explanted from healthy hamstring tendon tissue samples obtained from anterior cruciate ligament replacement surgery in accordance with methods described by Torricelli *et al.* (277). Tissue samples were obtained from the Musculoskeletal Biobank and were collected with informed donor consent in full compliance with National and Institutional ethical requirements, the United Kingdom Human Tissue Act, and the Declaration of Helsinki (HTA Licence 12217 and Oxford REC C 09/H0606/11).

5.1.2 Long-term cell storage

Cells were prepared for storage as a single-cell suspension in a freezing medium of foetal calf serum (FCS) (Biosera, Ringmer, United Kingdom) with 10 % (v/v) dimethyl sulfoxide (DMSO) (Sigma Aldrich, United Kingdom) and stocks were maintained in a liquid nitrogen cell bank at −195 °C.

5.1.3 Monolayer culture & growth to confluency

Tenocytes were maintained in Dulbecco's modified Eagle medium (DMEM):F12 with HEPES (Lonza, United Kingdom), supplemented with 10 % (v/v) FCS and 1 % (v/v) penicillin-streptomycin solution (PS) (Invitrogen, United Kingdom). Cells were kept at 37 °C in a humidified incubator supplied with 5 % (v/v) CO_2. After reaching confluency, cells were scraped to produce a cell suspension, diluted in DMEM and propogated into new culture dishes (each propagation is a new passage). At passage two, cells were propogated in to six-well plates in preparation for stimulation at passage three when confluent.

All investigations were performed on cells up to passage three which are well characterised with no phenotypic drift of major tendon cell markers. Yao *et al.* (278) have shown that tenocyte markers significantly change after passage five.

5.1.4 Mechanical stimulation

Twenty-four hours prior to stimulation, media was removed and replaced with 2 ml of 0.5 % (v/v) FCS 1 % (v/v) PS, DMEM:F12 added to each well. Low serum was used in order to inhibit usual cell proliferative activity.

5.2 Cell viability

The extent of cell death was measured to investigate the effect of cyclic flow using a live/dead stain (Invitrogen, United Kingdom). Culture medium was removed and cells washed twice with PBS to remove any serum that may interfere with staining. To each well within a six-well plate, 1 µl of Calcein-AM solution (live stain) and 1 µl of ethidium homodimer-1 (dead stain) were added to 1 ml of DMEM:F12. Plates were incubated for 30 minutes at 37 °C and protected from light. After incubation, imaging was completed using a fluorescence microscope (Nikon inverted microscope, Nikon Instruments Inc., United States of America). Calcein-AM is a colourless compound which is cleaved by esterases in living cells to give a green fluorescent dye. Ethidium homodimer-1 is excluded by live cells only.

5.3 Collagen measurement & analysis

Collagen levels were quantified using picrosirius-red dye techniques that binds to collagen structures. These techniques can be used to quantify collagen retained at the cell layer as newly formed extracellular matrix as well as that released into cell culture medium.

5.3.1 Quantification of collagen at the cell layer and within the medium

Collagen quantification was completed with a Sircol assay kit (Biocolor Ltd, United Kingdom). The cell layer was scraped from the culture well at room temperature in 1 ml of a 0.5 M solution of acetic acid with 0.1 mg pepsin, to which 100 µl of acid neutralising reagent (TRIS-HCl & NaOH) was added. 1 ml of culture medium was aspirated from each well. To all samples 200 µl of isolation concentration reagent at 4 °C (polyethylene glycol & TRIS-HCl buffer) was added. After mixing by inversion and overnight incubation on ice, tubes were centrifuged at 12, 000 rpm for ten minutes. Subsequently, 1 ml of supernatant was removed and 1 ml of picrosirius-red dye added. Each tube was mixed by inversion and placed on a lateral shaker at a medium frequency for 30 minutes. Post shaking, tubes were centrifuged at 12, 000 rpm for ten minutes and the supernatant removed. To each tube, 750 µl of acid-salt wash reagent at 4 °C was gently layered on to the pellet, then centrifuged at 12, 000 rpm for ten minutes, and again, the supernatant removed. Finally, 250 µl of alkali reagent (0.5 M sodium hydroxide) was added to each tube, vortex mixed, and 200 µl transferred to a 96-well plate for absorbance measurement at a wavelength of 540 nm on a SpectraMax Plus plate reader (Molecular Devices LLC, California, United States of America).

Quantification of collagen content was achieved using a linear absorbance standard curve. Concentrations of collagen type I were diluted in a 0.5 M solution of acetic acid with 0.1 mg of pepsin or DMEM:F12 (Table 5.1). To each tube 1 ml of picrosirius-red dye was added and the protocol followed as detailed in the previous paragraph. Absorbance values for the standards were plotted in Matlab and a linear trend relationship used to quantify the collagen content of samples.

Collagen (µg)	Collagen (µl)	0.5 M acetic acid with 0.1 mg pepsin / DMEM:F12 (µl)
0	0	100
5	10	90
10	20	80
15	30	70

Table 5.1: Collagen-ECM quantification standard curve formulation

5.3.2 Imaging collagen structures

5.3.2.1 Staining collagen at the cell layer

In order to prepare culture wells for imaging, cells and collagen were fixed in Bouins solution for one hour at room temperature (15 ml saturated aqueous pircric acid, 1 ml glacial acid, 35 % (v/v) formaldehyde in double-distilled H_2O (ddH_2O)). The Bouins solution supernatant was removed and cells subjected to two gentle washes with 2 ml of PBS at room temperature. Picrosirius-red dye was added to the well base and plates were incubated for one hour at 37 °C as the minimum duration to ensure that staining was complete (279). After incubation, the supernatant was removed and the well base washed twice for five minutes with acid (0.5 % (v/v) glacial acetic acid). Finally, the wash was removed and imaging completed using a colour, inverted light microscope (Zeiss Axio Imager, Carl Zeiss AG, Germany).

5.3.2.2 High-level staining maps

Images of entire six-well plates stained with picrosirius-red dye were obtained using a high resolution scanner (Epson Perfection V700 Photo, Seiko Epson Corporation, Japan).

5.4 Glycosaminoglycan measurement & analysis

GAG levels were quantified using a Dimethylmethylene Blue (DMB)-based spectrophotometry assay that required three main reagents as detailed in Table 5.2. The assay was developed from work performed by Farndale *et al.* (280, 281) who specifically looked at musculoskeletal (cartilage) cultures.

The medium was aspirated from the well and the cell layer gently washed twice with 2 ml of PBS at room temperature. Cells and ECM structures were scraped in 1 ml of papain digestion buffer and incubated at 60 °C for two hours with occasional mixing. To a 96-well plate, 40 µl of each sample was added in duplicate, followed by 100 µl of DMB reagent and immediately read at a wavelength of 520 nm.

Quantification of GAG content was achieved using a linear absorbance chondroitin sulphate standard curve. In order to make the standard curve, 5 mg of chondroitin sulphate was vortex mixed with 10 ml of double-distilled H_2O and left to dissolve at room temperature for in excess of one hour. Once mixed, dilutions were made at 0, 50, 125, 250 and 500 $\mu g\,ml^{-1}$ so that a standard curve could be generated. To a 96-well plate, 4 µl of each standard was added in duplicate, followed by 100 µl of DMB reagent and immediately read at a wavelength of 520 nm. To remove 'background' values 100 µl of papain digestion buffer was used as a blank.

Reagent	
Papain digestion buffer	210 mM sodium phosphate buffer (pH 6.8) (328 mg) 1 mM EDTA (29.24 mg) 2 mM dithiothreitol (200 µl of 1 M DTT) 300 $\mu g\,ml^{-1}$ papain (30 mg)
DMB colour reagent	40.55 mM glycine (304 mg) 40.55 mM NaCl (237 mg) 9.5 mM 0.1 M HCl (9.5 ml) 0.0016 % (w/v) 1,9-Dimethylmethylene blue (1.6 mg) pH 3.0, A_{525} 0.31
Standard curve	Chondroitin sulphate (Sigma Aldrich C9819)

Table 5.2: GAG assay reagents: *(values in brackets for 100 ml)*

5.5 Normalisation of extracellular matrix quantifications

Collagen and GAG readings were normalised to double-stranded DNA content as an estimate of cell number. Double-stranded DNA (dsDNA) levels were quantified using a Quant-iT PicoGreen assay (Invitrogen United Kingdom); a fluorescent nucleic acid stain

that utilises a spectrofluorometer and fluorescein excitation and emission wavelengths (490 nm and 540 nm).

The medium was aspirated from the well and the cell layer washed twice with PBS before being scraped in 1 ml of PBS. Subsequently, the liquid was sonicated for 15 seconds to disrupt cells (Sonicator W-225, Heat Systems-Ultrasonics Inc., USA).

The dsDNA reagent was thawed at room temperature from 4 °C for one hour and 10 µl diluted with 1.99 ml of TE buffer (10 mM Tris-HCl, 1 mM EDTA, pH 7.5), while being protected from light.

Lamba DNA standard was diluted in TE buffer to a concentration of 0.2 µg ml^{-1} and 2.0 µg ml^{-1} to make the standard curve (Table 5.3).

To a 96-well plate, 10 µl of each sample was loaded in duplicate, then to each sample, 100 µl of TE buffer was added. To create a blank 10 µl of PBS and 100 µl of TE buffer was added to a well.

For each sample and standard, 100 µl of the dsDNA diluted reagent was added. All samples were protected from light and placed on a lateral shaker at a medium frequency for 30 minutes at room temperature.

Post-shaking, fluorescence was read using: excitation 490 nm; emission 540 nm; cut off filter 530 nm; and a gain of 1500, using a Fluostar Optima plate reader (BMG Labtech GmbH, Allmendgruen, Germany).

Fluorescence values for the standards were plotted in Microsoft Excel and a linear trend relationship used to quantify the dsDNA content of samples.

dsDNA (ng)	2.0 µg ml^{-1} dsDNA (µl)	0.2 µg ml^{-1} dsDNA (µl)	1× TE buffer (µl)	PBS (µl)
0	0	0	100	10
0.2	0	1	99	10
2	0	10	90	10
4	0	20	80	10
10	5	0	95	10
20	10	0	90	10
40	20	0	80	10

Table 5.3: PicoGreen standard curve summary: quantities were loaded directly in to a 96-well plate for fluorescence measurement.

5.6 Bovine digital tendon extraction

Bovine hooves, obtained from the local abattoir immediately after sacrifice were stored at 4 °C for 24 h prior to dissection. An incision was made along the posterior surface of the bovine hoof to expose the superficial flexor tendon. The tendon was severed just past the point of transition into the deep flexor tendon and the sheath removed with a scalpel. A longitudinal cross section was cut from the tendon for immunohistochemistry (Section 5.7.2.1). Cross sections were taken from the centre of the tendon length and at the middle of the tendon depth.

5.7 Primary cilia abrogation & immunohistochemistry

5.7.1 Abrogation of the primary cilium in cell culture

Abrogation of primary cilia in tenocyte cultures was achieved using chloral hydrate (Sigma Aldrich, United Kingdom). Chloral hydrate was dissolved in ddH_2O at 37 °C using a magnetic stir bar to create a 1000× 4 mM concentration. Stocks were kept at −20 °C, thawed in a 37 °C water bath and 2 µl diluted in 2 ml of 10 % (v/v) FBS, DMEM:F12. The chloral hydrate/DMEM solution was subsequently added to each well containing tenocytes.

After incubation for 24 hours at 37 °C the medium containing chloral hydrate was removed from each well, washed twice with DMEM:F12 and 2 ml of 10 % (v/v) FBS, DMEM:F12 added. Primary cilia are reported to be abrogated from a culture for 24 hours following chloral hydrate treatment (120).

5.7.2 Immunostaining of primary cilia

α-tubulin is the primary protein found in the central structure of cilia and as such staining tenocytes using an α-tubulin antibody allowed for imaging of primary cilia in tissue and tenocyte cultures.

5.7.2.1 Tissue section immunohistochemistry

Bovine flexor tendon tissue was harvested (Section 5.6) and structures cross-linked by fixation in 10 % (v/v) formalin, ddH_2O for 14 days. Sections were cut into 2 mm × 2 mm × 3 mm pieces, embedded in hot wax and then cooled. Once solidified, 20 micron

slices of wax and tendon tissue were made using a microtome. Slices were placed on individual glass slides and baked for two hours at 60 °C, followed by one hour at 37 °C in an oven.

Wax was removed by placing slides in two successive five minute clearene baths, followed by three minutes in 100 % ethanol, three minutes in 90 % (v/v) ethanol in ddH_2O, and 30 minutes in 3 % (v/v) hydrogen peroxide 97 % (v/v) methanol. A gentle wash was completed by pipetting ddH_2O on to each slide for three minutes. This was repeated ten times to ensure all chemicals were removed.

Non-specific binding sites were blocked by applying 5 % (v/v) horse serum 0.1 % (v/v) TritonX in PBS to tissue sections for 30 minutes. The primary antibody, acetyl-α-tubulin (Lys40) (D20G3) rabbit antibody (New England Biolabs, United Kingdom) diluted 1:50 (v/v) in 1 % (v/v) horse serum 0.1 % TritonX (v/v) in PBS was applied to all tissue sections and incubated overnight at 4 °C in a humidified incubator.

The following day, the secondary antibody, anti-rabbit IgG (H+L) (New England Biolabs, United Kingdom), was diluted 1:100 (v/v) in PBS, with a 1:500 (v/v) concentration of DAPI, added to each tissue section, protected from light, and incubated for 30 minutes at room temperature.

Finally, tissue sections were gently washed twice with PBS, 10 µl of mounting medium added, and a coverslip applied. Coverslips were sealed with clear nail varnish to prevent mounting media evaporation and sample de-hydration.

5.7.2.2 Cell monolayer immunohistochemistry

All culture medium was removed and the cell layer gently washed twice with 2 ml of PBS at room temperature. To fix the cells, 2 ml of 10 % (v/v) formalin (Fisher Scientific, United Kingdom) in ddH_2O was added to the monolayer for 30 minutes at room temperature. After fixation, the formalin was removed and cell layer gently washed twice with PBS. In order to permeabilise the cell membranes, a soft detergent, TritonX-100 (Sigma Aldrich, United Kingdom) was applied to the cell layer for six minutes. The TritonX-100 was subsequently removed and the cell layer washed twice with PBS at room temperature. To block non-specific binding sites, 1 ml of horse serum (Sigma Aldrich, United Kingdom) was added to the cell layer for 30 minutes. Excess serum was then removed and a 0.5 cm diameter hydrophobic barrier circle created in the area of interest using an ImmEdge pen (Vector Labs, United Kingdom). Within the

circle, 50 µl of 1:50 (v/v) dilution of acetyl-α-tubulin (Lys40) (D20G3) rabbit antibody (New England Biolabs, United Kingdom) in 0.2 % (v/v) TweenX-20 in PBS (PBST) was added and incubated at 4 °C overnight. Parafilm was used to ensure that the primary antibody did not evaporate from the cell layer. The following day, the cell layer was then washed three times with 2 ml of PBS at room temperature to remove any unbound primary antibody. A 1:100 (v/v) dilution of anti-rabbit IgG (H+L) (New England Biolabs, United Kingdom) in PBS was mixed with a 1:500 (v/v) dilution of DAPI (Sigma Aldrich, United Kingdom) in PBS and added to the cell layer for 30 minutes and protected from light. The cell layer was subsequently washed twice with 2 ml of PBS at room temperature and images taken using a fluorescence microscope (Nikon inverted microscope, Nikon Instruments Inc., United States of America).

5.8 Matrix immunohistochemistry

Matrix immunohistochemistry staining and imaging was completed for tenocyte monolayers using the same protocol outlined in Section 5.7.2.2 adapted for use with the primary and secondary antibodies detailed in Table 5.4 as required.

Structure	Primary antibody	Secondary antibody
Collagen I	Human raised in rabbit monoclonal (2150-0020)	Anti-rabbit IgG rhodamine raised in goat (red) (D20G3)
Collagen VI	Human raised in mouse polyclonal (AB49273)	Anti-mouse IgG fluorescein raised in goat (green) (AP124R)
Elastin	Human raised in mouse monoclonal (AB9519)	Anti-mouse IgG fluorescein raised in goat (green) (AP124R)
Fibrillin-I	Human raised in mouse monoclonal (MAB2502)	Anti-mouse IgG fluorescein raised in goat (green) (AP124R)
Connexin-32	Human raised in mouse monoclonal (MAB3069)	Anti-mouse IgG fluorescein raised in goat (green) (AP124R)

Table 5.4: Pericellular matrix immunohistochemistry primary and secondary antibodies: all antibodies were purchased from EMD Millipore Corporation, USA, except for the elastin primary antibody (Abcam, United Kingdom) and the collagen type-I primary antibody (ABD Serotec, United States of America).

5.9 Kinase, transcription factor & gene expression

Expression of tendon-relevant kinases, transcription factors and genes were investigated using qPCR through a collaboration with Dr. Andrew Jones and Dr. Philippa Hulley (Nuffield Department of Orthopaedics, Rheumotology & Musculoskeletal Science). All RNA extraction and qPCR reactions were performed by Dr. Andrew Jones. Tenocytes were subjected to the same mechanical stimulation preparation methods detailed in Section 5.1.

RNA was extracted from tenocytes using the standard Qiagen extraction kit protocol (Qiagen, Netherlands). A reverse transcriptase reaction was performed using a superscript III Invitrogen kit (Invitrogen, United States of America) with random hexamers to make cDNA, which was used as a template for SYBR Green qPCR. 18s RNA was used as an internal reference for all PCR reactions. Relative quantification (RQ) was determined using the comparative Ct method. For each gene analysed, samples were completed in triplicate and results were averaged for two patients.

ERK activation was measured by western blot on lysed cells using antibodies specific for phosphorylated ERK 1 and 2. Blots were stripped and re-probed with pan ERK antibody.

5.10 Statistical analysis

Values are presented as mean ± S.E.M. unless otherwise stated. n is the number of experiments. All statistical analysis was completed within Prism (GraphPad Software Inc., California, USA) using an independent-samples t-test. Results are significant where p was calculated to be less than 0.05.

Chapter 6

Application in tendon mechanobiology: validation & basic science

To ensure the use of the see-saw rocker is valid for biological investigations, tenocytes, exemplary to the musculoskeletal system, were subjected to a variety of loading regimes and their response investigated in order to achieve objective five, six and seven of this thesis (Section 1.9). These investigations were performed at a variety of model parameters to identify whether the model arrangement may be used for the study of a wide-range of tenocyte behaviours.

Within this chapter several investigations are presented. Firstly, preliminary investigations that were performed to establish the effect of a rocking frequency of 0.083 Hz on collagen and glycosaminoglycan secretion using biochemical assays. Subsequently, these findings are used to formulate a system-approach model for predicting collagen secretion at a range of fluid-induced shear stresses at a rocking frequency of 0.5 Hz . Interrogation of model predictions was completed using a combination of biochemical assays and immunohistochemistry. A system approach was developed to act as a foundation for building up future signal and investigation complexity with ease. Additionally, the effect of various shear stress magnitudes on tenocyte alignment and elongation was evaluated using a custom image intensity-based algorithm. Furthermore, evidence of the primary cilium within tenocyte tissue and cell cultures is presented and finally, collaborative research completed to investigate the effect of cyclic flow on tenocyte:

kinase signalling; transcription factor activation; and gene activation is presented.

6.1 Fluid flow affects tenocyte protein secretion

6.1.1 Preliminary investigations - continuous stimulation *vs.* rest insertion

Two stimulation protocols were designed taking into account previous tenocyte fluid flow investigations (Section 1.6.2). One of the loading regimes was a low-frequency seven-day shear stress stimulation henceforth known as 'continuous stimulation', whereas the other, an intermittent application of flow over two days, was aimed at identifying whether rest-insertion, shown to enhance osteogenesis (282), had an impact on tenocyte matrix formation, and is henceforth known as 'short-interval stimulation'. Both protocols were completed at a rocking frequency of 0.083 Hz. Computational modelling has indicated mean shear stress of 0.012 Pa at a frequency of 0.083 Hz, which was within estimated *in vivo* ranges and previous tenocyte *in vitro* investigations (Section 1.6.2).

6.1.1.1 Stimulation protocols

Human tenocytes (up to passage three) were grown in a monolayer in a six-well plate until confluence was achieved (1-2 weeks growth) and prepared for mechanical stimulation per methods described in Section 5.1. The six-well plate was placed centrally on the see-saw rocker platform, and subjected to 0.083 Hz at 37 °C in a humidified incubator for a duration dictated by the stimulation regime detailed in Table 6.1.

For the continuous stimulation regime, after day three, culture medium was refreshed. Used culture medium was retained and frozen at −20 °C for matrix quantification biochemical assays.

All biochemical assays were performed at the end of respective stimulation regimes after a period of rest (Table 6.1) at 37 °C in a humidified incubator to allow for cell response to be of a suitable magnitude to ensure differences were measurable. Collagen, GAG and dsDNA biochemical assays were subsequently performed. Healthy cells from two patients were tested (n = 5).

Stimulation regime	Protocol
Continuous stimulation (8 days)	7 days stimulation
	24 hours rest
	Complete assay
Short-interval stimulation (2 days)	4 hours stimulation
	20 hours rest
	4 hours stimulation
	20 hours rest
	Complete assay

Table 6.1: Continuous stimulation and short-interval stimulation protocols

6.1.1.2 Results

Continuous stimulation over seven days produced a significant increase in collagen secretion both retained in the cell layer ($p < 0.0001$) and released into the culture medium ($p < 0.0001$) (Figure 6.1). At the cell layer collagen secretion showed a 4.24-fold increase from 6.50 $\mu g\,ng^{-1}$ under control conditions to 27.59 $\mu g\,ng^{-1}$ in tested wells. Within the culture medium this was reduced to a 2.86-fold increase from 7.67 $\mu g\,ng^{-1}$ to 21.90 $\mu g\,ng^{-1}$. Analysis of GAG secretion showed no difference in the average content for test and control conditions ($p = 0.0707$) (Figure 6.1). Measurement of dsDNA content indicated that control conditions have 193 % more dsDNA than test wells (Figure 6.2).

Short-interval stimulation showed a significant increase in the secretion of: collagen at the cell layer ($p < 0.0001$); collagen released in to the culture medium ($p < 0.0001$); and GAG at the cell layer ($p < 0.0001$) (Figure 6.1). Collagen retained at the cell layer exhibited a 2.56-fold increase in test wells in comparison to controls. In addition, collagen secreted into the culture medium exhibited a 2.07-fold increase in comparison to controls. In tested cultures, collagen at the cell layer and within the medium were 19.09 $\mu g\,ng^{-1}$ and 7.13 $\mu g\,ng^{-1}$ respectively, indicating that at a low frequency of 0.083 Hz, newly secreted collagen is more likely to be retained at the cell layer as newly formed matrix, rather than be released into the culture medium. GAG retained at the cell layer exhibited a significant 2.48-fold increase in test wells in comparison to controls. GAG content under test conditions was 9.19 $\mu g\,ng^{-1}$, whereas control conditions

was $3.99\,\mu g\,ng^{-1}$. Measurement of dsDNA content indicates that control conditions have 110 % more dsDNA than test wells (Figure 6.2).

When compared with short-interval stimulation, continous stimulation caused tenocytes to secrete significantly more collagen at the cell layer ($p < 0.0001$), within the media ($p < 0.0001$) and also to secrete significantly more GAG ($p < 0.0001$) (Figure 6.3); however this increase was not consistent with an increase in the number of applied cycles (Figure 6.4).

6.1.1.3 Discussion

Prior to normalisation of results, all GAG, collagen matrix and media samples indicated that collagen and GAG content in control conditions was larger than stimulated cultures. Double-stranded DNA quantification signified that, although wells in both control and stimulated dishes were grown to 100 % confluency, control conditions showed a larger 'cell number', and as such, collagen production per cell was lower when compared to stimulated conditions (Figures 6.2 & 6.1). Differences were not due to cell necrosis as live/dead images confirmed viability under test conditions (data not shown).

It is hypothesised that fluid-flow stimulation allows tenocytes to become more 'tendon-like', differentiating rather than proliferating (209). In control conditions, the lack of stimulus causes tenocytes to continue proliferative activities, even with a low amount of serum.

Short-interval stimulation cells were subjected to a total of eight hours of rocking (2,400 complete cycles) compared to continuous stimulation cells that were subjected to seven days of rocking (168 hours / 50,400 complete cycles). It is clear that an increased duration of stimulus caused a significant increase in the secretion of matrix proteins per cell (Figure 6.3) ($p < 0.0001$). Continuous stimulation cells secreted more collagen, both as matrix at the cell layer and that which was released into the culture medium, as well as more GAG as matrix at the cell layer, than short-interval stimulation; however the increase was not proportional to the number of cycles that cells were stimulated for (50,400 *vs.* 2,400) (Equation 6.1) (Table 6.2).

$$Q_{C(S)} = Q_{SI(C)} + 50,400 \times \frac{Q_{SI(S)} - Q_{C(C)}}{2,400} \tag{6.1}$$

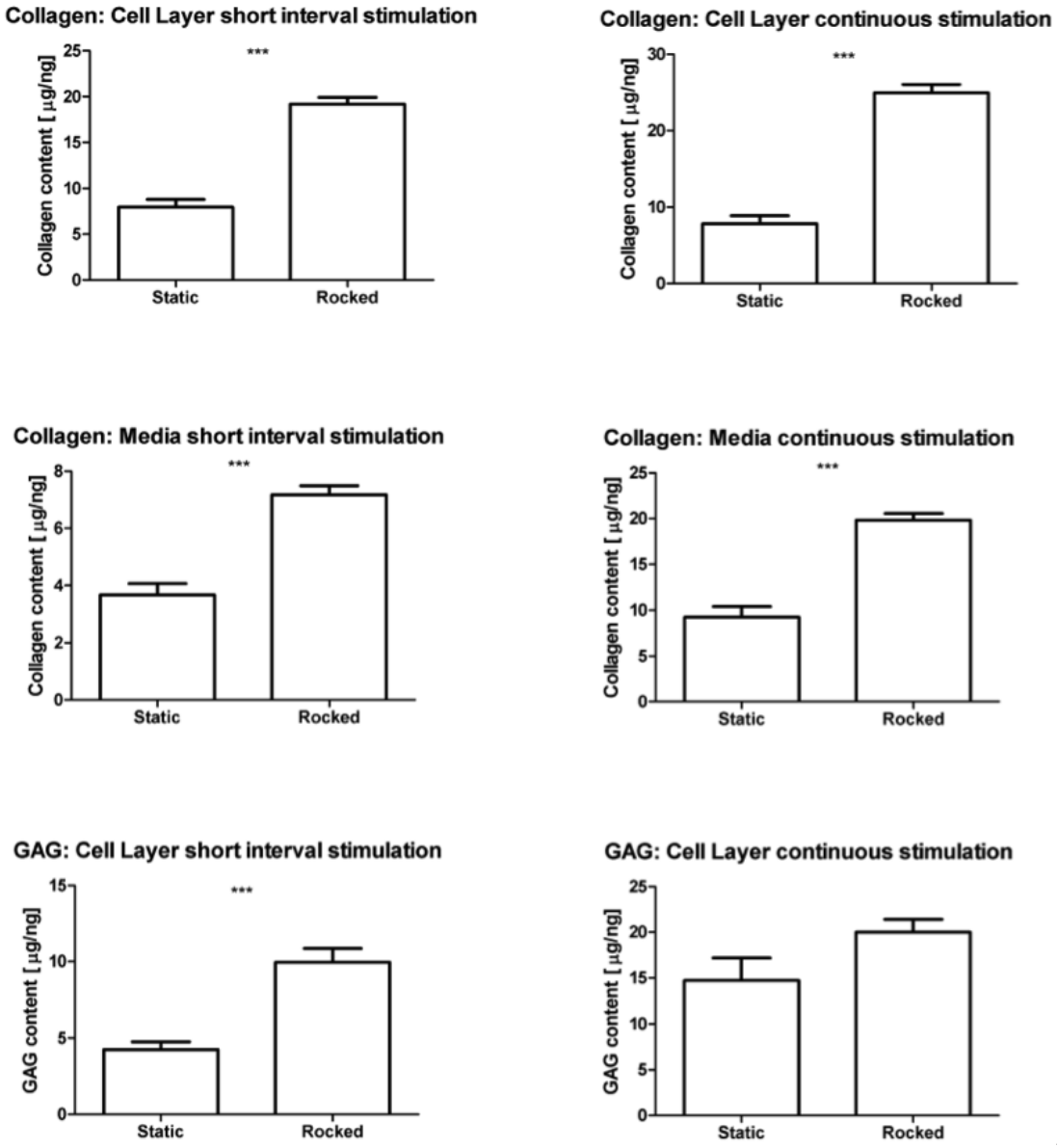

Figure 6.1: Collagen and GAG secretion is significantly up-regulated following rocker stimulation: collagen secreted and bound to the cell layer as newly formed matrix is significantly up-regulated after short-interval and continuous loading regimes (top row). In addition, collagen secreted and released into the culture medium is significantly up-regulated for both loading regimes (middle row). GAG secretion is significantly up-regulated under short-interval stimulation conditions, but not during continuous stimulation (bottom row). *** = ($p < 0.0001$). Results are normalised to ng of dsDNA (Figure 6.2).

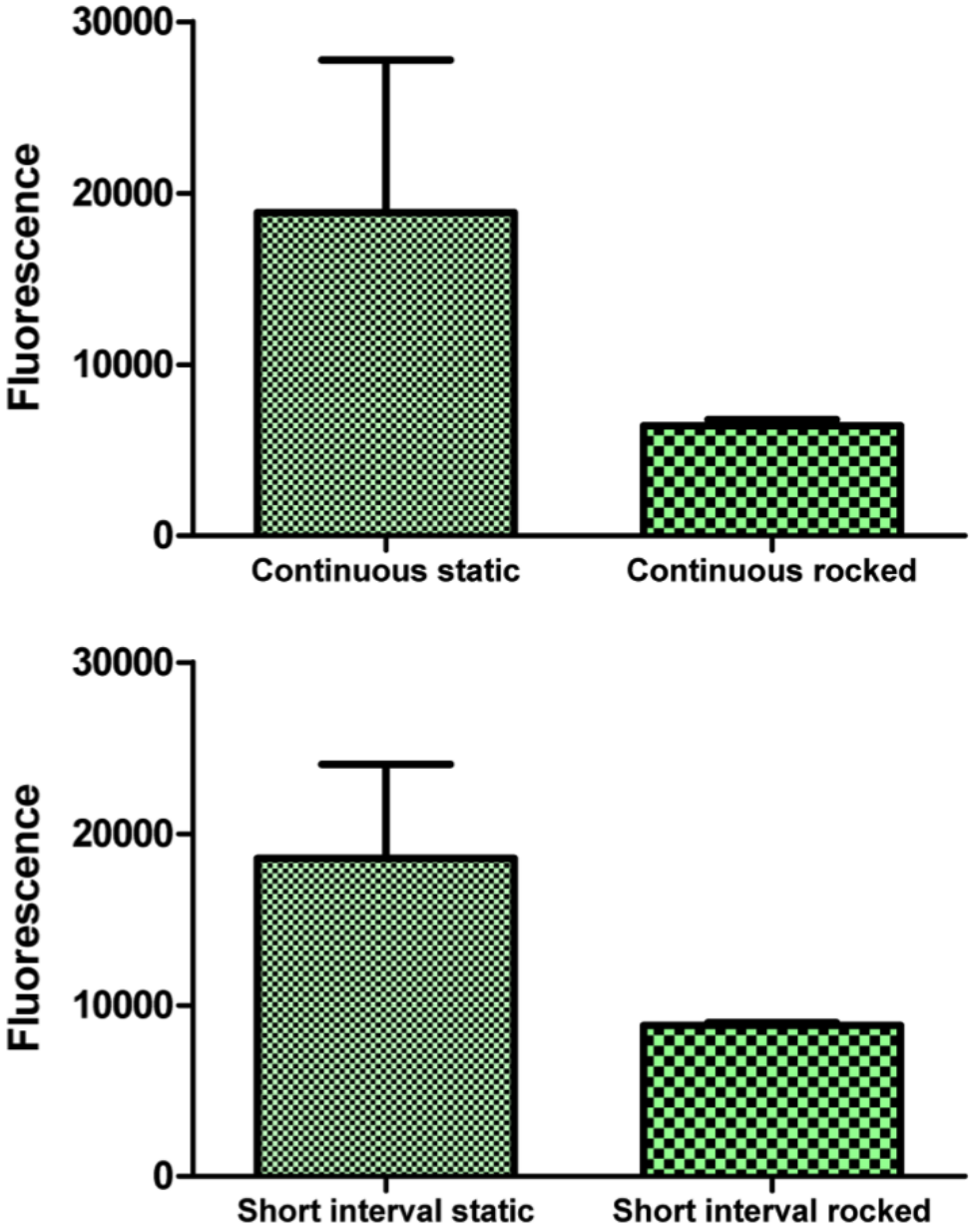

Figure 6.2: dsDNA content: control groups for both short-interval stimulation and continuous stimulation show a larger dsDNA fluorescence in comparison to test groups. Statistical analysis has not been performed as results are obtained in duplicate.

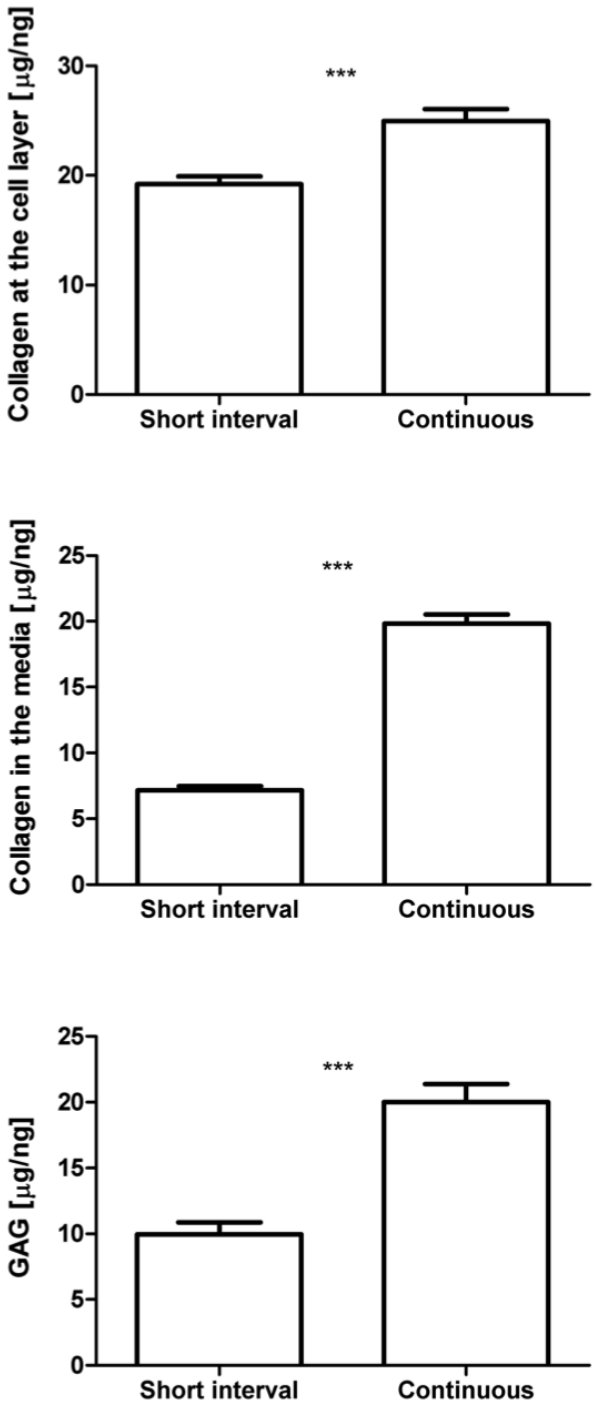

Figure 6.3: Short-interval *vs.* continuous stimulation: continuous stimulation produces significantly more matrix in comparison to short-interval stimulation for collagen at the cell layer (top), collagen released into the medium (middle) and GAG at the cell layer (bottom) ($p < 0.0001$). Results are normalised to ng of dsDNA (Figure 6.2).

where $Q_{C(S)}$ and $Q_{SI(S)}$ are the quantities of collagen after stimulus and $Q_{C(C)}$ and $Q_{SI(C)}$ are the quantities of collagen in control conditions, for continuous and short-interval stimulation respectively.

Matrix component	Increase in secretion
Collagen at the cell layer	1.30-fold
Collagen released into the medium	2.77-fold
GAG at the cell layer	2.01-fold

Table 6.2: Quantification of collagen and GAG secretion normalised increase for continuous stimulation *vs.* short-interval stimulation

Rest-insertion may have a very positive impact on the rate of collagen and GAG secretion in human tenocytes, as collagen secretion per cycle is higher in short-interval stimulation over continuous stimulation. This may be so that the cell has functionality to respond to a given mechanical stimulus. In addition, a review of the literature indicated that cilia extend during periods of stress deprivation, and suggested that a longer cilium may 'amplify' a given mechanotransductive signal when a stimulus is applied (Section 1.3.3). Periods of rest would allow cilia extension and later detection of a stimulus when flow is started again.

Experiments were performed without the addition of supplementary ascorbic acid, known as essential for the synthesis of collagen. Thus, results are representative of the secretion of collagen pre-synthesised, or collagen synthesised using ascorbic acid already present in the cell or media. Importantly, results presented may be a rate-limited view of collagen secretion and the addition of supplementary ascorbic acid is essential for further experiments. This may explain why continuous stimulation tenocytes did not secrete more collagen per cycle than short-interval stimulation tenocytes. For all future collagen investigations, ascorbic acid and proline was supplemented to culture medium at a concentration of $50\,\mu g\,ml^{-1}$ to ensure that the rate of collagen secretion was not limited.

The secretion of matrix at the start of the stimulus may be a form of the pericellular matrix. Cells may rapidly produce PCM as an attempt at mimicking their *in vivo* environment. Once a layer of PCM is secreted, ECM is subsequently secreted and the rate of ECM secretion is reduced in comparison to the PCM. This two-rate hypothesis

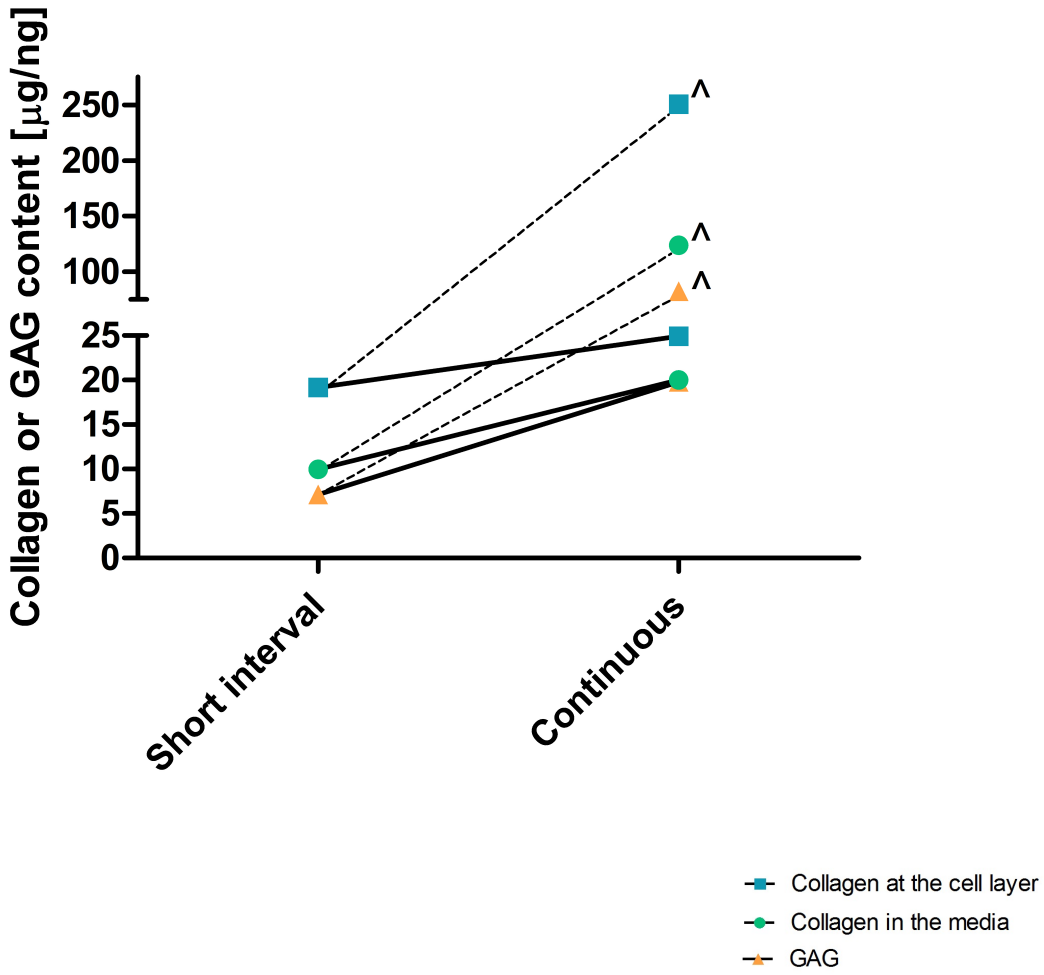

Figure 6.4: Comparison of matrix secretion for continuous stimulation and short-interval loading regimes with predicted secretion values: an increased period of stimulus increases secretion of all matrix components investigated. A calculated increase in short-interval secretion results generates predicted values much larger than experimental results (Equation 6.1). Collagen at the cell layer = blue; collagen released into the media = green; GAG = orange. Predicted values are denoted by $\wedge$ and are based on the number of cycles (Equation 6.1).

may explain why the increase in matrix production across the two stimulation regimes is not as expected. Pericellular matrix immunohistochemistry was completed after tenocyte stimulation at varying shear stress magnitudes.

Cell response may not be proportional to the duration of stimulus and a large increase in matrix secretion may be achieved in a short period of time. Only a short duration of stimulus is required for cell signalling (283). Additionally cells may only detect the first part of the stimulus and then become desensitised to the fluid force (284). There may be a mechanotransducer that detects the fluid force at first, causing a large initial response, and then subsequent flow detection may be performed by a secondary mechanotransducer that does not detect flow as effectively.

It may be argued that the increase in collagen and GAG secretion is due to the circulation of the culture medium within the dish caused by the rocker motion, thus increasing the rate of transport of key nutrients to cells and increasing the rate at which they synthesise proteins. This is not considered to be the reason for the increase in matrix secretion, as the rate of diffusion of metabolites and waste products is widely recognised as sufficient in monolayer cultures.

6.1.1.4 Conclusion

In conclusion:

- Preliminary investigations have confirmed that the see-saw rocker model is a successful *in vitro* stimulation tool for fluid shear stress experiments.
- Extracellular matrix secretion per cell significantly increases with application of fluid-induced shear stress at 0.012 Pa.
- The rate of matrix secretion as a result of fluid-induced shear stress does not appear to be linear, but requires further investigation.
- The measured secretion occurs both during stimulation and at rest.
- Fluid flow stimulation may be encouraging cell differentiation rather than cell proliferation, indicated by reported dsDNA numbers.

6.2 Predicting the effect of fluid flow on tenocyte collagen secretion

Preliminary investigations have indicated that human tenocytes are responsive to fluid-induced shear stress (Section 6.1). This finding supports gene expression and calcium signalling work reported in the literature (Section 1.6.2). Tendon homeostasis is a fine balance between damage and repair, the latter managed by tenocytes embedded between collagen fibres.

For tenocytes to be able to repair damaged tissue, or remodel existing fibrils, they must either be aware that repair or remodelling is required, or respond directly to a primary signal that caused the initial damage or a secondary signal induced by damage. These responses may be induced by either chemical or mechanical signals.

Thus, it was hypothesised the tenocyte rate of collagen secretion would increase with an increase in the magnitude of applied shear stress.

Within this section of the chapter, a system approach to predicting tenocyte collagen secretion is presented.

Validation is performed using further biological experiments and the system's capabilities evaluated. Modelling is focused on collagen secreted and released in to the culture medium as preliminary investigations have indicated a clear difference between test and control conditions (Figure 6.1), and a clear difference between two testing regimes (Figure 6.4). Furthermore, collagen detected within the medium is entirely a result of experiment conditions, where as some of the collagen at the cell layer may have been manufactured and secreted prior to stimulus.

6.2.1 A mathematical model

It was hypothesised that the rate of collagen secretion is affected by the magnitude of shear stress and the type of the stimulus signal, *i.e.* rest insertion or continous stimulation (Equation 6.2).

$$\frac{dQ}{dt} = f(\tau, K) \tag{6.2}$$

where $\frac{dQ}{dt}$ is the rate of protein secretion, τ is the average shear stress, K is the stimulus signal.

An applied shear stress τ with frequency ω and amplitude A in the form of a sine wave can be transformed using fourier analysis to obtain a periodic signal consistent with stimulation protocol design considerations, such as rest-insertion. The conversion of the signal to a rate of protein secretion is dependent on understanding the effect of signal frequency ω, shear stress amplitude A and the lag in matrix production after a signal, which may be represented by a phase shift ϕ. The integration of the computed secretion rate results in a predicted quantity of protein secretion (Figure 6.5).

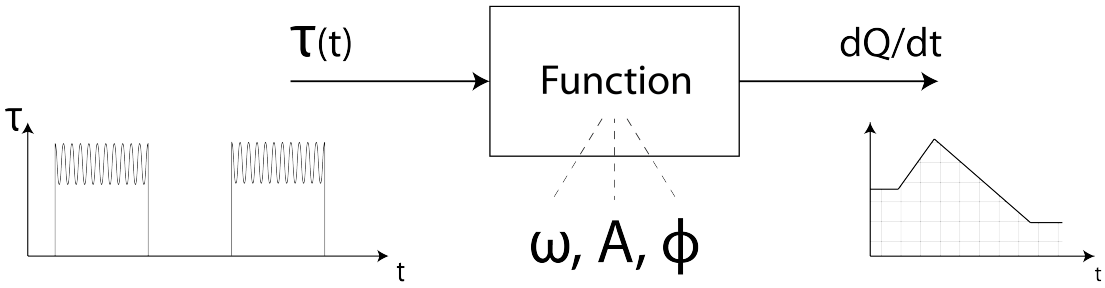

Figure 6.5: System approach to determining the relationship between shear stress and secretion rate: the application of a shear stress with an amplitude A, frequency ω for varying durations over a time period is converted into a rate of collagen secretion.

The addition of multiple sine wave inputs representing a variety of model conditions can be achieved using the Euler relationship, where exponential relationships are combined; however further experiments are required to fully understand the function that transforms a shear stress input to a rate of secretion output.

Preliminary investigations allowed a hypothesis on the shape and magnitude of the rate of secretion ($\frac{dQ}{dt}$) to be formed for a shear stress magnitude of 0.012 Pa.

This rate of secretion was subsequently altered for a new stimulation protocol and varying applied shear stress at 0.5 Hz in order to generate predictions for collagen quantities that were interrogated using experimental procedures. The model assumed that shear stress magnitude was the driving force behind secretion response, thus the increase in frequency from 0.083 Hz to 0.5 Hz was not built into the model design.

This work presents a hypothesis for the change in the rate of secretion over the duration of an experiment, in essence, forming the shape of $\frac{dQ}{dt}$ in Figure 6.5 for integration in order to predict the amount of secreted collagen Q.

6.2.1.1 Establishing rate of secretion

Within this section, the rate of secretion at 0.012 Pa for the preliminary investigation is presented. A mathematical model was developed using a system approach to build up components of collagen secretion rate, before integrating over a time period to establish a predicted collagen secreted quantity. Within this section the model is constructed in three stages:

1. Firstly, the impact of collagen secretion under non-stimulated conditions is considered;
2. Secondly, the application of a stimulus signal is built into the system; and
3. Finally, the impact of an increase in the applied shear stress magnitude is considered and added to the model.

Subsequently, the model is interrogated using a rest-insertion stimulation protocol outlined in Section 6.2.2.1.

6.2.1.2 Rate of secretion under control conditions

From preliminary results it was identified that for each experiment condition tencoytes continued to secrete collagen when no applied stimulus was present. It was therefore concluded that part of the quantities secreted under test conditions are the result of a 'normal' tenocyte secretion rate, *i.e.* the collagen secretion rate in control wells.

Thus, the first stage of the model design was to determine the control 'normal secretion' signal (Figure 6.6). This was achieved by assuming a constant rate of collagen secretion over the entire duration of stimulus and was calculated from control conditions for each testing regime.

The control signals for rest-insertion and continuous stimulation regimes were established by dividing the average control quantity secreted by the duration of the experiment in hours (Figure 6.7).

6.2.1.3 Rate of secretion induced by mechanical stimulation

Using results from preliminary investigations in Section 6.1, the change in the rate of secretion over time was hypothesised. The hypothesis divided the rate of secretion induced by stimulation into two distinct regions:

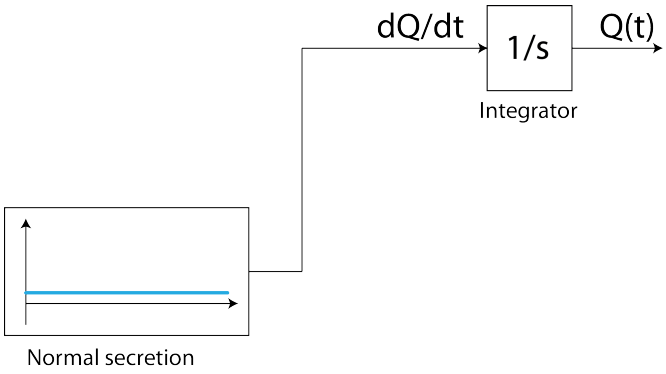

Figure 6.6: Collagen secretion model - control rate: a constant rate of secretion was established using data from control wells to establish secretion quantities under unstimulated conditions. This was called 'normal secretion'. 1/s represents an integrator function that establishes the quantity of collagen over an applied time period.

1. Firstly, a period where the rate of secretion is constant that is equal to the period of time that cells are stimulated for, as it is suggested that collagen is made during stimulus as well as during rest (region one).

2. Secondly, immediately post-stimulation the rate of secretion rises instantaneously, before falling linearly over a period of 20 hours. Initial investigations indicated that collagen differences between test and control conditions as a result of stimulus were identifiable after 20 hours, hence the selection of this time period for the second region of secretion rate (region two).

Using this hypothesis, simultaneous equations were formed based on data from preliminary investigations to determine the magnitudes of the rate of secretion in the first and second region (Equation 6.3).

$$\begin{aligned} Q_T &= Q_C + (h_s x) + (h_r y) \\ 7.13 &= 3.44 + 8x + 40y \\ 21.90 &= 7.67 + 168x + 20y \end{aligned} \tag{6.3}$$

where Q_T is the quantity of collagen secreted under test conditions, Q_C is the quantity of collagen secreted under control conditions, h_s is the total hours of stimulation (region one), h_r is the total hours at rest where secretion as a result of stimulation occurs (region two), x is the rate of secretion when stimulated in region one, and y is

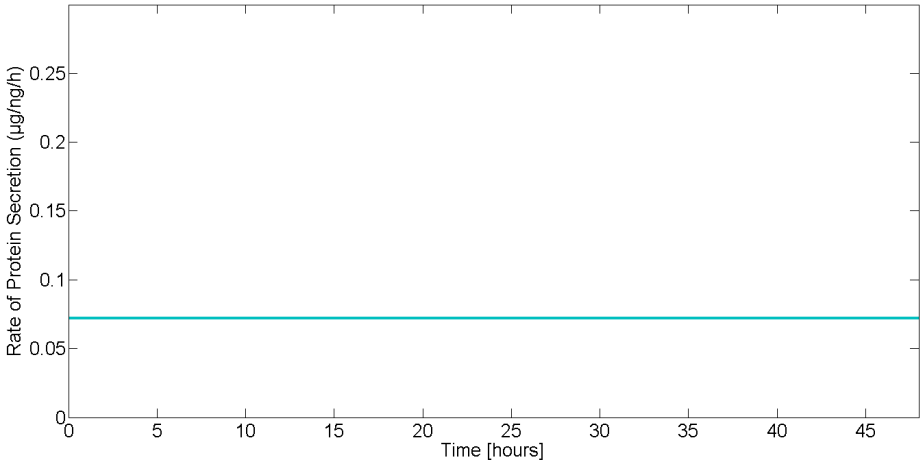

(a) Short-interval stimulation - normal, unstimulated rate of secretion

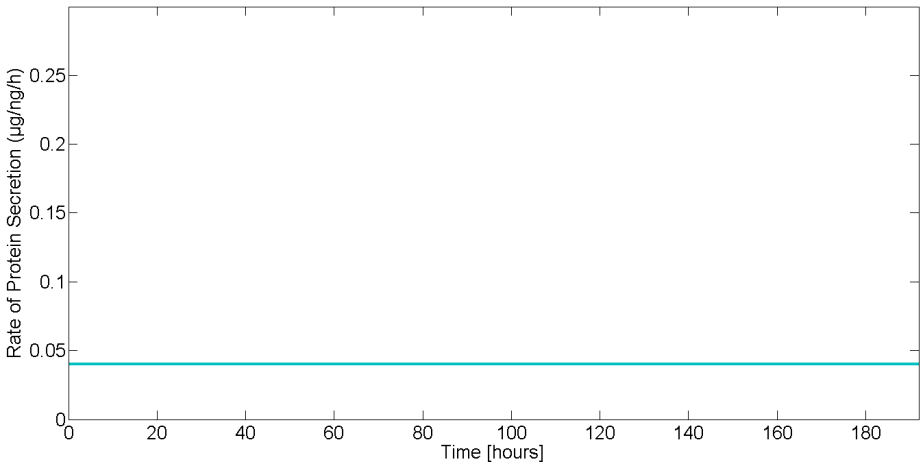

(b) Continuous stimulation - normal, unstimulated rate of secretion

Figure 6.7: Model input - rate of secretion for control conditions: when unstimulated, control wells continue to produce collagen. This rate of collagen production is assumed to be constant and is calculated from the Sircol assay collagen quantifications for control wells.

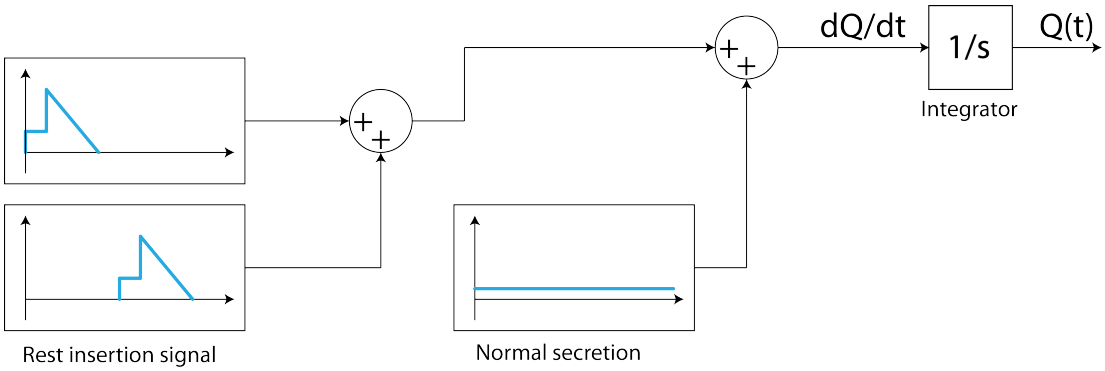

Figure 6.8: Collagen secretion model: a systematic approach to predicting collagen secretion allows for manipulating the duration and type of stimulus at varying shear stress magnitudes.

the average rate of secretion at rest in region two. Sub-equations were populated with numbers from Figure 6.1, *e.g.* for sub-equation one, after rocked conditions lasting eight hours in total (h_s) and static conditions lasting 40 hours (h_r), 7.13 $\mu g\, ng^{-1}$ of collagen was secreted (Q_T) in the rocked well, compared to 3.44 $\mu g\, ng^{-1}$ of secreted collagen in the static well (Q_C).

Evaluation of the simultaneous equations to obtain the rate of secretions during stimulation and at rest results in a constant rate of secretion during stimulation (x) of 0.0755 $\mu g\, ng^{-1}\, h^{-1}$ and an average rate of secretion after stimulation (y), lasting 20 hours of 0.0771 $\mu g\, ng^{-1}\, h^{-1}$. These values were used to determine the signal for the rate of secretion as the primary input into the model (Figure 6.9).

Evaluation of the model for the preliminary investigations into short-interval stimulation and continuous stimulation confirmed that system-generated results matched very closely to experimental results (Table 6.3).

Stimulation condition	Actual ($\mu g\, ng^{-1}$)	System generated ($\mu g\, ng^{-1}$)
Rest-insertion	7.13	7.15
Continous	21.90	21.91

Table 6.3: Comparison of secretion model to experimental results for short-interval stimulation and continuous stimulation at 0.083 Hz

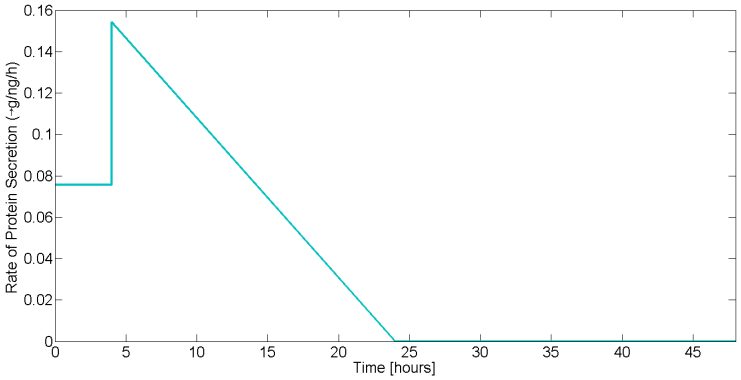

(a) Short-interval stimulation - first rest-insertion rate of secretion

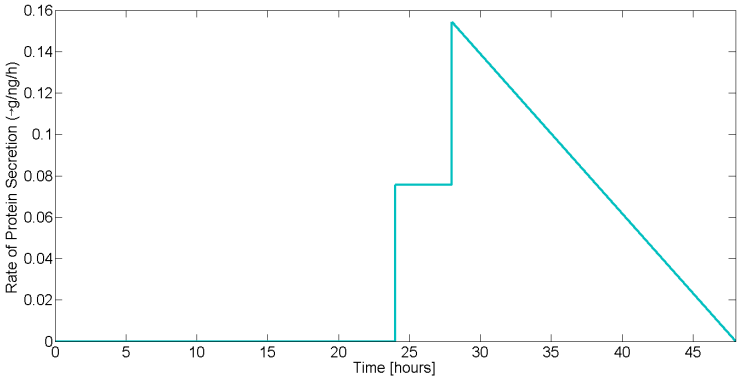

(b) Short-interval stimulation - second rest-insertion rate of secretion

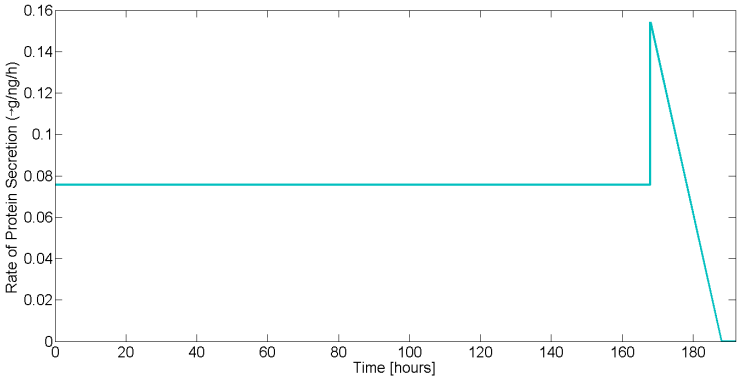

(c) Continuous stimulation rate of secretion

Figure 6.9: Model signal input - short-interval and continuous stimulation rates of secretion: during stimulation the rate of secretion is constant. Immediately after stimulus, collagen secretion rate peaks as tenocytes respond to the shear stress. The effect of the stimulus on secretion rate is hypothesised to have completed after 20 hours.

6.2.1.4 Shear stress magnitude effect on the rate of secretion induced by mechanical stimulation

The rate of secretion due to stimulation was then increased or decreased based on the magnitude of the applied shear stress through a simple product system (Figure 6.10). Average shear stress reported for each condition (Table 6.4) was utilised to develop a 'shear factor', based upon a normalised multiple increase of the mean shear stress from the 0.083 Hz condition. This shear factor was input into the collagen prediction model to establish predicted collagen secretion quantities for each condition (Table 6.5).

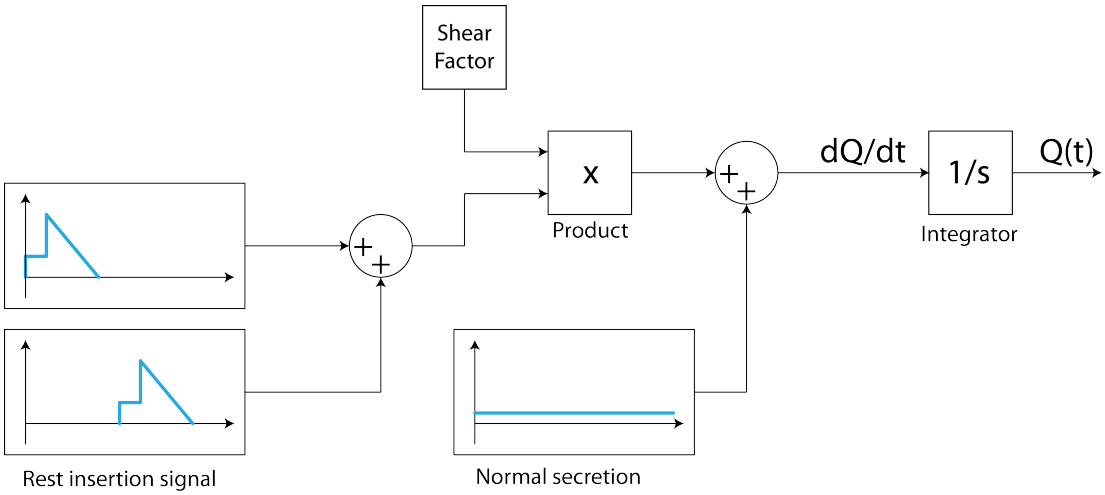

Figure 6.10: Collagen secretion model: a systematic approach to predicting collagen secretion allows for manipulating the duration and type of stimulus at varying shear stress magnitudes. The rate of collagen secretion is estimated using a 'shear factor'.

Altered parameter	Mean shear stress (Pa)
0.5 Hz base-scenario	0.033
Placed at the platform edge	0.053
0.1 % CMC, 20.0 mPa s	0.714
0.2 % CMC, 31.0 mPa s	1.023

Table 6.4: Shear stress condition and model parameter: all stimulation conditions are performed at 0.5 Hz.

Mean shear stress (Pa)	Shear factor	Predicted collagen secretion ($\mu g\, ng^{-1}$)
0.012	1.00	-
0.033	2.75	28.55
0.053	4.42	39.97
0.714	59.50	395.90
1.023	85.25	562.60

Table 6.5: Predicted increase in secreted collagen for each shear stress magnitude using shear factors determined from the 0.083 Hz model

6.2.2 Experimental investigations

To interrogate the prediction model, an experiment protocol was developed to investigate the affect of a rest-insertion stimulus on the secretion and release of collagen in to the culture medium over eight days.

6.2.2.1 Experimental design, methods & model predictions

Human tenocytes were grown to confluency and prepared for mechanical stimulation (Section 5.1). To ensure secretion results were not rate limited, ascorbic acid and proline were supplemented to culture medium at a concentration of $50\,\mu g\,ml^{-1}$ for all wells. In addition, FCS was removed from stimulation and control medium to further encourage the inhibition of cellular proliferation in all wells.

Four periods of one hour rest-insertion at 0.5 Hz was applied at different shear stresses using models developed in Chapter 4 and summarised in Table 6.4. For each condition, cells from two healthy patients were used (n = 12). Culture medium was refreshed at t = 3 & 6 days and stored at $-20\,^{\circ}C$ until day 8 when culture medium was combined for the Sircol assay.

The control signal was obtained from collagen quantities measured for cells at rest for 8 days with no stimulus. Using the signals from preliminary investigations for the rate of secretion (Figure 6.7), manipulated for the new testing protocol, and altered dependent on the 'shear factor' of each condition, predictions of collagen quantities were established.

6.2.2.2 Experimental results

Application of fluid-induced shear stress at 0.5 Hz to tenocytes at the centre of the rocking platform and at the extremity significantly increases the secretion of collagen in to the culture medium ($p < 0.0001$) (Figure 6.12). In addition, the increased shear stress of 0.053 Pa at the platform extremity causes tenocytes to secrete significantly more collagen than those at the centre of the platform exposed to 0.033 Pa ($p = 0.0005$). Application of 0.714 Pa significantly increases the quantity of collagen released in to the media in comparison to controls ($p = 0.0156$), but is significantly less than the collagen secreted under the base condition of 0.033 Pa (0.78 mPa s) ($p < 0.0001$). At 1.023 Pa collagen secreted in to the media is significantly less than the controls ($p < 0.0001$), suggesting that a catabolic state is present within the culture well. In addition, collagen released in to the media at 1.023 Pa is significantly less than the base-scenario of 0.033 Pa ($p < 0.0001$) and the 0.1 % CMC condition of 0.714 Pa ($p < 0.0001$).

For the base-scenario (0.033 Pa) and the extremity condition (0.053 Pa), system generated predictions were close to the actual results (Table 6.5). However, when a large magnitude of shear stress was applied, compared to the 0.033 Pa condition, experimentally measured collagen was reduced, and ultimately falls to below quantities observed in control cultures after an application of 1.023 Pa of shear stress (Figure 6.12).

Stimulation condition (Pa)	Predicted ($\mu g\,ng^{-1}$)	Actual ($\mu g\,ng^{-1}$)
0.033	28.55	41.58
0.053	39.97	43.31
0.714	395.90	32.63
1.023	562.60	12.34

Table 6.6: Comparison of secretion model to experimental results for short-interval stimulation and continuous stimulation at 0.083 Hz

Evaluation of the relationship of secreted collagen quantity with applied shear stress indicated that a quadratic relationship can be used to estimate tenocyte response ($y = -52.51x^2 + 25.23x + 41.45$) with a root mean square error (RMSE) of 0.9322 $\mu g\,ng^{-1}$ (Figure 6.13) that is indicative of anabolic and catabolic response regions. It was

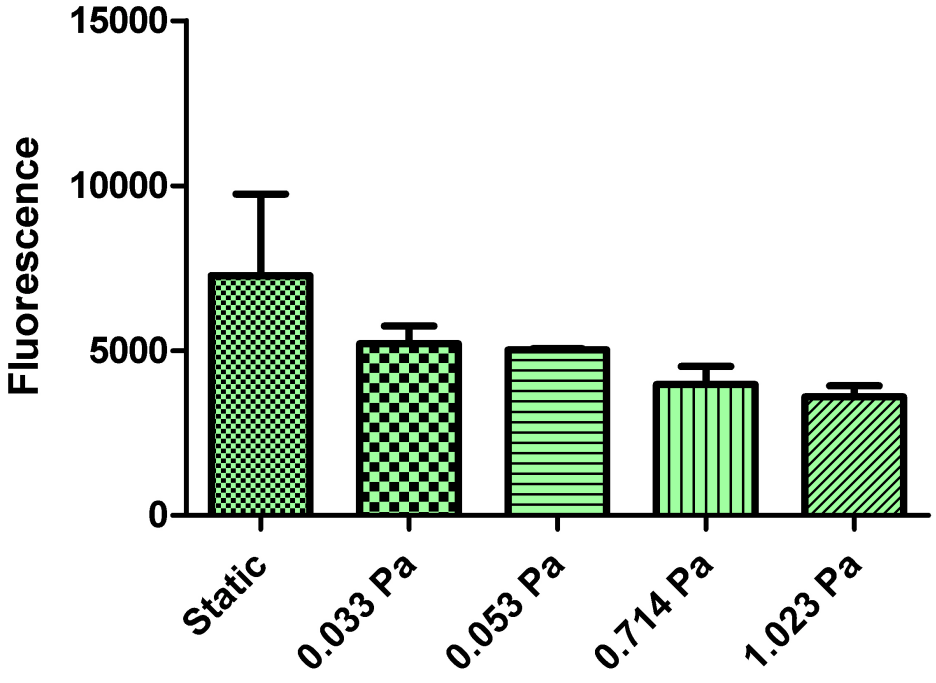

Figure 6.11: dsDNA content for experimental interrogation of model predictions: control wells have increased dsDNA content in comparison to stimulated wells. dsDNA values were used to normalise collagen quantification.

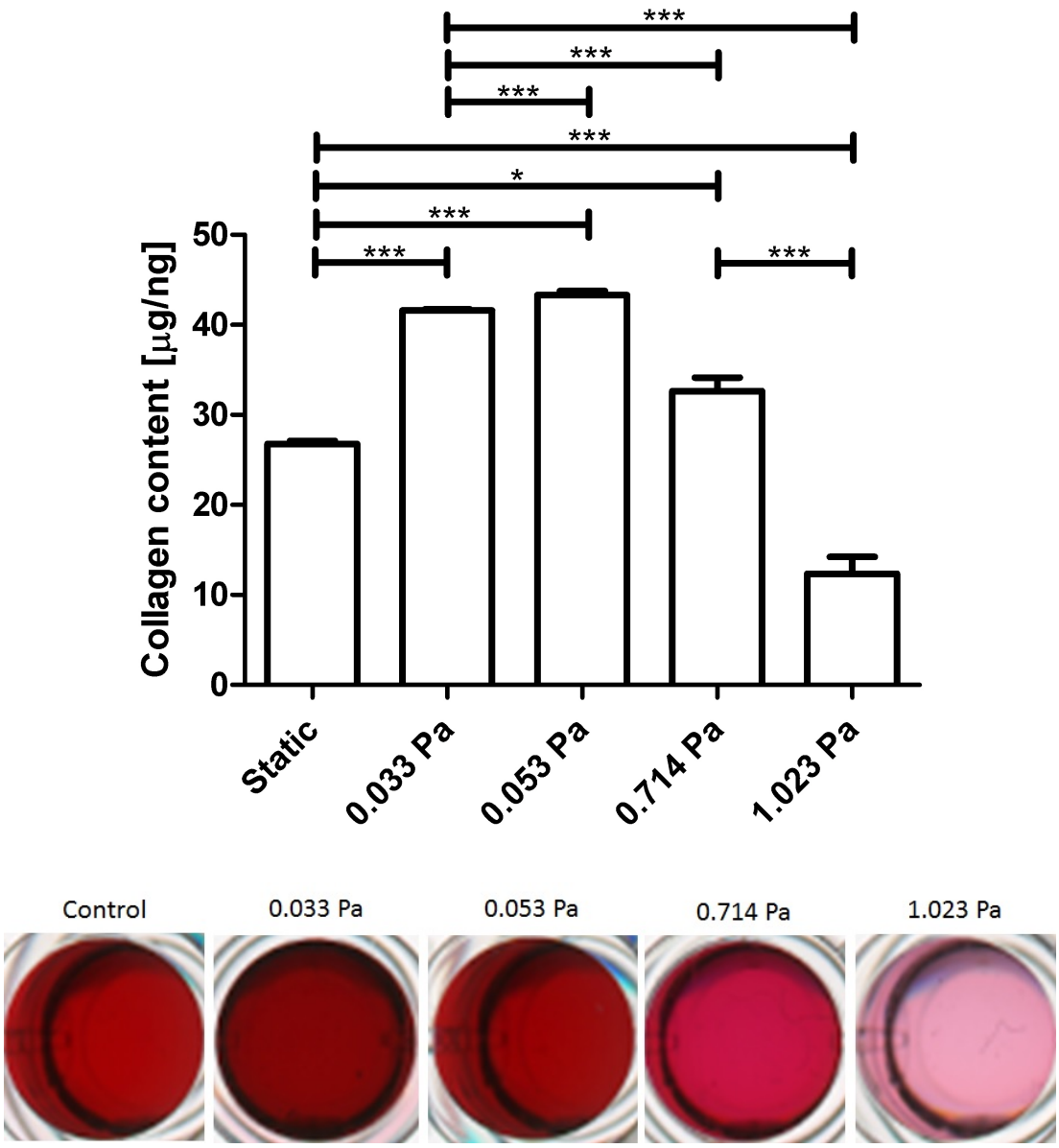

Figure 6.12: Collagen viscosities: top - comparison of collagen content for each model condition (* = p <0.05, *** = p <0.001). Bottom - representative capture of Sircol assay picrosirius red gradients for each model condition.

identified that the rate of protein secretion with respect to a change in shear stress falls linearly at a slope of -105.20 $\mu g\, ng^{-1}\, Pa^{-2}$.

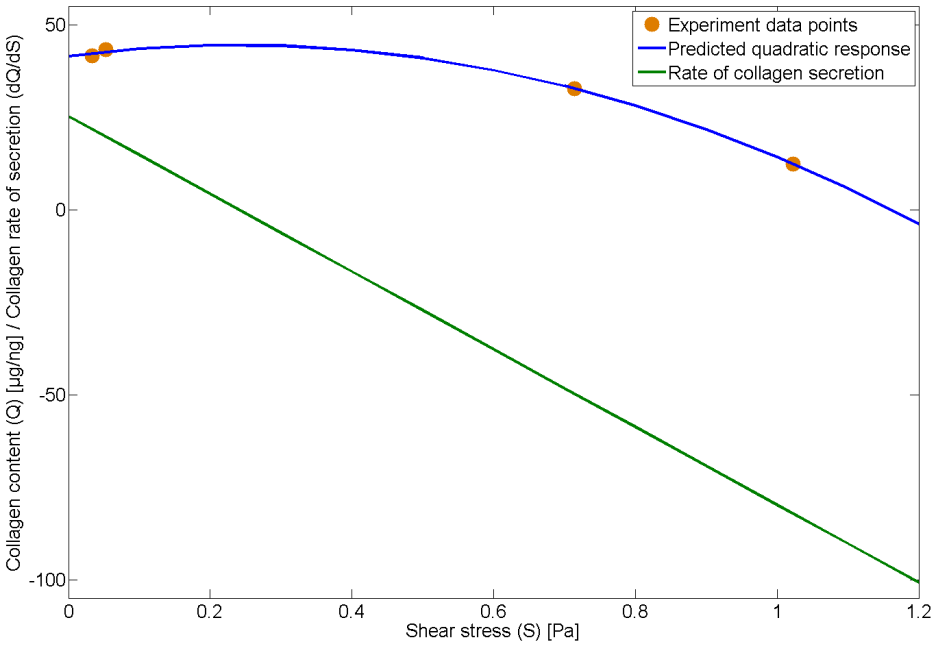

Figure 6.13: Collagen rate analysis: experimental data points can be represented by a quadratic fit. Differentiation of the quadratic expression provides the rate of collagen secretion at each shear stress condition. The rate of collagen secretion linearly decreases with an increase in shear stress at a slope of -105.20 $\mu g\, ng^{-1}\, Pa^{-2}$.

6.2.3 Discussion

Preliminary investigations indicated that rest-insertion was a more effective method of stimulus than continuous stimulation; however results were completed without ascorbic acid supplementation and only limited conclusions can be drawn. Significant differences were identified between control conditions and tenocytes exposed to rest-insertion for: collagen retained at the cell layer; collagen released into the culture medium; and GAG retained at the cell layer; however, staining of the cell layer identified that picro-sirius red is an anionic dye that binds to other parts of the cell, and although normalisation ensures that this background data does not impact on the difference between results,

the reported quantity of collagen secreted may be inflated (Figure 6.14). Thus, collagen secreted into the culture medium was the focus of future investigations, supported by immunohistochemistry staining (Section 6.3).

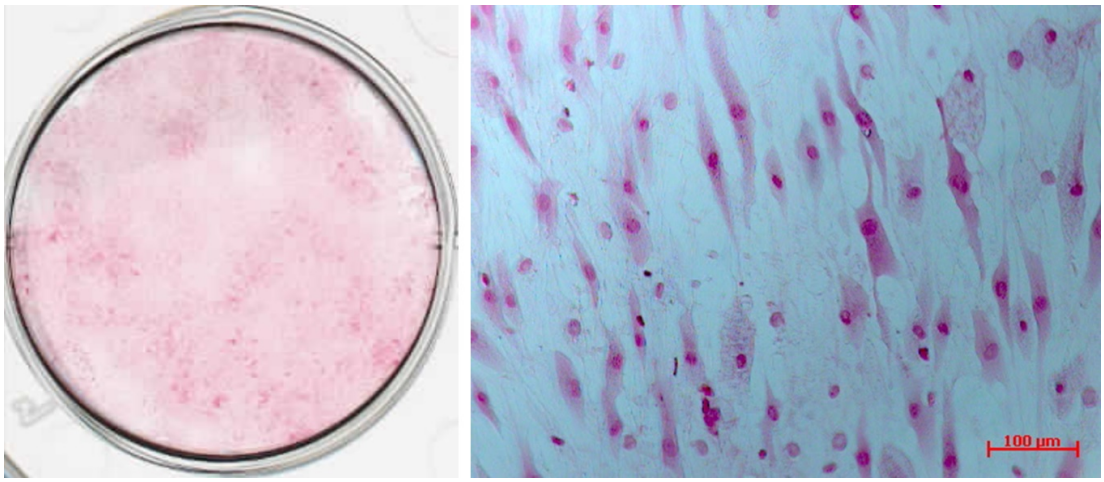

Figure 6.14: Sirius red appears to stain collagen as well as other structures at the cell layer: left - high-level staining map of the cell layer shows homogenous staining. Right - microscopy at 20× highlights staining of individual cells. Staining next to the nucleus may be due to the presence of the collagen monomer inside the cell, or could be the staining of non-collagenous cytoplasm structures creating a background reading in quantification results.

Experimental interrogation of a mathematical model built to predict collagen secretion indicated that a linear shear stress multiple, known as a 'shear factor' produced promising results for low shear stress values, but an identified quadratic relationship between the quantity of collagen secreted and the shear stress magnitude caused large differences between actual results and linear predictions at applied shear stresses of 0.714 Pa and 1.023 Pa. The difference was especially large after application of a shear stress magnitude of 1.023 Pa as a Sircol biochemical assay identified that secreted collagen was significantly less than in control conditions ($p < 0.0001$), suggesting that tenocytes had entered a catabolic state. Whether 0.714 Pa was additionally a catabolic state, rather than a reduced anabolic state, requires further investigation. It may be that by extending the time frame of the experiment, any matrix degrading enzymes released under the 0.714 Pa condition would have additional time to degrade measured collagen.

Results at the centre of the platform and at the edge are significantly different ($p = 0.0005$). Clearly the location of the six-well plate on the rocker platform has an important role in establishing collagen secretion levels.

The quadratic relationship suggests that collagen secretion is at a maximum when an average shear stress of 0.25 Pa is applied. This only applies for the specific experiment condition; however it is hypothesised that this relationship may be present across other test conditions. The first order and second order terms of the equation could be the foundation of the relationship between collagen quantities secreted and shear stress, and the y-intercept determined as a function of collagen quantities determined in control conditions. This may be a useful manipulation of the model going forward. A quadratic relationship provides a local maximum, suggesting the change between anabolic and catabolic conditions. Alternatively, the relationship identified may not be quadratic, and be a combination of linear anabolic and catabolic responses to applied shear stresses. Further investigation is required, where anabolic and catabolic cell responses are investigated.

6.3 Fluid flow alters tenocyte communication & secretion at the cell layer

Using the same conditions for evaluating the secretion prediction model as described in Section 6.2, collagen type-I, collagen type-VI, fibrillin-I and elastin were investigated at the cell layer using immunohistochemistry (methods detailed in Section 5.8) to evaluate whether differences identified in the media were similar to that at the cell layer, and whether suggested catabolic conditions indicated at a shear stress of 1.023 Pa had an effect on key pericellular matrix proteins that are linked with tendon damage. In addition, the impact of fluid-shear stress on tenocyte communication pathways was also considered by investigating connexin-32.

It is hypothesised that the relationship of collagen type-I at the cell layer to applied shear stress will be similar to the Sircol biochemical assay results in Section 6.2.2.2, as collagen content in tendon *in vivo* is dominated by collagen type-I (Section 1.2.1). Hence, identified differences in Sircol quantification results were most likely due to collagen type-I quantities.

It is further hypothesised that shear stress will encourage the formation of pericellular matrix at the cell layer, however, the impact of shear stress magnitude on tenocyte pericellular matrix genes or secretion has so far not been investigated (Sections 1.6.2 & 1.2.4). The existence of a pericellular matrix may be a pre-cursor to the secretion of collagen type-I.

The presence of connexin-32 is expected to increase with the application of shear stress as tenocytes exposed to 0.1 Pa of shear stress in a laminar flow chamber upregulated the expression of the connexin-43 gene (239). However, a ten-fold increase in this shear stress in the rocker model using the CMC concentration of 0.2 % CMC to produce a shear stress of 1.023 Pa, may inhibit the presence of connexin-32.

6.3.1 Collagen type-I

The application of fluid shear stress changed the appearance of collagen type-I formed at the cell layer (Figure 6.15). Under control conditions, collagen type-I appeared to form in clusters at different sites within a well, resulting in areas of high and low collagen density. The collagen type-I structures appeared spider-like, spanning in every direction. Some cells had little or no collagen type-I in their immediate vicinity. With the application of 0.033 Pa of shear stress, there was a marked increase in collagen type-I at the cell layer. Every cell appeared to be associated with the accumulation of collagen type-I and close inspection showed that the cytoplasm of cells were stained, suggesting that tenocytes have manufactured collagen that has not yet been secreted. The collagen type-I appeared aligned in one direction (analysis of matrix and cell alignment is completed in Section 6.4). As the shear stress magnitude was increased to 0.714 Pa, the collagen type-I presence reduced; however several cells appeared to show deposits of collagen type-I in their vicinity. No large collagen type-I structures were present (relative to control and 0.033 Pa conditions), instead the collagen type-I formed small globules, with the occasional amalgamation to create a slightly larger structure. At 1.023 Pa, collagen type-I appeared similar to the 0.714 Pa condition; however larger areas with minimal collagen type-I quantities were present, a sharp contrast to cells exposed to a stimulus of 0.033 Pa.

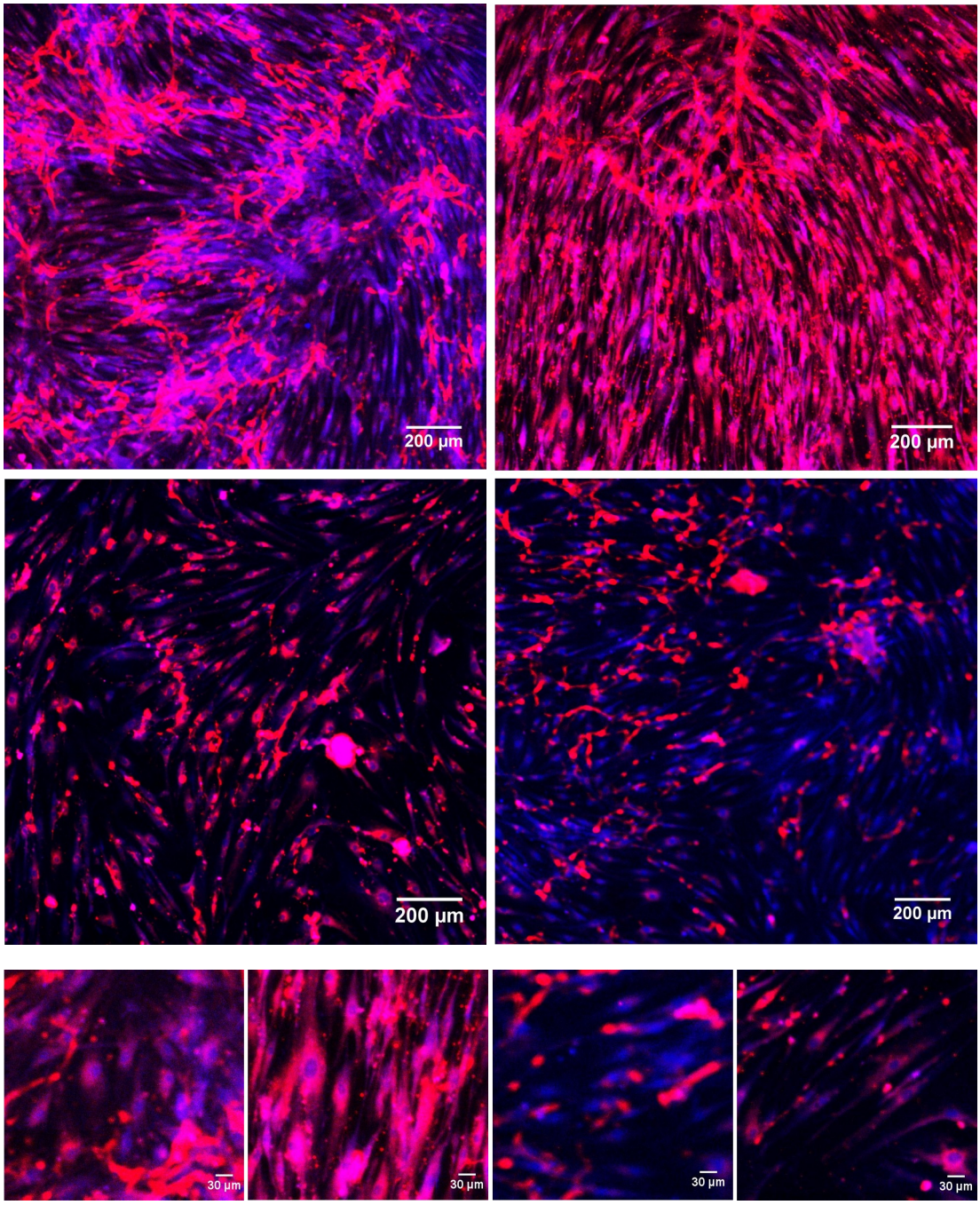

Figure 6.15: Collagen type-I immunohistochemistry: tenocytes exposed to varying magnitudes of shear stress exhibit changes in collagen type-1 secretion. Top - clockwise from top left: control; 0.033 Pa; 1.023 Pa; 0.714 Pa. Bottom - from left to right: control; 0.033 Pa; 0.714 Pa; 1.023 Pa. Red - collagen type-I, blue - whole cell stain.

6.3.2 Collagen type-VI

Collagen type-VI is associated with the pericellular matrix, and increases in gene expression have been identified in rotator-cuff tendon where medium and large tears are present (D. Thakkar - unpublished, Nuffield Department of Orthopaedics, Rheumatology, and Musculoskeletal Sciences, University of Oxford).

Inspection of control conditions indicated that collagen type-VI was secreted in very minimal amounts compared to cells exposed to shear stress (Figure 6.16). Within all three stimulated conditions, collagen type-VI was present outside of cells in small bright spots. There were no large collagen type-VI structures similar to those identified in collagen type-I imaging. This result is in agreement with the understanding of the composition of tendon where collagen type-VI contributes only trace amounts (Section 1.2.1).

Collagen type-VI is present in both healthy and damaged tendon; amounts identified are not indicative of whether cells are exposed to a 'healthy' or 'damaging' stimulus.

6.3.3 Fibrillin-I and elastin

Fibillin is a pre-cursor to the formation of elastin that contributes 2 % to the composition of mature, healthy tendon (Section 1.2.1) and was identified in all control and test conditions; however quantities in cells exposed to 0.033 Pa appear slightly larger than other conditions, potentially indicating that fluid-induced shear stress of 0.033 Pa supports the increased secretion of fibrillin-I. In control conditions and tenocyte cultures exposed to 0.714 Pa and 1.023 Pa, fibrillin appeared to amalgamate into localised bright spots that are not present in 0.033 Pa conditions. Elastin immuno-staining was also performed for all conditions (data not shown), but no elastin was observed in control or test conditions. The lack of elastin secretion may be due to the low quantity of fibrillin-I, but also there is a suggestion that elastin is only synthesised during development and growth and not in mature tendon (285).

6.3.4 Connexin-32

Connexin-32 is a protein that forms gap junctions (Section 1.3.1). Under all conditions, connexin-32 was present at the cell layer (Figure 6.18). Under control conditions, gap junctions were present in localised groups. However, after the application of 0.033 Pa of

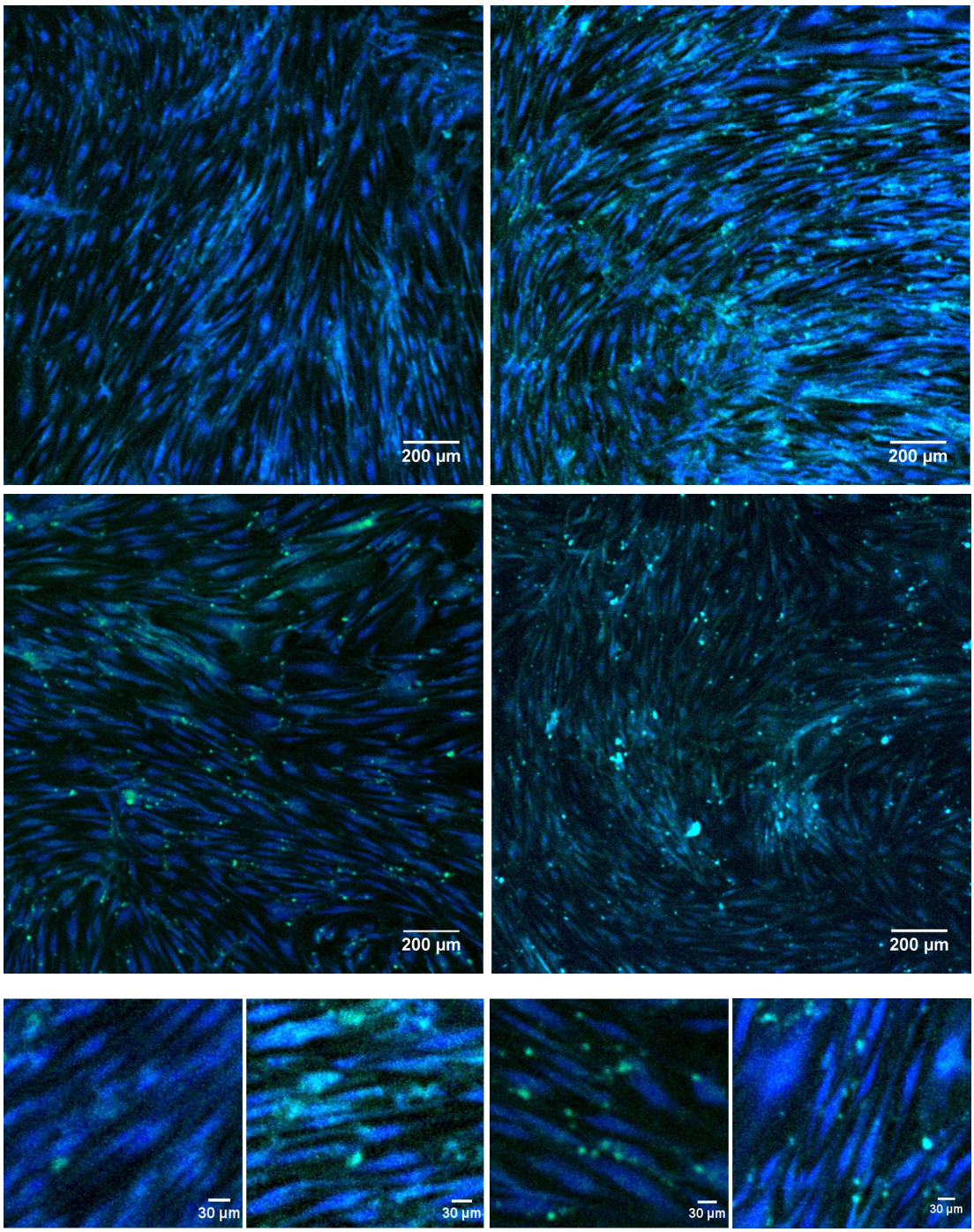

Figure 6.16: Collagen type-VI immunohistochemistry: tenocytes exposed to varying magnitudes of shear stress exhibit changes in collagen type-VI secretion. Top - clockwise from top left: control; 0.033 Pa; 1.023 Pa; 0.714 Pa. Bottom - from left to right: control; 0.033 Pa; 0.714 Pa; 1.023 Pa. Green - collagen type-VI, blue - whole cell stain.

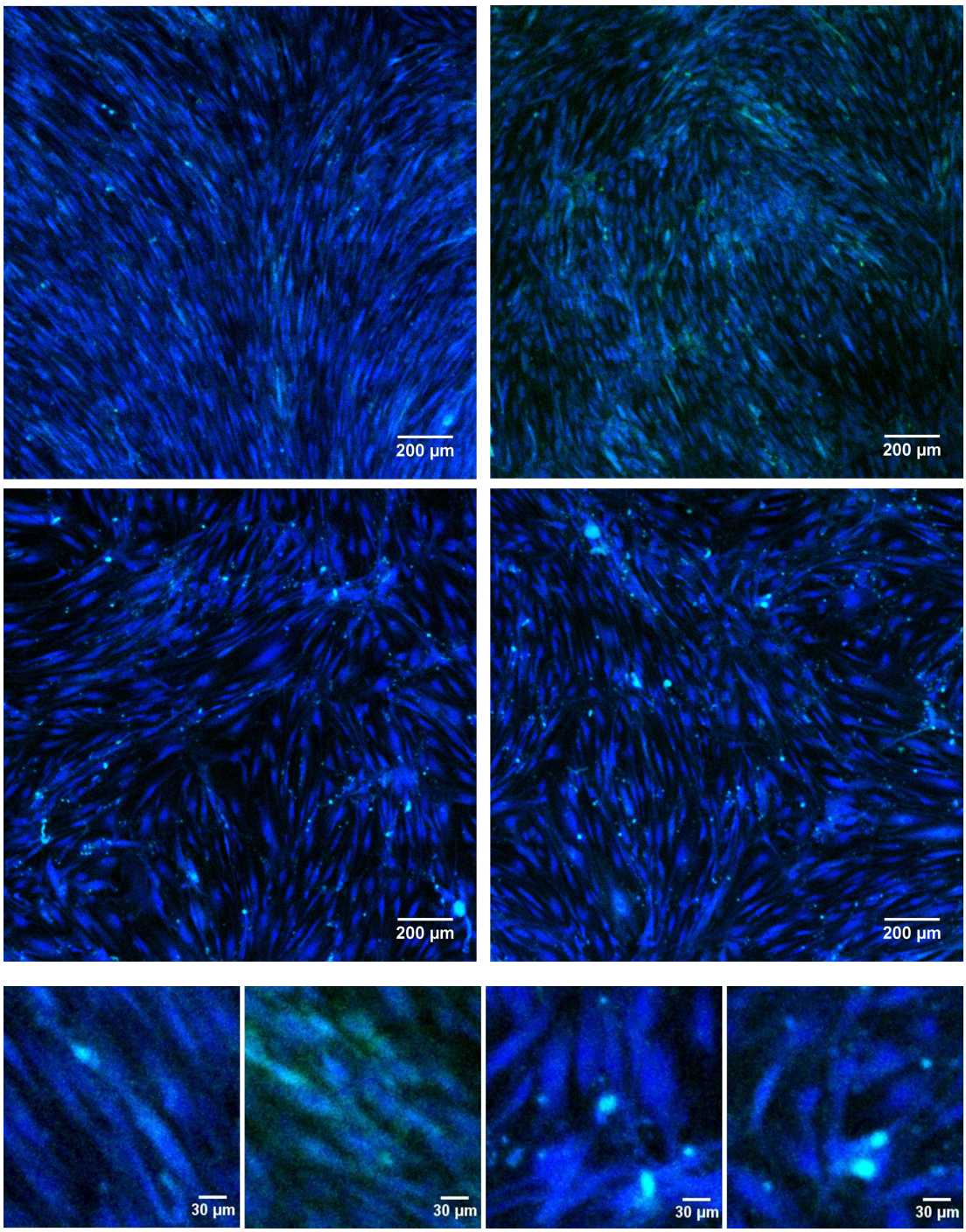

Figure 6.17: Fibrillin-I immunohistochemistry: tenocytes exposed to varying magnitudes of shear stress exhibit changes in fibrillin-1 secretion. Top - clockwise from top left: control; 0.033 Pa; 1.023 Pa; 0.714 Pa. Bottom - from left to right: control; 0.033 Pa; 0.714 Pa; 1.023 Pa. Green - fibrillin-I, blue - whole cell stain.

shear stress, the presence of connexin-32 was greatly increased and was spread across the entirety of the cell layer. Connexin-32 appeared to co-localise distribution of collagen type-I under this condition.

After the application of 0.714 Pa of shear stress, the presence of connexin-32 appeared less widely distributed than that of 0.033 Pa and where it was present, slightly more concentrated. This may occur as tenocytes focus on forming large, strong gap junction plaques, rather than numerous smaller gap junction plaques.

Large areas of connexin-32 staining were also identified after the application of 1.023 Pa of shear stress; however they were much sparser than the 0.714 Pa condition and some areas of cells of 400×400 μm showed little if any gap junction staining at all.

6.3.5 Discussion

For both 0.714 Pa and 1.023 Pa conditions, it may be hypothesised that the quantity of collagen secreted equals that of the other conditions, but the shear stress magnitude prevents the formation of collagen as extracellular matrix. By cross-analysing culture medium collagen quantifications with immunohistochemistry confocal images, this was confirmed to not be the case for the 1.023 Pa condition as collagen quantities were less than the control in both situations; however it may be the case for the 0.714 Pa condition as collagen released into the media was higher than the control condition, but collagen retained at the cell layer was less than the control. It would be of interest to perform immunohistochemistry, identifying key catabolic enzymes (MMPs) for each condition to establish whether shear stresses are inducing catabolic effects.

Immunohistochemistry indicated that stimulation at 0.033 Pa increased the secretion of pericellular matrix components, collagen type-VI and fibrillin-I; however quantities were much smaller than that identified in collagen type-I immunohistochemistry, a result that mimics the tendon *in vivo* composition. Increasing shear stress magnitude to 0.714 Pa and 1.023 Pa caused collagen type-VI and fibrillin-I to appear aggregated, taking on the shape of circular 'globules' in areas of particularly high tenocyte density. The presence of collagen type-VI appeared to be much higher than fibrillin-I and no elastin was identified in either the control or any of the test conditions.

Results suggest that when connexin-32 is present, it is found at the tips of the long axis of each tenocyte. This corresponds with findings that suggest connexin-32 is responsible for longitudinal connections in tendon, and connexin-43 is responsible

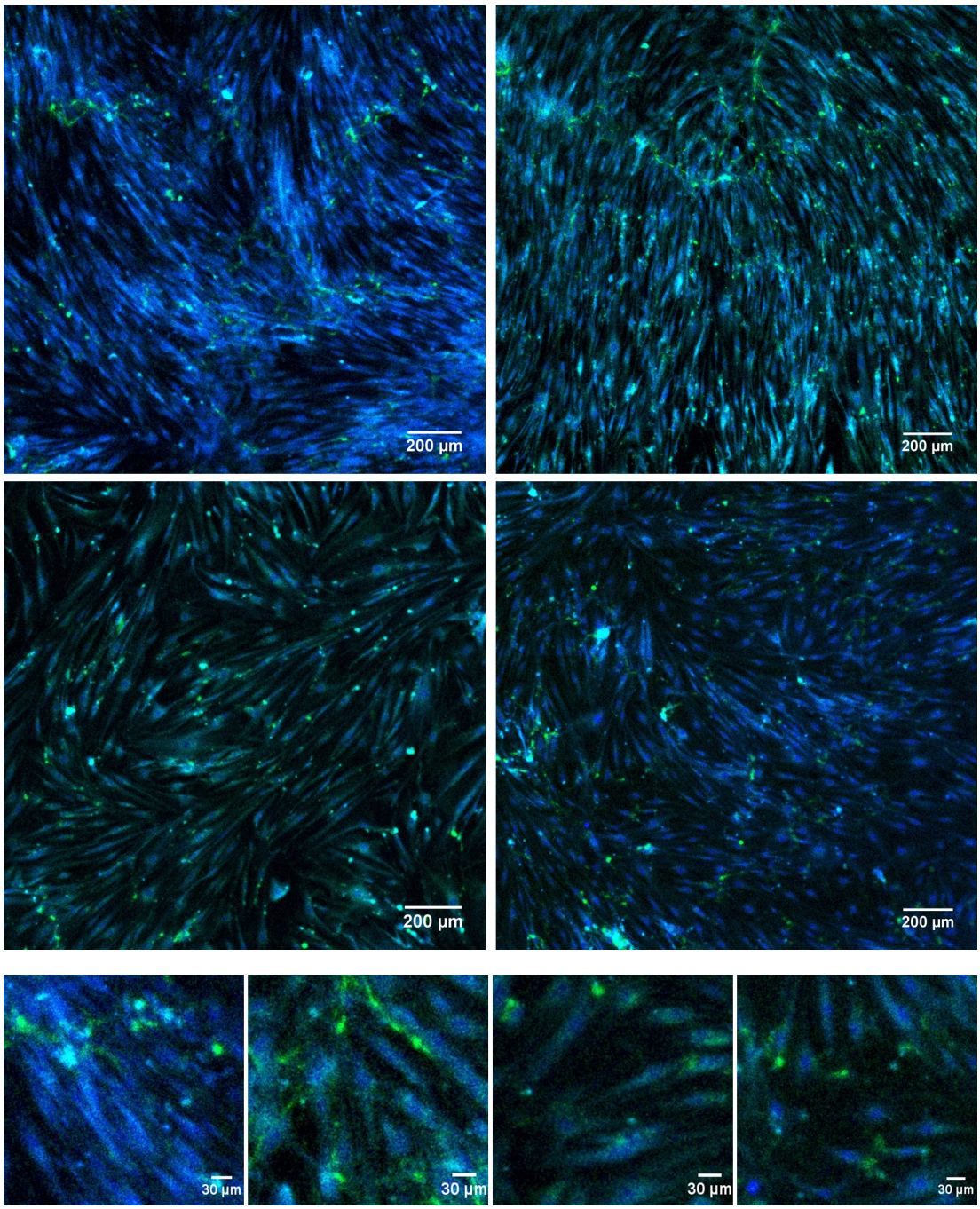

Figure 6.18: Connexin-32 immunohistochemistry: tenocytes exposed to varying magnitudes of shear stress exhibit changes in connexin-32 quantities. Top - clockwise from top left: control; 0.033 Pa; 1.023 Pa; 0.714 Pa. Bottom - from left to right: control; 0.033 Pa; 0.714 Pa; 1.023 Pa. Green - connexin-32, blue - whole cell stain.

for lateral connections (286). The formation of an increased quantity of connexin-32 may be a by-product of increased cellular alignment as the alignment gives tenocytes polarity.

Closer inspection of each condition, indicated that under the 0.033 Pa condition, gap junctions were present on every cell, even if only at a small quantity. Gap junctions may be essential in coordinating the response of a cell layer and tenocytes may secrete collagen type-I preferentially with an increase in gap junction formation. Comparison of connexin-32 with collagen type-I indicated that the direction of collagen formation strongly correlated with the direction of connexin-32 presence (Figure 6.19), suggesting that cell-cell communication may play a key role in collagen type-I secretion.

It has been suggested that connexin-32 plays a stimulatory role in collagen secretion and connexin-43 plays an inhibitory role (286), therefore it would be interesting to see the presence of connexin-43 under each testing condition.

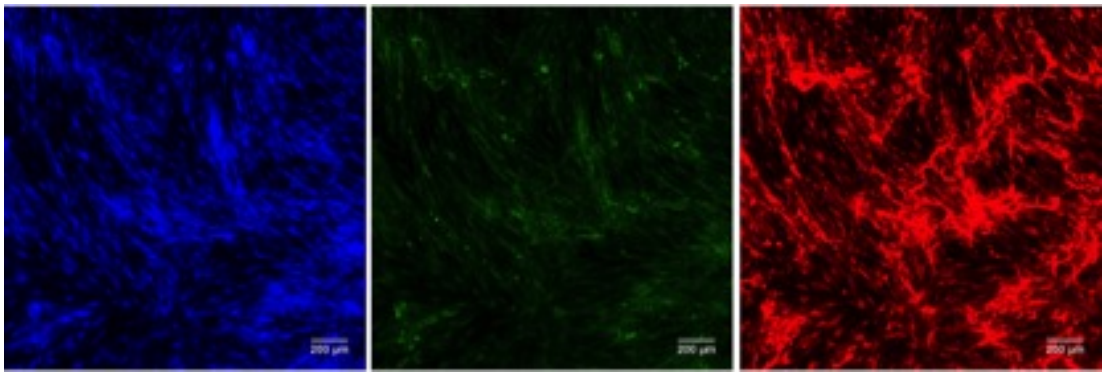

Figure 6.19: Whole cell stain, collagen type-I and connexin-32: collagen type-I structures form above cells and appear localised where high concentrations of gap junctions are present. Left - whole cell stain, middle - connexin-32, right - collagen type-I

To confirm whether differences identified in collagen type-I secretion are the result of catabolic effects, further scrutiny is required. This could include the use of an MMP zymogram (an experiment to measure the breakdown of a collagen gel by MMPs released into the culture medium) to confirm the presence of MMP-1 in test conditions. Additionally, qPCR to identify the presence of key oxidative stress markers, such as Forkhead-1, may provide an interesting insight into cell behaviour.

Finally, although CMC is reported to be a biologically inert compound, confirmation that results are not due to toxicity induced by its presence would be beneficial.

6.4 Fluid flow alters tenocyte alignment & elongation

Within tendon, tenocytes are aligned in the direction of the load-bearing collagen hierarchy, with processes reaching out in each direction to make cell-cell connections (Section 1.6). Cell motility is driven by the cytoskeleton; the polymerisation and depolymerisation of filaments and microtubules allows a cell to move in a specific direction (103). Cells have chemical receptors to help assimilate the information from their immediate environment and this may assist in alignment or movement in a specific direction, but there are also mechanical triggers that could impact on cell alignment (287, 288). The alignment could be due to a number of factors, such as, but not limited to: the direction of an applied force; the presence of an aligned extracellular matrix; and/or the location of vital nutrients. Tenocyte elongation could be a response to shear stress for cells to form gap junctions, or it may be a by-product of increasing cell-substrate attachments to withstand an applied force (85).

The purpose of this study was to ascertain whether tenocyte morphology, defined by alignment and elongation, was influenced by fluid flow stimulation. This was achieved using a custom image analysis technique and tendon cell culture in the validated rocker model. Analysis of the velocity vectors in the x-y plane of a stimulated six-well plate indicated that at 0.5 Hz, fluid flow moves perpendicular to the angle of rotation for all angles of tilt (Figure 6.20). It was therefore hypothesised that tenocytes would align at 90 ° to the axis of rotation to achieve a more favourable stress across the cell profile as seen in endothelial cell simulations (289).

6.4.1 Algorithm design and experimental approach

Tenocytes are heterogeneous, with a variety of compartments and structures (Section 1.6). Previous cell alignment techniques have involved using edge detection techniques (290); however problems with computerised cell identification algorithms have also resulted in time-intensive manual drawing of an angle for every cell (291). An intensity-based approach was taken for establishing the alignment of tenocytes subjected to fluid forces. Intensity analysis interrogates the texture of the image. If the

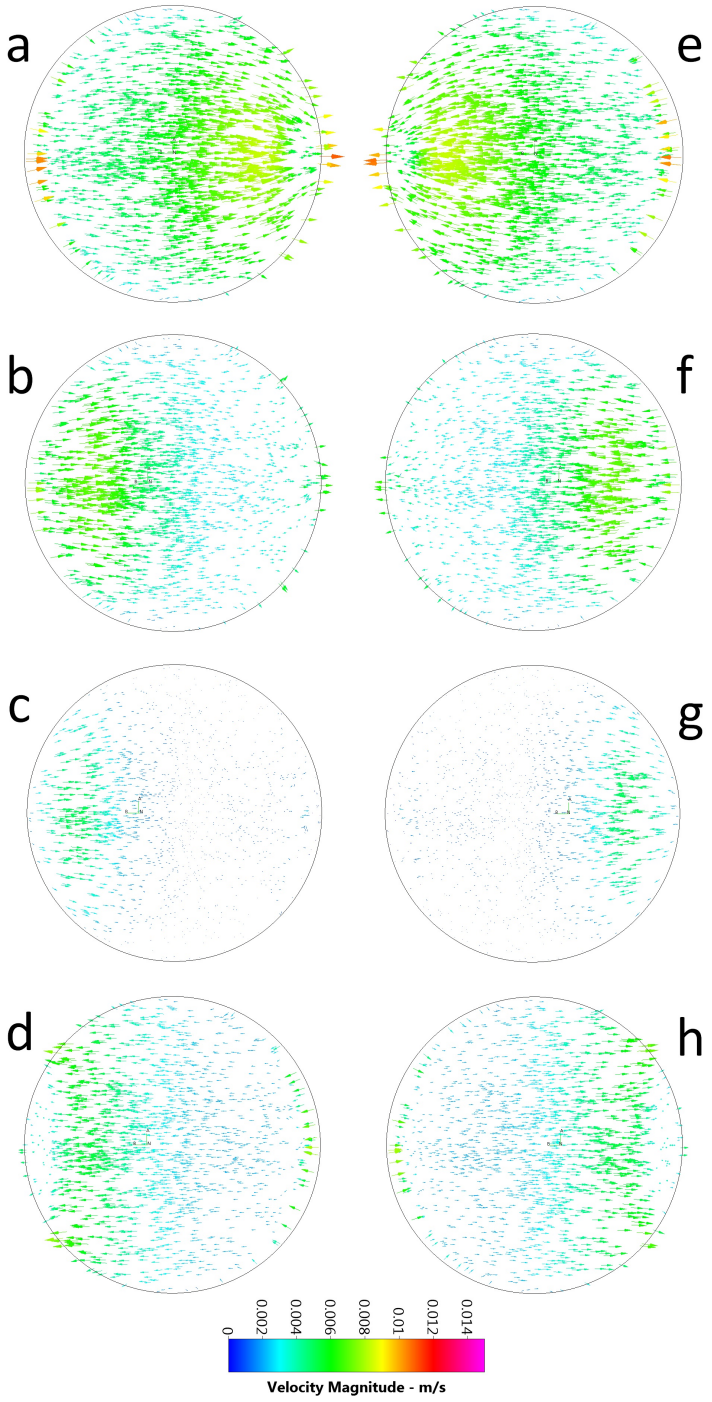

Figure 6.20: Velocity magnitude vectors at the well base: inspection indicates that fluid flow vectors are at 90 ° to the axis of rotation, indicating that tenocytes in the central area of the well are influenced by oscillating flow. For the purposes of generating an image, a thinning process has been applied to obtain a vector density at which individual vectors are identifiable. [a = 0, b = 0.25 … h = 2 s].

image has a characteristic pattern this is reported as part of the analysis, and issues such as thresholding required for cell identification are not present.

Phase-contrast images were taken from the centre of culture wells and subjected to a custom intensity analysis technique based on a previously described method for analysing the fibre alignment of composite materials (292). Images were rotated in 10 ° steps through 180 ° from the y-axis, and the cumulative intensity variance over a pixel window (size $n \times n$) calculated for each rotation angle (θ = 10, 20, ... 180). The angle that produced the minimum variance for each pixel was reported and a map showing the angle with the minimum intensity variance produced, ($\Theta(x, y)$) (Equation 6.4).

$$\Theta(x, y) = \min_{\theta=0}^{180} \left(\sum_{i=1}^{n} \sigma(\overline{\gamma_n}) \right) \tag{6.4}$$

where σ is the intensity variance and $\overline{\gamma_n}$ is a vector across n pixels.

From the angle map, frequency distributions of the minimum reported angle for each pixel were formed, identifying trends in alignment.

In order to quantitatively evaluate the orientation of tenocytes subjected to fluid flow compared with a control group, tenocyte alignment congruity, Ψ, was calculated from the angle map frequency distributions (Equation 6.5).

$$\Psi = \sum_{i=1}^{k} (\chi - \overline{\chi})^2 \tag{6.5}$$

where χ is reported for each angle of rotation k and is the frequency of pixels that reported that angle as having the minimum intensity variance, and $\overline{\chi}$ is the mean pixel frequency across all angles, *i.e.* the total number of pixels in the image divided by the number of stages of rotation.

Tenocyte alignment congruity values are normalised to the control group, (*i.e.* control Ψ=1) for comparison across cultures and statistical analysis.

Cell elongation $\Lambda(x, y)$ was determined from the aspect ratio of each pixel within an image. This was achieved by evaluating the maximum and minimum cumulative intensity variances from a captured image (Equation 6.6).

$$\Lambda(x, y) = \frac{\max_{\theta=0}^{180} \left(\sum_{i=1}^{n} \sigma(\overline{\Gamma_n}) \right)}{\min_{\theta=0}^{180} \left(\sum_{i=1}^{n} \sigma(\overline{\Gamma_n}) \right)} \tag{6.6}$$

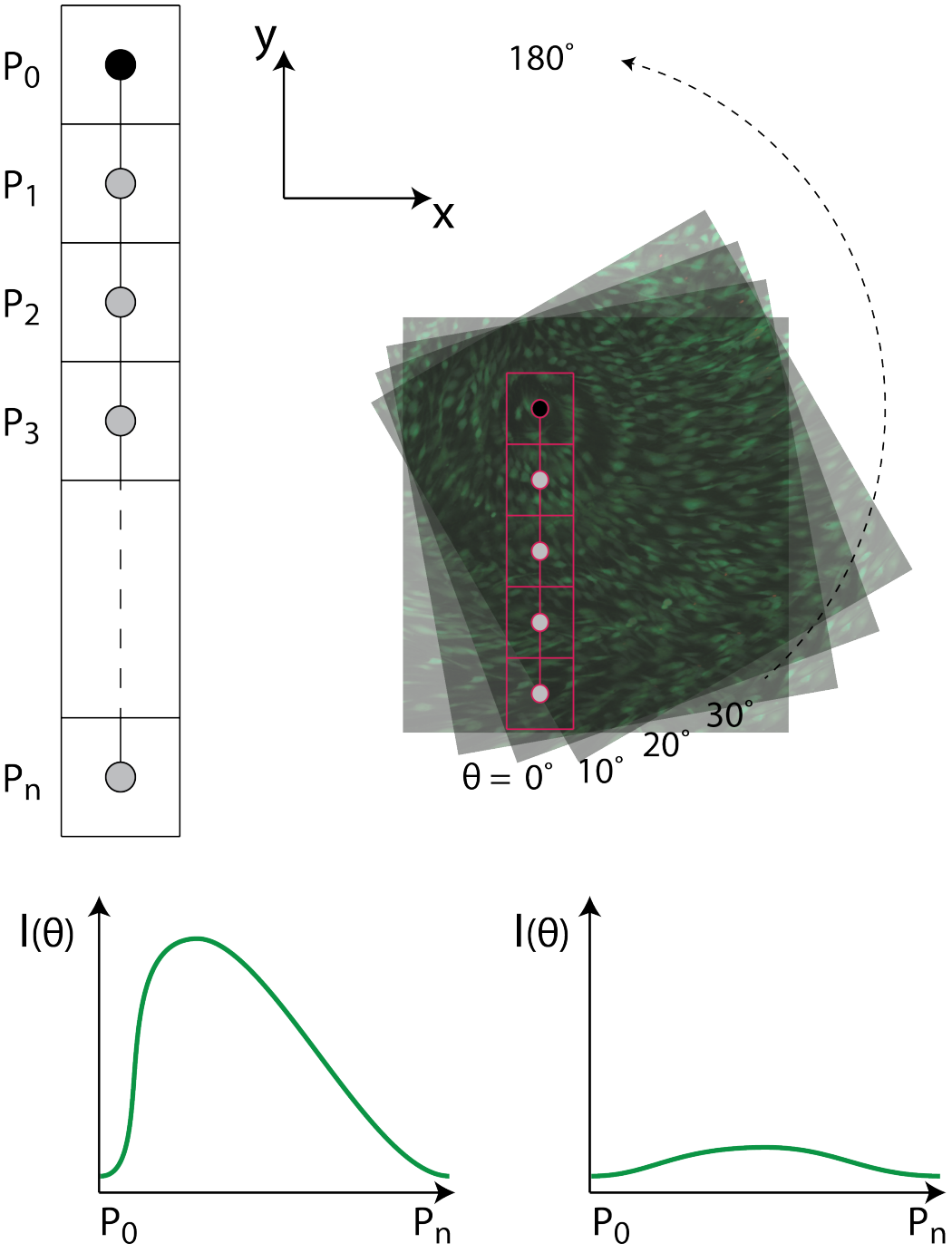

Figure 6.21: Alignment and elongation algorithm principle: a pixel array (top left) is determined by the user and an image rotated in ten degree intervals (top right) for every pixel P_0. At each angle, the variance in intensity across the array is measured. Alignment is concluded to occur at the angle with the smallest intensity variance (bottom right). Elongation is defined by an aspect ratio, which is the maximum intensity variance (bottom left) divided by the minimum intensity variance (bottom right).

To experimentally investigate the effect of fluid shear stress on alignment and elongation in tenocyte cultures exposed to the same range of shear stresses and loading regime as detailed in Section 6.2.2.1, the algorithm was completed for 25 images, using cells from two healthy patients (n = 25). Images were taken at a magnification of 4x (Figure 6.22) and analysis was completed using 5×5 pixel windows, equivalent to *circa* $8\,\mu m \times 8\,\mu m$. This was deemed an appropriate pixel window size in order to capture individual cells as opposed to clusters of cell populations. As cells are compartments, any alignment and elongation evaluation will not result in a single angle or aspect ratio output. There will always be distribution of the angles with the maximum and minimum frequency as the curved ends of cell processes are taken into consideration.

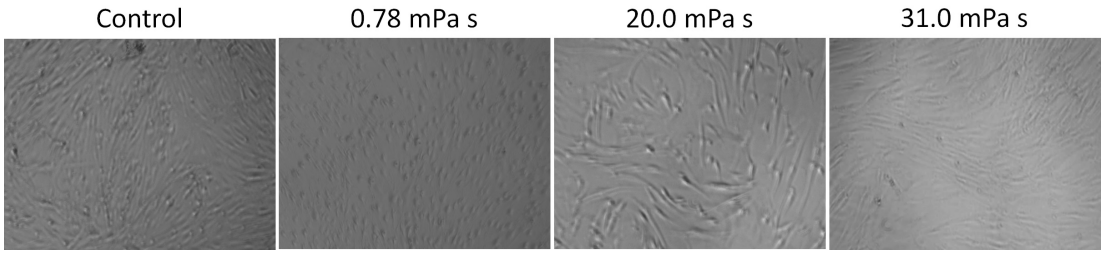

Figure 6.22: Representative images used for alignment and elongation analysis: phase contrast images of tenocytes at a magnification of 4x were obtained for analysis using the alignment and elongation algorithm.

6.4.2 Alignment results

Comparison of various viscosities indicates that at 0.78 mPa s (0.033 Pa), tenocytes become aligned in the direction of fluid flow (180 °) (Figure 6.23). Results of control conditions are similar to viscosity conditions of 20.0 mPa s (0.714 Pa) and 31.0 mPa s (1.023 Pa) (n = 25) (Figure 6.23).

Tenocytes exposed to a culture medium viscosity of 0.78 mPa s (0.033 Pa), are significantly more aligned than tenocytes exposed to no stimulus and tenocytes exposed to a culture medium viscosity of 20.0 mPa s (0.714 Pa) ($p < 0.001$) (Figure 6.24).

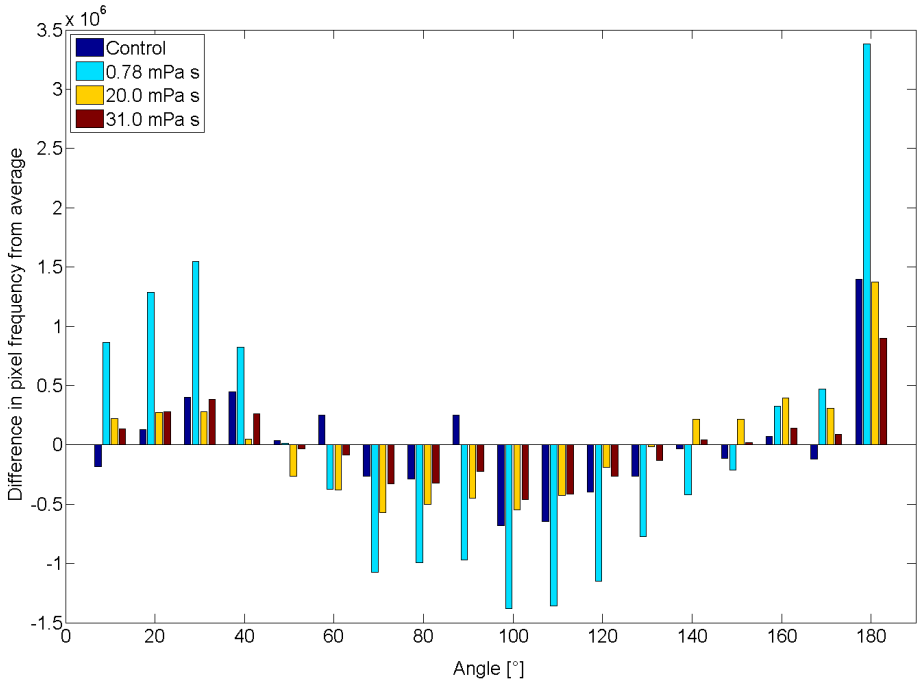

Figure 6.23: Alignment analysis: X-axis represents each stage of rotation (10, 20, 30, ... , 180). The Y-axis represents the number of pixels reporting that stage of rotation as having the minimum intensity variance compared to all other stages of rotation. For each stage of rotation, reported frequencies have been set a baseline of the average pixel density assuming alignment was equal in all directions. n = 25 for each condition.

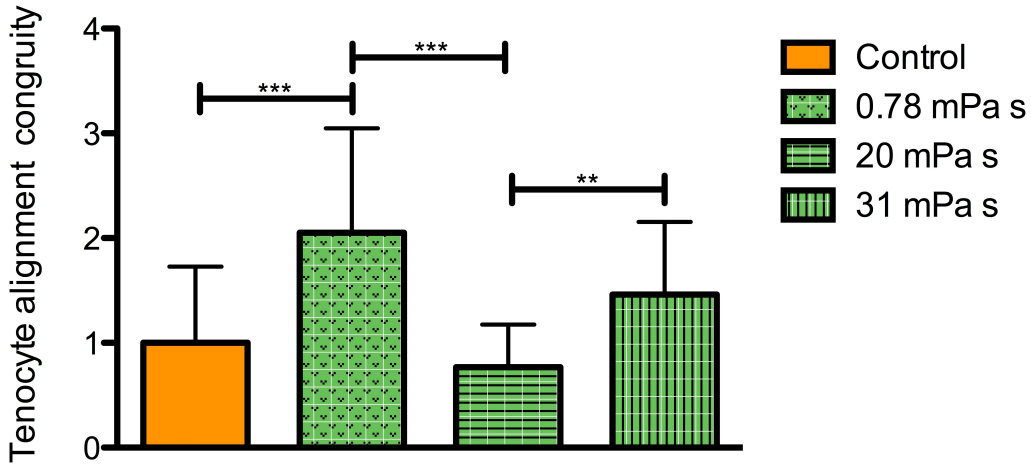

Figure 6.24: Alignment congruity: X-axis represents each fluid viscosity condition. Y-axis is tenocyte alignment congruity calculated from Equation 6.5. (** = p <0.01, *** = p <0.001).

6.4.3 Elongation results

Analysis of tenocytes exposed to fluid-induced shear stress of 0.033 Pa, 0.714 Pa, 1.023 Pa and cells that were exposed to no stimulus (controls), indicated that tenocytes become significantly more elongated after shear stress of 0.033 Pa in comparison to all other conditions ($p < 0.05$) (Figure 6.25).

6.4.4 Discussion

The application of fluid-induced shear stress of 0.033 Pa caused tenocytes to become significantly more aligned and elongated in comparison to control conditions ($p < 0.05$).

Although significant differences in elongation are identified between the different conditions, the difference in aspect ratio is only 0.4 between the control condition and cells exposed to a shear stress magnitude of 0.033 Pa, therefore they may not be meaningful. It is hypothesised that tenocytes alter their structure to find a more 'favourable' shear stress condition, that is, by becoming aligned and elongated in the direction of fluid flow, the magnitude of shear stress acting on the tenocyte structure would be reduced. It may be interesting to model the differences in stress between

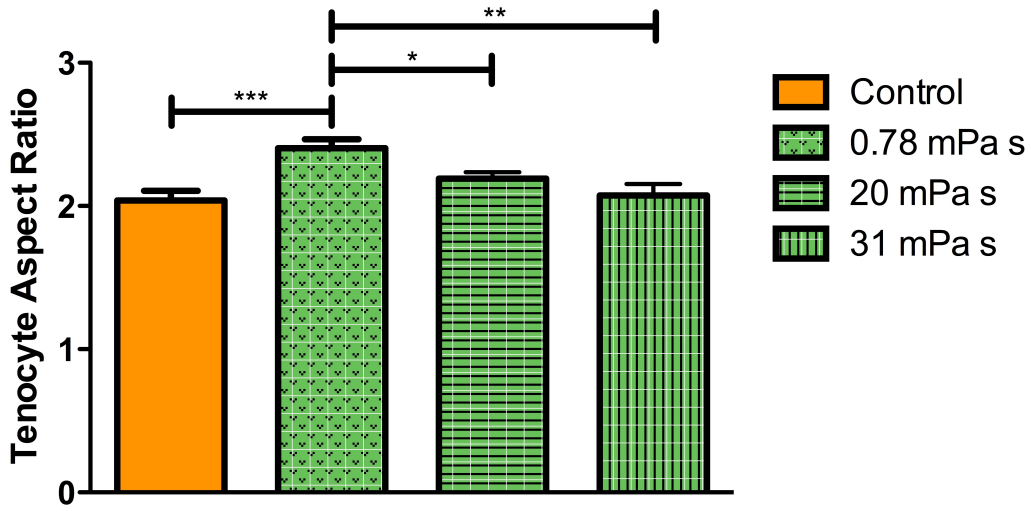

Figure 6.25: Elongation: tenocytes exposed to a culture medium viscosity of 0.78 mPa s (0.033 Pa), are significantly more elongated than controls and tenocytes exposed to higher viscosities. (* = p <0.05, ** = p <0.01, *** = p <0.001).

tenocytes with an aspect ratio of 2.0 and 2.4 similar to endothelial computations by Yamaguchi *et al.* (289).

Cell alignment is permitted by changes in cytoskeleton structures (287, 288). Therefore an investigation into actin and intermediate filaments, as well as microtubules, to identify whether the structures of the cytoskeleton become aligned in the direction of fluid flow may be beneficial and provide a more detailed understanding of the method of cell alignment.

An increase in shear stress, past an unidentified threshold, appears to reduce alignment. It is hypothesised that this may be because cells are using energy for non-alignment cell processes at 0.714 Pa, such as the production of catabolic enzymes.

As the custom image analysis algorithm analyses the entirety of an image, in establishing alignment and elongation, it includes the intensity of non-tenocyte structures in its variance analysis. As such, although tenocytes are the clear, visible structures from phase-contrast images, the results included any other structures, such as secreted proteins, that were large enough to be captured by phase-contrast imaging at a magnification of 4x. Thus, the results were truly a quantification of the alignment of all

visible structures at the cell layer.

The custom algorithm has some limitations. Firstly, calculations are performed for every pixel within an image, resulting in a large computation time. Going forward an assessment of whether computations for a selection of pixels is representative of the overall behaviour would be beneficial to improve the speed of analysis. Additionally, the location of image capture was estimated to be the centre of culture wells; however a more accurate system of location identification and comparison with the CFD-derived velocity vectors may provide more insight to cell response. Finally, the algorithm does not separate out the alignment of cells and matrix structures for phase-contrast images; however this limitation may be circumvented by using targeted imaging techniques as using immunohistochemistry results from Section 6.3.1, 0.033 Pa was shown to produce collagen aligned with the direction of applied fluid flow (Figure 6.26).

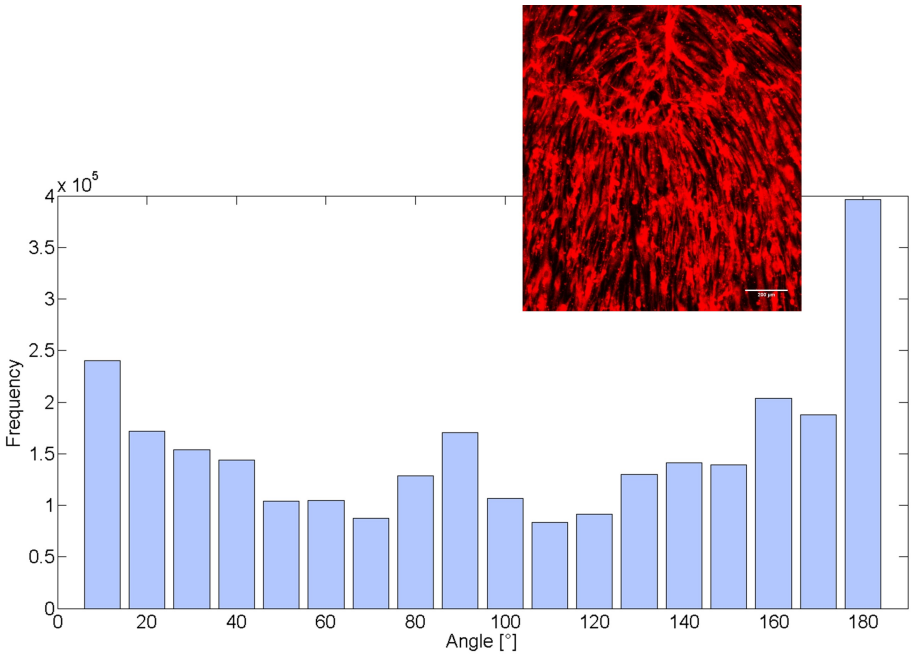

Figure 6.26: Collagen type-I aligns with the direction of fluid flow: after the application of 0.033 Pa, collagen type-I becomes aligned with the direction of fluid flow (180 °). Analysis is performed on the collagen type-I immunohistochemistry results (Section 6.3.1 & inset).

6.5 Tenocyte detection of fluid flow: the primary cilium

Several investigations have shown the role of the primary cilium in detecting fluid forces in bone tissue *in vitro* (29, 120, 198, 293). In addition, the primary cilium has been detected in rat tendon tissue *ex vivo* (294); however, whether the primary cilium is involved in the detection of fluid forces by human tenocytes remains unclear.

The aims of the presented investigation into the primary cilium are:

1. to identify the primary cilium in tendon tissue;
2. to identify the primary cilium in tendon cell culture; and
3. to assess the effect of experimental procedures designed to abrogate primary cilia from cell cultures on response to fluid shear stress

6.5.1 Primary cilia in tendon tissue

Evidence that primary cilia are oriented with the direction of collagen and the long axis of tendon has been obtained for rat extensor tissue (294). Immunohistochemistry was performed on bovine flexor tendon to identify whether this orientation was present in other tendon tissue (methods as per Sections 5.6 5.7.2.1).

6.5.2 Primary cilia in tenocyte cultures

Preliminary work showed that for the maximum amount of cilia expression in a tenocyte culture, 100 % confluency is required, and cells should be exposed to 0 % FCS for 24 hours (Figure 6.29). This finding is consistent with studies of other tissue where confluency and starvation are concluded to be consistent drivers of cilia growth (295).

6.5.3 Abrogating primary cilia

Chemical abrogation, or retraction, of primary cilia in cell cultures has been achieved successfully in bone cells using chloral hydrate (120) following its development for Madin-Darby canine kidney (MDCK) cells (296). The bone cell protocol uses 4 mM of chloral hydrate applied to cells for 72 h, washing with PBS and providing fresh culture medium for 24 h prior to the application of fluid flow. Chloral hydrate causes the destabilisation of microtubules as well as primary cilia. The application of fresh medium

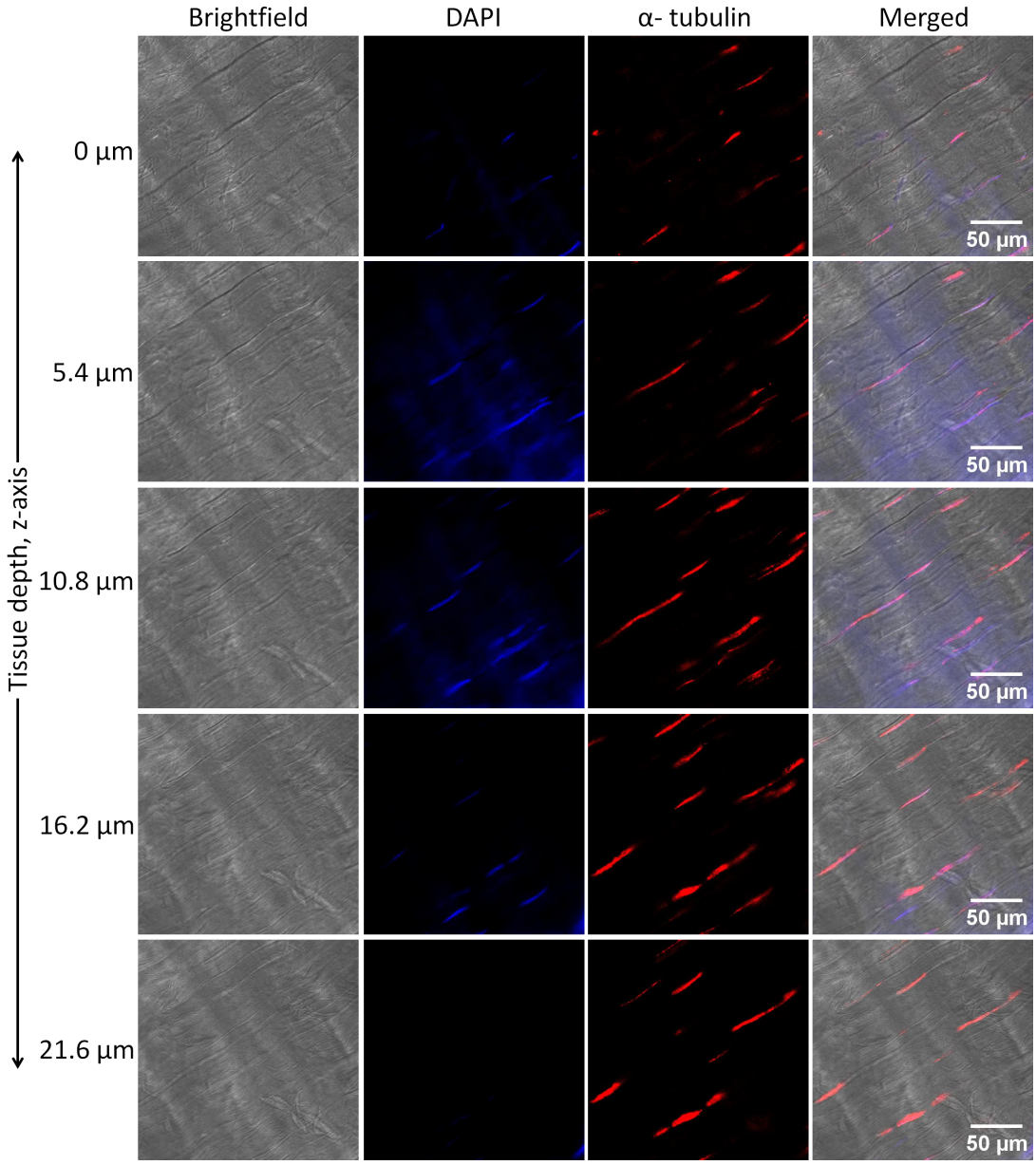

Figure 6.27: Primary cilia in bovine tissue: primary cilia are orientated with the direction of collagen fibrils and protrude into the extracellular space through the tissue. Cell nuclei are stained by DAPI (blue) and primary cilium are stained using a primary antibody targeting acetylated alpha-tubulin (red). Confocal microscopy is used to obtain a z-stack at 5.4 micron intervals. Tissue extraction methods detailed in Section 5.6.

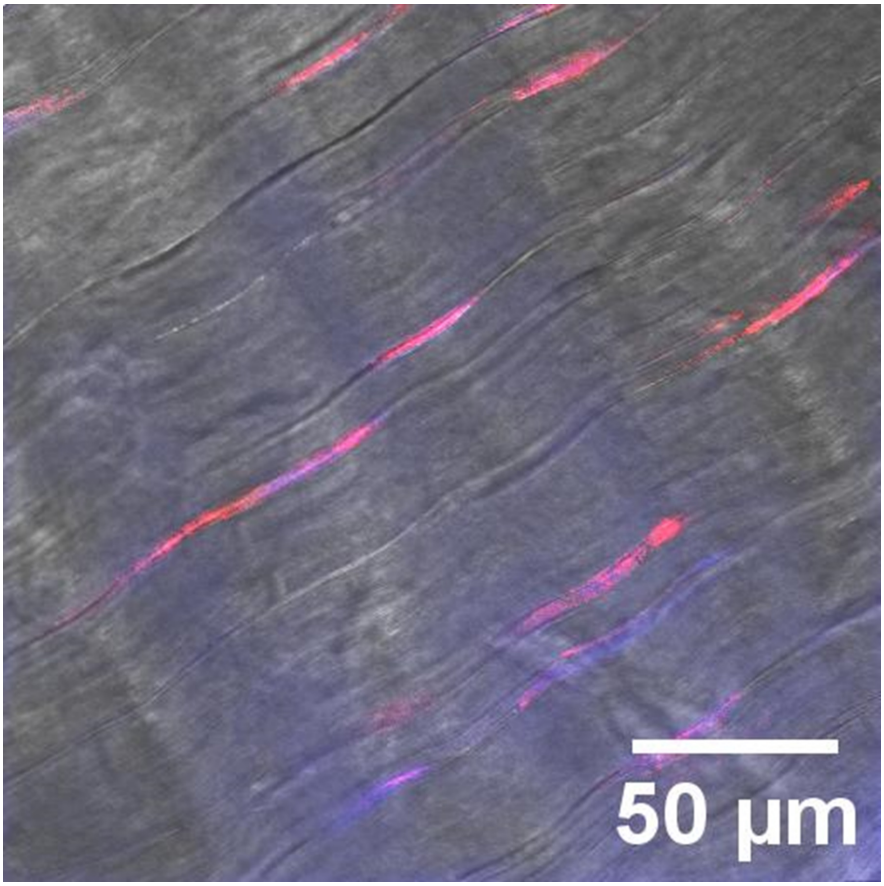

Figure 6.28: Primary cilia are located near tenocyte nuclei and are aligned in the direction of collagen fibrils: clear alignment of primary cilia with the direction of collagen fibrils is present. Cilia are located near tenocyte nuclei. Cell spacing is consistent with reports of tenocytes being found surrounding bundles of fibrils, named as fibres.

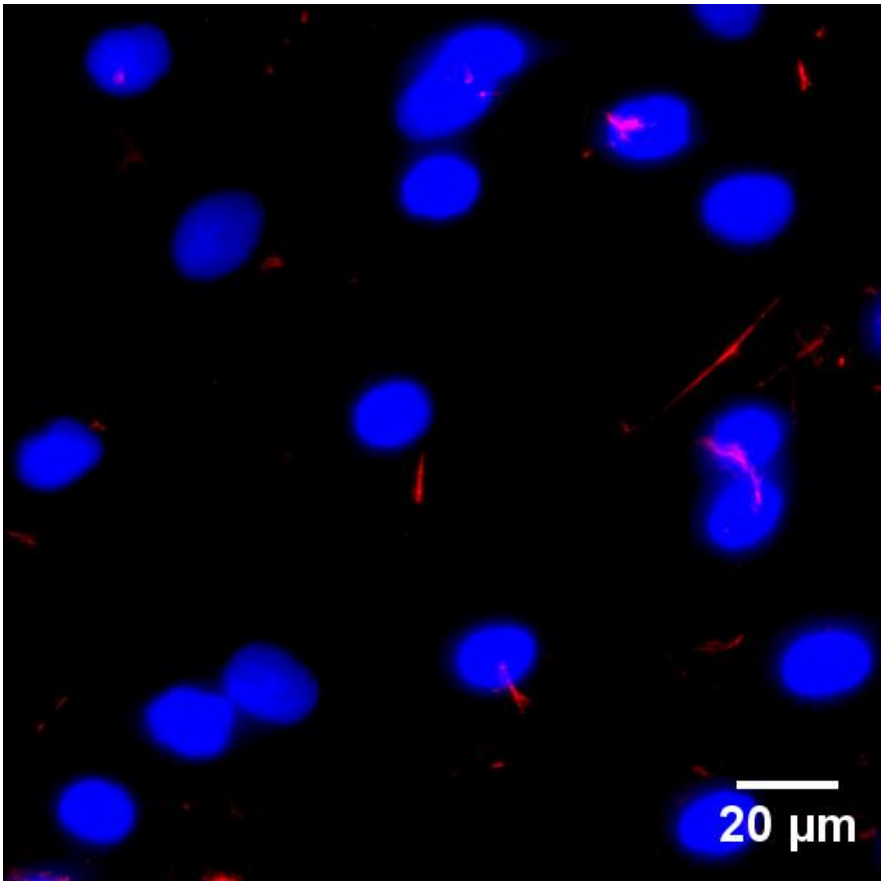

Figure 6.29: Primary cilia in cell culture: culturing tenocytes to a high confluency, followed by application of serum free culture medium for 24 hours provides ideal conditions for primary cilium expression. Cell nuclei are stained by DAPI (blue) and primary cilia are stained using a primary antibody targeting acetylated alpha-tubulin (red). Cilia may appear as small specks as they orientate in the vertical direction, or as clear hair-like structures orientated with the imaging plane.

for 24 hours prior to stimulation is hypothesised to give the cell time to re-stabilise microtubule structures, but is not enough time for the primary cilium to re-form.

Application of the same protocol to tenocytes caused widespread cell necrosis. Reducing the chloral hydrate concentration continued to cause cell necrosis until a concentration of 1 nM was applied (Figure 6.30). Live and dead imaging indicated that chloral hydrate treatment had a severe effect on tendon cell viability at a concentration of 4 nM. At a concentration of 1 nM viability was not affected (Figure 6.30); however, immunohistochemistry of tenocytes exposed to 1 nM of chloral hydrate for 24 hours confirmed that the primary cilium was not abrogated across the entire culture. At 1 nM, pH levels increase to 7.65 from a range of 7.0-7.4 for untreated culture medium.

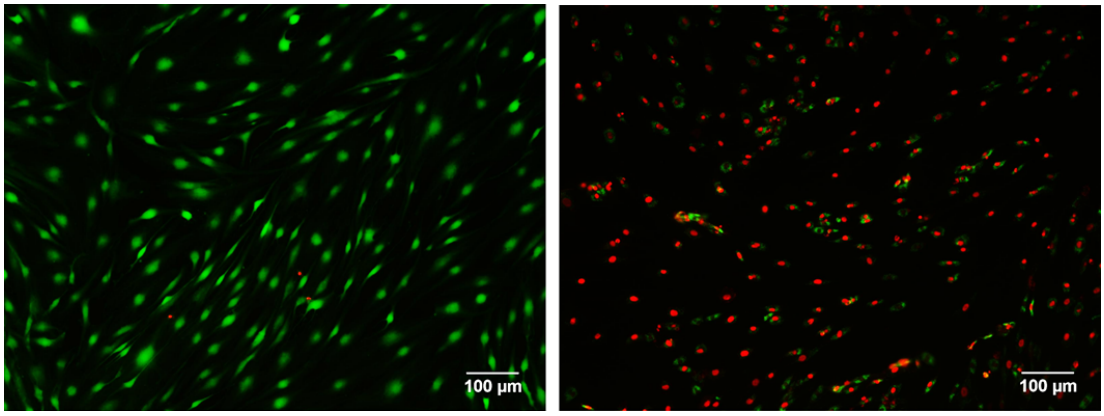

Figure 6.30: Live & dead cell staining: green cells are live and red cells are dead. Left - tenocytes exposed to 1 nM of chloral hydrate for 24 hours. Right - tenocytes exposed to 4 nM of chloral hydrate for 24 hours, 1/1000 of the dosage used in previous successful bone cell investigations (120).

6.5.4 Discussion

Evidence of the existence and orientation of the primary cilium *ex vivo* has been obtained for bovine flexor tendon using immunohistochemistry, correlating with previously findings for rat extensor tendon (294). In addition, the optimum conditions for the expression of the primary cilium in tenocyte cultures has been established; however chemical removal of the primary cilium has proved complicated and the application of previously successful methodologies in bone cultures lead to tenocyte necrosis. As a result it was not possible to establish whether the primary cilium is a key detector of

fluid flow in tenocyte cultures. A systematic approach to varying durations of 1 nM of chloral hydrate should be applied in future experiments to determine when primary cilia are abrogated. To prevent cell necrosis, extremely low concentrations of chloral hydrate, relative to bone cells, may be required due to the importance of tenocyte morphology, partly maintained by microtubules. Interestingly it was identified that in water the pH values for concentrations of 1 nM and 4 nM of chloral hydrate were 4.90 and 4.23 respectively, suggesting that the buffer HEPES in DMEM:F-12 may play a significant role in maintaining pH levels when chloral hydrate is added to culture medium.

In providing the optimum conditions for cilia expression, it is considered that the confluent layer could be providing tenocytes with a more *in vivo* like environment, where cell-cell communication is at a peak. Starvation is also likely similar to the *in vivo* environment, as cells are focused on differentiation-type activities rather than proliferation. Part of this may include the expression of a primary cilium. In addition, the primary cilium is not expressed in cultures that are undergoing division as part of the process of proliferation. Once the cell has divided, the primary cilium is expressed through the polymerisation of the axoneme and ultimate extension in to the pericellular space.

6.6 Fluid flow affects tenocyte signalling and gene activity

In addition to the results already presented, collaborations were undertaken with Dr. Philippa Hulley and Dr. Andrew Jones (Nuffield Department of Orthopaedics, Rheumatology and Musculoskeletal Sciences, University of Oxford) to investigate the impact of fluid-induced shear stress on tenocyte: kinase signalling, transcription factor C-fos response; and matrix & communication gene activity.

6.6.1 Kinase signalling

Confluent tenocytes were grown without FCS for 24 hours before being subjected to cyclic rocking at 0.083 Hz for various durations up to a maximum of 60 minutes (t=0, 5, 10, 15, 20, 30, 60). Relative intensity of phosphorylated ERK was measured as per methods described in Section 5.9.

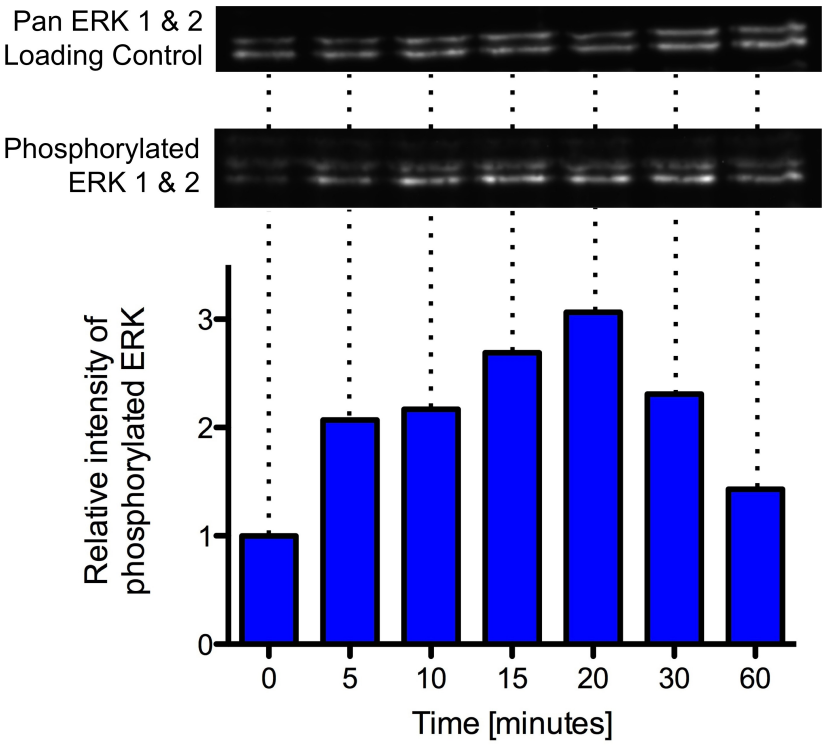

Figure 6.31: Fluid-induced shear stress of 0.012 Pa induced kinase signalling: the relative intensity of phosphorylated ERK reached a maximum after 20 minutes of rocking.

Results showed that ERK signalling increased with an applied fluid shear stress and peaked after twenty minutes of rocking (Figure 6.31). The ERK signalling pathway has been shown to be downstream of primary cilium flow detection (Section 1.3.3).

6.6.2 Transcription factor response

c-Fos is a gene transcription factor, converting extracellular signals into gene expression. Confluent tenocytes were grown without serum in DMEM:F12 for 24 hours before being subjected to rocking at 0.083 Hz for varying durations up to a maximum of 60 minutes (t=0, 5, 10, 15, 20, 30, 60). c-Fos levels were measured as per methods described in Section 5.9.

c-Fos mRNA levels increased when tenocytes were subjected to rocking, with maximum responses at 20 and 30 minutes (Figure 6.32).

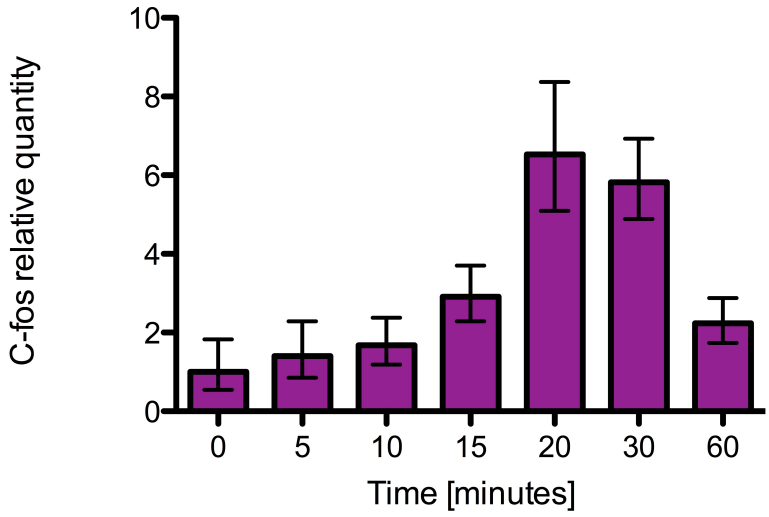

Figure 6.32: Transcription factor c-Fos is affected by fluid-induced shear stress: rocking at 0.083 Hz induced a maximum c-Fos response after 20 minutes of rocking.

6.6.3 Matrix & communication gene activity

Confluent tenocytes were grown in 0.5 % (v/v) FCS, DMEM F:12 for 24 hours before the application of 0.012 Pa of shear stress (Section 5.1), induced by a rocking oscillation of 0.083 Hz for 48 hours, and a subsequent rest period of 24 hours.

mRNA expression of collagen type-1α1, collagen type-IIIα1, collagen type-VIα1, collagen type-VIα2, collagen type-VIα3, connexin-43 and decor in were measured using qPCR as per methods described in Section 5.9.

Shear stress of 0.012 Pa caused the relative increase in the expression of mRNA for all genes investigated (Figure 6.33). The relative increase in collagen type-VI mRNA was particularly high, suggesting that 0.012 Pa may be a stimulus conducive to activating pathways that result in the secretion of pericellular matrix proteins. Additionally, an increase in collagen type-I appeared small, but this increase may be much larger than other genes in real terms, potentially inducing the secretion of significant quantities of collagen type-I extracellular matrix. Connexin-43 expression increased also. This may have been a result of tenocytes becoming aligned at 0.083 Hz allowing the formation of more gap junctions, or it may be the start of tenocytes forming more gap junctions for cell-cell communication after receiving a stimulus.

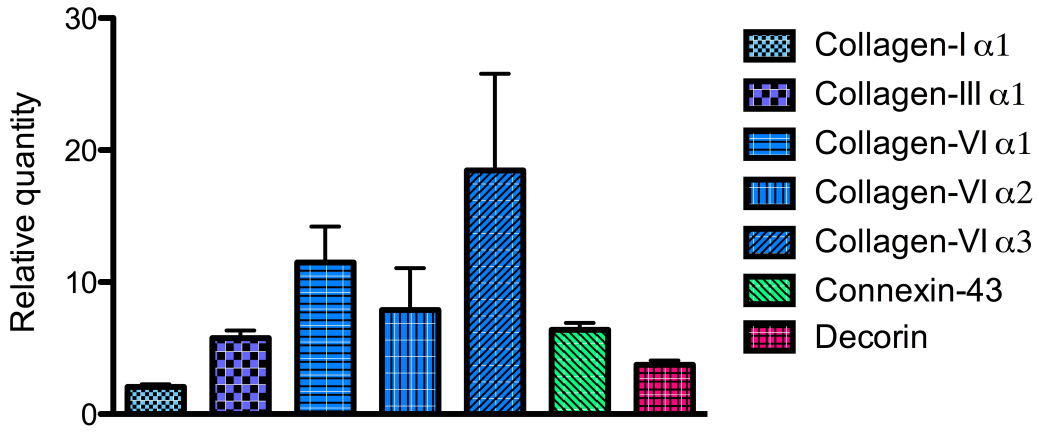

Figure 6.33: Relative gene expression increased for key matrix and cell communication genes after 48 hours at 0.083 Hz: quantification of collagen type-I, collagen type-III, collagen type-VI, connexin-43 and decorin mRNA levels indicated that fluid-induced shear stress of 0.012 Pa increased mRNA expression. All values are relative to control conditions for respective genes that are normalised to a value of 1 (not shown).

6.6.4 Discussion

Analysis of signalling pathways indicated that ERK peaks 20 minutes after stimulation at 0.083 Hz, corresponding with an increase in the transcription factor c-Fos after 20-30 minutes. Investigation into anabolic gene expression levels identified an increase in relative quantities for collagen type-I, type-III, type-VI, connexin-43 and decorin genes, suggesting that the activation of identified signalling pathways may be causing the downstream increase in gene expression. The increase in gene expression is potentially a pre-cursor to the change in quantities of collagen secreted from tenocytes.

The 20-30 minute peak in cell signalling correlates with a further investigation that identified no difference between tenocytes exposed to 0.083 Hz and control conditions for varying durations, where collagen assays were performed immediately after stimulation (Figure 6.34).

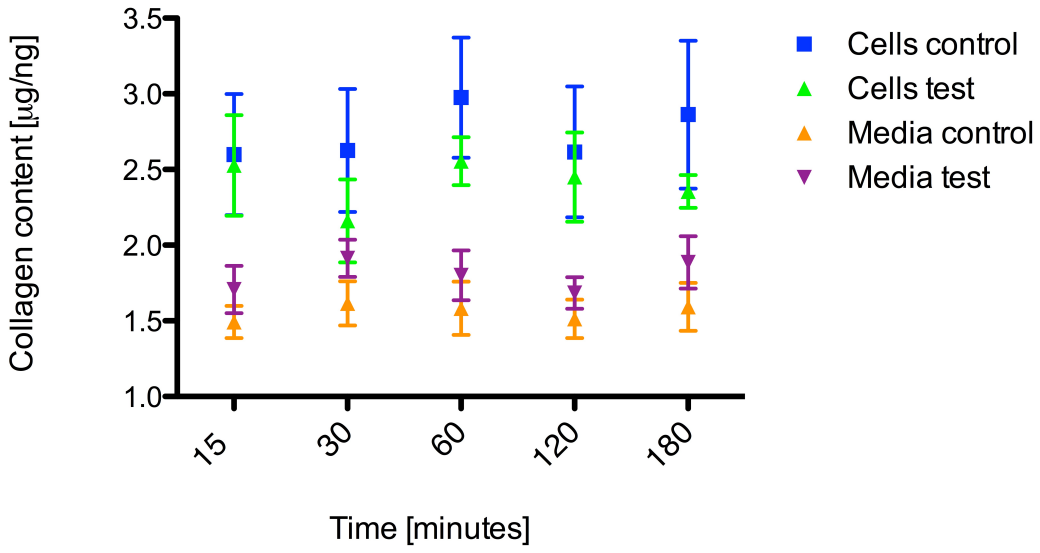

Figure 6.34: Collagen initial response time course: no significant differences between collagen at the cell layer and within culture medium for test and control conditions was identified when assays were performed immediately after stimulation at 0.083 Hz for $15 - 180$ minutes.

6.7 Summary

Investigations have validated the see-saw rocker as a reliable and adaptable tool for the study of tenocyte response to fluid-induced shear stress. The versatility of this simple, validated *in vitro* tool has been demonstrated and the following key conclusions have been drawn:

- Fluid induced shear stress of 0.012 Pa applied using rest-insertion and continuous stimulation regimes significantly increased secreted collagen retained at the cell layer, released into the media and GAG retained at the cell layer in comparison to controls.
- Collagen quantities within cell culture medium after the application of fluid-induced shear stress of 0.033, 0.053 and 0.714 Pa is significantly higher than controls.
- The application of fluid-shear stress of 0.033 Pa increased the aspect ratio of the cell layer and encourages tenocyte alignment with the direction of fluid flow in comparison to static controls.
- Immunohistochemistry has indicated a similar relationship between collagen type-I presence at the cell layer and quantities reported in cell culture medium using a Sircol biochemical assay. In addition connexin-32 presence appeared to be co-localised with collagen type-I at the cell layer.
- Collagen type-VI and fibrillin-I immunohistochemistry indicated an increase in their presence after the application of 0.033 Pa in comparison to control conditions, and under increased shear stress magnitude conditions of 0.714 and 1.023 Pa, collagen type-VI and fibrillin-I appeared to amalgamate into localised bright-spots.
- Shear stress of 0.083 Hz induced a peak in ERK and c-Fos after 20 minutes and relative quantities of collagen type-I, III and VI genes, as well as connexin-43 and decorin genes, have all been shown to up-regulate after 48 hours of rocking in collaborative investigations.

In addition, the foundation of a mathematical model has been created to act as a platform for predicting and characterising the secretion of matrix and the development of an algorithm allows for the easy measurement of alignment and aspect ratios of whole cell monolayer populations.

Finally, primary cilia have been identified in bovine tendon tissue and human tenocyte cell cultures. Cilia abrogation has proved difficult and protocols require further investigation in order to identify whether the primary cilium is a key transducer of fluid forces in tenocytes.

Chapter 7

Discussion

Within this chapter the important findings of this work are summarised. The background, including general literature and motivation, that lead to the development of this thesis are presented, followed by an overview of the project aims and the approaches taken to achieve them. The achievements are discussed in the context of the work of other authors and groups. The limitations of each study are also addressed and finally, the direction of future work is suggested.

7.1 Background

Recent work has validated an orbital shaker as a model for *in vitro* cell stimulation (36); however, stress generated at high frequencies is more indicative of studies for endothelial cells, and musculoskeletal investigations have demonstrated changes in cell response at low frequency, cyclic shear stress applied with a see-saw rocker model (197, 198).

Although a rocking model has been mathematically analysed (199), reported shear stresses are without validation, necessary for a biological response to confidently be attributed to an applied stimulus.

As fluid-induced shear stress continues to take a firm footing in mechanobiological investigations of bone cells, the requirement for a tool that applies physiologically relevant shear stress to musculoskeletal cells in a simple, effective, and cyclic manner is essential. Previously, device design has caused a primary stretch to generate a significant fluid-induced shear stress, causing difficulty in identifying the trigger behind a measured biological change (38).

In addition, the use of devices across research groups with the same principle, but different dimensions, has led to the generation of uncomparable results as they are based on reported shear stresses that are different and remain unvalidated.

Due to few previous investigations, focussed on gene expression and calcium signalling, the characterisation of tenocyte response to fluid flow is limited, and most studies have been performed using animal cells in laminar flow chambers (Section 1.6.2).

Tendon injury is painful and debilitating, affecting sports participants and the middle-aged (297, 298). Of all reported sports injuries, $30 - 50\,\%$ are tendon disorders (299), while the incidence of rotator cuff tears is suggested to be as high as $30\,\%$ in cadaveric studies (300). Achilles' tendon injury impacts daily living and $25 - 45\,\%$ of patients eventually require surgery (301).

Understanding how tendon cells respond to fluid forces could form the foundations for the development of new drug therapies and physio-therapies, targeting a particular cell response by activating fluid flow mechanosensation pathways.

This thesis has presented an experimentally-validated *in vitro* model for the investigation of musculoskeletal cell response to shear stress and some preliminary results on tendon cell response. The tool is inexpensive, commercially-available, and allows results from multiple institutions to be directly comparable, thus accelerating the rate of scientific advancement.

7.2 Aims, objectives & approaches

This project had two over-arching aims.

1. To identify, design, characterise and validate an *in vitro* model for the application of cyclic, flow-induced shear stress to cell monolayers.

2. To biologically validate the *in vitro* model for use with human tenocytes and to capture their response using a computational model.

These aims were achieved using specific project objectives which will now be assessed in turn.

- *Establish an in vitro tool for applying physically-relevant, fluid-shear stress to cell culture monolayers as the sole method of stimulation*

- *Within the established tool, determine the range of shear stress using computational fluid dynamics.*

Within Chapter 2, computational fluid dynamics was used to estimate the shear stress within a well of a six-well plate induced by cyclic fluid flow from the motion of a see-saw rocker. Base-scenario frequency of 0.5 Hz in conjunction with a time-step size of 0.001 s generated the transient results from six complete cycles for ten models with a mesh density ranging from 5265 to 1470150 control volumes. Analysis verified that results were independent of mesh density and that transient initial effects were not present in the analysed cycle. From the computational model, shear stresses at the base of the well were obtained showing a mean shear stress of 0.033 ± 0.017 Pa with a range of $0 - 0.22$ Pa. The maximum shear stress was identified near the edge of the well and occurred at 0.9 s as the well approached the 0° position. Maximal velocity within the well was $\pm 0.08\,\mathrm{m\,s^{-1}}$ and occurred at the media-air interface. Throughout the entirety of the well, numerical analysis based on open-channel flow estimated that fluid flow was laminar. Sinusoidal velocity profiles oscillated at the driving frequency of the rocker.

- *From the fluid dynamics model, the pattern of flow velocities influencing cell characteristics will be determined and compared to an experimental flow measurement technique. Agreement will result in the validation of reported shear stresses at the cell layer.*

Particle image velocimetry was used to capture two-dimensional flow velocities on the x-z central plane of the well placed on the rocking platform. Proper orthogonal decomposition was used to eliminate non-periodic signals by comparison of the first 20 modes. Subsequently, further noise reduction was achieved using a low-pass filter. Qualitative analysis confirmed that the pattern of velocity magnitude across an entire cycle matched that of the CFD, validating the assumptions used in CFD modelling. Quantitative analysis indicated good agreement at different time points, acknowledging some error due to difficulty in identifying the base of the well.

- *A change in relevant model parameters will be considered by adapting the validated tool and performing further computational fluid dynamics for a change in frequency of rocking and the viscosity of the added culture medium.*

The CFD model presented in Chapter 2 was modified to generate new models: firstly at new fluid viscosities based on the addition of a biologically-inert cellulose to culture medium at concentrations of 0.1 % and 0.2 % (v/v); secondly at 5 cpm and 70 cpm to establish fluid-induced shear stress at the operational limits of the rocker; and finally the displacement of the well to the extremity of the rocker platform dimensions.

Results identified that an increase in viscosity caused an increase in fluid-induced shear stress, and that the shear stress magnitude varied approximately proportional to the culture medium viscosity. Shear stress patterns were similar to the base condition, with the vast majority of the well experiencing the same average shear stress, and the same edge location of peaks in shear stress were identified near the 0 ° position. Time-averaged shear stress of 0.714 ± 0.509 Pa and 1.023 ± 0.702 Pa were found for the 20 mPa s and 31 mPa s conditions respectively.

A rocking frequency of 5 cpm (0.083 Hz) was modelled and indicated an estimated mean shear stress of 0.012 ± 0.004 Pa. In addition, a model at 70 cpm (1.167 Hz) concluded mean shear stress to be 0.248 ± 0.169 Pa. Both models produced different shear stress profiles to the 0.5 Hz base-scenario; however time-averaged shear stress appeared to remain uniform across the well radius.

Displacement of the well to the platform extremity caused phase asymmetry of velocities and shear stress about the y-axis of the well, as the axis of rotation was shifted from beneath the well. Mean shear stress was computed to be 0.055 ± 0.025 Pa, a 1.61-fold increase on the base-scenario condition.

- *To ensure that the tool is useful for in vitro cell investigations, a series of preliminary tenocyte biological validations will be completed, focussing on tenocyte alignment and matrix secretion. This will be achieved using microscopy techniques and biochemical assays; and*

- *the adapted computational models and preliminary biological validations will act as a foundation for the formulation of a mathematical model to predict tenocyte response to fluid-induced shear stress, and further biological investigations will be completed to establish whether relationships can be validated experimentally.*

Investigations completed at the lowest identified shear stress of 0.012 Pa, induced by a rocking frequency of 0.083 Hz, resulted in the significant up-regulation of secreted collagen and glycosaminoglycans for two stimulation regimes. Using the results from these

stimulation regimes, a numerical model was defined to predict the quantities of collagen secreted into the culture medium at four different shear stresses, induced by a change in the location of the well on the rocking platform or the culture medium viscosity, and a rocking frequency of 0.5 Hz. As the secretory response at 0.012 Pa of shear stress was entirely anabolic for the first two stimulation regimes, the resulting model predicting future responses was also entirely anabolic. Findings from experimental investigations to validate the model predictions indicated that with a large increase in shear stress magnitude, induced by an increase in culture medium viscosity, tenocytes most likely enter a catabolic state, resulting in the reduction of collagen quantities compared to control conditions. Analysis of the relationship between applied shear stress and secreted collagen indicated a negative quadratic fit, suggesting that tenocytes may switch from a predominantly anabolic role to a catabolic one at 0.25 Pa.

Confocal imaging of immunohistochemistry targeting collagen type-I, collagen type-VI, fibrillin-I and connexin-32, indicated that shear stress has a significant affect on matrix proteins at the cell layer and tenocyte communication pathways. Collagen type-I content was present across an entire cell monolayer, next to every cell, after the application of 0.033 Pa in comparison to controls, where spider-like clusters of collagen were identified. Additionally, collagen type-I appeared to be more aligned in the 0.033 Pa condition, as were the cells with the predominant direction of fluid flow. After the application of 0.714 and 1.023 Pa, collagen type-I content at the cell layer appeared reduced, potentially as the result of an induced catabolic effect causing the release of MMPs and breakdown of collagen structures formed during cell growth to confluency. Collagen type-VI quantities appeared higher in tenocyte cultures exposed to fluid-induced shear stress; at 0.033 Pa the entire confluent cell layer appeared to have collagen type-VI structures, whereas at 0.714 and 1.023 Pa type-VI content appeared to be more aggregated into globule-like structures. Fibrillin-I results were similar, with an increase in content at 0.033 Pa in comparison to all other conditions, where fibrillin-I appeared to amalgamate into bright spots. Connexin-32 was particularly strong at 0.033 Pa and analysis identified that collagen type-I localisation corresponded with connexion-32 presence. At increased shear stress magnitudes, connexin-32 was less widely distributed and where it was present, appeared more concentrated, suggesting that potentially cells are focused on forming few strong gap junction plaque pathways rather than many less-strong pathways.

A custom algorithm was developed for the analysis of cell alignment and elongation using an image intensity interrogation technique. After the application of 0.033 Pa, tenocytes became significantly more aligned and elongated in comparison to controls. In addition, the application of shear stress of 0.714 Pa or 1.023 Pa reduced elongation to control levels. A link between cell elongation and matrix secretion is likely - the role of cell slope in detecting phenotype is well documented (302).

Collaborative investigations considered the impact of mechano-loading on kinase signalling, transcription factor response and gene expression. ERK pathways peaked after the application of 0.012 Pa for 20 minutes and c-Fos transcription factor response peaked after 20-30 minutes. In addition, the relative quantities for anabolic matrix genes increased for collagen types-I,III & VI and decorin after an applied fluid-induced shear stress of 0.012 Pa for 48 hours. Furthermore using the same stimulation regime, the relative quantity of connexin-43 also increased.

- *Finally, an investigation into the mechanosensor responsible for tenocyte flow detection will be performed.*

Primary cilia were identified *ex vivo* in bovine tendon tissue, orientated with the direction of collagen fibrils and the long axis of the tendon tissue. *In vitro* primary cilia were found to express in tenocytes when the cell layer was confluent and cells had been starved of FCS for 24 hours. Abrogation techniques utilised proved damaging to cell viability and resulted in widespread cell necrosis. The concentration of chloral hydrate required over a 24 hour period to ensure cell necrosis was eliminated was 1 nM; however this concentration did not abrogate cilia and experimental investigations designed to measure collagen secretion after the application of chloral hydrate were not performed.

7.3 Study limitations

7.3.1 Experimental validation of fluid dynamics

Two key limitations from the CFD validation were identified. Firstly, the ability to accurately identify PIV vectors at the base of the culture well. Secondly, the effect of potentially over-smoothing by the low-pass filter. The result of these limitations was that PIV and CFD measurements did not match precisely.

Identification of the base of the well proved difficult and the movement of data across a static grid led to some rounding and interpolation of data across a distance of 0.44 mm. This may have caused the inclusion of vectors further into the flow field at a higher velocity in the final solution used for comparison with the CFD output.

The low-pass filter caused the over-smoothing of some data points, potentially causing the loss of part of the signal. Comparison of the raw PIV data with the CFD results indicated areas of matching that were subsequently lost after smoothing.

7.3.2 Fluid dynamics estimation of shear stresses

A minor limitation of the study was that the fluid flow calculations did not consider the cell layer or the secreted matrix in deriving flow behaviour and shear stress patterns. The shape and structure of the cell layer would have a small impact on the derived local shear stresses; however the global impact on the model would be minimal. The free surface would continue to move over a confluent layer of cells, most likely within the boundary layer of flow, having a limited impact on the velocity conditions within the 2 mm of fluid directly above. Tenocytes are *circa* 10 µm in height, thus protruding in to only 0.5 % of the height of the fluid.

Secreted matrix, formed on top of a confluent layer of cells, may have the same level of impact as the cell layer itself on shear stress magnitudes; however, importantly, the secreted matrix may act as a buffer between the shear stress and the mechanotransducers of the cell. A reduction in the secretion rate of proteins may be influenced by previously secreted proteins that block a fluid flow signal from influencing the cell, as such, coupling a fluid dynamics model with a secretory response may be of particular interest in the future. This hypothesis could explain the change in the rate of secretion per cycle identified in preliminary investigations (Section 6.1).

7.3.3 Matrix quantification experiments

Imaging of a confluent cell layer identified that the picro-sirius red dye may bind to non-collagenous structures. If homogenous across all cells, this 'noise' is normalised to cell number and differences between tested and control conditions remain relevant and significant where identified; however establishing the exact quantity of collagen secreted as a result of stimulus proved difficult. Biochemical assay quantification of collagen content proved most successful by inspection of culture medium, although this

result did not quantify extracellular matrix found at the cell layer and the relationship between culture medium collagen content and matrix collagen content may not always be mirrored.

Two-dimensional testing of cell cultures is not representative of the three-dimensional *in vivo* environment. Tenocytes in tissue form attachments on all sides, whereas in culture, tenocyte attachment is limited to the area of the tenocyte that interfaces with the base of the culture well. This may induce tenocyte behaviour that is not indicative of an *in vivo* response.

Finally, normalisation of cell culture results was achieved using a picogreen biochemical assay. As this assay is destructive to the cell layer, it was performed for one control and one tested culture well, and the results used to normalise the biochemical assay results from the same condition. Although, tenocytes in control and tested conditions are exposed to the same conditions, imperfect seeding techniques may have resulted in an inflated secretion value after normalisation. However, the impact of this is considered to be minimal as standard deviations for collagen assays are minimal and in the 0.5 Hz experiment (Figure 6.12) differences identified were only intensified by normalisation.

7.3.4 Alignment & elongation algorithm

The alignment algorithm identifies the direction of the least intensity variance for the pattern of structures at the base of the well. Alignment that may be present in cells could be lost during analysis due to the lack of alignment of newly formed structures, such as secreted collagen.

Furthermore, the algorithm is designed so that when the intensity variance is equal for more than one inspected angle, the lowest reported angle is used in the final analysis. Although this condition is likely to occur only minimally due to the nature of the heterogenous cell surface, it may cause discrepancies in the results that are not immediately identified.

7.3.5 Primary cilium abrogation

The chemical abrogation of primary cilia from cell cultures using chloral hydrate proved extremely damaging to cell viability. Although a concentration was identified that limits cell necrosis, its ability to cause primary cilia to retract across a culture has not been

confirmed as a duration of 24 hours was shown not to be long enough. As chloral hydrate severely impacts cell viability, any further work completed to identify whether abrogation of the cilium using chloral hydrate affects collagen secretion should consider whether any changes identified are truly due to a lack of the cilium, or a change in the biochemical behaviour of tenocytes, influenced by the presence of chloral hydrate.

7.4 Further work

7.4.1 System for targeted collagen quantification at the cell layer

Due to difficulties identified in establishing the secreted collagen quantities at the cell layer, a new approach is required. Collagen is a birefringent material, that is, when rotated through a field of polarised light, the refractive index of the structure changes, causing a change in image intensity obtained by microscopy.

By generating a custom rig, the specific location of a six-well plate can be identified and rotated through a polarised light field and images captured to identify collagenous structures. As the process is not destructive, by taking images before and after an experiment the difference in identified collagenous structures may be assumed to be that which has been synthesised by the cell. The process could also be used to quantify the shape and alignment of the synthesised collagen using the custom developed algorithm.

By using a targeted approach to obtaining collagen images from specific well locations, the results of the birefringence imaging may be compared to CFD results and location specific shear stresses used to understand the results. As physiologically relevant stimuli, such as a 'stress-kick' have been shown to cause cells to respond to shear stress (35), it may be identified that secretion is caused by a group of cells that then distribute the secretion 'signal' to other cells using communication pathways such as gap junctions. Furthermore, it may be identified that some of the tenocytes are behaving anabolically and that other cells within the same culture well are behaving catabolically.

The change in intensity of collagen structures using polarised light microscopy has been shown using a collagen standard and the hypothesis of image comparison for two different angles shown in Figure A.9.

7.4.2 Investigate MMPs and extended experiment durations

Investigations at increased levels of shear stress magnitude have shown that cells are behaving in either a reduced anabolic capacity, or have entered a catabolic state. To establish which of these is occurring, an investigation into the expression of MMPs should be performed. This coupled with immunohistochemisty of collagen type-I at varying durations before and after stimulation should identify whether collagen is aggregated as cells grow to confluency and is then subsequently broken down by MMPs, or if an increase in shear stress magnitude causes less collagen to be synthesised and secreted.

7.4.3 Mechanoreceptor identification

Chemical removal of the primary cilium has proved difficult. Further work would benefit from a less crude method of primary cilium abrogation and it is recommended that the use of silencing RNA (siRNA) of the polaris gene (120) would indicate whether cilia play a key role in detecting fluid forces across tenocyte cultures.

Identification of the mechanoreceptor involved in the detection of fluid flow could provide the basis for the development of new drug therapies.

7.4.4 Damage and recovery

Establishing a shear stress that induces catabolic effects may be a useful *in vitro* tool for understanding the break down of collagen, associated with damage *in vivo*. It would be interesting to identify whether tenocytes that have entered a catabolic state can be induced into an anabolic state through a lower shear stress magnitude that has been shown to have clear anabolic effects. By using the system approach model, different stages of stimulus could indicate what might happen *in vitro*. Changing cells from a catabolic to an anabolic state could be the foundation for the development of new physiotherapies.

7.4.5 Coupled fluid dynamics model to investigate multiple secretion rates

The computational model could be adapted to include a coupled calculation of fluid flow properties and matrix secretion. This could be achieved by altering the porosity of control volumes near the cell layer when a certain shear stress condition is satisfied,

or it could be achieved by incorporating a shape and structure of the cell layer into the model design and subsequently updating this shape and structure with each time step in accordance with whether shear stress criteria have been satisfied.

The disadvantage of such a model is that it would add computation time to an already time-intensive simulation.

7.4.6 Further biological investigations

The versatility of the rocking model, and identification of shear stress magnitudes that generate different secretion patterns, allows for the application of a multitude of biological manipulations, including, but not limited to: hypoxic conditions; high and low glucose levels; silencing various genes to identify communication pathways using siRNA techniques; and targeting cell-cell communication pathways, by blocking gap junctions.

7.4.7 Development of the mathematical model

The foundation of a mathematical model has been defined and further work is required to establish the relationship between anabolic and catabolic cell response and applied fluid induced shear stress. By developing a strategy to break down cell behaviour using targeted experiments, the complexity of model predictions can be built up using the addition of fourier representations of sine waves to represent the applied shear stress and model input.

7.5 Conclusions

The validation of shear stresses generated by the see-saw rocker within a culture well gives confidence to the reported shear stress magnitudes that caused specific cell monolayer responses. Biological experiments have shown that a see-saw rocker is a reliable platform for varied investigations into the response of cell monolayers. In addition, the adaptability of the rocker has been identified, and results indicate that the range of shear stresses generated may be ideal for the investigation of both tenocyte anabolic and catabolic effects *in vitro*. The see-saw rocker model is a simple, commercially-available device, that now validated for use with six-well plates, allows the results of research institutions to be comparable and attributed shear stresses to be reliable.

Appendix A

Supplementary figures

Within this appendix, supplementary figures are provided as additional detail to results reported in the main chapters, as well as preliminary results for recommended further work. This includes:

1. Standard curves from biological investigations
2. Alignment validation
3. Collagen birefringence imaging

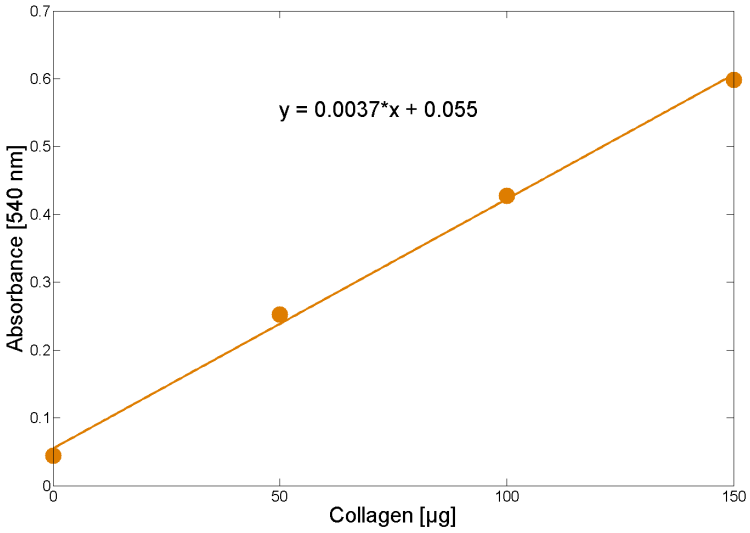

Figure A.1: Cell layer collagen standard curve: short interval and continuous stimulation (Section 6.1).

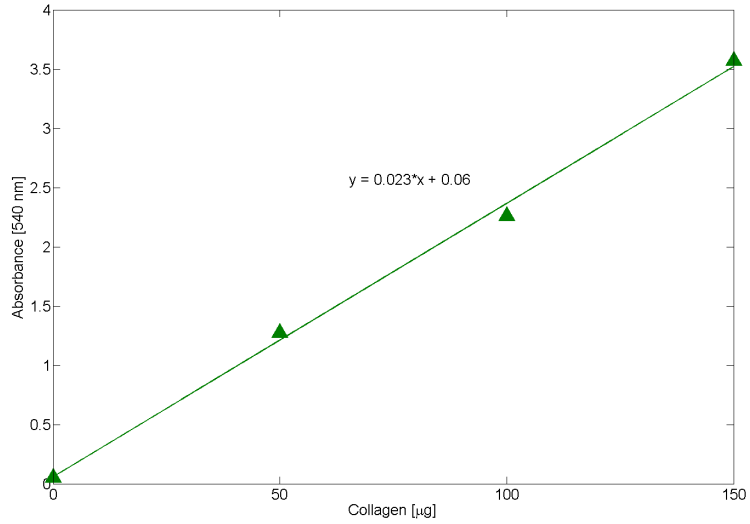

Figure A.2: Culture medium collagen standard curve: short interval and continuous stimulation (Section 6.1).

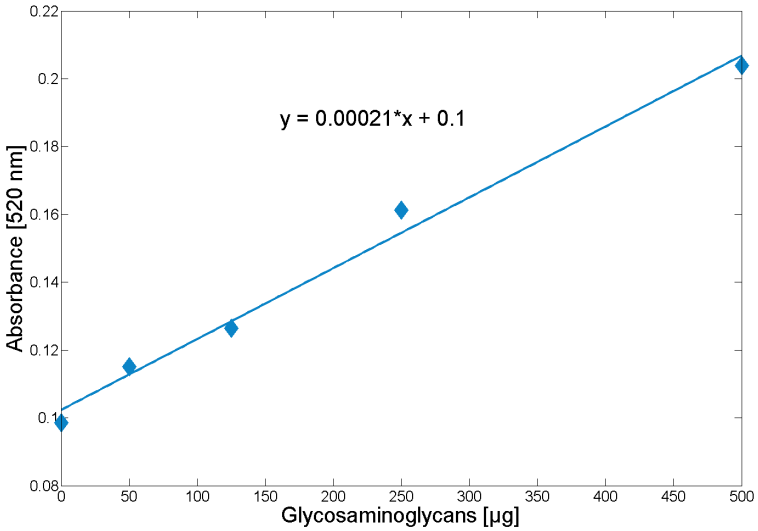

Figure A.3: Cell layer GAG standard curve: short interval and continuous stimulation (Section 6.1).

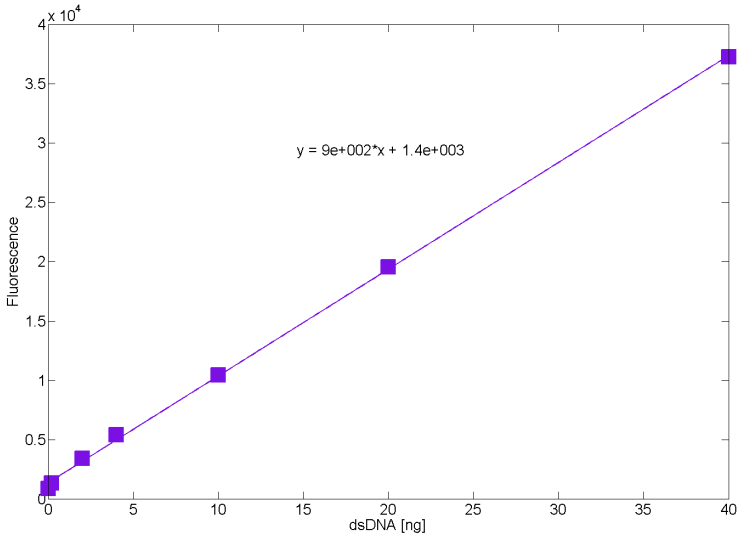

Figure A.4: dsDNA standard curve: short interval and continuous stimulation (Section 6.1).

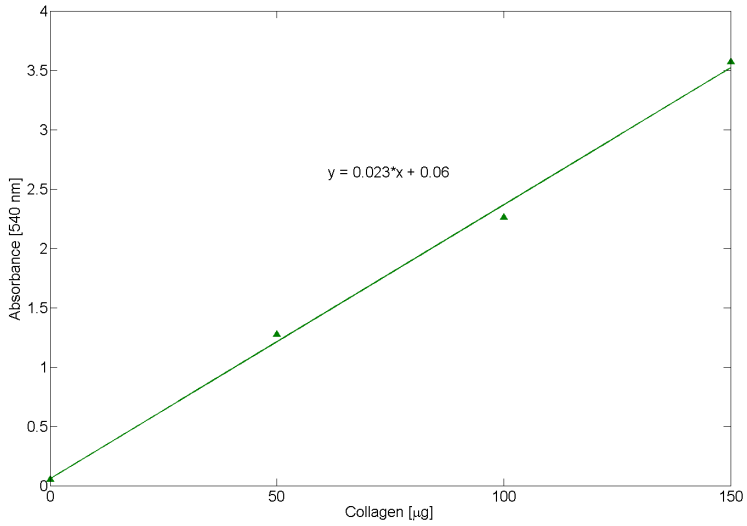

Figure A.5: Culture medium collagen quantification standard curve: stimulation at varying shear stress magnitudes (Section 6.2.2.2).

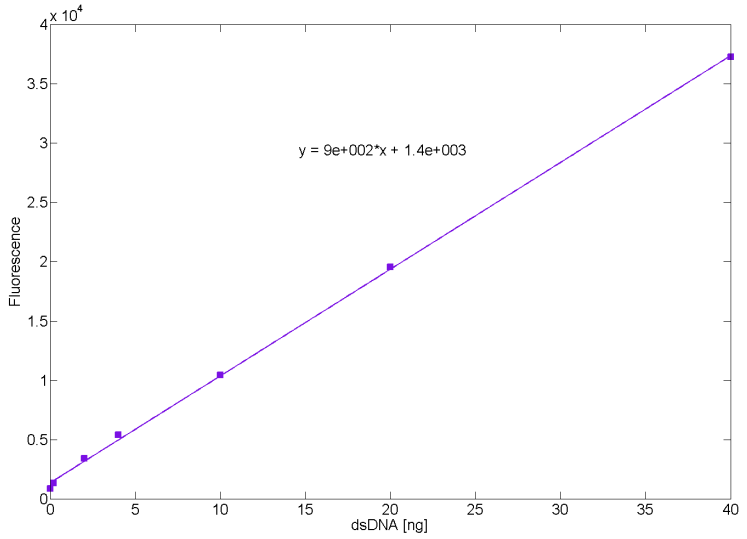

Figure A.6: dsDNA quantification standard curve: stimulation at varying shear stress magnitudes (Section 6.2.2.2).

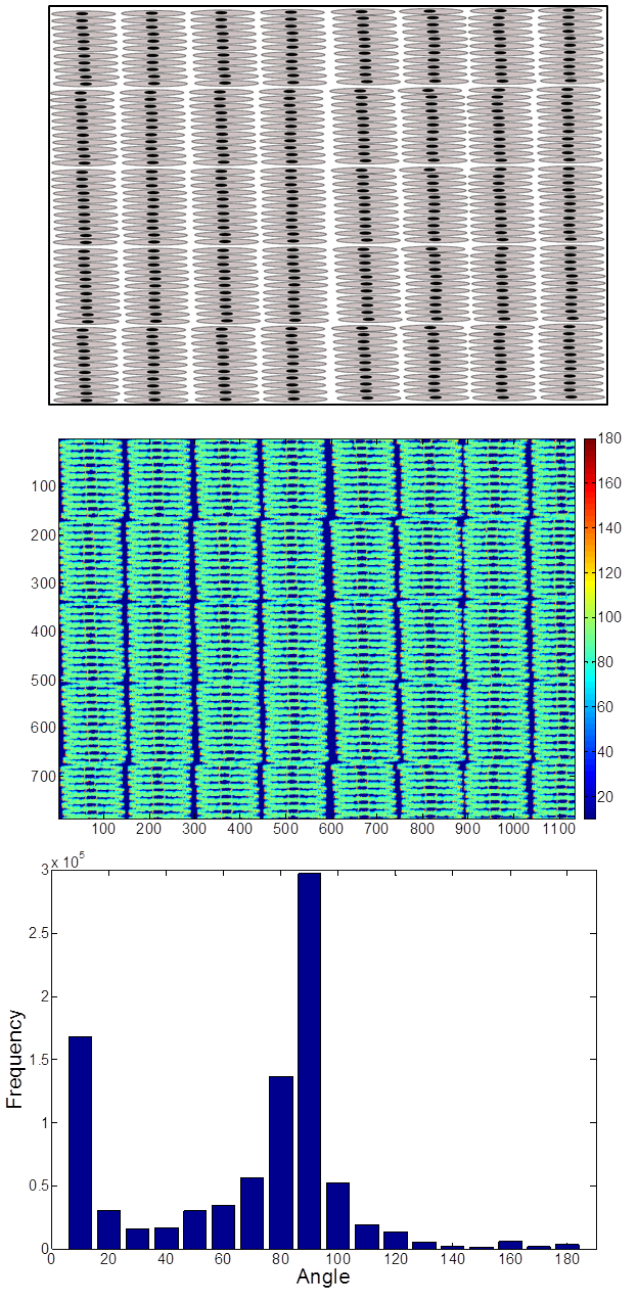

Figure A.7: Alignment algorithm evaluation: Top: cartoon cells are aligned at 90 ° from the y-axis. Middle: Angle map representing the angle where the minimum cumulative intensity variance was calculated. Bottom: Frequency distribution of angle map. A peak at 10 ° is present as when intensity is equal for more than one angle, the lowest angle was reported (Section 6.4).

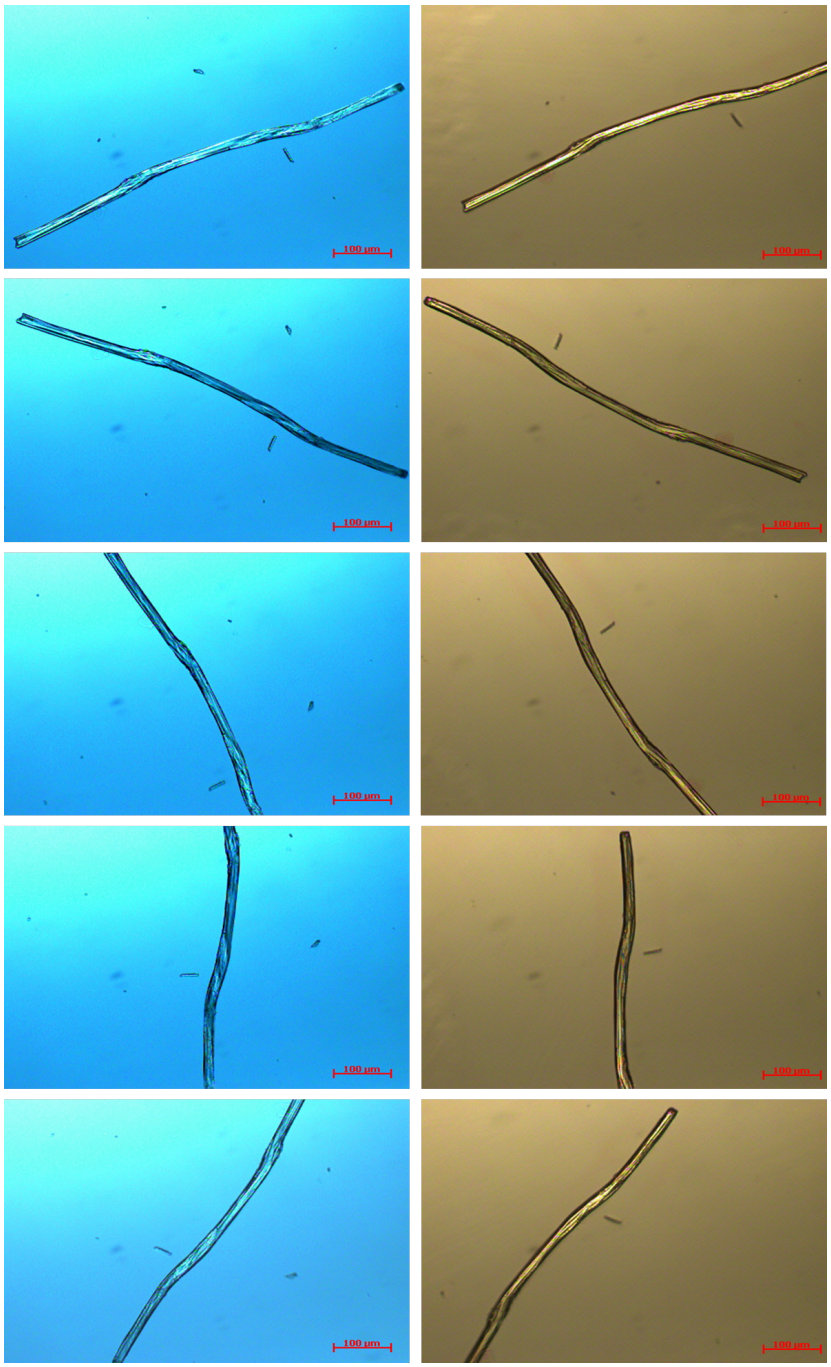

Figure A.8: Collagen birefringence: polarised light microscopy of type I collagen structure, untreated (left) and treated with picrosirius red stain (right). The structure is rotated at different stages of tilt. A change in the refractive index is identified as collagen is birefringent. The picrosirius red stain intensifies the change in refractive index. (Section 7.4.1).

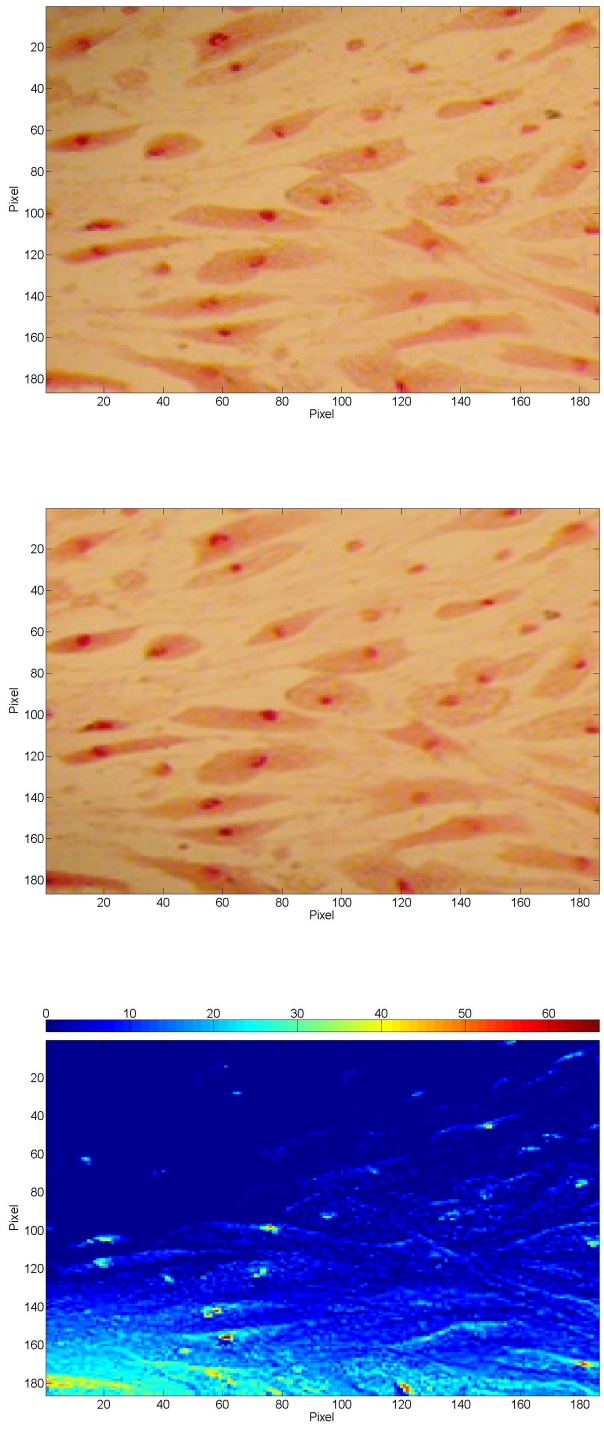

Figure A.9: Collagen birefringence: a polarised light microscope image is taken (top) and then rotated through 90 ° to acquire a second image, rotated back to 0 ° (middle) and the difference between image intensity identified (bottom) (Section 7.4.1).

References

[1] Margareta Nordin and Victor Hirsch Frankel. *Basic biomechanics of the musculoskeletal system.* Wolters Kluwer Health, 2001. 1

[2] RL Duncan and CH Turner. **Mechanotransduction and the functional response of bone to mechanical strain**. *Calcified tissue international*, **57**(5):344–358, 1995. 1

[3] Pauline Beery Mack, Paul A Lacuance, George P Vose, and Fred B Vogt. **Bone demineralization of foot and hand of Gemini-Titan IV, V and VII astronauts during orbital flight**. *American Journal of Roentgenology*, **100**(3):503–511, 1967. 1

[4] Hartmut Krahl, Ulf Michaelis, Hans-Gerd Pieper, Gerhard Quack, and Michael Montag. **Stimulation of Bone Growth Through Sports A Radiologic Investigation of the Upper Extremities in Professional Tennis Players**. *The American journal of sports medicine*, **22**(6):751–757, 1994. 1

[5] John A Kanis, L Joseph Melton, Claus Christiansen, Conrad C Johnston, and Nikolai Khaltaev. **The diagnosis of osteoporosis**. *Journal of Bone and Mineral Research*, **9**(8):1137–1141, 1994. 1

[6] Karim M Khan and Jill L Cook. **Overuse Tendon Injuries:: Where Does the Pain Come From?** *Sports Medicine and Arthroscopy Review*, **8**(1):17–31, 2000. 1

[7] M Kvist. **Achilles tendon injuries in athletes.** In *Annales chirurgiae et gynaecologiae*, **80**, pages 188–201, 1990. 1

[8] W.L. Haskell, I. Lee, et al. **Physical activity and public health. Updated recommendation for adults from the American College of Sports Medicine and the American Heart Association**. *Circulation*, pages CIRCULATIONAHA–107, 2007. 2

[9] Joanne M Archambault, J Preston Wiley, and Robert C Bray. **Exercise loading of tendons and the development of overuse injuries**. *Sports Medicine*, **20**(2):77–89, 1995. 2, 7

[10] GP Riley. **Gene expression and matrix turnover in overused and damaged tendons**. *Scandinavian journal of medicine & science in sports*, **15**(4):241–251, 2005. 2

[11] P. Sharma and N. Maffulli. **Biology of tendon injury: healing, modeling and remodeling**. *JOURNAL OF MUSCULOSKELETAL AND NEURONAL INTERACTIONS*, **6**(2):181, 2006. 2, 4, 5

[12] Pankaj Sharma and Nicola Maffulli. **Tendinopathy and tendon injury: the future**. *Disability & Rehabilitation*, **30**(20-22):1733–1745, 2008. 2

[13] Per Aspenberg. **Stimulation of tendon repair: mechanical loading, GDFs and platelets. A mini-review**. *International orthopaedics*, **31**(6):783–789, 2007. 2

[14] J. H. Wang. **Mechanobiology of tendon**. *Journal of Biomechanics*, **39**(9):1563–82, 2006. 2, 3, 4, 7, 9, 29

[15] JT Shearn, KRC Kinneberg, NA Dyment, MT Galloway, K Kenter, C Wylie, and DL Butler. **Tendon tissue engineering: progress, challenges, and translation to the clinic**. *J Musculoskelet Neuronal Interact*, **11**(2):163–73, 2011. 2

[16] Osnat Hakimi, Pierre-Alexis Mouthuy, and Andrew Carr. **Synthetic and degradable patches: an emerging solution for rotator cuff repair**. *International Journal of Experimental Pathology*, **94**(4):287–292, 2013. 2

[17] Jimin Chen, Jiake Xu, Allan Wang, and Minghao Zheng. **Scaffolds for tendon and ligament repair: review of the efficacy of commercial products**. 2009. 2

[18] K Hampson, NR Forsyth, A El Haj, and N Maffulli. **Tendon tissue engineering**. *E-book: Topics in tissue engineering*, **4**, 2008. 2

[19] Sarah Calve, Robert G Dennis, Paul E Kosnik, Keith Baar, Karl Grosh, and Ellen M Arruda. **Engineering of functional tendon**. *Tissue engineering*, **10**(5-6):755–761, 2004. 2, 20

[20] CH Turner, MR Forwood, and MW Otter. **Mechanotransduction in bone: do bone cells act as sensors of fluid flow?** *The FASEB journal*, **8**(11):875, 1994. 2

[21] S. L. Butler, S. S. Kohles, R. J. Thielke, C. Chen, and Jr. Vanderby, R. **Interstitial fluid flow in tendons or ligaments: a porous medium finite element simulation**. *Med Biol Eng Comput*, **35**(6):742–6, 1997. 2, 32

[22] Chih-Tung Chen, David S Malkus, and Ray Vanderby Jr. **A fiber matrix model for interstitial fluid flow and permeability in ligaments and tendons**. *Biorheology*, **35**(2):103–118, 1998. 2

[23] NP Cohen, RJ Foster, and VC Mow. **Composition and dynamics of articular cartilage: structure, function, and maintaining healthy state.** *The Journal of orthopaedic and sports physical therapy*, **28**(4):203–215, 1998. 2

[24] Albert J Banes, Jerome Gilbert, Duane Taylor, and OLIVIER Monbureau. **A new vacuum-operated stress-providing instrument that applies static or variable duration cyclic tension or compression to cells in vitro**. *Journal of cell science*, **75**(1):35–42, 1985. 2, 24

[25] Tae-Hwa Chun, Hiroshi Itoh, Yoshihiro Ogawa, Naohisa Tamura, Kazuhiko Takaya, Toshio Igaki, Jun Yamashita, Kentaro Doi, Mayumi Inoue, Ken Masatsugu, et al. **Shear stress augments expression of C-type natriuretic peptide and adrenomedullin**. *Hypertension*, **29**(6):1296–1302, 1997. 2, 26

[26] Thomas G Diacovo, Stephen J Roth, Craig T Morita, Jean-Pierre Rosat, Michael B Brenner, and Timothy A Springer. **Interactions of human alpha/beta and gamma/delta T lymphocyte subsets in shear flow with E-selectin and P-selectin.** *The Journal of experimental medicine*, **183**(3):1193–1203, 1996. 2, 26

[27] JA Frangos, LV McIntire, and SG Eskin. **Shear stress induced stimulation of mammalian cell metabolism**. *Biotechnology and Bioengineering*, **32**(8):1053–1060, 1988. 2, 26

[28] Clark T Hung, Solomon R Pollack, Thomas M Reilly, and Carl T Brighton. **Real-time calcium response of cultured bone cells to fluid flow**. *Clinical orthopaedics and related research*, **313**:256–269, 1995. 2, 26

[29] CR Jacobs, CE Yellowley, BR Davis, Z Zhou, JM Cimbala, and HJ Donahue. **Differential effect of steady versus oscillating flow on bone cells**. *Journal of biomechanics*, **31**(11):969–976, 1998. 2, 26, 189

[30] PH Kuijper, HI Gallardo Torres, JA Van Der Linden, JW Lammers, JJ Sixma, L Koenderman, and JJ Zwaginga. **Platelet-dependent primary hemostasis promotes selectin-and integrin-mediated neutrophil adhesion to damaged endothelium under flow conditions**. *Blood*, **87**(8):3271–3281, 1996. 2, 26

[31] MJ Levesque and RM Nerem. **The elongation and orientation of cultured endothelial cells in response to shear stress.** *Journal of biomechanical engineering*, **107**(4):341, 1985. 2, 26

[32] S Li, RS Piotrowicz, EG Levin, YJ Shyy, and S Chien. **Fluid shear stress induces the phosphorylation of small heat shock proteins in vascular endothelial cells**. *American Journal of Physiology-Cell Physiology*, **271**(3):C994–C1000, 1996. 2, 26

[33] Hennessey Tseng, Timothy E Peterson, and Bradford C Berk. **Fluid shear stress stimulates mitogen-activated protein kinase in endothelial cells**. *Circulation research*, **77**(5):869–878, 1995. 2, 26

[34] Thomas D Brown. **Techniques for mechanical stimulation of cells in vitro: a review**. *Journal of biomechanics*, **33**(1):3–14, 2000. 2, 24, 25, 26

[35] R. G. Bacabac, T. H. Smit, S. C. Cowin, J. J. Van Loon, F. T. Nieuwstadt, R. Heethaar, and J. Klein-Nulend. **Dynamic shear stress in parallel-plate flow chambers**. *Journal of Biomechanics*, **38**(1):159–67, 2005. 2, 26, 40, 50, 209

[36] M Mehdi Salek, Pooria Sattari, and Robert J Martinuzzi. **Analysis of fluid flow and wall shear stress patterns inside partially filled agitated culture well plates**. *Annals of biomedical engineering*, **40**(3):707–728, 2012. 2, 25, 82, 201

[37] THOMAS D BROWN, MICHAEL BOTTLANG, DOUGLAS R PEDERSEN, and ALBERT J BANES. **Loading paradigms-intentional and unintentional-for cell culture mechanostimulus**. *The American journal of the medical sciences*, **316**(3):162–168, 1998. 3, 24

[38] M. S. Thompson, S. R. Abercrombie, C. E. Ott, F. H. Bieler, G. N. Duda, and Y. Ventikos. **Quantification and significance of fluid shear stress field in biaxial cell stretching device**. *Biomech Model Mechanobiol*, 2010. Journal article Biomechanics and modeling in mechanobiology Biomech Model Mechanobiol. 2010 Sep 18. 3, 24, 65, 109, 201

[39] P Kannus. **Structure of the tendon connective tissue**. *Scandinavian journal of medicine & science in sports*, **10**(6):312–320, 2000. 3, 29

[40] S. P. Lake, K. S. Miller, D. M. Elliott, and L. J. Soslowsky. **Effect of Fiber Distribution and Realignment on the Nonlinear and Inhomogeneous Mechanical Properties of Human Supraspinatus Tendon under Longitudinal Tensile Loading**. *Journal of Orthopaedic Research*, **27**(12):1596–1602, 2009. 4

[41] Håkan Alfredson and Ronny Lorentzon. **Chronic achilles tendinosis**. *Sports Medicine*, **29**(2):135–146, 2000. 4

[42] P.V. Komi. **Relevance of in vivo force measurements to human biomechanics**. *Journal of Biomechanics*, **23**:23–25, 1990. 4

[43] J. H. Evans and J. C. Barbenel. **Structural and mechanical properties of tendon related to function**. *Equine Vet J*, **7**(1):1–8, 1975. Evans, J H Barbenel, J C England Equine veterinary journal Equine Vet J. 1975 Jan;7(1):1-8. 4

[44] GP Riley, RL Harrall, CR Constant, MD Chard, TE Cawston, and BL Hazleman. **Tendon degeneration and chronic shoulder pain: changes in the collagen composition of the human rotator cuff tendons in rotator cuff tendinitis**. *Annals of the rheumatic diseases*, **53**(6):359, 1994. 4

[45] S. Fukuta, M. Oyama, K. Kavalkovich, F.H. Fu, and C. Niyibizi. **Identification of types II, IX and X collagens at the insertion site of the bovine achilles tendon**. *Matrix biology*, **17**(1):65–73, 1998. 4

[46] L. Jozsa and P. Kannus. *Human tendon: anatomy and physiology and pathology*. Human Kinetics, Champaign, USA, 1997. 4, 8, 9

[47] Lindahl Kjellen and Ulf Lindahl. **Proteoglycans: structures and interactions**. *Annual review of biochemistry*, **60**(1):443–475, 1991. 4

[48] K.G. Vogel and T.J. Koob. **Structural specialization in tendons under compression**. *International review of cytology*, **115**:267–293, 1989. 4

[49] G. D. Pins, D. L. Christiansen, R. Patel, and F. H. Silver. **Self-assembly of collagen fibers. Influence of fibrillar alignment and decorin on mechanical properties**. *Biophysical Journal*, **73**(4):2164–2172, 1997. 4

[50] GP Riley, RL Harrall, CR Constant, MD Chard, TE Cawston, and BL Hazleman. **Glycosaminoglycans of human rotator cuff tendons: changes with age and in chronic rotator cuff tendinitis**. *Annals of the rheumatic diseases*, **53**(6):367, 1994. 4

[51] M. O'Brien. **Structure and metabolism of tendons**. *Scandinavian journal of medicine science in sports*, **7**(2):55–61, 1997. 5

[52] JG Williams. **Achilles tendon lesions in sport.** *Sports medicine (Auckland, NZ)*, **16**(3):216, 1993. 5

[53] M. Benjamin and J.R. Ralphs. **Functional and developmental anatomy of tendons and ligaments**. *Repetitive motion disorders of the upper extremity*, pages 185–203, 1995. 5

[54] L. Jozsa, P. Kannus, JB Balint, and A. Reffy. **Three-Dimensional infrastructure of Human Tendons**. *Cells Tissues Organs*, **142**(4):306–312, 1991. 5

[55] DC Stouffer, DL Butler, and D Hosny. **The relationship between crimp pattern and mechanical response of human patellar tendon-bone units.** *Journal of biomechanical engineering*, **107**(2):158, 1985. 5

[56] Peter Whittaker and Peter B Canham. **Demonstration of quantitative fabric analysis of tendon collagen using two-dimensional polarized light microscopy**. *Matrix*, **11**(1):56–62, 1991. 5

[57] F.H. Silver, J.W. Freeman, and G.P. Seehra. **Collagen self-assembly and the development of tendon mechanical properties**. *Journal of biomechanics*, **36**(10):1529–1553, 2003. 5

[58] SP Magnusson, P Hansen, and M Kjaer. **Tendon properties in relation to muscular activity and physical training**. *Scandinavian journal of medicine & science in sports*, **13**(4):211–223, 2003. 6

[59] J Wilmink, AM Wilson, and AE Goodship. **Functional significance of the morphology and micromechanics of collagen fibres in relation to partial rupture of the superficial digital flexor tendon in racehorses**. *Research in veterinary science*, **53**(3):354–359, 1992. 6

[60] Tishya AL Wren, Gary S Beaupre, Dennis R Carter, et al. **Mechanobiology of tendon adaptation to compressive loading through fibrocartilaginous metaplasia**. *Journal of rehabilitation research and development*, **37**(2):135–144, 2000. 6

[61] Tishya AL Wren, Gary S Beaupre, and Dennis R Carter. **Tendon and ligament adaptation to exercise, immobilization, and remobilization**. *Journal of rehabilitation research and development*, **37**(2):217–224, 2000. 6

[62] COLLEEN M Pollock and ROBERT E Shadwick. **Relationship between body mass and biomechanical properties of limb tendons in adult mammals**. *American Journal of Physiology-Regulatory, Integrative and Comparative Physiology*, **266**(3):R1016–R1021, 1994. 7

[63] L David, Edward S Grood, Frank R Noyes, Ronald E Zernicke, et al. **Biomechanics of ligaments and tendons**. *Exercise and sport sciences reviews*, **6**(1):125–182, 1978. 7

[64] David JS Hulmes. **Building collagen molecules, fibrils, and suprafibrillar structures**. *Journal of structural biology*, **137**(1):2–10, 2002. 7

[65] MB Bennett, RF Ker, Nicola J Imery, and R Alexander. **Mechanical properties of various mammalian tendons**. *Journal of Zoology*, **209**(4):537–548, 1986. 7

[66] Greg A Johnson, Dawn M Tramaglini, Rebecca E Levine, Kazunori Ohno, Nam-Yong Choi, and Savio L-Y Woo. **Tensile and viscoelastic properties of human patellar tendon**. *Journal of Orthopaedic Research*, **12**(6):796–803, 1994. 7

[67] Klaus Hedman, Markku Kurkinen, Kari Alitalo, Antti Vaheri, Staffan Johansson, and Magnus Höök. **Isolation of the pericellular matrix of human fibroblast cultures.** *The Journal of cell biology*, **81**(1):83–91, 1979. 7

[68] Graham Riley. **Chronic tendon pathology: molecular basis and therapeutic implications**. *Expert reviews in molecular medicine*, **7**(5):1–25, 2005. 8

[69] Tyler M Grant, Mark S Thompson, Jill Urban, and Jing Yu. **Elastic fibres are broadly distributed in tendon and highly localized around tenocytes**. *Journal of anatomy*, 2013. 8

[70] Helen K Graham, David F Holmes, Rod B Watson, and Karl E Kadler. **Identification of collagen fibril fusion during vertebrate tendon morphogenesis. The process relies on unipolar fibrils and is regulated by collagen-proteoglycan interaction**. *Journal of molecular biology*, **295**(4):891–902, 2000. 8

[71] George D Pins, David L Christiansen, Raj Patel, and Frederick H Silver. **Self-assembly of collagen fibers. Influence of fibrillar alignment and decorin on mechanical properties**. *Biophysical Journal*, **73**(4):2164–2172, 1997. 8

[72] Christopher A Squier and WH Bausch. **Three-dimensional organization of fibroblasts and collagen fibrils in rat tail tendon**. *Cell and tissue research*, **238**(2):319–327, 1984. 8

[73] Christopher M Larson, Scott S Kelley, A Denene Blackwood, Albert J Banes, and Greta M Lee. **Retention of the native chondrocyte pericellular matrix results in significantly improved matrix production**. *Matrix biology*, **21**(4):349–359, 2002. 8

[74] Stephen P Evanko, Markku I Tammi, Raija H Tammi, and Thomas N Wight. **Hyaluronan-dependent pericellular matrix**. *Advanced drug delivery reviews*, **59**(13):1351–1365, 2007. 8

[75] Olga Camacho Vanegas, Enrico Bertini, Rui-Zhu Zhang, Stefania Petrini, Claudia Minosse, Patrizia Sabatelli, Betti Giusti, Mon-Li Chu, and Guglielmina Pepe. **Ullrich scleroatonic muscular dystrophy is caused by recessive mutations in collagen type VI**. *Proceedings of the National Academy of Sciences*, **98**(13):7516–7521, 2001. 8

[76] G Joost Jöbsis, H Keizers, Jeroen P Vreijling, Marianne de Visser, Marcy C Speer, Ruud A Wolterman, Frank Baas, and Pieter A Bolhuis. **Type VI collagen mutations in Bethlem myopathy, an autosomal dominant myopathy with contractures**. *Nature genetics*, **14**(1):113–115, 1996. 8

[77] Sergio A Jimenez, Elena Hitraya, and John Varga. **Pathogenesis of scleroderma: collagen**. *Rheumatic Disease Clinics of North America*, **22**(4):647–674, 1996. 8

[78] Brendan Lee, Maurice Godfrey, Emilia Vitale, Hisae Hori, Marie-Geneviéve Mattei, Mansoor Sarfarazi, Petros Tsipouras, Francesco Ramirez, and David W Hollister. **Linkage of Marfan syndrome and a phenotypically related disorder to two different fibrillin genes**. *Nature*, **352**(6333):330–334, 1991. 8

[79] P. Renström and RJ Johnson. **Overuse injuries in sports. A review**. *Sports medicine (Auckland, NZ)*, **2**(5):316, 1985. 8

[80] S. Curwin and W.D. Stanish. *Tendinitis: its etiology and treatment*. Collamore Press (Lexington, Mass.), 1984. 8

[81] GP Hess, WL Cappiello, RM Poole, and SC Hunter. **Prevention and treatment of overuse tendon injuries**. *Sports medicine*, **8**(6):371–384, 1989. 8

[82] LJ Micheli and AF Fehlandt. **Overuse injuries to tendons and apophyses in children and adolescents**. *Clinics in sports medicine*, **11**:713–713, 1992. 8

[83] JM Robinson, Jillianne Leigh Cook, Craig Purdam, PJ Visentini, J Ross, Nicola Maffulli, JE Taunton, and KM Khan. **The VISA-A questionnaire: a valid and reliable index of the clinical severity of Achilles tendinopathy**. *British journal of sports medicine*, **35**(5):335–341, 2001. 8

[84] L. Perugia, F. Postacchini, and E. Ippolito. *The tendons: biology, pathology, clinical aspects*. Kurtis, 1986. 9

[85] N. Wang, J.P. Butler, and D.E. Ingber. **Mechanotransduction across the cell surface and through the cytoskeleton**. *Science*, **260**(5111):1124, 1993. 9, 180

[86] Y. Fung. *Biomechanics: mechanical properties of living tissues*, **12**. Springer, 1993. 9

[87] Albert J Banes, Greta Lee, Ronald Graff, Carol Otey, Joanne Archambault, Mari Tsuzaki, Michelle Elfervig, and Jie Qi. **Mechanical forces and signaling in connective tissue cells: cellular mechanisms of detection, transduction, and responses to mechanical deformation**. *Current Opinion in Orthopaedics*, **12**(5):389–396, 2001. 10

[88] M. E. Wall and A. J. Banes. **Early responses to mechanical load in tendon: role for calcium signaling, gap junctions and intercellular communication**. *J Musculoskelet Neuronal Interact*, **5**(1):70–84, 2005. 9, 11

[89] R. Bruzzone, T.W. White, and D.L. Paul. **Connections with connexins: the molecular basis of direct intercellular signaling**. *European Journal of Biochemistry*, **238**(1):1–27, 1996. 11

[90] CM McNeilly, AJ Banes, M Benjamin, and JR Ralphs. **Tendon cells in vivo form a three dimensional network of cell processes linked by gap junctions.** *Journal of anatomy*, **189**(Pt 3):593, 1996. 11

[91] Shaohua Hu, Jianxin Chen, Ben Fabry, Yasushi Numaguchi, Andrew Gouldstone, Donald E Ingber, Jeffrey J Fredberg, James P Butler, and Ning Wang. **Intracellular stress tomography reveals stress focusing and structural anisotropy in cytoskeleton of living cells**. *American Journal of Physiology-Cell Physiology*, **285**(5):C1082–C1090, 2003. 11

[92] D.E. Ingber. **Tensegrity: the architectural basis of cellular mechanotransduction**. *Annual Review of Physiology*, **59**(1):575–599, 1997. 11

[93] Benjamin Geiger, Alexander Bershadsky, Roumen Pankov, and Kenneth M Yamada. **Transmembrane crosstalk between the extracellular matrix and the cytoskeleton**. *Nature Reviews Molecular Cell Biology*, **2**(11):793–805, 2001. 11

[94] KOAO EGB and C lngegneria Genetica. **Mechanotransduction across the cell surface and through the cytoskeleton**. *Science*, **260**:21, 1993. 11

[95] Michelle E Wall, Paul S Weinhold, Tung Siu, Thomas D Brown, and Albert J Banes. **Comparison of cellular strain with applied substrate strain in vitro**. *Journal of biomechanics*, **40**(1):173–181, 2007. 11

[96] K. Burridge and M. Chrzanowska-Wodnicka. **Focal adhesions, contractility, and signaling**. *Annual review of cell and developmental biology*, **12**(1):463–519, 1996. 12

[97] Michelle E Wall, Carol Otey, Jie Qi, and Albert J Banes. **Connexin 43 is localized with actin in tenocytes**. *Cell motility and the cytoskeleton*, **64**(2):121–130, 2007. 12

[98] Kimihide Hayakawa, Hitoshi Tatsumi, and Masahiro Sokabe. **Actin stress fibers transmit and focus force to activate mechanosensitive channels**. *Journal of cell science*, **121**(4):496–503, 2008. 12

[99] F.J. Alenghat and D.E. Ingber. **Mechanotransduction: all signals point to cytoskeleton, matrix, and integrins**. *Sci STKE*, **2002**(119):E6, 2002. 12

[100] Konstantinos A Lazopoulos and Dimitrije Stamenović. **Durotaxis as an elastic stability phenomenon**. *Journal of biomechanics*, **41**(6):1289–1294, 2008. 12

[101] Ben Fabry, Geoffrey N Maksym, James P Butler, Michael Glogauer, Daniel Navajas, and Jeffrey J Fredberg. **Scaling the microrheology of living cells**. *Physical Review Letters*, **87**(14):148102, 2001. 12

[102] Bram G Sengers, Mark Taylor, Colin P Please, and Richard OC Oreffo. **Computational modelling of cell spreading and tissue regeneration in porous scaffolds**. *Biomaterials*, **28**(10):1926–1940, 2007. 12

[103] Chun-Min Lo, Hong-Bei Wang, Micah Dembo, and Yu-li Wang. **Cell movement is guided by the rigidity of the substrate**. *Biophysical journal*, **79**(1):144–152, 2000. 13, 180

[104] Adam S Meshel, Qize Wei, Robert S Adelstein, and Michael P Sheetz. **Basic mechanism of three-dimensional collagen fibre transport by fibroblasts**. *Nature cell biology*, **7**(2):157–164, 2005. 13, 29

[105] Massimo Marenzana, Nick Wilson-Jones, Vivek Mudera, and Robert A Brown. **The origins and regulation of tissue tension: identification of collagen tension-fixation process in vitro**. *Experimental cell research*, **312**(4):423–433, 2006. 13

[106] DENYS N WHEATLEY, AI MEI WANG, and GILLIAN E STRUGNELL. **Expression of primary cilia in mammalian cells**. *Cell biology international*, **20**(1):73–81, 1996. 13

[107] M. Fliegauf, T. Benzing, and H. Omran. **When cilia go bad: cilia defects and ciliopathies (vol 8, pg 880, 2007)**. *Nature Reviews Molecular Cell Biology*, **9**(1):88–88, 2008. 249MA Times Cited:1 Cited References Count:4. 13, 15, 16

[108] K.W. Zimmerman. **Beiträge zur Kenntniss einiger Drüsen und Epithelien**. *Archiv für Mikroskopische Anatomie*, 1898. 13

[109] B.G. Barnes. **Ciliated secretory cells in the pars distalis of the mouse hypophysis**. *Journal of Ultrastructure Research*, **5**(5):453–467, 1961. 13

[110] DN Wheatley. **Primary cilia in normal and pathological tissues**. *Pathobiology*, **63**(4):222–238, 1995. 13

[111] Peter C Harris and Vicente E Torres. **Polycystic kidney disease**. *Annual review of medicine*, **60**:321, 2009. 13

[112] R. Ross and S.J. Klebanoff. **Fine structural changes in uterine smooth muscle and fibroblasts in response to estrogen**. *The Journal of cell biology*, **32**(1):155, 1967. 13, 14

[113] BE Brooker, LG Goodwin, and MW Guy. **Ciliated fibroblasts in rabbit ear chambers**. *Journal of Anatomy*, **110**(Pt 3):363, 1971. 13, 14

[114] W. Beertsen, V. Everts, and JM Houtkooper. **Frequency of occurrence and position of cilia in fibroblasts of the periodontal ligament of the mouse incisor**. *Cell and Tissue Research*, **163**(4):415–431, 1975. 13, 14

[115] Eve Donnelly, Maria-Grazia Ascenzi, and Cornelia Farnum. **Primary cilia are highly oriented with respect to collagen direction and long axis of extensor tendon**. *Journal of Orthopaedic Research*, **28**(1):77–82, 2010. 13

[116] Veena Singla and Jeremy F Reiter. **The primary cilium as the cell's antenna: signaling at a sensory organelle**. *science*, **313**(5787):629–633, 2006. 13

[117] C. A. Poole, M. H. Flint, and B. W. Beaumont. **Analysis of the morphology and function of primary cilia in connective tissues: a cellular cybernetic probe?** *Cell Motil*, **5**(3):175–93, 1985. 15

[118] D.T. Moran, F.J. Varela, and J.C. Rowley. **Evidence for active role of cilia in sensory transduction**. *Proceedings of the National Academy of Sciences*, **74**(2):793, 1977. 15

[119] G. Dalagiorgou, E.K. Basdra, and A.G. Papavassiliou. **Polycystin-1: Function as a mechanosensor**. *The International Journal of Biochemistry & Cell Biology*, **42**(10):1610–1613, 2010. 16

[120] A. Malone, C.T. Anderson, P. Tummala, R.Y. Kwon, T.R. Johnston, T. Stearns, and C.R. Jacobs. **Primary cilia mediate mechanosensing in bone cells by a calcium-independent mechanism**. *Proceedings of the National Academy of Sciences*, **104**(33):13325, 2007. 15, 143, 189, 193, 210

[121] G.C. Reilly, T.R. Haut, C.E. Yellowley, H.J. Donahue, and C.R. Jacobs. **Fluid flow induced PGE 2 release by bone cells is reduced by glycocalyx degradation whereas calcium signals are not**. *Biorheology*, **40**(6):591–604, 2003. 15

[122] K. Gardner, S. P. Arnoczky, and M. Lavagnino. **Effect of in vitro stress-deprivation and cyclic loading on the length of tendon cell cilia in situ**. *J Orthop Res*, 2010. Journal article Journal of orthopaedic research : official publication of the Orthopaedic Research Society J Orthop Res. 2010 Oct 18. 15

[123] A. Resnick and U. Hopfer. **Force-response considerations in ciliary mechanosensation**. *Biophys J*, **93**(4):1380–90, 2007. 15

[124] S. Rydholm, G. Zwartz, J.M. Kowalewski, P. Kamali-Zare, T. Frisk, and H. Brismar. **Mechanical properties of primary cilia regulate the response to fluid flow**. *American Journal of Physiology-Renal Physiology*, **298**(5):F1096, 2010. 17

[125] D. Chen, D. Norris, and Y. Ventikos. **The active and passive ciliary motion in the embryo node: A computational fluid dynamics model**. *Journal of Biomechanics*, **42**(3):210–216, 2009. 411NZ Times Cited:0 Cited References Count:44. 17

[126] E. A. Schwartz, M. L. Leonard, R. Bizios, and S. S. Bowser. **Analysis and modeling of the primary cilium bending response to fluid shear**. *American Journal of Physiology-Renal Physiology*, **41**(1):F132–F138, 1997. 17, 18

[127] B. Martinac. **Mechanosensitive ion channels: molecules of mechanotransduction**. *Journal of cell science*, **117**(12):2449, 2004. 18

[128] Bertil Hille. *Ion channels of excitable membranes*, **507**. Sinauer Sunderland, MA, 2001. 18

[129] A Mobasheri, S Carter, P Martin-Vasallo, and M Shakibaei. **Integrins and stretch activated ion channels; putative components of functional cell surface mechanoreceptors in articular chondrocytes**. *Cell biology international*, **26**:1–18, 2002. 18

[130] J.J. Katz and W.C. Halstead. **Protein organization and mental function**. *Comp. Psychol. Monogr*, 1950. 18

[131] M.C. Gustin, X.L. Zhou, B. Martinac, and C. Kung. **A mechanosensitive ion channel in the yeast plasma membrane**. *Science*, **242**(4879):762, 1988. 18

[132] M. Sokabe and F. Sachs. **The structure and dynamics of patch-clamped membranes: a study using differential interference contrast light microscopy.** *The Journal of cell biology*, **111**(2):599, 1990. 18

[133] M. Sokabe, F. Sachs, and ZQ Jing. **Quantitative video microscopy of patch clamped membranes stress, strain, capacitance, and stretch channel activation**. *Biophysical journal*, **59**(3):722–728, 1991. 18

[134] O.P. Hamill and D.W. McBride Jr. **Induced membrane hypo/hyper-mechanosensitivity: a limitation of patch-clamp recording**. *Annual review of physiology*, **59**(1):621–631, 1997. 18

[135] Sheldon Weinbaum, John M Tarbell, and Edward R Damiano. **The structure and function of the endothelial glycocalyx layer**. *Annu. Rev. Biomed. Eng.*, **9**:121–167, 2007. 18

[136] J.M. Squire, M. Chew, G. Nneji, C. Neal, J. Barry, and C. Michel. **Quasi-periodic substructure in the microvessel endothelial glycocalyx: A possible explanation for molecular filtering?** *Journal of structural biology*, **136**(3):239–255, 2001. 18

[137] S. Weinbaum, X. Zhang, Y. Han, H. Vink, and S. C. Cowin. **Mechanotransduction and flow across the endothelial glycocalyx**. *Proc Natl Acad Sci U S A*, **100**(13):7988–95, 2003. 19

[138] J.M. Tarbell and MY Pahakis. **Mechanotransduction and the glycocalyx**. *Journal of internal medicine*, **259**(4):339–350, 2006. 19

[139] P. Sharma and N. Maffulli. **Tendon injury and tendinopathy: healing and repair**. *J Bone Joint Surg Am*, **87**(1):187–202, 2005. 19, 29

[140] Matthew D Shoulders and Ronald T Raines. **Collagen structure and stability**. *Annual review of biochemistry*, **78**:929, 2009. 19

[141] Endre A Balazs. *Chemistry and molecular biology of the intercellular matrix*, **3**. Academic Press, 1970. 20

[142] Jean-Paul Revel and Elizabeth D Hay. **An autoradiographic and electron microscopic study of collagen synthesis in differentiating cartilage**. *Zeitschrift für Zellforschung und mikroskopische Anatomie*, **61**(1):110–144, 1963. 20

[143] EG Canty and KE Kadler. **Collagen fibril biosynthesis in tendon: a review and recent insights**. *Comparative Biochemistry and Physiology-Part A: Molecular & Integrative Physiology*, **133**(4):979–985, 2002. 20

[144] Elizabeth G Canty and Karl E Kadler. **Procollagen trafficking, processing and fibrillogenesis**. *Journal of cell science*, **118**(7):1341–1353, 2005. 20, 21

[145] D.E. Birk, M.V. Nurminskaya, and E.I. Zycband. **Collagen fibrillogenesis in situ: Fibril segments undergo post depositional modifications resulting in linear and lateral growth during matrix development**. *American Journal of Anatomy*, **202**(3):229–243, 1995. 20

[146] S Murad, D Grove, KA Lindberg, G Reynolds, A Sivarajah, and SR Pinnell. **Regulation of collagen synthesis by ascorbic acid**. *Proceedings of the National Academy of Sciences*, **78**(5):2879–2882, 1981. 20

[147] Beverly Peterkofsky. **The effect of ascorbic acid on collagen polypeptide synthesis and proline hydroxylation during the growth of cultured fibroblasts**. *Archives of biochemistry and biophysics*, **152**(1):318–328, 1972. 20

[148] Richard H Gelberman, Paul R Manske, Jerry S Vande Berg, Peggy A Lesker, and Wayne H Akeson. **Flexor tendon repair in vitro: a comparative histologic study of the rabbit, chicken, dog, and monkey**. *Journal of orthopaedic research*, **2**(1):39–48, 1984. 20

[149] PAUL R Manske, RH Gelberman, JS Vande Berg, and PA Lesker. **Intrinsic flexor-tendon repair**. *J Bone Joint Surg A*, **66**:385–396, 1984. 20

[150] Jean E Russell and Paul R Manske. **Collagen synthesis during primate flexor tendon repair in vitro**. *Journal of orthopaedic research*, **8**(1):13–20, 1990. 20

[151] Hideki Tanaka, Paul R Manske, Donald L Pruitt, and Brian J Larson. **Effect of cyclic tension on lacerated flexor tendons in vitro**. *The Journal of hand surgery*, **20**(3):467–473, 1995. 20

[152] Eduardo L Abreu, Diane Leigh, and Kathleen A Derwin. **Effect of altered mechanical load conditions on the structure and function of cultured tendon fascicles**. *Journal of Orthopaedic Research*, **26**(3):364–373, 2008. 20

[153] Jo A Hannafin, Steven P Arnoczky, Amardeep Hoonjan, and Peter A Torzilli. **Effect of stress deprivation and cyclic tensile loading on the material and morphologic properties of canine flexor digitorum profundus tendon: an in vitro study**. *Journal of orthopaedic research*, **13**(6):907–914, 1995. 20

[154] Hazel RC Screen, Julia C Shelton, Dan L Bader, and David A Lee. **Cyclic tensile strain upregulates collagen synthesis in isolated tendon fascicles**. *Biochemical and biophysical research communications*, **336**(2):424–429, 2005. 20

[155] Hazel RC Screen, DL Bader, DA Lee, and Julia C Shelton. **Local strain measurement within tendon**. *Strain*, **40**(4):157–163, 2004. 20, 29

[156] Hazel RC Screen, Julia C Shelton, Vivek H Chhaya, Michael V Kayser, Dan L Bader, and David A Lee. **The influence of noncollagenous matrix components on the micromechanical environment of tendon fascicles**. *Annals of biomedical engineering*, **33**(8):1090–1099, 2005. 20

[157] HRC Screen, DA Lee, DL Bader, and JC Shelton. **An investigation into the effects of the hierarchical structure of tendon fascicles on micromechanical properties**. *Proceedings of the Institution of Mechanical Engineers, Part H: Journal of Engineering in Medicine*, **218**(2):109–119, 2004. 20

[158] E Yamamoto, K Hayashi, and N Yamamoto. **Mechanical properties of collagen fascicles from the rabbit patellar tendon.** *Journal of biomechanical engineering*, **121**(1):124–131, 1999. 20

[159] Steven P Arnoczky, Michael Lavagnino, Joanne H Whallon, and Amardeep Hoonjan. **In situ cell nucleus deformation in tendons under tensile load; a morphological analysis using confocal laser microscopy**. *Journal of orthopaedic research*, **20**(1):29–35, 2002. 20

[160] SA Goodman, SA May, D Heinegård, and RKW Smith. **Tenocyte response to cyclical strain and transforming growth factor beta is dependent upon age and site of origin**. *Biorheology*, **41**(5):613–628, 2004. 20

[161] Louis Lippiello. **Collagen synthesis in tenocytes, ligament cells and chondrocytes exposed to a combination of glucosamine HCl and chondroitin sulfate**. *Evidence-Based Complementary and Alternative Medicine*, **4**(2):219–224, 2007. 20

[162] Nanette Scutt, Christer G Rolf, and Andrew Scutt. **Glucocorticoids inhibit tenocyte proliferation and tendon progenitor cell recruitment**. *Journal of orthopaedic research*, **24**(2):173–182, 2006. 20

[163] Charles A Vacanti, Yi Lin Cao, Robert S Langer, Joseph P Vacanti, Keith Paige, and Joseph Upton. **Tissue engineered tendons and ligaments**, September 26 2000. US Patent 6,123,727. 20

[164] S-i Kurata and R Hata. **Epidermal growth factor inhibits transcription of type I collagen genes and production of type I collagen in cultured human skin fibroblasts in the presence and absence of L-ascorbic acid 2-phosphate, a long-acting vitamin C derivative.** *Journal of Biological Chemistry*, **266**(15):9997–10003, 1991. 20

[165] JH Yoon, J Halper, et al. **Tendon proteoglycans: biochemistry and function**. *J Musculoskelet Neuronal Interact*, **5**(1):22–34, 2005. 22

[166] John Parkinson, Tom Samiric, MZ Ilic, Jillianne Cook, and CJ Handley. **Involvement of proteoglycans in tendinopathy**. *The Journal of Musculoskeletal and Neuronal Interactions*, **11**(2):86–93, 2011. 22

[167] Elizabeth D Hay. *Cell biology of extracellular matrix*. Springer, 1991. 22

[168] Gerd Binnig, Calvin F Quate, and Ch Gerber. **Atomic force microscope**. *Physical review letters*, **56**(9):930, 1986. 22

[169] Thomas Gutsmann, Georg E Fantner, Johannes H Kindt, Manuela Venturoni, Signe Danielsen, and Paul K Hansma. **Force spectroscopy of collagen fibers to investigate their mechanical properties and structural organization**. *Biophysical journal*, **86**(5):3186–3193, 2004. 22

[170] José Luis Alonso and Wolfgang H Goldmann. **Feeling the forces: atomic force microscopy in cell biology**. *Life sciences*, **72**(23):2553–2560, 2003. 22

[171] Eric Henderson, PG Haydon, and DS Sakaguchi. **Actin filament dynamics in living glial cells imaged by atomic force microscopy**. *American Association for the Advancement of Science*, pages 1944–1944, 1992. 22

[172] Daniel J Müller and Yves F Dufrene. **Atomic force microscopy as a multifunctional molecular toolbox in nanobiotechnology**. *Nature nanotechnology*, **3**(5):261–269, 2008. 22

[173] Stefan W Schneider, Kumudesh C Sritharan, John P Geibel, Hans Oberleithner, and Bhanu P Jena. **Surface dynamics in living acinar cells imaged by atomic force microscopy: identification of plasma membrane structures involved in exocytosis**. *Proceedings of the National Academy of Sciences*, **94**(1):316–321, 1997. 22

[174] Valerie M Laurent, Sylvie Hénon, Emmanuelle Planus, Redouane Fodil, Martial Balland, Daniel Isabey, and Francois Gallet. **Assessment of mechanical properties of adherent living cells by bead micromanipulation: comparison of magnetic twisting cytometry vs optical tweezers.** *Journal of biomechanical engineering*, **124**(4):408–421, 2002. 23

[175] G Bao and S Suresh. **Cell and molecular mechanics of biological materials**. *Nature materials*, **2**(11):715–725, 2003. 23

[176] Ben Fabry, Geoffrey N Maksym, Rolf D Hubmayr, James P Butler, and Jeffrey J Fredberg. **Implications of heterogeneous bead behavior on cell mechanical properties measured with magnetic twisting cytometry**. *Journal of magnetism and magnetic materials*, **194**(1):120–125, 1999. 23

[177] Evan A Evans and Robert M Hochmuth. **A solid-liquid composite model of the red cell membrane**. *The Journal of membrane biology*, **30**(1):351–362, 1976. 23

[178] Robert M Hochmuth. **Micropipette aspiration of living cells**. *Journal of biomechanics*, **33**(1):15–22, 2000. 23

[179] Didier P Theret, MJ Levesque, M Sato, RM Nerem, and LT Wheeler. **The application of a homogeneous half-space model in the analysis of endothelial cell micropipette measurements.** *Journal of biomechanical engineering*, **110**(3):190–199, 1988. 23

[180] M Bottlang, M Simnacher, H Schmitt, RA Brand, and L Claes. **A Cell Strain System for Small Homogeneous Strain Applications**. *Biomedizinische Technik/Biomedical Engineering*, **42**(11):305–309, 1997. 24

[181] DB Jones, H Nolte, JG Scholübbers, E Turner, and D Veltel. **Biochemical signal transduction of mechanical strain in osteoblast-like cells**. *Biomaterials*, **12**(2):101–110, 1991. 24, 25

[182] C Neidlinger-Wilke, HJ Wilke, and L Claes. **Dynamic stretching of human osteoblasts: an experimental model for in vitro simulation of fracture gap micromotion**. *Journal of Orthopaedic Research*, **12**:70–78, 1994. 24

[183] ANDREW A Pitsillides, SC Rawlinson, RF Suswillo, S Bourrin, G Zaman, and LE Lanyon. **Mechanical strain-induced NO production by bone cells: a possible role in adaptive bone (re) modeling?** *The FASEB journal*, **9**(15):1614–1622, 1995. 24

[184] Jonathan L Schaffer, Michael Rizen, Gilbert J L'Italien, Aziz Benbrahim, Joseph Megerman, Louis C Gerstenfeld, and Martha L Gray. **Device for the application of a dynamic biaxially uniform and isotropic strain to a flexible cell culture membrane**. *Journal of Orthopaedic Research*, **12**(5):709–719, 1994. 24

[185] Herman H Vandenburgh. **A computerized mechanical cell stimulator for tissue culture: effects on skeletal muscle organogenesis**. *In vitro cellular & developmental biology*, **24**(7):609–619, 1988. 24

[186] THOMAS D BROWN, MICHAEL BOTTLANG, DOUGLAS R PEDERSEN, and ALBERT J BANES. **Development and Experimental Validationof a Fluid/Structure-Interaction Finite Element Model of a Vacuum-Driven Cell Culture Mechanostimulus System**. *Computer methods in biomechanics and biomedical engineering*, **3**(1):65–78, 2000. 24

[187] N Caille, Y Tardy, and JJ Meister. **Assessment of strain field in endothelial cells subjected to uniaxial deformation of their substrate**. *Annals of biomedical engineering*, **26**(3):409–416, 1998. 25

[188] DYM Leung, S Glagov, and MB Mathews. **A new in vitro system for studying cell response to mechanical stimulation: different effects of cyclic stretching and agitation on smooth muscle cell biosynthesis**. *Experimental cell research*, **109**(2):285–298, 1977. 25

[189] Mohammad Sotoudeh, Shila Jalali, Shunichi Usami, John YJ Shyy, and Shu Chien. **A strain device imposing dynamic and uniform equi-biaxial strain to cultured cells**. *Annals of biomedical engineering*, **26**(2):181–189, 1998. 25

[190] DK Bynum, M Tsuzaki, X Yang, A Sood, TD Brown, A Ross, P Weinhold, and AJ Banes. **Inhibiting intercellular communication blocks wound induced mitogenesis in flexor tendons**. In *Transaction of 45th Annual Meeting Orthopaedic Research Society*, page 44, 1999. 25

[191] Eric Mourgeon, Jing Xu, A Keith Tanswell, Mingyao Liu, and Martin Post. **Mechanical strain-induced posttranscriptional regulation of fibronectin production in fetal lung cells**. *American Journal of Physiology-Lung Cellular and Molecular Physiology*, **277**(1):L142–L149, 1999. 25

[192] Santa J Tumminia, Kenneth P Mitton, Jaspreet Arora, Peggy Zelenka, David L Epstein, and Paul Russell. **Mechanical stretch alters the actin cytoskeletal network and signal transduction in human trabecular meshwork cells.** *Investigative ophthalmology & visual science*, **39**(8):1361–1371, 1998. 25

[193] Alan Dardik, Leiling Chen, Jared Frattini, Hidenori Asada, Faisal Aziz, Fabio A Kudo, and Bauer E Sumpio. **Differential effects of orbital and laminar shear stress on endothelial cells**. *Journal of vascular surgery*, **41**(5):869–880, 2005. 25

[194] Larry W Kraiss, Andrew S Weyrich, Neal M Alto, Dan A Dixon, Tina M Ennis, Vijayanand Modur, Thomas M McIntyre, Stephen M Prescott, and Guy A Zimmerman. **Fluid flow activates a regulator of translation, p70/p85 S6 kinase, in human endothelial cells**. *American Journal of Physiology-Heart and Circulatory Physiology*, **278**(5):H1537–H1544, 2000. 25

[195] WG Owen and CT Esmon. **Functional properties of an endothelial cell cofactor for thrombin-catalyzed activation of protein C.** *Journal of Biological Chemistry*, **256**(11):5532–5535, 1981. 25

[196] Michael J Pearce, Thomas M McIntyre, Stephen M Prescott, Guy A Zimmerman, and Ralph E Whatley. **Shear Stress Activates Cytosolic Phospholipase A2 (cPLA2) and MAP Kinase in Human Endothelial Cells**. *Biochemical and biophysical research communications*, **218**(2):500–504, 1996. 25

[197] RM Delaine-Smith, S Macneil, and GC Reilly. **Matrix production and collagen structure are enhanced in two types of osteogenic progenitor cells by a simple fluid shear stress stimulus**. *European cells & materials*, **24**:162–174, 2012. 26, 201

[198] David A Hoey, Daniel J Kelly, and Christopher R Jacobs. **A role for the primary cilium in paracrine signaling between mechanically stimulated osteocytes and mesenchymal stem cells**. *Biochemical and biophysical research communications*, **412**(1):182–187, 2011. 26, 189, 201

[199] X. Zhou, D. Liu, L. You, and L. Wang. **Quantifying fluid shear stress in a rocking culture dish**. *Journal of Biomechanics*, **43**(8):1598–1602, 2010. 26, 79, 201

[200] James N Topper, Jiexing Cai, Yubin Qiu, Keith R Anderson, Yong-Yao Xu, James D Deeds, Roslyn Feeley, Carlos J Gimeno, Elizabeth A Woolf, Olga Tayber, et al. **Vascular MADs: two novel MAD-related genes selectively inducible by flow in human vascular endothelium**. *Proceedings of the National Academy of Sciences*, **94**(17):9314–9319, 1997. 26

[201] Steven R Bussolari, C Forbes Dewey, and Michael A Gimbrone. **Apparatus for subjecting living cells to fluid shear stress**. *Review of Scientific Instruments*, **53**(12):1851–1854, 1982. 26

[202] CF Dewey Jr. **Effects of fluid flow on living vascular cells.** *Journal of biomechanical engineering*, **106**(1):31, 1984. 26

[203] A van van Grondelle, G SCOTT Worthen, DONALD Ellis, MELVIN M Mathias, ROBERT C Murphy, ROBERT J Strife, JOHN T Reeves, and NORBERT F Voelkel. **Altering hydrodynamic variables influences PGI2 production by isolated lungs and endothelial cells**. *Journal of Applied Physiology*, **57**(2):388–395, 1984. 26

[204] M Mohtai, MK Gupta, B Donlon, B Ellison, J Cooke, G Gibbons, DJ Schurman, and R Lane Smith. **Expression of interleukin-6 in osteoarthritic chondrocytes and effects of fluid-induced shear on this expression in normal human chondrocytes in vitro**. *Journal of Orthopaedic Research*, **14**(1):67–73, 1996. 26

[205] Peter Angele, Detlef Schumann, Martin Angele, Bernd Kinner, Carsten Englert, Reiner Hente, Bernd Füchtmeier, Michael Nerlich, Carsten Neumann, and Richard

Kujat. **Cyclic, mechanical compression enhances chondrogenesis of mesenchymal progenitor cells in tissue engineering scaffolds**. *Biorheology*, **41**(3):335–346, 2004. 27

[206] Steven R Caliari, Daniel W Weisgerber, Manuel A Ramirez, Douglas O Kelkhoff, and Brendan AC Harley. **The influence of collagen–glycosaminoglycan scaffold relative density and microstructural anisotropy on tenocyte bioactivity and transcriptomic stability**. *Journal of the Mechanical Behavior of Biomedical Materials*, **11**:27–40, 2012. 27

[207] JMR Tilley, S Chaudhury, O Hakimi, AJ Carr, and JT Czernuszka. **Tenocyte proliferation on collagen scaffolds protects against degradation and improves scaffold properties**. *Journal of Materials Science: Materials in Medicine*, **23**(3):823–833, 2012. 27

[208] Dejun Cao, Wei Liu, Xian Wei, Feng Xu, Lei Cui, and Yilin Cao. **In vitro tendon engineering with avian tenocytes and polyglycolic acids: a preliminary report**. *Tissue engineering*, **12**(5):1369–1377, 2006. 27, 30

[209] Joanne Garvin, Jie Qi, Melissa Maloney, and Albert J Banes. **Novel system for engineering bioartificial tendons and application of mechanical load**. *Tissue engineering*, **9**(5):967–979, 2003. 27, 150

[210] Gregory N Bancroft, Vassilios I Sikavitsas, and Antonios G Mikos. **Technical note: Design of a flow perfusion bioreactor system for bone tissue-engineering applications**. *Tissue Engineering*, **9**(3):549–554, 2003. 28

[211] Jerry Bonham-Carter and Jerry Shevitz. **A Brief History of Perfusion Biomanufacturing**. *BioProcess Int*, **9**(9), 2011. 28

[212] Guoping Chen, Takashi Ushida, and Tetsuya Tateishi. **Scaffold design for tissue engineering**. *Macromolecular Bioscience*, **2**(2):67–77, 2002. 28

[213] Scott J Hollister. **Porous scaffold design for tissue engineering**. *Nature materials*, **4**(7):518–524, 2005. 28

[214] Dietmar W Hutmacher. **Scaffold design and fabrication technologies for engineering tissues—state of the art and future perspectives**. *Journal of Biomaterials Science, Polymer Edition*, **12**(1):107–124, 2001. 28

[215] KF Leong, CM Cheah, and CK Chua. **Solid freeform fabrication of three-dimensional scaffolds for engineering replacement tissues and organs**. *Biomaterials*, **24**(13):2363–2378, 2003. 28

[216] D.W. Hutmacher and H. Singh. **Computational fluid dynamics for improved bioreactor design and 3D culture**. *Trends in biotechnology*, **26**(4):166–172, 2008. 28

[217] Sarah H Cartmell, Blaise D Porter, Andrés J García, and Robert E Guldberg. **Effects of medium perfusion rate on cell-seeded three-dimensional bone constructs in vitro**. *Tissue engineering*, **9**(6):1197–1203, 2003. 28

[218] Cynthia M Begley and Stanley J Kleis. **The fluid dynamic and shear environment in the NASA/JSC rotating-wall perfused-vessel bioreactor**. *Biotechnology and bioengineering*, **70**(1):32–40, 2000. 28

[219] Yanming Bi, Driss Ehirchiou, Tina M Kilts, Colette A Inkson, Mildred C Embree, Wataru Sonoyama, Li Li, Arabella I Leet, Byoung-Moo Seo, Li Zhang, et al. **Identification of tendon stem/progenitor cells and the role of the extracellular matrix in their niche**. *Nature medicine*, **13**(10):1219–1227, 2007. 29

[220] Yun-Feng Rui, Pauline Po Yee Lui, Gang Li, Sai Chuen Fu, Yuk Wa Lee, and Kai Ming Chan. **Isolation and characterization of multipotent rat tendon-derived stem cells**. *Tissue Engineering Part A*, **16**(5):1549–1558, 2010. 29

[221] Denitsa Docheva, Ernst B Hunziker, Reinhard Fässler, and Oliver Brandau. **Tenomodulin is necessary for tenocyte proliferation and tendon maturation**. *Molecular and cellular biology*, **25**(2):699–705, 2005. 29

[222] James HC Wang, Qianping Guo, and Bin Li. **Tendon biomechanics and mechanobiology—a minireview of basic concepts and recent advancements**. *Journal of Hand Therapy*, **25**(2):133–141, 2012. 29, 30

[223] Ernesto Ippolito, Pier Giorgio Natali, Franco Postacchini, Lidia Accinni, and Cesare De Martino. **Morphological, immunochemical, and biochemical study of rabbit achilles tendon at various ages**. *The Journal of Bone & Joint Surgery*, **62**(4):583–598, 1980. 29

[224] Andreas Herchenhan, Nicholas S Kalson, David F Holmes, Patrick Hill, Karl E Kadler, and Lee Margetts. **Tenocyte contraction induces crimp formation in tendon-like tissue**. *Biomechanics and modeling in mechanobiology*, **11**(3-4):449–459, 2012. 29

[225] SL Woo, THAY Q Lee, STEVEN D Abramowitch, and THOMAS W Gilbert. **Structure and function of ligaments and tendons**. *Basic orthopaedic biomechanics and mechano-biology. Philadelphia: Lippincott Williams & Wilkins*, pages 301–42, 2005. 29, 32

[226] Pierre-Olivier Bagnaninchi, Ying Yang, Alicia J El Haj, and Nicola Maffulli. **Tissue engineering for tendon repair**. *British journal of sports medicine*, **41**(8):e10–e10, 2007. 29

[227] Thilo John, Dörte Lodka, Benjamin Kohl, Wolfgang Ertel, Jennifer Jammrath, Claudia Conrad, Christiane Stoll, Catharina Busch, and Gundula Schulze-Tanzil. **Effect of pro-inflammatory and immunoregulatory cytokines on human tenocytes**. *Journal of Orthopaedic Research*, **28**(8):1071–1077, 2010. 29

[228] Michael Lavagnino, Steven P Arnoczky, Tao Tian, and Zachary Vaupel. **Effect of amplitude and frequency of cyclic tensile strain on the inhibition of MMP-1 mRNA expression in tendon cells: an in vitro study**. *Connective tissue research*, **44**(3-4):181–187, 2003. 29, 31, 33

[229] Zhaozhu Li, Guoguang Yang, Mustafa Khan, David Stone, Savio LY Woo, and James HC Wang. **Inflammatory response of human tendon fibroblasts to cyclic mechanical stretching**. *The American journal of sports medicine*, **32**(2):435–440, 2004. 29, 31

[230] James H-C Wang, Fengyan Jia, Guoguang Yang, Shaohua Yang, Brian H Campbell, David Stone, and Savio L-Y Woo. **Cyclic mechanical stretching of human tendon fibroblasts increases the production of prostaglandin E 2 and levels of cyclooxygenase expression: a novel in vitro model study**. *Connective tissue research*, **44**(3-4):128–133, 2003. 29

[231] James H-C Wang, Bhavani P Thampatty, Jeen-Shang Lin, and Hee-Jeong Im. **Mechanoregulation of gene expression in fibroblasts**. *Gene*, **391**(1):1–15, 2007. 29

[232] Guoguang Yang, Richard C Crawford, and James HC Wang. **Proliferation and collagen production of human patellar tendon fibroblasts in response to cyclic uniaxial stretching in serum-free conditions**. *Journal of biomechanics*, **37**(10):1543–1550, 2004. 29

[233] Johannes Zeichen, Martijn van Griensven, and Ulrich Bosch. **The proliferative response of isolated human tendon fibroblasts to cyclic biaxial mechanical strain**. *The American journal of sports medicine*, **28**(6):888–892, 2000. 29

[234] D Mehr, PD Pardubsky, JA Martin, and JA Buckwalter. **Tenascin-C in tendon regions subjected to compression**. *Journal of Orthopaedic Research*, **18**(4):537–545, 2000. 29

[235] James HC Wang, Zhaozhu Li, Guoguang Yang, and Mustafa Khan. **Repetitively stretched tendon fibroblasts produce inflammatory mediators**. *Clinical orthopaedics and related research*, **422**:243–250, 2004. 31

[236] Isaiah Adekanmbi, Sarah Franklin, and Mark S Thompson. **A novel in vitro loading system for high frequency loading of cultured tendon fascicles**. *Medical engineering & physics*, 2012. 31

[237] Steven P Arnoczky, Michael Lavagnino, Monika Egerbacher, Oscar Caballero, and Keri Gardner. **Matrix metalloproteinase inhibitors prevent a decrease in the mechanical properties of stress-deprived tendons an in vitro experimental study**. *The American journal of sports medicine*, **35**(5):763–769, 2007. 31

[238] E Francke, A Banes, M Elfervig, T Brown, and D Bynum. **Fluid induced shear stress increases [Ca 2+] ic in cultured human tendon epitenon cells**. In *Transactions of the 46th Annual Meeting of the Orthopaedic Research Society*, **25**, page 638, 2000. 31

[239] MLM Elfervig, M Tsuzaki, J Faber, and A Banes. **Fluid-induced shear stress modulates cx-43 expression in avian tendon cells but does not induce a ca2+ signal**. In *47th Annual Meeting, Orthopaedic research society*, **26**, page 570, 2001. 31, 172

[240] J. M. Archambault, M. K. Elfervig-Wall, M. Tsuzaki, W. Herzog, and A. J. Banes. **Rabbit tendon cells produce MMP-3 in response to fluid flow without significant calcium transients**. *Journal of Biomechanics*, **35**(3):303–309, 2002. 31

[241] K. D. Fong, M. C. Trindade, Z. Wang, R. P. Nacamuli, H. Pham, T. D. Fang, H. M. Song, R. L. Smith, M. T. Longaker, and J. Chang. **Microarray analysis of mechanical shear effects on flexor tendon cells**. *Plast Reconstr Surg*, **116**(5):1393–404; discussion 1405–6, 2005. 31

[242] Kenton D Fong, Hung Pham, Michael C Trindade, Zhen Wang, Hanjoon M Song, Tony D Fang, Randall P Nacamuli, R Lane Smith, Michael T Longaker, and James Chang. **Fluid-Induced Shear Stress Effects on Tenocyte Biology**. 2003. 31

[243] Timothy Molloy, Yao Wang, and George AC Murrell. **The roles of growth factors in tendon and ligament healing**. *Sports Medicine*, **33**(5):381–394, 2003. 31

[244] Chee Ping Ng, Boris Hinz, and Melody A Swartz. **Interstitial fluid flow induces myofibroblast differentiation and collagen alignment in vitro**. *Journal of cell science*, **118**(20):4731–4739, 2005. 32, 33

[245] P Bagnaninchi, Y Yang, N Maffulli, RK Wang, and A El Haj. **Three-dimensional culture of tenocytes in uniaxial microchannels for tendon engineering**. *Journal of Bone & Joint Surgery, British Volume*, **90**(SUPP III):501–501, 2008. 32

[246] Jo A Hannafin and Steven P Arnoczky. **Effect of cyclic and static tensile loading on water content and solute diffusion in canine flexor tendons: an in vitro study**. *Journal of orthopaedic research*, **12**(3):350–356, 1994. 32

[247] KG Helmer, G Nair, M Cannella, and P Grigg. **Water movement in tendon in response to a repeated static tensile load using one-dimensional magnetic resonance imaging**. *Journal of biomechanical engineering*, **128**(5):733–741, 2006. 32

[248] Y Lanir, EL Salant, and A Foux. **Physico-chemical and microstructural changes in collagen fiber bundles following stretch in-vitro.** *Biorheology*, **25**(4):591, 1988. 32

[249] TS Atkinson, RC Haut, and NJ Altiero. **A poroelastic model that predicts some phenomenological responses of ligaments and tendons.** *Journal of biomechanical engineering*, **119**(4):400–405, 1997. 32

[250] Paul S Robinson, Tony W Lin, Abbas F Jawad, Renato V Iozzo, and Louis J Soslowsky. **Investigating tendon fascicle structure–function relationships in a transgenic-age mouse model using multiple regression models**. *Annals of biomedical engineering*, **32**(7):924–931, 2004. 32, 33

[251] Tammy L Haut and Roger C Haut. **The state of tissue hydration determines the strain-rate-sensitive stiffness of human patellar tendon**. *Journal of biomechanics*, **30**(1):79–81, 1997. 32

[252] NJ Giori, GS Beaupre, and DR Carter. **Cellular shape and pressure may mediate mechanical control of tissue composition in tendons**. *Journal of orthopaedic research*, **11**(4):581–591, 1993. 32

[253] M. Lavagnino, S. P. Arnoczky, E. Kepich, O. Caballero, and R. C. Haut. **A finite element model predicts the mechanotransduction response of tendon cells to cyclic tensile loading**. *Biomech Model Mechanobiol*, **7**(5):405–16, 2008. 32

[254] LE Lanyon, WG Hampson, AE Goodship, and JS Shah. **Bone deformation recorded in vivo from strain gauges attached to the human tibial shaft.** *Acta Orthopaedica Scandinavica*, **46**(2):256, 1975. 32

[255] EH Burger and JP Veldhuijzen. **Influence of mechanical factors on bone formation, resorption and growth in vitro**. *Bone: Bone Growth-B*, **7**:37–56, 1993. 32

[256] J. You, CE Yellowley, HJ Donahue, Y. Zhang, Q. Chen, and CR Jacobs. **Substrate deformation levels associated with routine physical activity are less stimulatory to bone cells relative to loading-induced oscillatory fluid flow**. *Journal of biomechanical engineering*, **122**:387, 2000. 32, 33

[257] Y. Han, S.C. Cowin, M.B. Schaffler, and S. Weinbaum. **Mechanotransduction and strain amplification in osteocyte cell processes**. *Proceedings of the National Academy of Sciences of the United States of America*, **101**(47):16689, 2004. 33

[258] Stefano P Bachmann, Kacy VandeWalle, Gordon Ramage, Thomas F Patterson, Brian L Wickes, John R Graybill, and José L López-Ribot. **In vitro activity of caspofungin against Candida albicans biofilms**. *Antimicrobial agents and chemotherapy*, **46**(11):3591–3596, 2002. 34

[259] Jeff G Leid, Mark E Shirtliff, JW Costerton, and Paul Stoodley. **Human leukocytes adhere to, penetrate, and respond to Staphylococcus aureus biofilms**. *Infection and immunity*, **70**(11):6339–6345, 2002. 34

[260] Akihiro Yoshida and Howard K Kuramitsu. **Multiple Streptococcus mutans genes are involved in biofilm formation**. *Applied and environmental microbiology*, **68**(12):6283–6291, 2002. 34

[261] Bruce Roy Munson, Donald F Young, and Theodore Hisao Okiishi. *Fundamentals of fluid mechanics*. New York, 1990. 40

[262] Osborne Reynolds. **An experimental investigation of the circumstances which determine whether the motion of water shall be direct or sinuous, and of the law of resistance in parallel channels.** *Proceedings of the Royal Society of London*, **35**(224-226):84–99, 1883. 40

[263] M Hanif Chaudhry. *Open-channel flow*. Springer, 2008. 40, 79

[264] JP Van Doormaal and GD Raithby. **Enhancements of the SIMPLE method for predicting incompressible fluid flows**. *Numerical Heat Transfer*, **7**:147–163, 1984. 46

[265] G. Lonsdale and A. Schueller. **Multigrid efficiency for complex flow simulations on distributed memory machines**. *Parallel computing*, **19**(1):23–32, 1993. 46

[266] C.W. Hirt and B.D. Nichols. **Volume of fluid (VOF) method for the dynamics of free boundaries* 1**. *Journal of computational physics*, **39**(1):201–225, 1981. 53

[267] William F Noh and Paul Woodward. **SLIC (simple line interface calculation)**. In *Proceedings of the Fifth International Conference on Numerical Methods in Fluid Dynamics June 28–July 2, 1976 Twente University, Enschede*, pages 330–340. Springer, 1976. 53

[268] ESI. **CFD-ACE V2011 User's Manual, ESI-CFD Inc**. *Huntsville, AL*, 2011. 56, 80

[269] Aikaterini Pachi and Tianjian Ji. **Frequency and velocity of people walking**. *Structural Engineer*, **83**(3), 2005. 81

[270] Matthew D Ford, Hristo N Nikolov, Jaques S Milner, Stephen P Lownie, Edwin M DeMont, Wojciech Kalata, Francis Loth, David W Holdsworth, and David A Steinman. **PIV-measured versus CFD-predicted flow dynamics in anatomically realistic cerebral aneurysm models**. *Journal of biomechanical engineering*, **130**(2):21015, 2008. 82

[271] Jian Sheng, Hui Meng, and Rodney O Fox. **Validation of CFD simulations of a stirred tank using particle image velocimetry data**. *The Canadian Journal of Chemical Engineering*, **76**(3):611–625, 1998. 82

[272] Gonçalo Silva, Nuno Leal, and Viriato Semiao. **Micro-PIV and CFD characterization of flows in a microchannel: velocity profiles, surface roughness and Poiseuille numbers**. *International Journal of Heat and Fluid Flow*, **29**(4):1211–1220, 2008. 82

[273] C Van Ertbruggen, P Corieri, R Theunissen, ML Riethmuller, and C Darquenne. **Validation of CFD predictions of flow in a 3D alveolated bend with experimental data**. *Journal of biomechanics*, **41**(2):399–405, 2008. 82

[274] Richard J Bomphrey, Nicholas J Lawson, Graham K Taylor, and Adrian LR Thomas. **Application of digital particle image velocimetry to insect aerodynamics: measurement of the leading-edge vortex and near wake of a hawkmoth**. *Experiments in fluids*, **40**(4):546–554, 2006. 82

[275] Gal Berkooz, Philip Holmes, and John L Lumley. **The proper orthogonal decomposition in the analysis of turbulent flows**. *Annual review of fluid mechanics*, **25**(1):539–575, 1993. 89

[276] Mamdouh T Ghannam and M Nabil Esmail. **Rheological properties of carboxymethyl cellulose**. *Journal of applied polymer science*, **64**(2):289–301, 1997. 109

[277] P. Torricelli, M. Fini, G. Giavaresi, A. Carpi, A. Nicolini, and R. Giardino. **Effects of systemic glucocorticoid administration on tenocytes**. *Biomedicine & pharmacotherapy*, **60**(8):380–385, 2006. 137

[278] L. Yao, CS Bestwick, LA Bestwick, N. Maffulli, and RM Aspden. **Phenotypic drift in human tenocyte culture**. *Tissue Engineering*, **12**(7):1843–1849, 2006. 138

[279] L CxU Junqueira, G Bignolas, and RR Brentani. **Picrosirius staining plus polarization microscopy, a specific method for collagen detection in tissue sections**. *The Histochemical journal*, **11**(4):447–455, 1979. 140

[280] R.W. Farndale, C.A. Sayers, and A.J. Barrett. **A direct spectrophotometric microassay for sulfated glycosaminoglycans in cartilage cultures**. *Connective tissue research*, **9**(4):247–248, 1982. 140

[281] R.W. Farndale, D.J. Buttle, and A.J. Barrett. **Improved quantitation and discrimination of sulphated glycosaminoglycans by use of dimethylmethylene blue**. *Biochimica et Biophysica Acta (BBA)-General Subjects*, **883**(2):173–177, 1986. 140

[282] Jeremy M LaMothe and Ronald F Zernicke. **Rest insertion combined with high-frequency loading enhances osteogenesis**. *Journal of Applied Physiology*, **96**(5):1788–1793, 2004. 148

[283] Albert J Banes, Mari Tsuzaki, Juro Yamamoto, Brian Brigman, Thomas Fischer, Thomas Brown, and Larry Miller. **Mechanoreception at the cellular level: the detection, interpretation, and diversity of responses to mechanical signals**. *Biochemistry and Cell Biology*, **73**(7-8):349–365, 1995. 156

[284] Jizhe Hao and Patrick Delmas. **Multiple desensitization mechanisms of mechanotransducer channels shape firing of mechanosensory neurons**. *The Journal of Neuroscience*, **30**(40):13384–13395, 2010. 156

[285] MA Ros, FB Rivero, JR Hinchliffe, and JM Hurle. **Immunohistological and ultrastructural study of the developing tendons of the avian foot**. *Anatomy and embryology*, **192**(6):483–496, 1995. 174

[286] Andrew D Waggett, Michael Benjamin, and James R Ralphs. **Connexin 32 and 43 gap junctions differentially modulate tenocyte response to cyclic mechanical load**. *European journal of cell biology*, **85**(11):1145–1154, 2006. 179

[287] MJ Levesque and RM Nerem. **The elongation and orientation of cultured endothelial cells in response to shear stress**. *Journal of Biomechanical Engineering*, **107**:341, 1985. 180, 187

[288] Amir Shamloo, Ning Ma, Mu-ming Poo, Lydia L Sohn, and Sarah C Heilshorn. **Endothelial cell polarization and chemotaxis in a microfluidic device**. *Lab on a chip*, **8**(8):1292–1299, 2008. 180, 187

[289] T. Yamaguchi, Y. Yamamoto, and H. Liu. **Computational mechanical model studies on the spontaneous emergent morphogenesis of the cultured endothelial cells**. *Journal of Biomechanics*, **33**(1):115–126, 2000. 180, 187

[290] John Canny. **A computational approach to edge detection**. *Pattern Analysis and Machine Intelligence, IEEE Transactions on*, (6):679–698, 1986. 180

[291] C Neidlinger-Wilke, ES Grood, JH-C Wang, RA Brand, and L Claes. **Cell alignment is induced by cyclic changes in cell length: studies of cells grown in cyclically stretched substrates**. *Journal of Orthopaedic Research*, **19**(2):286–293, 2001. 180

[292] CJ Creighton, MPF Sutcliffe, and TW Clyne. **A multiple field image analysis procedure for characterisation of fibre alignment in composites**. *Composites Part A: Applied Science and Manufacturing*, **32**(2):221–229, 2001. 182

[293] C.T. Anderson, A.B. Castillo, S.A. Brugmann, J.A. Helms, C.R. Jacobs, and T. Stearns. **Primary cilia: cellular sensors for the skeleton**. *The Anatomical Record: Advances in Integrative Anatomy and Evolutionary Biology*, **291**(9):1074–1078, 2008. 189

[294] E. Donnelly, M. G. Ascenzi, and C. Farnum. **Primary cilia are highly oriented with respect to collagen direction and long axis of extensor tendon**. *Journal of Orthopaedic Research*, **28**(1):77–82, 2010. 536WG Times Cited:1 Cited References Count:38. 189, 193

[295] Olga V Plotnikova, Elena N Pugacheva, and Erica A Golemis. **Primary cilia and the cell cycle**. *Methods in cell biology*, **94**:137–160, 2009. 189

[296] HA Praetorius and Kenneth R Spring. **Removal of the MDCK cell primary cilium abolishes flow sensing**. *The Journal of membrane biology*, **191**(1):69–76, 2003. 189

[297] Håkan Alfredson. **Chronic midportion Achilles tendinopathy: an update on research and treatment**. *Clinics in sports medicine*, **22**(4):727–741, 2003. 202

[298] Nicola Maffulli, Jason Wong, and Louis C Almekinders. **Types and epidemiology of tendinopathy**. *Clinics in sports medicine*, **22**(4):675–692, 2003. 202

[299] Tero AH Järvinen, Pekka Kannus, Nicola Maffulli, and Karim M Khan. **Achilles tendon disorders: etiology and epidemiology**. *Foot and ankle clinics*, **10**(2):255–266, 2005. 202

[300] P Reilly, I Macleod, R Macfarlane, J Windley, and RJH Emery. **Dead men and radiologists don't lie: a review of cadaveric and radiological studies of rotator cuff tear prevalence**. *Annals of the royal college of surgeons of England*, **88**(2):116, 2006. 202

[301] Nicola Maffulli, Pankaj Sharma, and Karen L Luscombe. **Achilles tendinopathy: aetiology and management**. *JRSM*, **97**(10):472–476, 2004. 202

[302] Bangshang Zhu, Qinghua Lu, Jie Yin, Jun Hu, and Zongguang Wang. **Alignment of osteoblast-like cells and cell-produced collagen matrix induced by nanogrooves**. *Tissue engineering*, **11**(5-6):825–834, 2005. 206

The page numbers upon which the reference appears are included after the reference entry.

These are hyperlinked on the digital copy.

Declaration

I, Russell Peter Tucker, confirm that the work presented in this thesis has been performed and interpreted solely by myself except where explicitly identified to the contrary. I confirm that this work is submitted in fulfilment for the degree of Doctor of Philosophy in Engineering Science and has not been submitted elsewhere in any other form for the fulfilment of any other degree or qualification.

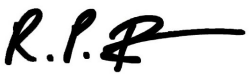

R P Tucker

Trinity 2013